

# Quantitative approaches to unravel bone marrow adipocyte site-specificity and its implication in hematopoiesis

Présentée le 14 février 2020

à la Faculté des sciences de la vie  
Groupe Naveiras  
Programme doctoral en biotechnologie et génie biologique

pour l'obtention du grade de Docteur ès Sciences

par

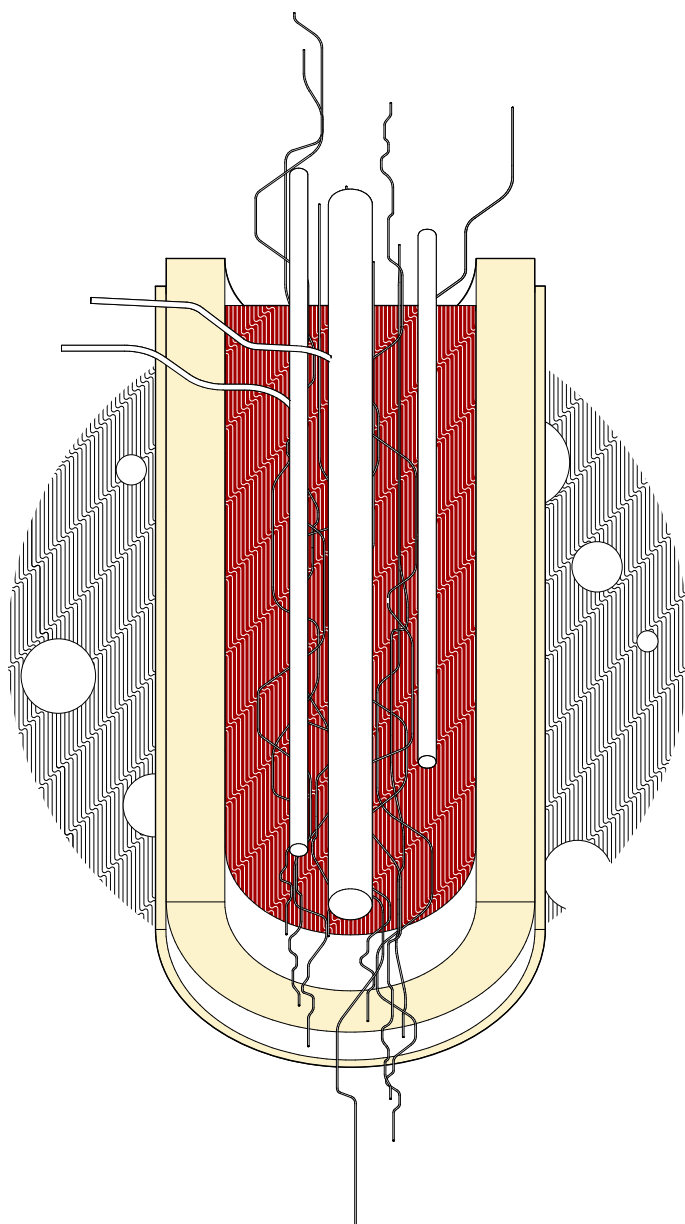
**Josefine Catharina Pedersen TRATWAL**

Acceptée sur proposition du jury

Prof. D. Pioletti, président du jury  
Prof. O. M. Naveiras Torres-Quiroga, directrice de thèse  
Prof. L. De Leval, rapporteuse  
Prof. C. J. Rosen, rapporteur  
Prof. C. Briskin, rapporteuse







Previous page:  
Carlheinz Von Geyso, *Bone Marrow Architecture*, 2019, illustration in Revit, Cape Town.

*To my parents,*  
for their endless love –  
who have shown us the world,  
and encourage us to find our way.

*To my brother,*  
for his lightness of spirit –  
who shares his passions  
and compassion readily with others.

*To my person,*  
for revealing the essence of dreams –  
who is my anchor,  
when I am swayed by the winds.



## Preface

On my road to science I've been blessed with many remarkable role-models and friends.

First, it was *my mother* who passionately engaged with me in the workings of chemistry and biology at the kitchen table after school. Later it would be my wonderful *teachers*, of high-school chemistry, Rebecca Bechard, who ignited in me a deep curiosity for the understanding of science, and then Annette Ekblond who patiently managed to mold me into a young medical researcher throughout my master thesis. I'm deeply grateful and remember the years fondly that I've been fortunate to learn from these incredible women.

“Every beginning is only a sequel, after all.” – Wysława Szymborska

As my first introduction to this new world, the Betz family were incredible *early role-models* in science and art. I was encouraged to write a school essay on Rudolf Virchow, the father of pathology, which first sparked my curiosity for patho/physiology. From there on and since my first understanding of stem cells, I was mesmerized and couldn't turn back.

I've been privileged to have opportunities that placed me in the company of many great scientists, not only at international meetings from early on but also through summer programs during my studies. I formed the first adult friendships with motivational and empathetic study-partners (Therese Julin and Julie Jacobsen) who understood the importance of supporting each other and keeping spirits high. At the same time, I also cherished the friendship of Viktor Avlon, open to all and any musings under the blue and star-filled *Copenhagen* skies. Ann-Kirstine Thor-Straten and Tine Schaer Popp have never wavered from my side, even when I decided to move to another country. While I was gaining my footing at university, I attended a summer school in *Berlin* where I would meet a handful of like-minded girls from different corners of the world (Aischarya Brahma, Aurora Bernal, Danijela Kostic, Anabela Cepa Areias), and with whom I would marvel at the seemingly endless possibilities of tissue engineering. Again, I found myself captivated by the wonders of science, and this time, of translational research.

I met other great scientists on my way, at the Center for Medical Research in *Barcelona* where I was a young student in awe of the pace and possibilities of science. I appreciate the attention that especially Núria Montserrat, Marianna Vita, Laetitia de la Lluna, and Erika Lorenzo Vivas gave a young intern seemingly lost in the big world of stem cell research. This moment in time would also serendipitously lead me to meet first Monica McCoy, then Borja Arañó Riba, and years later Bente Malmberg and Maria Trullàs whose constant support from afar has meant the world and more importantly, with whom years later I would celebrate momentous life events.

The European Summer School for Stem Cells and Regenerative Medicine in *Hydra* is somehow where it really all began on an island in the Aegean Sea, that cemented my pursuit for stem cell research and led me to EPFL. Here, Yann Barrandon would introduce me to my future thesis supervisor.

Aside from scientific experiences (and meeting many more influential people that cannot all be made mention of here), I know the importance of *friends* and sometimes in extension also their caring families.

There is a value in relationships from way back when that persevere throughout the years. From *Warsaw* to Tokyo, to Amsterdam, to Ho Chi Minh City, and back to Copenhagen, Hiromi Mizuki, Nora Goppel, Hieu Nguyen, and Ingrid Christoffersen have shown me the significance in nurturing such connections.

By chance, one of my first encounters in *Lausanne* hailed from the Swiss Plasma Center (Umar Sheikh), whose kind heart presented me to many more (Pedro Molina Cabrera, Cedric Tsui, Aylwin Iantchenko, Hugo De Oliveira, Hamish Patten, Federico Nespoli, amongst many others). This community has flavored life on- and off-campus through their openness and laughs that abound. Even scientific collaborations during my thesis have planted the seeds for true friendships to blossom. The path was made more colorful by the fantastic ladies: Olha Novokhatska, Magda Zachara, Pernille Yde Rainer, and Shanti Rojas-Sutterlin. Their positivity and encouragement is enormously uplifting.

I'm also lucky to know Carlheinz Von Geyso, which was a meeting of two kindred souls that has since taken root and grown from deepest darkest Africa. Meanwhile, Paola Paruta has been my earthly protector from the very first time we met. I immensely appreciate her loyalty and vivacity, and for introducing me to Justin Ball who always manages to bring a smile to my lips.

As with any chapter in one's life there have been some hardships along the way. However also these pass.

“The cure for anything is salt water – sweat, tears, and the sea.” – Karen Blixen

Thankfully I have been fortunate to be by *the oceans and seas* on multiple occasions over the past years. This has brought immense joy accompanied with new outlooks. I've also had friends who pushed me to sweat beyond my comfort. Taking up climbing in its many forms has taught me strength and perseverance. My *fellow climbers* (particularly Kristina Gkintzou and Manuela Arici) not only showed me the ropes but are always ready to provide a fresh breath and perspective. Another important outlet and saving grace have been experiences with other *music aficionados* (especially those whose music is transcending as that of Florian Majcherczyk and Hendrik van Boetzelear), providing a relief when I didn't know I needed it. They have reminded me how important it is not only to share one's passions and also to submit to unforgettable fun, but to open the world to inclusivity, acceptance, and metamorphosis through freedom of expression. All of these channels have received me, including the tears, so that I could unfold and progress toward what awaited next.

I am grateful to have landed in Switzerland, for the (literal and figurative) mountains I have summited, the friendships I have formed, and the people I have been able to work with while embarking on a wonderfully exciting research topic. In the following pages I hope to share if just a sliver of my passion for biomedicine in the form of some of the experiments carried out during my doctorate to study the adipocytic and stromal niche of the bone marrow in regenerative hematopoiesis.

*Josefine Tratwal*

Lausanne, 19<sup>th</sup> of November 2019







## Abstract

Over the last decade, bone marrow (BM) adipose tissue (BMAT) has emerged as a distinct adipose depot with unique metabolic properties and effects both in homeostasis and in the progression of disease.

We provide a first comprehensive review of existing and emerging technologies including accompanying challenges for the study of bone marrow adipocytes (BMAd). The recommendations specified through this consensus opinion for standardization of methodological approaches are imperative on our quest to uncover the meaning, the sense, and the significance of BMAd. Due to its challenging localization within the bone and its fragile nature, imaging methods provide powerful tools for *ex vivo* or *in vivo* BMAT quantification as well as characterization through lipid profiling. While isolation methods are still evolving in the pursuit of *the* BMAd and its progenitor, lineage tracing and BMAT (environmental, pharmacological, or pathological) modulation studies have identified two sub-populations of BMAd dependent on skeletal location in the hematopoietic red or fatty yellow marrow.

We uncover changes to these compartments in the mouse skeleton with age or irradiation and bone marrow transplantation induced aplastic conversion of the marrow, through our novel imaging quantification tool for histological sections. Following this progression by magnetic resonance imaging *in vivo* emphasized a differential hematopoietic recovery within the long bones of mice. In order to delineate the subtle differences between BMAd of red and fatty marrow, we established first an adipocytic differentiation, and then a co-culture system to recapitulate the BM niche *in vitro* with the OP9 stromal cell line. Notably, Raman microspectroscopic analysis revealed nuances of lipid saturation levels previously reported in primary BMAd at the single droplet level that we propose is indicative of their maturation state. This may have implication for the documented differential hematopoietic support capacity of BMAd that we elucidate through co-culture with hematopoietic stem and progenitor cells. We were able to translate the established co-culture system onto a three-dimensional scaffold for construction of a tissue-engineered BM model. In combination with a novel approach for preparation of its *in vivo* injection, we have established the direct *in vitro* to *in vivo* transfer of a biomimetic BM niche.

The novel methodological approaches presented here to study BMAd and the hematopoietic microenvironment, have far-reaching applications for improving the outcome of BM disease modeling, biomolecular and drug screening, as well as in regenerative medicine at large.

## Keywords

skeletal | bone marrow | adipocyte | lipid | stroma | stem and progenitor cell  
hematopoiesis | microenvironment | transplantation | model | imaging



## Résumé

Au cours de la dernière décennie, le tissu adipeux de la moelle osseuse (BMAT) est devenu un dépôt adipeux distinct avec des propriétés métaboliques uniques et des effets à la fois sur l'homéostasie et la progression de la maladie.

Nous fournissons un premier examen complet des technologies existantes et émergentes, y compris des défis pour l'étude des adipocytes de la moelle osseuse (BMAd). Les recommandations spécifiées dans cet avis de consensus pour la normalisation des approches méthodologiques sont impératives dans notre quête pour découvrir le sens, le sens et la signification des BMAd. En raison de leur localisation difficile dans l'os et de leur nature fragile, les méthodes d'imagerie fournissent des outils puissants pour la quantification *ex vivo* ou *in vivo* du BMAT, ainsi que pour la caractérisation par profil lipidique. Bien que les méthodes d'isolement évoluent dans la poursuite du BMAd et de ses progéniteurs, des études de traçage de lignage et de modulation du BMAT (environnementales, pharmacologiques ou pathologiques) ont permis d'identifier deux sous-populations de BMAd dépendant de la localisation du squelette dans la rouge moelle hématopoïétique ou jaune moelle grasse.

Nous découvrons des modifications de ces compartiments dans le squelette de la souris avec l'âge ou l'irradiation et la conversion aplastique induite par la greffe de moelle osseuse, grâce à notre nouvel outil de quantification d'imagerie pour les coupes histologiques. Suite à cette progression par imagerie par résonance magnétique *in vivo*, une récupération hématopoïétique différentielle au sein des os longs de souris a été soulignée. Afin de délimiter les différences subtiles entre les BMAd de la moelle hématopoïétique et de la moelle adipeuse, nous avons d'abord établi une différenciation adipocytaire, puis un système de co-culture permettant de récapituler la niche de BM *in vitro* avec des cellules stromales OP9. L'analyse de Raman microspectroscopique a notamment révélé des nuances au niveaux de saturation lipidique précédemment rapportés dans les BMAd primaires au niveau d'une seule gouttelette que nous proposons est révélateur de leur état de maturation. Cela pourrait avoir des implications pour la capacité documentée de support différenciée hématopoïétique des BMAds que nous élucidons par co-culture avec des cellules souches et progénitrices hématopoïétiques. Nous avons pu traduire le système de co-culture établi sur un échafaudage tridimensionnel pour la construction d'un modèle de BM à ingénierie tissulaire. En combinaison avec une nouvelle approche pour la préparation de son injection *in vivo*, nous avons établi le transfert direct *in vitro* à *in vivo* d'une niche biomimétique de BM.

Les nouvelles approches méthodologiques présentées ici pour étudier les BMAd et le microenvironnement hématopoïétique ont de nombreuses applications pour améliorer les résultats de la modélisation de la maladie, du criblage biomoléculaire et médicamenteux, ainsi que de la médecine régénérative en général.

### Mots-clés

squelette | moelle osseuse | adipocyte | lipide | stroma | cellules souches et progénitrice  
hématopoïèse | microenvironnement | transplantation | modèle | imagerie



## Zusammenfassung

In den letzten zehn Jahren hat sich das Fettgewebe des Knochenmarks (BMAT) als eigenständiges Fettdepot mit einzigartigen metabolischen Eigenschaften und Auswirkungen sowohl auf die Homöostase als auch auf das Fortschreiten der Erkrankung herauskristallisiert.

Wir bieten einen ersten umfassenden Überblick über bestehende und aufkommende Technologien, einschließlich begleitender Herausforderungen für die Untersuchung von Knochenmark Adipozyten (BMAds). Die in dieser Konsensmeinung enthaltenen Empfehlungen zur Standardisierung methodischer Ansätze sind für unser Bestreben, den Sinn und die Bedeutung von BMAds aufzudecken, von entscheidender Bedeutung. Aufgrund seiner schwierigen Lokalisierung im Knochen und seiner Fragilität bieten bildgebende Verfahren leistungsstarke Werkzeuge für die *ex vivo* oder *in vivo* BMAT-Quantifizierung sowie die Charakterisierung durch Lipidprofilierung. Während sich Isolierungsmethoden bei der Verfolgung des BMAd und seines Vorläufers noch weiterentwickeln, haben Studien zur Herkunftsverfolgung und BMAT (Umwelt-, Pharmakologische oder Pathologische) Modulationen zwei Subpopulationen von BMAds identifiziert, die von der Skelettllokation im hämatopoetischen roten oder fettgelben Knochenmark abhängen.

Mit unserem neuartigen bildgebenden Quantifizierungsinstrument für histologische Schnitte decken wir Veränderungen dieser Kompartimente im Mausskelett mit dem Alter oder der Bestrahlung sowie Knochenmarktransplantationen auf, die eine aplastische Umwandlung des Marks bewirken. Im Anschluss an dieses Fortschreiten durch Magnetresonanztomographie *in vivo* wurde eine variierte hämatopoetische Erholung innerhalb der langen Knochen von Mäusen hervorgehoben. Um die subtilen Unterschiede zwischen BMAds von rotem und gelben Knochenmark abzugrenzen, haben wir zuerst eine adipozytische Differenzierung und dann ein Co-Kultursystem etabliert, um die BM-Nische *in vitro* mit der OP9-Stromazelllinie zu rekapitulieren. Bemerkenswerterweise ergab die mikrospektroskopische Raman-Analyse Nuancen der Lipidsättigungsniveaus, die zuvor in primären BMAds auf der Ebene einzelner Tröpfchen berichtet wurden. Dies könnte Auswirkungen auf die dokumentierte unterschiedliche hämatopoetische Unterstützungskapazität von BMAds haben, die wir durch Co-Kultur mit hämatopoetischen Stamm- und Vorläuferzellen aufklären. Wir konnten das etablierte Co-Kultursystem auf ein dreidimensionales Gerüst für die Konstruktion eines Tissue Engineered BM-Modells übertragen. In Kombination mit einem neuartigen Ansatz zur Herstellung seiner In-vivo-Injektion haben wir den direkten *In-vitro* zu *In-vivo* Transfer einer biomimetischen BM-Nische etabliert.

Die hier vorgestellten neuen methodischen Ansätze zur Untersuchung von BMAds und der hämatopoetischen Mikroumgebung haben weitreichende Anwendungen zur Verbesserung der Ergebnisse der BM-Krankheitsmodellierung, des Biomolekular- und Wirkstoff-Screenings sowie der gesamten regenerativen Medizin.

**Stichworte:** Skelett | Knochenmark | Adipozyten | Lipid | Stroma | Stamm- und Vorläuferzellen  
Hämatopoese | Mikroumgebung | Transplantation | Modell | Bildgebung



## Resumé

I løbet af det sidste årti er fedtvæv af knoglemarv (BMAT) fremkommet som et distinkt fedtdepot med unikke metaboliske egenskaber og virkninger både i homeostase og i udviklingen af sygdom.

Vi leverer en hidtil første omfattende gennemgang af eksisterende og nye teknologier inklusive ledsagende udfordringer til studiet af knoglemarvsadipocytter (BMAds). Anbefalingerne, der er specificeret gennem denne konsensusudtalelse til standardisering af metodologiske tilgange, er afgørende for vores søgen efter at afsløre forstanden og betydningen af BMAds. På grund af dens udfordrende lokalisering inden i knoglen og dens skrøbelige karakter giver billedbehandlingsmetoder betydningsfulde værktøjer til *ex vivo* eller *in vivo* BMAT-kvantificering samt karakterisering gennem lipidprofilering. Mens isoleringsmetoder stadig udvikles i søgen af BMAd og dens forfader, har afstamningssporing og BMAT (miljømæssige, farmakologiske eller patologiske) moduleringsundersøgelser identificeret to underpopulationer af BMAds afhængig af skeletplacering i den hæmatopoietiske røde eller fedtholdige marv.

Vi finder ændringer i disse to partier af museskelettet med stigende alder eller bestråling samt knoglemarvstransplantation-induceret aplastisk omdannelse af margen, gennem vores nye billeddannelseskvantificeringsværktøj til histologiske sektioner. Følgende denne progression ved hjælp af magnetisk resonansbillede *in vivo* understregedes forskellig hæmatopoietisk forbedring i musens lange knogler. For at afgrænse de subtile forskelle mellem BMAds af rød og fedtholdig marv, etablerede vi først en adipocytisk differentiering og derefter et co-kultur-system for at rekapitulere BM-niche *in vitro* med OP9 stromacellelinjen. Bemærkelsesværdigt afslørede mikrospektroskopiske Raman-analyser nuancer af lipidmætningniveauer, som også har været rapporteret i primære BMAds, på enkelt dråbe-niveau som vi foreslår er tegn på deres modningstilstand. Dette kan have betydning for den dokumenterede differentielle hæmatopoietiske understøttelseskapacitet for BMAds, som vi belyste gennem co-kultur med hæmatopoietiske stamceller. Vi var i stand til at omsætte det etablerede co-kultur-system til et tredimensionelt stillads til konstruktion af en celle-ladet BM-model. I kombination med en ny fremgangsmåde til fremstilling af *in vivo*-injektion har vi etableret den direkte *in vitro* til *in vivo* overførsel af en biomimetisk BM-niche.

De nye metodologiske tilgange der er præsenteret her for at studere BMAds og det hæmatopoietiske mikromiljø, har vidtrækkende anvendelser til forbedring af BM-sygdomsmodellering, biomolekylær og medikamentscreening samt i regenerativ medicin generelt.

### Nøgleord

knoglemarv | adipocyt | lipid | stroma | stam- og afkomstcelle  
bloddannelse | mikromiljø | transplantation | model | billedbehandling





## Acknowledgements

A collection of work is the culmination of countless exchanges and contributions.

Over the past years it's been a privilege to experience and share in the maturation of the **Laboratory of Regenerative Hematopoiesis** in all its stages. Together, we have created an environment of utmost collegiality from which have sprung some beautiful friendships and a range of work with great potential. **Shanti** Rojas-Sutterlin in particular, has been my greatest ally and inspiration in countless ways. Since the beginning, **Vasco** Campos was always by my side. Although we could at times “behave like an old married couple” (in the words of Shanti), I am deeply grateful for his open heart and generous advice. **Aurélien** Oggier has been extraordinarily kind and understanding, offering endless mental and scientific support, for which I count myself incredibly lucky. It has been a pleasure getting to know, work alongside, and learn from **Mukul** Girotra throughout the years since we first met at Hydra. I also appreciate the coffee talks shared with **Nicola** Vannini who could make light of every situation. **Benoit** von der Weid quickly grew into a member that the lab would not be the same without and whom I take much inspiration from both for staying on course and going off-piste. **Tanja** Hausherr was a very supportive member in the lab, and I've always admired **Frédérica** Schyrr's helpful and **Rita** Sarki's positive attitudes. I've had the opportunity to work directly with many motivated **students** (Chiheb Boussema, Tereza Koliqi, Naveed Tavakol, Ibrahim Bekri, also Michael Silverstein, Samuele Mercan, Manon Subilia, Aaron Petruzzella) who teach just as much as they learn. Their generosity can be astounding and many projects would not have advanced as far without them. The same is true for the first lab managers, **Evangelos** Panopoulos and **Yannick** Yersin, who showed immense patience in the face of some packed experimental days.

There has been great support from outside the laboratory at **EPFL and beyond**. I thank **Freddy** Radtke for taking on the role of mentor and I appreciate the help of **Ute** Koch for being one of my first contacts when I was still green in the lab. Much of the work would not be possible without the competence and patience of the **core facilities** including the Bioimaging and Optics Core Facility, Histology Core Facility, Flow Cytometry Core Facility, Gene Expression Core Facility, Bio-Electron Microscopy Facility, Proteomics and Lipidomics Core Facility, Center of PhenoGenomics especially the veterinarians, as well as the broader Life Science department infrastructures whose members brighten the day with their kindness and helpfulness. Sometimes evenings would turn into nights that I was working on other exciting projects not mentioned in this thesis. On one of these occasions, **Lalit** Kumar Dubey's kind spirit found me at the flow cytometer and promptly drove me home to sleep. Miguel Garcia, Loïc Tauzin, Valeri Glutz, and Andre Mozes deserve a special mention for their hard work to maintain the facility operating smoothly while keeping us current with some of the newest technological advancements. My curiosity for the data I was analyzing that night is still hard to still, which will probably find me going back to it after a good night's rest, knowing I'm lucky for having been able to explore so many avenues of research. For the work presented here, I'm indebted to my kind **collaborators** who I've been very fortunate to work with over the past years. Not only are they all rigorous scientists but inherently wonderful people. A generous thank you to **Nicolas** Kunz who worked at the Center for Biomedical

Imaging, for his trust and perseverance to develop a project that seemed implausible. It has also been exciting to work with Guillaume Falgayrac and Alexandrine During of the **Penel lab** at the University of Lille, and continues to be so. The undertakings with Thomas himself and Fabien Bonini of the **Braschler lab** have likewise been an adventure that I enjoy now more than ever, appreciative of the cross-disciplinary team we have formed. A heartfelt *thank you* to the brilliant **pathologists** (Bettina Bisig, Rossella Sarro, Valentina Nardi, Carmen Barcena) is imperative, with whom I've had the pleasure of developing a quantitative bone marrow imaging tool that I hope will translate into the clinic in the not-too-distant future. A kind thank you also to **Frédéric** Schütz at the Swiss Institute of Bioinformatics for his willingness to guide a flailing PhD student with basic questions. From the beginning, the **Deplancke lab** (Petra Schwalie and Rachana Pradhan) were open to interesting discussions on biology that spans tissues. Many members of the **Lutolf lab** (Yoji Tabata, Nathalie Brandenberg, Sylke Höhnle, Laura Kolb, Nikolce Gjorevski, then Sonja Giger, Andrea Manfrin, and still many others) welcomed me initially for which I will always be grateful, and (Vincent Trachsel, Thibaut Cherbuin, Gena Nikitin) never failed to engage in philosophical discussions. Daily lab-life was enhanced by our former (Naef lab, Gräff lab) and new (Huelsken lab, Hanahan lab, Briskin lab, and Oricchio lab) neighbors with their positivity and helpfulness at all the right times, while members of the Constam lab, in particular **Simon** Fortier, were especially kind and supportive. I'm appreciative of **mentors** along the way, including Jan Nehlin for supporting me as a nascent student of regenerative biomedicine, and those whose courses I've assisted during the last years: Barbara Grisoni, Horst Pick, Diego Ghezzi, and Mathias Lutolf. I'm also very grateful for the **administrative support** and positive reinforcement of Laura Bischoff, Sonja Bodmer, and Sandra Roux when it was direly needed.

My deepfelt appreciation goes to the community of the **Bone Marrow Adiposity Society** for fostering a warm, collaborative spirit across labs and nations. I have particularly treasured the proximity with the **Bianco/Riminucci lab** for the heartfelt personal and scientific discussions. It has been an honor getting to know and work with the entire **Methodologies working group** on completing our first review together. I also take inspiration from the **Cawthorn lab** and **Kassem lab** – via discussions not only on the interesting nature of bone marrow adipocytes, but other occupational contemplations also – with Karla Suchacki and Domenico Mattiucci, as well as Michaela Tencerova (who is currently setting up her own lab). I wish them the best of luck as they embark on their exciting scientific journeys ahead.

The support of **funding agencies** (Swiss National Science Foundation and Anna Fuller Fund) throughout my doctoral studies have made this work possible, while **grants** from the Lausanne Integrative Metabolism and Nutrition Alliance as well as the International Society of Endocrinology have allowed me to partake in international conferences worldwide.

To my **thesis committee**, **Dominique Pioletti**, **Cathrin Briskin**, **Laurence de Leval**, and **Clifford Rosen**: thank you sincerely for your open nature, engagement, and source of true inspiration that I will continue to carry with me moving forward.

A great role-model, a scientific leader, now a life mentor, once trusted in me and gave me her support for joining on a journey to start some of the first projects in her newly-minted lab. I'm most grateful to **my advisor**, **Olaia Naveiras**, for breeding independence and unassumingly offering a steady guidance with the utmost kindness, generosity, patience, and unwavering encouragement, scientific rigor and curiosity – envisioning the impossible showing us that anything is possible. I deeply treasure the past years that we have shared together and all that I have been so fortunate to learn from you, Olaia.

In Memory

**Paolo Bianco**

*1955 – 2015*



Olaia Naveiras (left), Josefine Tratwal (center), and Paolo Bianco (right)

# Contents

|  |              |
|--|--------------|
| Preface  | v            |
| Abstract   | ix           |
| Résumé   | xi           |
| Zusammenfassung  | xiii         |
| Resumé   | xv           |
| Acknowledgements   | xvii         |
| LIST OF ABBREVIATIONS  | xxii         |
| <b>SCOPE OF THE THESIS</b>   | <b>xxvii</b> |
| <b>CHAPTER 1 The bone marrow microenvironment</b>                        | <b>1</b>     |
| What's in a niche?   | 2            |
| The Phat Fat!  | 9            |
| Challenging Methods  | 12           |
| <b>CHAPTER 2 Methodologies of bone marrow adiposity research</b>         | <b>15</b>    |
| Preface  | 18           |
| Introduction   | 19           |
| Synthesis  | 22           |
| Conclusion   | 60           |
| <b>CHAPTER 3 Quantitative imaging of the bone marrow</b>                 | <b>63</b>    |
| Preface  | 66           |
| Introduction   | 68           |
| Results  | 70           |
| Conclusion   | 79           |
| Methods  | 82           |
| <b>CHAPTER 4 <i>In vitro</i> model of bone marrow adipocyte subtypes</b> | <b>86</b>    |
| Preface  | 88           |
| Introduction   | 89           |
| Results  | 91           |
| Conclusions  | 102          |
| Methods  | 103          |

## Contents (continued)

|                         |  |             |
|-------------------------|--|-------------|
| <b>CHAPTER 5</b>        | <b>Biomimetic transplantable bone marrow co-culture system</b> | <b>109</b>  |
|                         | Preface  | 112         |
|                         | Introduction   | 113         |
|                         | Results  | 115         |
|                         | Conclusions  | 123         |
|                         | Methods  | 126         |
| <b>CHAPTER 6</b>        | <b>Perspectives and Future Directions</b>                      | <b>133</b>  |
|                         | Synthesis  | 134         |
|                         | Discussion   | 136         |
|                         | Concluding remarks   | 142         |
| <b>APPENDIX</b>         |  | <b>xxx</b>  |
|                         | Appendix A   | xxxi        |
|                         | Appendix B   | xl          |
| <b>BIBLIOGRAPHY</b>     |  | <b>xlii</b> |
| <b>CURRICULUM VITAE</b> |  | <b>lxx</b>  |

## LIST OF ABBREVIATIONS

| Abbreviation | Definition   |
|--------------|--|
| 2D / 3D      | Two / three dimensional                                    |
| $\beta$ 3-AR | Beta-3 adrenergic receptor                                 |
| $\Sigma$     | Summation  |
| $\mu$ CT     | Microfocus computed tomography                             |
| ACTb         | Actin beta   |
| ACTH         | Adrenocorticotrophic hormone                               |
| Ad.Ar        | Adipocyte Area   |
| Ad.Dm        | Adipocyte Diameter   |
| Ad.N         | Adipocyte Number   |
| Ad.Pm        | Adipocyte Perimeter  |
| AdipoQ       | Adiponectin  |
| Angpt1       | Angiopoietin 1   |
| ANOVA        | Analysis of variance                                       |
| ATGL         | Adipose triglyceride lipase                                |
| Ap2          | Activating protein 2                                       |
| BADGE        | Bisphenol A Diglycidyl Ether                               |
| BAT          | Brown adipose tissue                                       |
| BC           | Bone chip  |
| BLC          | Bone lining cell   |
| BM           | Bone marrow  |
| BMA          | Bone marrow adiposity                                      |
| BMAS         | Bone Marrow Adiposity Society                              |
| BMAds        | Bone marrow adipocytes                                     |
| BMAT         | Bone marrow adipose tissue                                 |
| BMD          | Bone Mineral Density                                       |
| BMFF         | Bone marrow fat fraction                                   |
| BMSC         | Bone marrow stromal cell                                   |
| BODIPY       | boron-dipyrromethene                                       |
| BSCL2        | Bernardinelli-Seip Congenital Lipodystrophy Type 2 protein |
| BV           | Bone Volume  |
| CAR cell     | CXCL12 abundant reticular cell                             |
| CB           | Compact bone   |
| cBMAds       | Constitutive bone marrow adipocytes                        |
| CD           | Cluster of differentiation                                 |
| CR           | Caloric Restriction  |
| cAMP         | Cyclic adenosine monophosphate                             |
| cDNA         | Complementary deoxyribonucleic acid                        |
| CCM          | Carboxymethylcellulose microscaffolds                      |
| CEBPa        | CCAAT Enhancer Binding Protein Alpha                       |
| CE-CT        | Contrast-enhanced computed tomography                      |
| CFU          | Colony-forming unit  |
| CFU-F        | Colony-forming unit-fibroblast                             |
| CGL          | Congenital generalized lipodystrophy                       |
| cKit         | Kit proto-oncogene, receptor tyrosine kinase               |
| CXCL12       | C-X-C motif chemokine ligand receptor 12                   |

## LIST OF ABBREVIATIONS (CONTINUED)

| Abbreviation       | Definition                                   |
|--------------------|--|
| <b>DAPI</b>        | 4',6-diamidino-2-phenylindole                |
| DECT               | dual-energy computed tomography              |
| DIO                | Diet Induced Obesity                         |
| DMI                | Cocktail for Dexamethasone, IBMX and insulin |
| DNA                | Deoxyribonucleic acid                        |
| DNL                | De novo lipogenesis                          |
| <b>EDTA</b>        | Ethylenediaminetetraacetic acid              |
| EGFP               | Enhanced green fluorescent protein           |
| EM                 | electron microscope                          |
| ER                 | Endoplasmic reticulum                        |
| EU                 | European Union                               |
| <b>FA</b>          | Fatty acid                                   |
| FABP4              | Fatty acid binding protein 4                 |
| FACS               | Fluorescence-activated cell sorting          |
| FADS               | Fatty acid desaturase                        |
| FASN               | Fatty acid synthase                          |
| FBS                | Fetal bovine serum                           |
| FDA                | Food and Drug Administration                 |
| FDR                | False discovery rate                         |
| FSH                | Follicle stimulating hormone                 |
| <b>GDPR</b>        | General Data Protection Regulation           |
| GFP                | Green fluorescent protein                    |
| Glut4              | Glucose transporter type 4                   |
| <b>H&amp;E</b>     | Hematoxylin and eosin                        |
| <sup>1</sup> H-MRS | proton magnetic resonance spectroscopy       |
| Hf-WD-POM          | Hafnium Wells-Dawson polyoxometalate         |
| Hm.Ar              | hematopoietic area                           |
| HFD                | High Fat Diet                                |
| HPLC               | High performance liquid chromatography       |
| HSC                | Hematopoietic stem cell                      |
| HSL                | Hormone sensitive lipase                     |
| HSPC               | Hematopoietic stem and progenitor cell       |
| IBMX               | isobutylmethylxanthin                        |
| IHC                | Immunohistochemistry                         |
| IMDM               | Iscove's Modified Dulbecco's Medium          |
| ISCT               | International Society for Cellular Therapy   |
| <b>KitL</b>        | cKit ligand                                  |
| KLS                | cKit <sup>+</sup> Lineage-Sca1 <sup>+</sup>  |
| <b>LD</b>          | Lipid droplet                                |
| Lep                | Leptin                                       |
| Lepr               | Leptin receptor                              |
| Lin                | Lineage                                      |
| LPL                | lipoprotein lipase                           |
| <b>mRNA</b>        | Messenger ribonucleic acid                   |
| MR                 | Methionine restriction                       |
| MRI                | Magnetic resonance imaging                   |

## LIST OF ABBREVIATIONS (CONTINUED)

| Abbreviation                      | Definition                                       |
|-----------------------------------|--|
| Ma.Ar                             | Marrow area                                      |
| Ma.V                              | Marrow volume                                    |
| MAGP1                             | Microfibril-associated glycoprotein-1            |
| MUFA                              | Monounsaturated fatty acid                       |
| M-CSF                             | Macrophage colony-stimulating factor             |
| MEM $\alpha$                      | Minimum Essential Medium alpha                   |
| NCD                               | Normal Chow Diet                                 |
| NSG                               | NOD SCID- $\gamma$                               |
| ORO                               | Oil red O  |
| OsO <sub>4</sub>                  | Osmium tetroxide                                 |
| Osx                               | Osterix  |
| LIST OF ABBREVIATIONS (CONTINUED) |  |
| OVX                               | Ovariectomized                                   |
| PLIN1                             | Perilipin 1                                      |
| PCA                               | Principle component analysis                     |
| PCR                               | Polymerase chain reaction                        |
| PDGFR $\alpha$                    | Platelet derived growth factor alpha             |
| PDFF                              | proton-density fat fraction                      |
| PDMS                              | Polydimethylsiloxane                             |
| PDX                               | Patient derived xenograft                        |
| PEG                               | Poly(ethylene glycol)                            |
| PFAS                              | performic acid Schiff                            |
| PLIN                              | Perilipin  |
| Ppm                               | Parts per million                                |
| PPAR $\gamma$                     | Peroxisome proliferator-activated receptor gamma |
| PRESS                             | point-resolved spectroscopy                      |
| PTH                               | Parathyroid hormone                              |
| PTRF                              | Polymerase I and transcript-release factor       |
| P/S                               | Penicillin/Streptomycin                          |
| PUFA                              | Polyunsaturated fatty acid                       |
| rAAV                              | Recombinant adeno-associated virus               |
| rBMAds                            | Regulated bone marrow adipocytes                 |
| RFP                               | Red Fluorescent Protein                          |
| RNA                               | Ribonucleic acid                                 |
| RNA-seq                           | Ribonucleic acid-sequencing                      |
| ROS                               | Reactive oxygen species                          |
| RT                                | Room temperature                                 |
| RT-qPCR                           | Real-time quantitative polymerase chain reaction |
| Sca1                              | Stem cell antigen 1                              |
| Scd                               | Stearyl-CoenzymeA desaturase                     |
| SCF                               | Stem cell factor                                 |
| SD                                | Standard deviation                               |
| SDF                               | Stromal cell derived factor                      |
| SEM                               | Standard error of the mean                       |
| SF                                | Steel factor                                     |
| SFA                               | Saturated fatty acid                             |



## LIST OF ABBREVIATIONS (CONTINUED)

| Abbreviation | Definition                          |
|--------------|-------------------------------------|
| SFF          | Signal fat fraction                 |
| SSC          | Skeletal stem cell                  |
| STEAM        | stimulated echo acquisition mode    |
| SVF          | Stromal Vascular Fraction           |
| <b>T.Ar</b>  | Total tissue area                   |
| TAG          | Triacylglycerols                    |
| TRAP         | Tartrate-resistant acid phosphatase |
| TV           | Total tissue Volume                 |
| TZD          | Thiazolidinediones                  |
| UCP1         | Uncoupling Protein 1                |
| v/v          | Volume/volume                       |
| VMH          | Ventromedial hypothalamus           |
| vWF          | Von willebrand factor               |
| <b>WAT</b>   | White adipose tissue                |
| WFI          | Water–fat MR imaging                |
| WT           | Wild Type                           |
| ZFP423       | Zinc finger protein 423             |



## SCOPE OF THE THESIS

The overall objective of this thesis is to address and contribute to emerging methodologies in bone marrow adiposity (BMA) research in order to begin to uncover the role and regulation of bone marrow adipocyte subtypes.

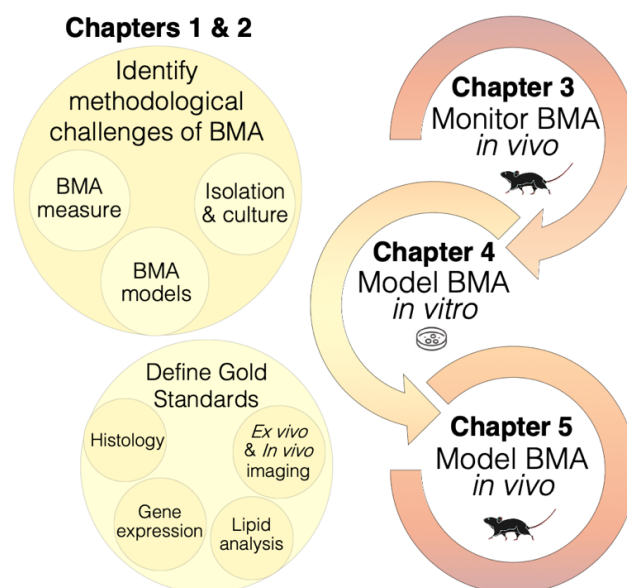
Inspired by history and seminal work identifying stem cells of the bone/marrow organ, **Chapter 1** guides us to our current position today with the aspiration of researchers to apply rigorous methodologies for the characterization of bone marrow adipocytes and their progenitors.

**Chapter 2** tackles important methodological challenges in the bone marrow adiposity field and proposes minimal reporting standards as outlined by members of the Bone Marrow Adiposity Society. The following chapters aim to address some of these concerns.

Even with rapid technological advancements, histomorphometry remains a pillar of pathologic analysis that is undergoing a revival in the form of digitalized automatization. In **Chapter 3** we present an in-house developed quantification tool for detection of bone marrow compartments in histological samples that will facilitate analysis standardization.

In **Chapter 4** we sought to establish an *in vitro* model for bone marrow adipogenesis that recapitulates *in vivo* adipocyte subtypes. Encouraged by our results, we translated this stromal-hematopoietic co-culture system into a three-dimensional matrix, as presented in **Chapter 5**. Finally, **Chapter 6** summarizes the methodological developments presented in this thesis, further challenges, and their implication for addressing complications of bone marrow malignancies as well as their potential in contributing towards our understanding of the elusive bone marrow adipocytes.

With the ambition to decipher some of the complexities of the bone marrow microenvironment, we may advance one step closer to helping patients through the advancement of science and technology.





## **CHAPTER 1**

### **The bone marrow microenvironment**

## What's in a niche?

“In stem cell biology at large, a stem cell niche has come to be seen as the specific tissue site in which stem cells receive instructive cues that determine their behavior, in particular, their self-renewal throughout life. Stated in a simple way, a niche is the tissue site where stem cells remain, or even become, stem cells...However, self-renewal of stem cells may have additional, intrinsic, as well as population-based, determinants, all of which need to be integrated with the microenvironmental cues conceptualized in the niche.” (Bianco, 2011).

## Origins of the marrow as the seedbed of our blood

### *Of two types of marrow and the stem cell theory*

Cell theory arose in the 1600–1800s and is often attributed to Mathias Schleiden (from plant biology) and Theodore Schwann (in animal biology) (Hooke, 1664; Schleiden, 1838; Schwann, 1847; Conklin, 1939). Although it was believed since the time of Hippocrates that marrow is the nutrient source of bone, the French anatomist Pierre Duverney, observed in 1700 that some bones have no marrow (like those of the middle ear) and it would therefore unlikely be essential for nutrition of bone (Robin, 1875; Duverney, 1700; Tavassoli, 1983). One and a half centuries later, Rudolf Virchow, regarded as the father of modern pathology, would build on this body of work to coin the phrase “*omnis cellula e cellula*” (every cell from a cell). Ernst Neumann and Giulio Bizzozero who studied with Virchow in Berlin, in 1868 first described the presence of nucleated blood cells in the marrow (Neumann, 1868; Bizzozero, 1868; Bizzozero, 1869). The following year, Neumann would ascertain that blood arises in the bone marrow (BM). He described that “it operates continually in the *de novo* formation of red blood cells” (Neumann, 1869), accepting their finite lifespan and the necessity for continuous replenishment.

“Also in the marrow rich in fat, the same cells are present but in lower quantity and their number decreases parallel to the decrease in the number of marrow cells and the increase in the number of fat cells.” (Neumann 1868).

This was followed by his identification of leukemia as a disease of the marrow (Neumann, 1870). Charles Robin would a few years later notice that in the course of development, marrow is formed after bone (Robin, 1875). Then in 1882, Neumann established the rule governing the development of yellow marrow, what is now referred to as *Neumann's law*, which states that: at birth, all bones that contain marrow contain red marrow, and with age, the blood-producing capacity contracts toward the center of the skeleton, leaving the more peripheral bones with only fatty marrow. (Neumann, 1882; Tavassoli, 1983).

However, it was actually Xavier Bichat who at the end of the 18<sup>th</sup> century first recognized the two types of marrow, coining them *red marrow* as seen in the fetus and *fatty marrow* of the adult. These sentiments would be echoed centuries later (Emery and Follet, 1964) long after the presence of red marrow in the

adult had been acknowledged, including the gelatinous transition state between the two (Gosselin and Regnault, 1849; Cheng, 1931; Tavassoli, 1983). Notably, Bichat already recognized that fatty marrow was distinct from other types of fat, which Dunlop and Nerking confirmed in the beginning of the 1900s through analysis of its chemical composition (Dunlop, 1907; Nerking, 1908; Cheng, 1931).

These seminal findings set the stage for eventually defining the hematopoietic stem cell (HSC). As early as 1896, Arthur Pappenheim used the term *stem cell* to describe a precursor cell capable of giving rise to red and white blood cells (Figure 1.1) (Haekcel, 1868; Pappenheim, 1896). Neumann followed, first designating the origin of all hematopoietic cells the “great lymphocyte” and later also adopting the term “stem cell” for the common precursor of the blood system (Neumann, 1868; Neumann, 1912).

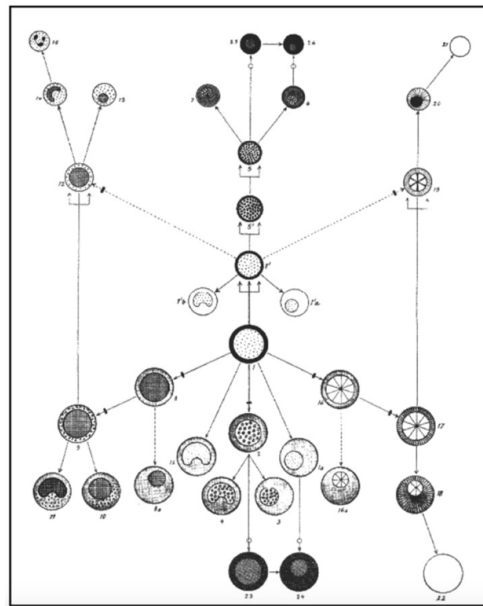


**Figure 1.1** | Stem cell origins. The recognition of a common progenitor as the source of hematopoietic cells by Ernst Neumann (1868), and the application of early staining techniques differentiating white blood cell lineages by Paul Ehrlich (1879), led to a discussion on the existence of a bona fide stem cell in the field. Arthur Pappenheim’s illustration in 1905 of a precursor stem cell at the center of the hematopoietic system still rings true to some extent today. (Ramalho-Santos and Willenbring, 2007)

Thus, the stage was set. Due to limitations of experimental methods at the time, it wasn’t until the 1960s however, that James Till, Ernest McCulloch, and others provided definitive evidence of the existence of the first stem cell ever described, the common hematopoietic stem cell, through the discovery of spleen colonies following irradiation and bone marrow transplantation (Till and McCulloch, 1961; Becker et al., 1963; Till et al., 1964). This laid the beautiful groundwork for clonal lineage tracing of cells *in vivo*, the isolation of stem cells, and the establishment of hematopoietic stem cell transplantation as a treatment for malignancies of the blood (the first and only rigorous stem cell therapy) through serial reconstitution. Today, there are various forms of beautifully elaborate roadmaps to hematopoietic fate (Velten et al., 2017; Rodriguez-Fraticelli, 2018; Carrelha, 2018) that take place within the marrow, for which bone provides an essential environment.

## Chapter 1 – The bone marrow microenvironment

### *Of the bone and its marrow*

As experimental medicine was beginning to thrive, the relation of bone and marrow would finally be addressed beyond the ongoing speculative debates. Some of the first marrow grafts to extramedullary sites (such as the abdomen) were performed in the later 19<sup>th</sup> century (Goujon, 1866; Goujon, 1869; Baillkow, 1870). Goujon and Baillkow noted that the grafted marrow would transform into bone, and as such made the first observations of the bone-forming potential of marrow cells. However, it wasn't until a century later (following the same time course as the discovery of the hematopoietic stem cell), that Mehdi Tavassoli and William Crosby, simultaneously with Friedenstein et al., determined that heterotopic transplants of marrow fragments could form not only bone but also marrow anew (Figure 1.2a) in the form of BM organoids (marroids) or ossicles (Tavassoli and Crosby, 1968; Friedenstein et al., 1966). The exploration of the bone marrow stroma had begun. Tavassoli would go on to define the stable and labile fatty components of the marrow with differential lipid composition, and Friedenstein showed that indeed the bone and marrow derived from an osteogenic progenitor cell through establishing the colony forming unit-fibroblast (CFU-F) assay. Seeding of BM cell suspensions at clonal density resulted in discrete colonies from single cells, with a linear dependence of colony formation on initial seeding (Friedenstein et al. 1970). Similarly, the colony forming unit (CFU) assay had been developed to quantify hematopoietic potential of HSCs plated in semi-solid medium (Bradley and Metcalf, 1966; Pluznik and Sachs, 1966).

At the same time as the identification of the multipotent BM stromal cell (BMSC), John J. Trentin first presented the concept of the hematopoietic microenvironment followed by the conceptualization of the stem cell niche hypothesis by Ray Schofield. (Wolf and Trentin, 1968; Trentin, 1970; Trentin, 1971; Schofield, 1978). This notion that HSCs are regulated by their association with a discrete microenvironment of the BM, was substantiated with the advent of Dexter cultures (Dexter and Lajtha, 1974; Dexter and Testa, 1976; Dexter et al., 1977). And so, the HSC or “seed” is supported by a base of (hematopoietic stromal microenvironment) “soil” while the BMSC simultaneously functions as a stem cell and provides a microenvironment for HSCs, thereby embodying properties of both the “seed” and the “soil” (Tavassoli, 1989; Bianco et al., 2008).

## The reticulous search for the progenitor

### *Space*

Schofield proposed that HSCs age, or lose part of their regenerative potential, in situations of stress when they are challenged to sustain hematopoietic reconstitution. He maintained that HSCs are stem cells in their niche where they remain quiescent or divide conservatively, but lose part of their potential when they are challenged and proliferate or differentiate as they move out of their niche (Bianco, 2011). Since HSCs were observed to localize to endosteal surfaces, Schofield named the endosteum as the HSC niche, which other studies have since supported (Gong, 1978; Nielsson et al., 2001; Zhang, 2003; Adams, 2006; Haylock, 2007; Jiang, 2009; Nakamura, 2010). Genetic mouse models allowed for the determination of the osteoblast as a regulatory component of the HSC niche (Visnjic et al., 2001; Calvi et al., 2003; Visnjic et al., 2004). Notably, endosteal regions are also enriched in intra- and trans-cortical microvessels (the former lined by an adventitial layer of alkaline phosphate positive (ALP<sup>+</sup>) cells). These capillaries connect the marrow circulation, bone, and periosteal circulation, thereby contributing to the unique endosteal microenvironment (Adams et al., 2006; Bianco et al., 2011; Grüneboom et al., 2019).



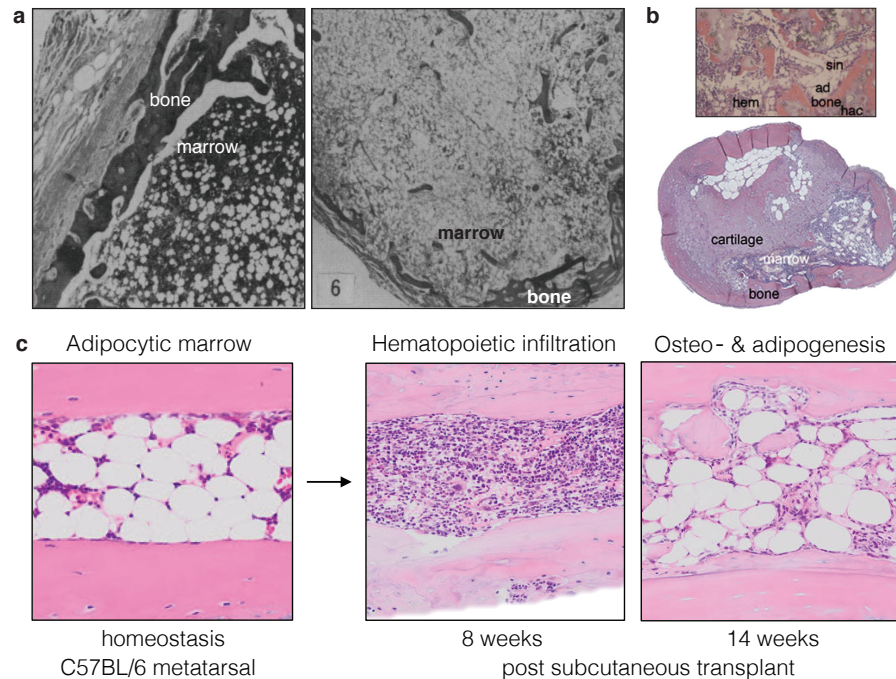


**Figure 1.2** | The hematopoietic microenvironment. **a** Heterotopic ossicle formation recapitulates native bone marrow ontogeny from sites of red (left) and fatty (right) marrow (Tavassoli and Crosby, 1970). **b** Ossicle formation *in vivo* occurs from CD146<sup>+</sup> clonogenic BMSCs with a scaffold carrier (top, note adipocytes lining the sinusoid) or from a BMSC cartilage pellet (bottom) (Sacchetti et al., 2007; Serafini et al., 2014). **c** Hematoxylin and eosin stains of C57BL/6 female 8 week-old metatarsals containing adipocytic marrow in homeostasis and its regeneration post subcutaneous implantation. After 8 weeks *in vivo*, hematopoietic infiltration is observed followed by renewed osteo- and adipogenesis after 14 weeks *in vivo*. Ad: adipocyte, bm: bone marrow; hac: hydroxyapatite carrier; hem: hematopoiesis; sin: sinusoid.

At the same time, evidence of another, perivascular niche was being provided. Hematopoiesis requires an established sinusoid network and HSCs localize to endothelial cells of the sinusoidal walls (Kiel et al., 2005; Sugiyama 2006; Kiel and Morrison, 2006). Interestingly, BMSCs also do so even prior to the establishment of hematopoiesis when modelled *in vivo* (Sacchetti et al., 2007). A third candidate was proposed as a player of the HSC niche, namely the CXCL12-expressing adventitial reticular (CAR) cell that resides on the subendothelial on the abluminal surface of BM sinusoids (Sugiyama 2006; Sacchetti et al., 2007; Omatsu et al., 2010; Nagasawa et al., 2011; Sugiyama and Nagasawa, 2012). Its skeletal stem cell (SSC) properties were delineated by stringent *in vivo* transplantation assays showing their *BM organizer* capacity (Figure 1.2b). We can then derive that this is a tale of two stem cells that share a common niche, and that there may in fact be multiple different microenvironments for a system in terms of quiescent precursors versus their rapidly proliferating progenitors (Bianco, 2011b; Ding and Morrison, 2013; Bianco and Robey, 2015).

Ultrastructural studies hint that bone marrow adipocytes (BMAds, further described below) seem to arise postnatally from anatomically-defined CAR-like cells (Tavassoli, 1976; Weiss, 1976; Robles et al., 2019). In chemotherapy-induced hematopoietic ablation, rapid lipid accumulation converts these cells to adipocytes. Due to the location of the CAR cells on the abluminal part of the sinus wall, this conversion causes a constriction of the sinusoid (Bianco, 1988). Through the loss of lipids by lipolysis, the BMAds

## Chapter 1 – The bone marrow microenvironment

would again release space so the sinusoids could dilate and resume blood flow to the microscopic anatomical region, followed by conversion of the marrow (from yellow to red) on the macroscopic scale (Bianco, 2011).

Adipose conversion of the BM may be explained as a physiological change of the niche, affecting HSCs in defined regions of the skeleton (Bianco, 2011). Indeed, BMAd themselves direct HSC quiescence (Naveiras et al., 2009). They originate from one or several, likely ALP<sup>+</sup>, stromal progenitors. These cells also contribute to the HSC niche responsible for instructive cues in the form of bound or secreted molecules for HSC quiescence, self-renewal, proliferation, and differentiation (Bianco, 1988). In concert with the extracellular matrix (ECM) they also contribute regulatory signals through physical cues including contractile forces, shear stress, temperature, and oxygen tension (reviewed in Mendelson and Frenette, 2014; Lee et al., 2013).

### *Time*

Importantly, the C-X-C motif chemokine ligand receptor 12 (CXCL12, so-called stromal cell derived factor 1 (SDF1) or pre-B cell growth stimulating factor) and its receptor CXCR4 regulate HSC progenitors (HSPCs) and is critical for BM colonization and engraftment (Janssens et al., 2018; Ara et al., 2003; Peled et al., 1999). Multiple stromal cells of the niche are characterized by their expression of CXCL12 and may be the precursors to some BMAds (Tavassoli, 1976). Stem cell factor (SCF, so-called steel factor (SF) or c-Kit Ligand, KitL) is produced by perivascular stromal cells for the maintenance of HSCs which express the cKit receptor (Ding et al., 2012). Furthermore, deletion of *Foxc1* in CAR cells during embryogenesis results in reduced HSPCs, normal appearance of osteoblasts, and increased bone marrow adiposity (BMA). *Foxc1* deletion in adulthood, was also shown to deplete HSPCs by reducing CXCL12 and SCF in CAR cells without a conversion to yellow marrow (Omatsu et al., 2014). *Foxc1* may thus be involved in CAR cell development, including CXCL12 and SCF expression, while inhibiting the adipogenic potential of these cells.

A wave of seminal studies carried out using transgenic mouse models show that most CXCL12 in the BM is derived from perivascular stromal cells marked by partially-overlapping rare populations of *Prx1-cre*, *Nestin-gfp*, or *Lepr-cre*, and *Osterix-cre* (Mendez-Ferrer et al., 2010; Pinho et al., 2013; Isetn et al., 2014; Zhou et al., 2014; Mizoguchi et al., 2014; Hanoun and Frenette, 2013). These markers are expressed to varying degrees in the marrow, even within the population themselves. For example, *Nestin-gfp*<sup>bright</sup> cells are localized to arterioles (preferentially found in endosteal BM) while *Nestin-gfp*<sup>dim</sup> cells are reticular in shape and associated with sinusoids (Figure 1.3) (Kunisaki et al., 2013). However, such results should be interpreted with some caution due to limitations of *gfp* turnover or rate and efficiency of *cre* recombination (Bernal and Arranz, 2018). Nevertheless, nestin-expressing cells are a promising putative therapeutic target since reduction of nestin<sup>+</sup> contributes to myeloproliferative neoplasms (Arranz et al., 2014).

### *Continuum*

The hematopoietic microenvironment is intricate and much remains to be elucidated. In the abnormal hematopoietic microenvironment of *Sl/Sl-d* mutant mice expressing only the soluble form of SCF, HSCs were depleted indicating need for cell-cell contact perhaps via Notch-mediated signaling (Barker et al., 1994; Corselli et al., 2013; Evans and Calvi, 2015). Bone marrow adipose tissue (BMAT) has been genetically ablated in kit-deficient mice. Specifically, loss of function mutations in kit receptor or kit ligand resulted in reduction of BMAd and precursors in long bones of *Kit<sup>W/W-v</sup>* and *Kit<sup>Sl/Sl-d</sup>* mice respectively.

Treatment with the kit receptor antagonist Gleevec (or imatinib mesylate), also reduced BMAT in normal rats (Turner et al. 2011). Current genetic models of BMAd depletion and other models of bone marrow adiposity (BMA) are discussed in detail below and in Chapter 2.

Relatively recently, *Sef* deletion was shown to negatively affect not only the stroma but also adiponectin-expressing cells generally allocated to BMAds and progenitors situated within the red marrow, and thus necessary for the survival and maintenance of HSCs (Zhou et al., 2017). Adiponectin that occurs with BMAT accumulation is likely involved in normal and pathological regulation of hematopoiesis (Yokota et al., 2000; Yokota et al., 2003; Cawthorn et al., 2014).

Acute myeloid leukemia (AML) is distinguished by the generation of dysfunctional leukemic blasts and impaired myelo-erythropoiesis through inhibition of adipogenic maturation (Döhner et al. 2010, Boyd et al. 2017). Neoplastic cells in AML are able to activate BMAd lipolysis through hormone sensitive lipase (HSL)-induced transfer of fatty acids (FAs) to AML blasts, impairing the BMAd niche by blast propagation (Shafat et al., 2017; Caho et al., 2017; reviewed in Mattiuci et al., 2018). Blocking this lipid transfer through inhibition of the fatty acid binding protein 4 (FABP4) increased survival of leukemic mice (Shafat et al., 2017). Interestingly, in an *in vitro* study with leukemic cells, BMAds remodeled to smaller adipocytes possibly through ATGL-mediated lipolysis contributing free fatty acids (FFA) that in turn enhanced leukemic cell proliferation (Lu et al., 2018). Thus, smaller BMAds were associated with leukemic growth. In xenotransplanted mice, peroxisome proliferator activated receptor- $\gamma$  (PPAR $\gamma$ ) agonist induced BMA and rescued healthy hematopoietic maturation while repressing leukemic growth (Boyd et al., 2017). Indeed, BM microenvironments of red and fatty marrow did imprint niche-specific features to leukemic cells associated with modified survival, metabolism, and cell-cycle progression related to chemo-resistance (Cahu et al., 2017). Other malignancies are also associated with BMAT. Multiple myeloma (MM), characterized by clonal proliferation of transformed plasma cells, resides in close contact with BMAds (Palumbo and Anderson, 2011). While adiponectin has been shown to inhibit MM, mature BMAds have been shown to support tumor growth and even protect MM cells from chemotherapy-induced apoptosis (Caers et al., 2007; Dalamaga et al., 2009; Fowler et al., 2011; Medina et al., 2014; Liu et al., 2015; reviewed in Falank et al., 2016). To truly understand these seemingly opposing effects, we must first turn to the detailed characterization of BMAds themselves.

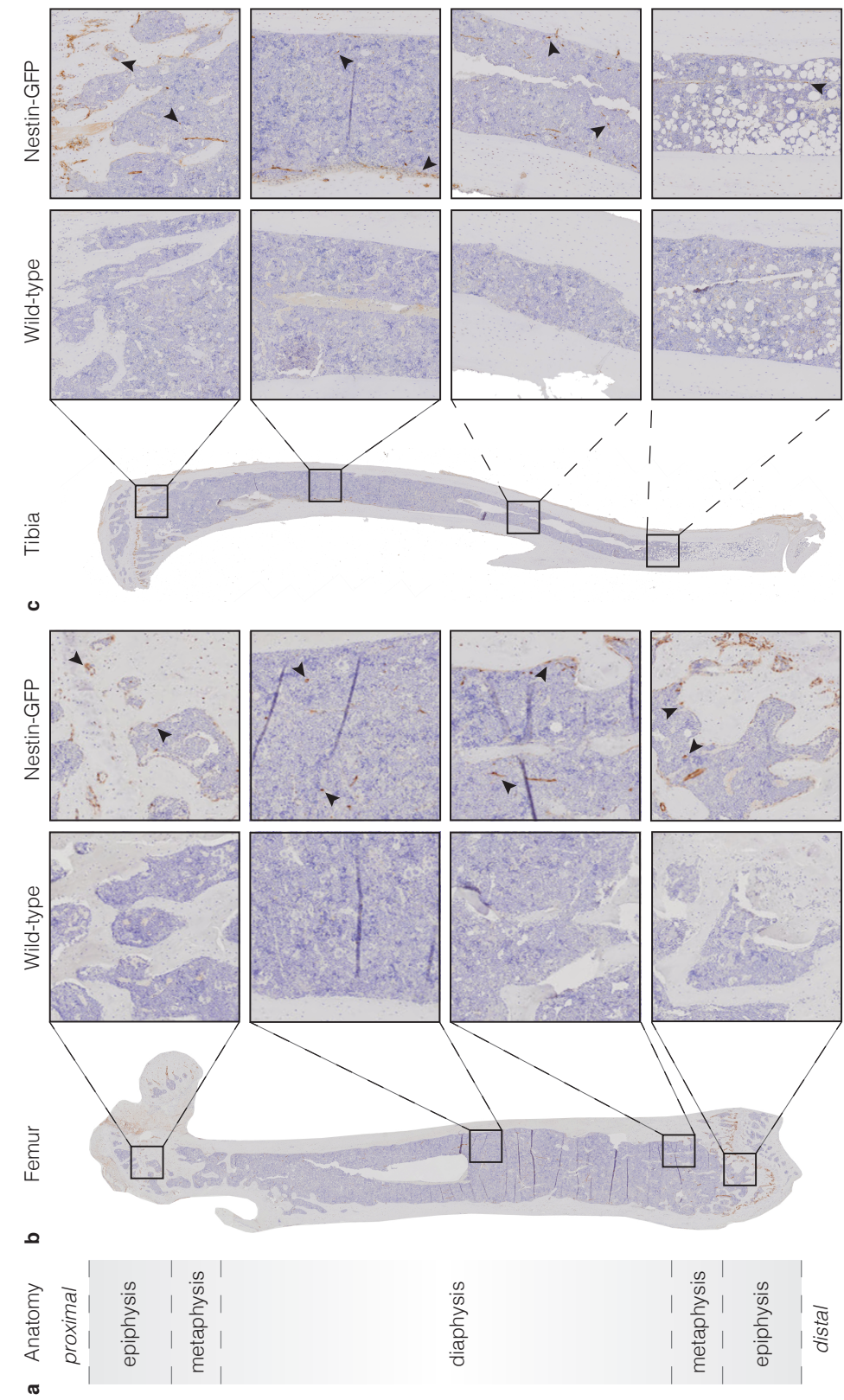


**Figure 1.3** | Niches within the marrow vary by localization of nestin expression. **a** The anatomical organization of long bones originates from two distinct ossification centers. **b** Femur and **c**, tibia isolated from 13 week-old C57BL/6 female wild-type or transgenic mice expressing GFP under the nestin promoter (Nestin-GFP), were processed for histology and stained against GFP with chromogenic detection (brown). Nestin<sup>+</sup> stromal cells (arrows) are located in the sinusoidal- and endosteal/arteriolar-defined niches of the red marrow. Figure produced in collaboration with Dr. Shanti Rojas-Sutterlin. GFP: green fluorescent protein.

## The Phat Fat!

### A unique adipose depot with distinct adipocyte subtypes

#### *Learning from others*

With BMAT emerging as a novel adipose depot, we take inspiration from the thoroughly described extramedullary adipose tissues for its characterization. BMAT has followed well in the footsteps laid out by extramedullary white adipose tissue (WAT) in that it was once considered an energy reservoir but now is recognized as an endocrine organ with central roles in energy or nutritional homeostasis, insulin sensitivity, and inflammation through adipokines (Majka et al., 2011). Leptin suppresses appetite, increasing metabolic rate and fat oxidation while adiponectin enhances insulin sensitivity and diminishes inflammation (Pellemounter et al., 1995; Brochu-Gaudreau et al., 2010). The implication of extramedullary adipose tissue at large ranges from metabolic to mechanical functions (reviewed in Rosen and Spiegelman 2014). The large unilocular adipocytes that mostly make up the visceral WAT differs significantly from the multilocular brown adipocytes (BAT) of the intrascapular region, known for dissipation of stored chemical energy in the form of heat through uncoupling of the mitochondrial membrane potential via uncoupling protein 1 (UCP1). Meanwhile subcutaneous adipose tissue contains a mixed morphology of inducible white (termed beige or brite: brown-in-white) adipocytes that have an overlapping but distinct signature compared to BAT (Wu et al., 2012). These cells have different origins. While BAT derives from a common muscle precursor (Seale et al., 2007; Seale et al., 2008), WAT has been shown to originate from perivascular progenitors through lineage tracing experiments (Tang et al., 2008; Gupta et al., 2010; Gupta et al., 2012; Berry and Rodeheffer, 2013). Naturally, pink adipocytes also exist. *Adiponectin*-expressing adipocytes make up the majority of the mammary gland that dedifferentiate to platelet-derived growth factor alpha (Pdgfr $\alpha$ <sup>+</sup>) preadipocytes and are replaced by alveolar structures during lactation to then reappear upon weaning (Wang et al., 2018; Zwick et al., 2018). This cyclical de- and re-differentiation of the pink adipocytes is indeed remarkable, and may shed light on another unique adipose depot: BMAT.

#### *Every one is unique*

It has been suggested to call BMAds “yellow adipocytes” due to the gross anatomical color they impart (Attané et al., 2019). However, this could lead to a misconception if applied to the entirety of BMAT due to differences incurred by its location (described below). The nature of the bone/marrow organ and the location of BMAds therein, including the methods of isolation and analysis used, complicate its study (discussed in detail in Chapter 2). Nevertheless, some things are becoming clear. While the SSC has been introduced above, a committed adipogenic progenitor and pre-adipocyte of the BM (also based on Zfp423 and Pdgfr $\alpha$  expression) have recently made their way onto the map (Ambrosi et al., 2017). BMA increases in numerous conditions including age, radiation/chemotherapy-induced aplasia, high fat diet, immobility and even hibernation and calorie restriction (although in extreme situations, BMAT delipidates to a gelatinous marrow) (Kricun et al., 1985; Blebea et al., 2007; Doucette et al., 2015; Scheller et al., 2016; Tencerova et al., 2018; Trudel et al., 2009; Trudel et al., 2017; Özçivici et al., 2013; Tavassoli 1974; Devlin 2011; Böhm 2000; Barbin and Oliveira, 2018; Shergill et al., 2017; Devlin et al., 2010; Cawthorn et al., 2014). Some of these changes are in stark contrast to those incurred on extramedullary adipose depots.



## Chapter 1 – The bone marrow microenvironment

This and other findings support BMAT as a unique adipose depot. Great efforts are being put forth for its characterization as presented in Chapter 2.

### *Location, location, location*

Similar patterns of BMAd formation occur in vertebrae species (including rodents, rabbits, and humans) at a decreasing rate relative to increasing lifespan and size of the animal, with larger skeletons containing more BMAT extending farther into the skeleton (Scheller et al., 2015). Generally, BMAT expansion occurs in a centripetal pattern, originating first in the very distal skeleton, then in the epiphyses and diaphysis of the long bones while appearing later in the axial skeleton (Blebea et al., 2007). This may correspond with distinct waves of Osterix<sup>+</sup> (Osx<sup>+</sup>) stromal, primitive, and definitive cells organizing the developing BM (Mizoguchi et al., 2014).

It is now well-established that the stable BMAds, also referred to by some as constitutive BMAds (cBMAds), form early in development appearing just after birth, are large in size with predominantly unsaturated lipids and are not mobilized readily. In mice, these stable BMAds extend from the malleolus in the medullary canal of the tibia until the tibia-fibular junction (Horowitz et al., 2017), while in rabbits they form a core through the center of the medullary canal of the long bones with surrounding rBMAds and hematopoietic marrow between the cBMAds and encompassing cortical bone (Bieglow and Tavassoli 1984). In humans, the very first appearance of cBMAds is in the terminal phalanges of the fetus just before birth when the marrow is fully hematopoietic (Emery and Follett, 1964). It is documented that the stable yellow marrow in the long bones first appears in the distal epiphyses and radiates from the mid-diaphyses mostly filling the medullary canal by adulthood with the exception of the proximal metaphysis that remains hematopoietic until old age (Kricun et al., 1985).

The labile, regulated BMAds (rBMAds) have been shown to fill the medullary canal just below the growth plate of the primary spongiosa and appear in the secondary ossification center (Horowitz et al., 2017). They extend through the metaphysis, accumulating preferentially along the endocortical surface of the diaphysis in mice (both during aging and with BMA induction) (Craft et al., 2018). These BMAds are small in size with mostly saturated lipids and are readily mobilized upon stimulation. Details on *in vivo* modulation of BMA by environmental and pharmacological factors are discussed in Chapter 2.

## The Essentials

### *Lessons from patients*

Diseases of congenital generalized lipodystrophy (CGL) that include a complete or partial loss of adipose depots reveal important insights into the consequences of genetic deficiencies involved in adipocytic maturation and function (reviewed in Scheller and Rosen, 2014) and may point us in the direction of the underlying nature of BMAd formation. CGL Type 1 (*AGPAT2* mutation) and Type 2 (Seipin/*BSCL2* mutation) are the most frequent forms with a high prevalence: of 45 pedigrees with CGL genotyped for *AGPAT2* and *BSCL2* loci, only eight had no substantial alteration in either gene (Agarwal et al., 2003). AGPATs are critical for the biosynthesis of triglycerides and phospholipids, whereas the function of seipin appears to be in lipid droplet assembly, maintenance, and endoplasmic reticulum (ER) communication at >90% of lipid droplet junctions (Szymanski et al., 2007, Cartwright and Goodman, 2012). CGL3 is associated with mutations in Calveolin-1 (*CAV1*) which encodes for a protein that is an integral component of plasma membrane indentations (calveolae) binding to fatty acids for translocation to lipid droplets. Type 4 is caused by mutations in polymerase I and transcript release factor (*PTRF*),

which is essential for the biogenesis of calveolae (Liu et al., 2008; Hill et al., 2008; Hayashi et al., 2009). Patients presenting with CGL1 have near-total loss of adipose depots including BMAT but have retained mechanical adipose tissue, while CGL2 results in complete loss of all adipose tissues and is the most severe form with half of patients having mild mental retardation (Lightbourne and Brown, 2017). This may indicate that seipin universally acts upstream of adipocyte formation or lipid storage and would also be a crucial component for BMAd formation. The general characteristics of CGL include a lack of adipose tissue, prominent muscularity, low leptin levels, and diabetes mellitus with hyperinsulinemia and dyslipidemia. Patients with CGL1 or CGL2 also have accelerated bone growth, cortical thickening, advanced skeletal age and sclerosis particularly in the appendicular skeleton as well as a prevalence of cystic lesions in the long bones, both locations where BMAT would normally be present (reviewed in Scheller and Rosen, 2014). Meanwhile, in patients with CGL3 or CGL4 prevalence of hyperinsulinemia and diabetes may be lower, sclerosis or cysts are not a common feature, and the initial accelerated bone growth slows to a normal or decreased skeletal age in childhood even leading to osteopenia and osteoporosis. Scheller and Rosen interestingly remark that these skeletal and endocrine differences may be linked to the persistence of BMAT in CGL3 and CGL4 which is not present in patients with CGL1 or CGL2 that indeed may have a shift towards osteoblast activity or number in the absence of BMAT.

### *Towards BMAT models*

Valuable insights can be learned from mouse models of CGL, but it is important to note that they diverge from the human phenotype to varying degrees mostly in the proportion of adipose tissue loss and accompanying metabolic phenotype. *Bsc12*<sup>-/-</sup> mice are not completely lipoatrophic before 6 months and have some visceral and subcutaneous WAT that show immature adipocytes with a defect in LD development (Cui et al., 2011; Chen et al., 2012; Prieur et al., 2013). These models have revealed that seipin is necessary for complete adipogenesis, since impairment in adipogenic gene (*Pparg*, *Lep*, *AdipoQ*, *Fabp4*, *Hsl*, *Plin1*) expression patterns worsen with adipocytic differentiation. This could partially be rescued by pioglitazone treatment inducing *Ap2* and *AdipoQ* expression *in vivo* through residual subcutaneous adipose tissue expansion, thus improving insulin sensitivity possibly through increased adiponectin secretion, and reducing lipotoxicity with improved liver steatosis (Prieur et al., 2013). Interestingly, although BAT mass is reduced in *Bsc12*<sup>-/-</sup> models, an increased expression of brown adipocyte markers (*Ucp1*, *Cidea*) in the residual WAT depots and functional browning during adipocytic differentiation *in vitro* has been observed where lipids are directed towards lipolysis, thereby contributing to the increased basal lipolysis of *Bsc12*<sup>-/-</sup> adipocytes (Prieur et al., 2013; Dollet et al., 2014). The effect is not mediated through beta3AR activation as this is downregulated in acquired *Bsc12* deficiency (Zhou et al., 2015). It has been proposed that seipin links neutral lipid synthesis with LD assembly and homeostasis, maintaining the ER bilayer and activation of adipogenesis through PPAR $\gamma$ . In the absence of seipin, neutral lipid accumulation due to the inability to channel TAGs into LDs would destabilize the ER bilayer (Cartwright and Goodman, 2012), affecting lipid synthesis and effectively lipid unsaturation ratio (Dollet et al., 2014).

### *Dropping in on lipid droplets*

LD formation (Guo et al., 2009) begins with fatty acids (FAs) that enter the cell via fatty acid transport proteins or fatty acid translocase (Ehehalt et al., 2006; Schaffer and Lodish et al., 1994), and can also be synthesized through endogenous de novo lipogenesis (DNL). These FAs then enter a bioactive pool to form fatty acyl-CoA to be used by glycerolipid synthesis enzymes in the endoplasmic reticulum (ER) to form neutral lipids such as triacylglycerols (TAGs) and eventually coalescing to nucleate to lipid lenses

## Chapter 1 – The bone marrow microenvironment

and forming LDs (Thiam and Beller et al., 2017). If attached to the ER, LDs may grow in size through diffusion of newly synthesized lipids to the LD, and if unattached through local synthesis or fusion of smaller LDs to larger ones. LDs increase in size during adipocytic differentiation and perilipins (PLINs) bind to promote their stabilization (Wollins et al., 2006; Kimmel and Sztalyrd et al., 2016). Lipases mobilize neutral lipids in LDs for metabolic energy by fatty acid oxidation which is triggered through nutritional, hormonal, or inflammatory activation. Adipose triglyceride lipase (ATGL) catalyzes the initial step of intracellular TAG hydrolysis followed by hormone sensitive lipase (HSL) and monoacylglycerol lipase into glycerol moieties (Zimmermann et al., 2004; Zechner et al., 2012). FAs are necessary for energy production and lipid synthesis for cellular signaling and membrane formation. Despite their importance, increased concentrations of non-esterified FAs can be detrimental contributing to lipotoxicity and thus TAG hydrolysis and FA cycling are carefully regulated (Unger et al., 2010; Zechner et al., 2012).

The primary product of DNL is palmitic acid (16:0), in the family of saturated FAs that have cytotoxic effects and induce reactive oxygen species (ROS) (Wang et al. 2013). The monounsaturated FA (MUFA) oleic acid (18:1) may counteract this effect possibly by activating esterification of palmitic acid into TAGs and lipid droplet storage (Ouchi et al., 2011). Palmitic acid accumulation is therefore prevented by increased desaturation to palmitoleic acid (16:1n-7) or elongation to stearic acid and further desaturation to oleic acid (Carta et al., 2017; Strable and Ntambi et al., 2010; Silbernagel et al., 2012). Notably, oleic acid inhibits palmitic-acid dependent osteoclastogenesis and palmitic acid is found to be increased in BM serum of osteoporotic women (Ouchi et al., 2011; Miranda et al., 2016). In fact, BMAT expansion throughout the red marrow with age and disease is associated with bone loss and fracture risk, while cBMAd formation is positively associated with bone accrual during early development through correlative and descriptive studies (Craft et al., 2018). Thus, we hypothesize that favoring the stabilization of cBMAds may be beneficial to reduce lipotoxicity.

## Challenging Methods

*In vitro* models and *in vivo* assays are imperative for delineating the BMAd differentiation axis to better understand these cells and their contribution to the malignant as well as homeostatic hematopoietic niche. However, development of such assays can be complex. The more we study the BM microenvironment, the more intricate it seems to become, with new cellular players being discovered as technologies to study the niche develop.

Working with primary BMAds is complicated by their fragile nature on isolation, culture, and handling. Moreover, contamination with other cells of hematopoietic or endothelial origin for example, is relatively high as these are in close contact. Isolation of stromal cells and subsequent adipocytic differentiation remains a mainstay for studying BM adipogenesis (discussed in Chapter 2). Isolation of the BM stromal compartment from mouse can be done by flushing, centrifugation, or crushing of the bone followed by enzymatic digestion of one or more of the resulting fractions (Figure 1.4a). Known cell populations are sometimes further purified by plastic adherence or based on surface marker expression, and multipotency of these cells can only be determined at the single cell level from clones of a single CFU-F (Bianco and Robey, 2015) (Figure 1.4b, 1.4c). However, heterotopic transplantation remains the gold standard for assessing differentiation capacity (Figure 1.4d). A multitude of different assays can be employed, whether via pre-differentiated cartilage pellets or cell-laden scaffolds (Serafini et al., 2014; Scotti et al., 2013; Chen et al., 2012; Vaiselbuh et al., 2010). Their commonality in recapitulating BM formation lies in completing



an initial ossification process, sometimes even with the help of exogenous bone morphogenic protein 2. This combination allows for the recruitment of hematopoietic cells to the ossicle (Torisawa et al., 2014).

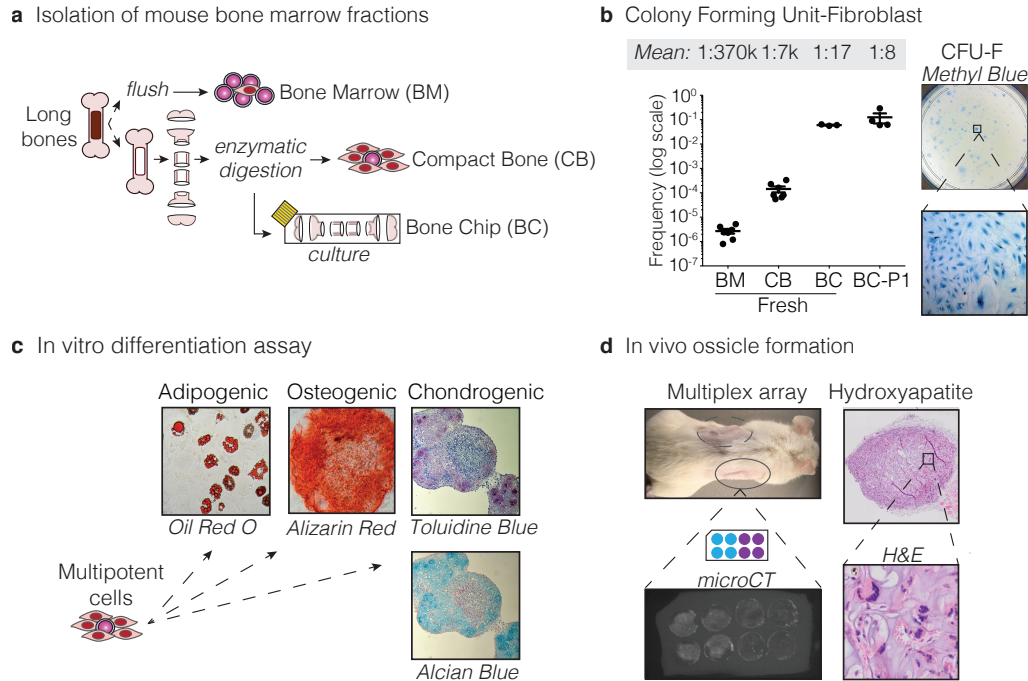


**Figure 1.4** | Isolation methods and multipotency assays for bone marrow stromal cells. **a** Methods vary significantly for isolating stromal populations. **b** Colony Forming Unit-Fibroblast (CFU-F) assays establish that enzymatic digestion and cell culture selects for cells with high clonal expansion capacity. The CFU-F capacity varies greatly between isolated fractions, correlating inversely with the number of hematopoietic cells contained in the respective fractions (data not shown). **c** Tri-lineage differentiation (here, of murine bone chip cells into adipocytic, osteogenic, and chondrogenic lineages) is conventionally and erroneously used to assess multipotency *in vitro*. **d** Transplantation *in vivo* is currently the only stringent test for multipotency by observing ossicle formation through differentiation of transplanted cells and recruitment of hematopoietic components.  $20 \times 10^6$  nucleated cells from a bone marrow biopsy of a 53-year-old female were isolated from hematopoietic (blue) and serum (purple) fractions and implanted together with PEG hydrogel in a multiplex PDMS array subcutaneously into 26-week old NSG female mice. Upon recovery after eight weeks, ossification (white) was observed by  $\mu$ CT scan. Hydroxyapatite scaffolds were seeded with  $1 \times 10^6$  OP9 cells, implanted subcutaneously into NSG female mice, and harvested after eight weeks for hematoxylin and eosin stain. Figures (a-c) were produced in collaboration with Dr. Shanti Rojas-Sutterlin. Subcutaneous implantation in (d) was performed with Dr. Queralt Vallmajo-Martin. BC: bone chip; BM: bone marrow; CB; compact bone; NSG: NOD SCID- $\gamma$ ; k: 1000, P1: passage one; PDMS: polydimethylsiloxane; PEG: poly(ethylene glycol).

*In vitro*, the first HSC-supportive systems were the Dexter cultures. Since then, protocols for culturing numerous different cell types in combination or without cytokines for HSC maintenance or hematopoietic expansion have been developed (Tajer et al., 2019; Isern et al., 2013; Butler et al., 2012; Jing et al., 2010; Li et al., 2007). Advancements in biomaterials and tissue engineering have promoted efforts to translate two dimensional (2D) cultures into three dimensional (3D) ones to better recapitulate the architecture of the hematopoietic niche. These include the use of poly(ethylene glycol) (PEG) hydrogels, collagen membranes, or mineralized scaffolds, and BM-on-a-chip PDMS constructs (Blache et al., 2016; Raic et

## Chapter 1 – The bone marrow microenvironment

al., 2014; Sieber et al., 2018; Torisawa et al., 2014; Lecarpentier et al., 2018; Bourguine et al., 2018). The *in vitro* to *in vivo* transfer of these types of niche constructs is usually not directly possible, requiring cell recovery first, which poses a significant problem for the adipocytic component due to the caveats mentioned above.

Establishing and building on robust 2D *in vitro* models of BM adipogenesis either through the differentiation of primary stroma or available BM cell lines, is the foundation for designing physiologically relevant 3D models to better study interactions of the niche. Thus, biomimetic 3D models of marrow adipogenesis in the form of BM organoids have a promising future in assisting the study of BMA and disease modeling.

## **CHAPTER 2**

### **Methodologies of bone marrow adiposity research**

## Chapter 2 – Methodologies of bone marrow adiposity research

*This chapter entails a modified post-print version of a manuscript  
accepted at Frontiers in Endocrinology on January 31<sup>st</sup> 2020, entitled*

## **Reporting Guidelines, Review of Methodological Standards, and Challenges Towards Harmonization in Bone Marrow Adiposity Research**

### ***Report of the Methodologies Working Group of the International Bone Marrow Adiposity Society***

Josefine Tratwal<sup>1‡</sup>, Rossella Labella<sup>2‡</sup>, Nathalie Bravenboer<sup>3,4‡</sup>, Greet Kerckhofs<sup>5,6‡</sup>, Eleni Douni<sup>7,8‡</sup>, Erica L. Scheller<sup>9</sup>, Sammy Badr<sup>10,11‡</sup>, Dimitrios C. Karampinos<sup>12‡</sup>, Sarah Beck-Cormier<sup>13,14‡</sup>, Biagio Palmisano<sup>15‡</sup>, Antonella Poloni<sup>16‡</sup>, Maria J. Moreno-Aliaga<sup>17,18‡</sup>, Jackie Fretz<sup>19</sup>, Matthew S. Rodeheffer<sup>20</sup>, Parastoo Boroumand<sup>21‡</sup>, Clifford J. Rosen<sup>22‡</sup>, Mark C. Horowitz<sup>23‡</sup>, Bram C.J. van der Eerden<sup>24‡</sup>, Annegreet G. Veldhuis-Vlug<sup>4,22,25‡</sup>, Olaia Naveiras<sup>1,26‡</sup>

‡ On behalf of the Methodologies Working Group for the International Bone Marrow Adiposity Society.

† These authors contributed equally.

Co-corresponding authors: Annegreet Veldhuis-Vlug and Olaia Naveiras

<sup>1</sup> Laboratory of Regenerative Hematopoiesis, Institute of Bioengineering (IBI) and Swiss Institute for Experimental Cancer Research (ISREC), Ecole Polytechnique Fédérale de Lausanne (EPFL), Lausanne, Switzerland

<sup>2</sup> Tissue and Tumour Microenvironments Lab, The Kennedy Institute of Rheumatology, University of Oxford, Oxford OX3 7FY, UK

<sup>3</sup> Department of Clinical Chemistry, Amsterdam University Medical Centers, Vrije Universiteit, Amsterdam Movement Sciences, Amsterdam, The Netherlands

<sup>4</sup> Department of Internal Medicine, Section Endocrinology, Center for Bone Quality, Leiden University medical Center, Leiden, The Netherlands.

<sup>5</sup> Biomechanics Lab, Institute of Mechanics, Materials and Civil Engineering, UCLouvain, Louvain-la-Neuve, Belgium.

<sup>6</sup> Department Materials Engineering, KU Leuven, Leuven, Belgium.

<sup>7</sup> Laboratory of Genetics, Department of Biotechnology, Agricultural University of Athens, Athens, Greece

<sup>8</sup> Institute for Bioinnovation, Biomedical Sciences Research Center "Alexander Fleming", Athens, Greece

<sup>9</sup> Department of Medicine, Division of Bone and Mineral Diseases, Washington University, Saint Louis, MO, USA

<sup>10</sup> Univ. Lille, EA 4490 - PMOI - Physiopathologie des Maladies Osseuses Inflammatoires, F-59000, Lille, France

<sup>11</sup> CHU Lille, Service de radiologie et imagerie musculosquelettique, F-59000 Lille, France

<sup>12</sup> Department of Diagnostic and Interventional Radiology, Technical University of Munich, Munich, Germany

<sup>13</sup> Inserm, UMR 1229, RMeS, Regenerative Medicine and Skeleton, Université de Nantes, ONIRIS, Nantes, F-44042, France

<sup>14</sup> Université de Nantes, UFR Odontologie, Nantes, F-44042, France

<sup>15</sup> Department of Genetics and Development, Columbia University Irving Medical Center, New York, NY, USA

<sup>16</sup> Hematology, Department of Clinic and Molecular Science, Università Politecnica Marche-AOU Ospedali Riuniti, Ancona, Italy.

<sup>17</sup> Centre for Nutrition Research and Department of Nutrition, Food Science and Physiology, School of Pharmacy and Nutrition, University of Navarra, Pamplona, Spain. IdiSNA, Navarra's Health Research Institute, Pamplona, Spain.

<sup>18</sup> CIBERObn Physiopathology of Obesity and Nutrition, Centre of Biomedical Research Network, ISCIII, Madrid, Spain.

<sup>19</sup> Department of Orthopaedics and Rehabilitation, Cellular and Developmental Biology, Yale University School of Medicine, New Haven, CT 06510, USA

<sup>20</sup> Department of Comparative Medicine and Molecular, Cellular and Developmental Biology, Yale University School of Medicine, New Haven, CT 06510, USA

<sup>21</sup> Cell Biology Program, The Hospital for Sick Children, Toronto, Ontario, M5G 0A4; Canada

<sup>22</sup> Maine Medical Center Research Institute, Center for Clinical and Translational Research, Scarborough, ME, USA

<sup>23</sup> Department of Orthopaedics and Rehabilitation, Yale University School of Medicine, New Haven, Connecticut.

<sup>24</sup> Laboratory for Calcium and Bone Metabolism, department of Internal medicine, Erasmus University Medical Center, Rotterdam, the Netherlands.

<sup>25</sup> Jan van Goyen Medical Center / OLVG Hospital, Department of Internal Medicine, Amsterdam, The Netherlands.

<sup>26</sup> Hematology Service, Departments of Oncology and Laboratory Medicine, Centre Hospitalier Universitaire Vaudois (CHUV), Lausanne, Switzerland

## Preface

It was through Paolo Bianco that Olaia and I learned of the first meeting on Bone Marrow Adiposity (BMA) in 2015 that we would attend in Lille, France. This was the beginning of a community of researchers and clinicians, coming together from the fields of bone, cancer, and endocrinology research to understand the meaning, the sense and the significance (Bianco, 2013) of bone marrow adipocytes. In the past few years, we have come a long way. In 2017, we hosted the 3<sup>rd</sup> International Meeting on BMA in Lausanne together with the ***Bianco/Riminucci lab***. This was a success in bringing additional leading experts from the fields of hematology and engineering to the community. It was an immense satisfaction to see a year of preparation come together, and I thank Olaia for entrusting me with the majority of the organization as well as the fellow organizers (in particular Mara Riminucci, Alessandro Corsi, and Biagio Palmisano) for bringing it to fruition. At the same time, the ***Bone Marrow Adiposity Society (BMAS)*** was born thanks to the vision and dedication of Olaia and many other prominent members who invested their efforts and time to make it a reality. Two years on, we now have established multiple working groups that are tackling important issues for the field moving forward. As coordinator of the ***Methodologies Working Group***, I have been fortunate to work with many passionate and talented people on addressing the current challenges of working with bone marrow adipocytes. In the process I have learned so much about other things than just these cells. Writing the review together was the collective effort of all the Working Group members and others of the Society who jumped on-board to help it come together. This was a truly positive collaborative effort with all members, and I'm appreciative to have been a part of it.

**Olaia Naveiras** and **Annegreet Veldhuis-Vlug** have been forces of nature taking calls in-between patient rounds at the hospital and their kid's afterschool activities, with nothing but smiles. Looking back, forming a trio together and being able to bounce or ideas around is something I greatly value having had.

I'm also grateful to the **librarians** at the Swiss Federal Institutes of Technology in Lausanne (EPFL) and Zürich (ETHZ) as well as Zürich University Hospital and University of Bern for finding the multitude of original historical research articles that I requested throughout the years, so that I could dive into the beautiful world of bone marrow adiposity and the hematopoietic niche.

**This chapter aims** to bring together the consensus of leading experts for a review of the current literature to set the first standards for bone marrow adiposity research. We have identified accepted standards in BMA research, emerging techniques, known confounding factors, and present minimal reporting standards to encourage facilitated comparison across studies. Challenges remain the harmonization of methodologies and the identification of methods to modulate BMA independently from other tissues. With this we hope to have provided common starting reference point for BMA and other researchers.

## Introduction

Bone marrow adipocytes (BMAd) reside in the bone marrow (BM) in close contact with bone, hematopoietic cells, marrow stromal cells, nerves, and blood vessels. Bone marrow adipose tissue (BMAT) thus refers to BM areas where BMAd are the predominant cell type, and bone marrow adiposity (BMA) refers more broadly to BMAT across all skeletal locations and metabolic states. Over the last decades, interest in the functional role of BMAd has gradually increased and it is now evident that BMAd are actively involved in bone metabolism, hematopoiesis, and energy metabolism (Cawthorn and Scheller, 2017; Li et al., 2018). In addition, a possible role for BMAd in many diseases has emerged (Veldhuis-Vlug and Rosen, 2018), and research groups all over the world are investigating the origin, function, and interaction of BMAd. However, different methods, models, and techniques are being used, which creates a challenge to compare or combine the results. Therefore, the International Bone Marrow Adiposity Society initiated a Methodologies Working Group to describe the existing methodologies, to identify associated challenges, and to establish standards in reporting as guidance for future studies in the field.

BMAT encompasses a heterogeneous population of mature adipocytes and preadipocytes, with distinct morphologies, lipid content, gene expression and function. Committed preadipocytes have a fibroblast-like morphology when observed *in vitro*, and are therefore morphologically indistinguishable from the progenitor populations encompassed within the term bone marrow stromal cells (BMSCs). However, preadipocytes are phenotypically very different from mature adipocytes. Preadipocytes are defined as cells committed through adipogenesis and characterized by the expression of early adipogenic genes (PPAR $\gamma$  and CEBP $\alpha$ ) (Raajendiran et al., 2016; Ambrosi et al., 2017). Mature BMAd express late adipogenic genes (ADIPOQ, GLUT4, FABP4, LPL, PLIN1, ZFP423) and contain a single large lipid droplet, therefore resembling white adipocytes in appearance. In particular, adiponectin (AdipoQ) expression is already present in BM preadipocytes and stromal precursors, then increases with differentiation (Mukohira et al., 2019a). Additionally, Krings et al. (2012) have revealed that BMAT from whole tibiae in C57BL/6 mice possibly have a distinctive phenotype, expressing genes characteristic of both WAT and BAT, congruent with the expression pattern of purified, primary human BMAd (Krings et al., 2012; Lecka-Czernik et al., 2017; Mattiucci et al., 2018a).

Indeed, Tavassoli et al. identified in 1976 two distinct populations of BMAd: after treatment with hemolytic anemia-inducing agent phenylhydrazine (Jain SK and Subrahmanyam D, 1978) one population remained stable while another population disappeared, and was described as labile BMAd. These two different “stable” and “labile” BMAd populations could be distinguished using performic acid Schiff (PFAS) staining (Tavassoli, 1976). The presence of two different populations of BMAd localized to different regions of the skeleton was also more recently shown by Scheller et al. In mice, smaller BMAd

## Chapter 2 – Methodologies of bone marrow adiposity research

(31-33µm cell diameter) are interspersed between hematopoietic cells in the femur, the proximal portion of the tibia, and almost all skeletal segments that contain hematopoietic BM, while larger BMAdS (38-39 µm) are localized in the distal portion of the tibiae and phalanx (Scheller et al., 2015) (Figure 2.1). When challenged with cold exposure, BMAdS interspersed in the red/hematopoietic marrow decreased in size and number, while the adipocytes localized in the yellow/adipocytic marrow did not change. The terms “regulated” and “constitutive” BMAT, respectively, have thus been proposed.

BMSCs and committed BM pre-adipocytes are more easily isolated and have seen a larger number of *in vitro* assays developed than mature BMAdS, which are more difficult to handle in culture or to process in whole bone samples. *In vivo* lineage tracing models have started to pave the way, while specific markers for BMAd maturation remain to be identified. If successful, identification of specific biomarkers at the different stages of BM adipogenesis in both mouse and human will provide tools to dissect the impact of BMA in physiology and disease. *In vivo* imaging technologies are being adapted from studies of different tissues (e.g. peripheral adipose tissue) and species (e.g. human to mouse), while novel *ex vivo* imaging techniques are being adapted and developed specifically for BMAdS and BM stromal imaging. All such techniques and their limitations and challenges are reviewed in the six sections that constitute this review, and guidelines for reporting of BMA-related results to maximize comparability are proposed in the concluding remarks (Table 2.1).

Of note, even with such significant technological advances over the last decade, histological analysis has been a historical contributor in the understanding of BM composition and architecture, and is rapidly evolving through automatization via Digital Pathology. Histomorphometry therefore remains an important aspect of standard methodological practices in basic or translational research as well as clinical laboratories

In addition, although rats and non-rodent animal models are recommended by the FDA or European Union as a model for osteoporosis, the field of BMA extends beyond bone health itself to the study of energy metabolism, hematopoiesis and metastatic bone disease, amongst other subfields. Mice constitute very important models for these other aspects of BMA research, especially in their quality of premier animal for genetic studies, and are thus recognized as preclinical model in this context. Nonetheless, we would like to encourage the study of BMA in larger animals and other rodents, especially when bone health and biomechanical properties of bone are being assessed.



**Table 2.1** | Challenges and goals ahead for the BMA field and the BMAS WG in Methodologies.

| CHALLENGES            |   | GOALS  |
|-----------------------|---|--|
| MAIN CHALLENGE        | <b>Standardize</b>                            | <p>Increase comparability by:</p> <ul style="list-style-type: none"> <li>• Homogenous definitions (c.f. BMAS consensus in nomenclature)</li> <li>• Homogenous reporting (c.f. BMAS Reporting Guidelines below)</li> </ul> <p>Increase reproducibility by:</p> <ul style="list-style-type: none"> <li>• Establishing consensus on standardized bone sites for analysis (e.g. rBMAT/cBMAT transition zones: tibia, caudal vertebrae)</li> <li>• Establishing consensus on reference groups</li> <li>• Establishing recommended standardized protocols: <ul style="list-style-type: none"> <li>○ for in vivo modulation</li> <li>○ for in vivo extraction of primary BMAd and BMSCs</li> <li>○ for method-specific thresholds for BMA detection</li> </ul> </li> <li>• Minimize effects of known confounding factors, to increase inter-study and multi-site comparison</li> <li>• Increase availability and accessibility of imaging techniques to implement use in routine clinical practice</li> </ul>   |
|                       | <b>Adhere to minimal reporting guidelines</b> | <p><u>Implement the following “BMAS reporting guidelines”:</u></p> <ul style="list-style-type: none"> <li>• Specify precise BMA skeletal location in all figure legends</li> <li>• Report known confounding factors for all experiments: <ul style="list-style-type: none"> <li>○ skeletal location, gender, age, strain</li> <li>○ ambient temperature (e.g. average housing temperature)</li> <li>○ nutritional status (e.g. average food intake, antibiotics)</li> <li>○ metabolic state (e.g. fasting, time of collection)</li> <li>○ exercise (e.g. type of enrichment material in cages)</li> </ul> </li> <li>• Report isolation technique with sufficient precision to reproduce; consider depositing protocol (e.g. protocol sharing platforms as recommended in the BMAS working group site at <a href="http://www.bma-society.org">www.bma-society.org</a>)</li> <li>• Report BMAd purity (e.g. hematopoietic/CD45+, endothelial contamination, and CFU-F/BMSC) and viability/intactness</li> <li>• Report detailed imaging parameters, postprocessing tools and algorithms</li> </ul> |
| TECHNICAL ASPECTS     | <b>Innovate</b>                               | <p>Development of:</p> <ul style="list-style-type: none"> <li>• models for specific BMAd deletion</li> <li>• specific BMA biomarkers</li> <li>• recommended reference gene-set for adipogenic differentiation</li> </ul> <p>Move from descriptive to mechanistic studies</p>   |
|                       | <b>Define standards</b>                       | <p>Define the normal physiological values and increase functional understanding:</p> <ul style="list-style-type: none"> <li>• in humans by age, gender, skeletal location and lipid composition</li> <li>• in animal models by establishing a consensus reference group to be included as comparison in all animal studies (i.e. C57BL/6J eight-week-old female mouse as homeostatic control group)</li> </ul>   |
| CLINICAL PERSPECTIVES | <b>Disseminate</b>                            | <p>Facilitate access and use of unbiased BMA methodologies to non-experts (e.g. automated imaging, reference gene sets, reference cell trajectory maps)</p>  |

BMA: bone marrow adiposity; BMAd: bone marrow adipocyte; BMAS: Bone Marrow Adiposity Society; BMSC: bone marrow stromal cell.

## Synthesis

### Histomorphometry

The field of bone histomorphometry was accelerated in 1976 when Dr. Parfitt published “Terminology and symbols in bone morphometry” which lay the foundation for the first Guideline on Bone histomorphometry (Parfitt, 1976). We can now build on this important consensus to establish additional guidelines on histomorphometry of BMAT. In 1987 Parfitt et al. listed three different meanings for bone; mineralized bone matrix, bone matrix, and bone tissue (Parfitt et al., 1987). Bone tissue encompasses bone and a soft tissue within it, the BM. The BM includes hematopoietic cells and its precursors, physically and functionally supported by diverse BM stromal cell populations (reviewed in (Mendelson and Frenette, 2014)). The latter is a three-dimensional network of cells in contact with developing blood cells in the extravascular space. The known main cell types that constitute this network are: osteogenic cells near bone surfaces, perivascular cells associated to sinusoids, and adipocytes. As discussed in this first section, methods to quantify marrow components via histomorphometry are based on different sample preparation, embedding and staining techniques, most requiring an intermediate step of decalcification and some allowing for epitope conservation for immunostaining. Paraffin-embedded samples have the advantage of access to large retrospective collections and potential comparability across sites, especially for the clinical setting where paraffin-embedding is standard. Other conservation procedures allow for more precise histomorphometric quantification, and some do not require decalcification (methyl methacrylate, MMA, or resin embedding, including technovit 900).

#### *Sample preparation*

Histomorphometric analysis relies predominantly on the quality of the sample. Therefore, careful consideration of the sample preparation is important. To prepare a BM sample, either calcified or decalcified bone samples can be embedded in paraffin or plastic, depending on the desired staining procedure (Erben and Glosmann, 2012; Malhan et al., 2018). For both procedures, the BM sample is regularly fixed in 4% Paraformaldehyde. Afterwards, the sample can be sectioned in conventionally 4–5µm sections.

#### *Decalcification*

Several options of decalcifying agents are available, though Ethylenediaminetetraacetic acid (EDTA) is advised as compared to acid-based decalcification to enable most enzymatic and immunohistochemical stainings (Prasad and Donoghue, 2013). Different factors can control the rate of the decalcification process: concentration of decalcifying agent, temperature, density of the sample, agitation and thickness of the tissue. In general, a large volume (e.g. 20x that of the sample), a high concentration of decalcifying agent and a high temperature (e.g. 20°C–37°C) during decalcification can speed up the reaction process. In contrast, increase of the size, density, and thickness of the sample may require longer decalcification time (Prasad and Donoghue, 2013; Malhan et al., 2018). For an optimal immunostaining, an uniform decalcification of the sample is important, and we recommend decalcification at room temperature or 4°C on constant shaking, a large volume of EDTA to sample (at least 10:1 v/v) and several refreshments of the solution (every 3–4 days) to prevent calcium saturation (Kusumbe et al., 2015).

Decalcification can also be performed using acidic agents to dissolve the calcium salts from the bone. This group of agents includes strong and weak acids. However, strong acid agents (nitric and hydrochloric

acid) should be avoided in order to preserve the integrity of the cells and the enzymatic activity if subsequent immunostainings are desired (Savi et al., 2017). Among the group of weak acids (picric, acetic, and formic acid), decalcification performed with Morse's solution (50% formic acid and 20% sodium citrate) can also preserve the integrity of the sample for immunohistochemistry while allowing for high quality architectural evaluation with Hematoxylin and Eosin (H&E) staining (González-Chávez et al., 2013). Dehydration is required prior to embedding. Ethanol dehydration, in graded increases of ethanol and xylene, can also allow for long-term storage of bones in 70% ethanol prior to embedding (Iwaniec and Turner, 2013).

### Embedding

To embed the samples after dehydration, several options exist. Most common and available is paraffin embedding. Decalcification is, however, necessary. This protocol is very useful to perform immunostaining, but the integrity of BM content, due to the juxtaposition of hard (decalcified bone) versus soft (marrow) tissue is not guaranteed. Alternatives to paraffin are MMA or technovit 900 embedding. These do not require decalcification and allow for better preservation of the adipocyte morphology. However MMA and technovit 900 are less available in most laboratories and immunohistochemical staining becomes a challenge due to the destruction of the antigen presentation with the conventional MMA embedding protocols (Yang et al., 2003). With all embedding methods the histological procedure dissolves all the lipids in the vacuole, therefore the adipocytes are referred to as 'ghosts', which makes it impossible to investigate lipid content and composition in combination with histology.

To resolve this issue, Erben et al. developed an alternative protocol for plastic embedding, that avoids the complete loss of enzymatic activity in the tissue by adding methylbenzoate during the infiltration process and polymerization of the plastic (Erben, 1997). Here, cold embedding seems to be crucial for antigen presentation in the immunohistochemical procedure. Enzymatic activity is also preserved by using another resin embedding system (e.g. Tecnovit 9100) that contains methyl methacrylate and catalysators that allow the polymerisation at low temperature (4°C) (Beck-Cormier et al., 2019).

### Staining

Although the adipocyte lipid vacuole is empty due to the ethanol-based dehydration necessary for histological procedures, these mature adipocyte ghosts are easily identifiable with several standardized staining procedures. The most frequently used in paraffin embedded bone is the H&E stain. Standardized staining procedures for plastic embedded bone, such as Goldner's trichrome, toluidine blue and Von Kossa staining can also be used to identify mature adipocyte ghost cells (Erben, 1997).

The discrimination between BMAdS and blood vessels in a cross section can be difficult since the BM microenvironment is densely populated by blood vessels of different types and diameter and the endothelial wall is not always identifiable (Bixel et al., 2017). Immunohistochemistry for Perilipin (Zhou et al., 2017), a marker of mature adipocytes, is therefore useful for identification of BMAdS in both human and murine tissues (Figure 2.1). Alternatively, immunostaining for Endomucin and/or CD31, markers for endothelial cells can be used to discriminate between blood vessels and adipocytes (Kusumbe et al., 2016b).

## Chapter 2 – Methodologies of bone marrow adiposity research

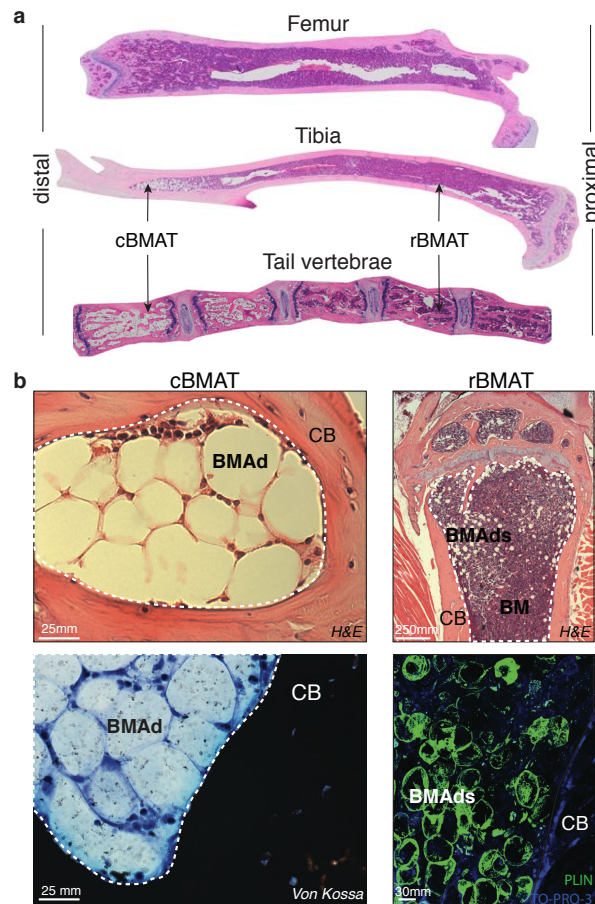


**Figure 2.1** | Histological characterization of BMAT. **a** Distal-proximal representative images in Hematoxylin & Eosin (H&E) stain of 4 $\mu$ m paraffin sections of femur, tibia and tail of eight-week-old mice. Note that the artefactually empty region in the center of tibia and femur corresponds to the expansion of the central vein lumen due to fixation-mediated retraction. **b** Left panels: Murine bone marrow adipocytes in the distal tibia of 24-week-old mice (cBMAT) of 3 $\mu$ m paraffin sections stained with H&E (top) and 6 $\mu$ m sections stained with von Kossa/Methylene Blue (bottom). Right panels: murine bone marrow adipocytes in the proximal tibia of 24 weeks-old mice (rBMAT) of 3 $\mu$ m paraffin sections stained with H&E (top) and 100 $\mu$ m sections stained with perilipin immunofluorescence (bottom, Perilipin in green and TO-PRO-3 nuclear counterstain) of 50-week-old mice. All images correspond to C57BL/6 female mice housed at room temperature fed ad libitum standard diet. BM: bone marrow; BMAAd: bone marrow adipocyte; CB: compact bone; cBMAT: constitutive bone marrow adipose tissue; H&E: hematoxylin and eosin; rBMAT: regulated bone marrow adipose tissue.

### Quantification

Two types of dimensional quantification are possible: two dimensional in terms of perimeter, diameter and area, and three dimensional in terms of volume and surface (Silva et al., 2015). Moreover, as described in the consensus on bone histomorphometry (Dempster et al., 2013) and extensively discussed in the BMAS nomenclature position paper, BMA parameters should be presented in relation to a reference region (Bravenboer et al., 2019). By using a common referent, it is possible to assess changes in the number or percentage of adipocytes following an intervention or comparing physiological and pathological states. For histological measures of BMAT, two-dimensional measurements of BMAT are applicable and two reference areas should be used: Marrow area (Ma.Ar) and total tissue area (T.Ar). It

is important to distinguish between these two areas since the interpretation is notably different. When bone mass is lost and replaced by other marrow tissue, the Ma.Ar is increased while T.Ar remains similar. Marrow adiposity increases only when the area of BMAds increases relative to the marrow space. For three-dimensional *ex vivo* or *in vivo* measurement, Marrow volume (Ma.V) and Total tissue Volume (TV) should be used. A priori, two-dimensional measures should be used in standard bone histomorphometry and three-dimensional measures should be reserved for techniques which rely on 3D measurements, as discussed in the *ex vivo* or *in vivo* sections. Three-dimensional measurements may be used in histomorphometry when analysis of serial sections is performed to approximate volumes.

Additionally, measurement of the size of individual adipocytes is important in the analysis of BMAT, since the changes in total adipose tissue can be due to either an increase in the number of adipocytes or an increase in the size of the adipocytes. This distinction is important since the mechanism behind these changes can reveal both differences in adipogenic differentiation (affecting the number) or in lipolysis (affecting the size). In consensus with the Nomenclature working group of the BMAS, we suggest to use the terms Perimeter (Ad.Pm), Diameter (Ad.Dm), and mean Adipocyte Area (Ad.Ar) to address adipocyte size. Adipocyte areas can be reported for individual BMAds, giving rise to the frequency distribution of BMAd areas and corresponding measurement of mean or median Ad.Ar. In addition, adipocyte area can be reported at the tissue level as % of total adipocyte area relative to hematopoietic area ( $\Sigma \text{Ad.Ar} / \text{Hm.Ar}$ ), tissue area ( $\Sigma \text{Ad.Ar} / \text{T.Ar}$ ) or, most commonly, to marrow area ( $\Sigma \text{Ad.Ar} / \text{Ma.Ar}$ ) also commonly reported as “marrow adipose area” or less precisely as “marrow adiposity”. Hematopoietic area is defined either by CD45 positivity in immunohistochemistry or, morphologically, by the areas defined by the high density of hematopoietic cell nuclei within the marrow space. Exhaustive recommendations on BMA nomenclature are available in a white paper authored by the BMAS Working Group in Nomenclature (Bravenboer et al., 2019).

Another important histological measure for adipocytes is the density of adipocytes. This is also used to differentiate between adipogenesis or enlargement of the adipocyte due to lipid storage. Adipocyte density can be measured as number of adipocytes per marrow area ( $\text{Ad.N} / \text{Ma.Ar}$ ), number of adipocytes per hematopoietic area ( $\text{Ad.N} / \text{Hm.Ar}$ ) or as number of adipocytes per tissue area ( $\text{Ad.N} / \text{T.Ar}$ ). Adipocyte density varies greatly in the endocortical versus trabecular regions of the bone, and thus detailed annotation and standardization of the quantified region is paramount, as detailed in the BMAS reporting guidelines (Table 2.1).

### Software

To quantify these parameters, a selection of software packages are available. Some have been developed for extramedullary adipose tissue and require manual adipocyte measurements, while others are designed for assessment of BM sections and are semi-automated, with a few entirely automated (listed in Table 2.2). Automated or semi-automated detection programs use shape (roundness, circularity) and the absence of color within the lipid vacuole for detection of BMAds. While such software packages are not yet routine, most laboratories have developed them in-house in order to perform adipocyte histomorphometry. Some of these software packages are freely available online (peerJ, fathisto, and MarrowQuant, see Table 2.2).

**Table 2.2|** Description of the most used software for bone marrow histomorphometry.

| REFERENCES                   | SOFTWARE          | SPECIES, SAMPLE              | AUTOMATIC OR MANUAL | OTHER METHODS               | REPORTED PARAMETERS                   | PROPOSED PARAMETERS  | OTHER MEASURES                 | STAINS (EMBEDDING)              |
|------------------------------|-------------------|------------------------------|---------------------|-----------------------------|---------------------------------------|--|--------------------------------|---------------------------------|
| Sato et al., 2004            | OsteoMeasure      | monkey, proximal femur       | manual              | -                           | -                                     | Ad.Ar/T.Ar   | -                              | -                               |
| Syed et al., 2008            | OsteoMeasure      | human, biopsy                | manual              | blinded count               | Ad.N; % Ad.V /TV (AV/TV); total Ad.Pm | $\Sigma$ Ad.Ar/T.Ar; Ad.N/T.Ar; total Ad.Pm                  | -                              | Goldner, 20x                    |
| Razidlo et al., 2010         | OsteoMeasure      | mouse, femur                 | manual              | -                           | AV/TV; Ad.Pm; N.Ar/T.Ar               | $\Sigma$ Ad.Ar/T.Ar; Ad.Pm; Ad.N/T.Ar                        | bone standard histomorphometry | Goldner's Trichrome / Von Kossa |
| Devlin et al., 2010          | OsteoMeasure      | mouse, distal femur          | manual              | -                           | Ad.N/T.Ar                             | Ad.N/T.Ar  | bone standard histomorphometry | -                               |
| Motyl et al., 2012           | OsteoMeasure      | proximal tibia metaphysis    | manual              | -                           | -                                     | Ad.N/T.Ar  | bone standard histomorphometry | unstained (paraffin)            |
| Duque G et al., 2013         | OsteoMeasure      | mouse, femur                 | semi-automatic      | -                           | Marrow fat content % (AV/TV)          | $\Sigma$ Ad.Ar/T.Ar  | bone standard histomorphometry | H&E                             |
| Nallamshetty et al., 2013    | OsteoMeasure      | mouse, tibia                 | manual              | -                           | Ad.N/T.Ar; Ad.Dm                      | Ad.N/T.Ar; Ad.Dm   | bone standard histomorphometry | TRAP / toluidine blue           |
| Turner et al., 2014          | OsteoMeasure      | mouse, distal femur          | manual              | -                           | Ad.Ar/T.Ar; Ad.N/T.Ar                 | Ad.Ar/T.Ar; N.Ar/T.Ar  | bone standard histomorphometry | TRAP / toluidine blue           |
| Philbrick et al., 2015       | OsteoMeasure      | ouse, distal femur metaphysi | manual              | fat extraction and analysis | Ma. adiposity; Ad. Density            | $\Sigma$ Ad.Ar/T.Ar; $\Sigma$ Ad.Ar/Ma.Ar; Ad.N/Ma.Ar        | bone standard histomorphometry | Methyl-methacrylate             |
| Wesseling-Perry et al., 2017 | OsteoMeasure      | human, bone biopsy           | manual              | -                           | Ad.Ar/Ma.Ar                           | Ad.Ar/Ma.Ar  | bone standard histomorphometry | unstained, (plastic) 10x        |
| Le et al., 2017              | Osteomeasure      | mouse, tibia                 | manual              | -                           | Ad.N/T.Ar Ad.Ar/T.Ar                  | Ad.N/T.Ar; Ad.Ar/T.Ar  | bone standard histomorphometry | H&E                             |
| Devlin et al., 2018          | OsteoMeasure      | mmouse, distal femur         | manual              | -                           | Ad.V/TV                               | $\Sigma$ Ad.Ar/T.Ar  | bone standard histomorphometry | -                               |
| Liu et al., 2011             | Image Pro         | mouse, distal femur          | manual              | -                           | Ad.N; Ad.Ar                           | Ad.Ar/T.Ar; Ad.N/Ma.Ar                                       | -                              | H&E                             |
| Wang et al., 2016            | Image Pro Plus    | mouse, tibia                 | manual              | -                           | -                                     | $\Sigma$ Ad.Ar/T.Ar; Ad.Ar/Ma.Ar                             | -                              | H&E                             |
| Zou et al., 2016             | Image Pro Plus    | mouse, tibia                 | manual              | -                           | Ad.Ar                                 | Ad.Ar/Ma.Ar  | bone standard histomorphometry | H&E                             |
| Li et al., 2014a             | Image Pro Plus v6 | rat, femur                   | manual              | manual count                | Ad.N; Ad.Ar; Ad.Dm, Ad. Density       | $\Sigma$ Ad.Ar/T.Ar; $\Sigma$ Ad.Ar/Ma.Ar; Ad.N/Ma.Ar; Ad.Dm | bone standard histomorphometry | H&E                             |
| Li et al., 2016              | Image Pro Plus v6 | rat, femur                   | manual              | -                           | Ad.Dm, Ad.N/Ma.Ar %Ad.Ar,             | Ad.Dm; $\Sigma$ Ad.Ar/T.Ar; $\Sigma$ Ad.Ar/Ma.Ar; Ad.N/Ma.Ar | bone standard histomorphometry | H&E                             |
| Li et al., 2016              | Image Pro Plus v6 | rabbit, distal femur         | manual              | -                           | Ad.Dm; Ad.N/Ma.Ar; Ad.Ar/Ma.Ar        | Ad.Dm; Ad.N/Ma.Ar; $\Sigma$ Ad.Ar/Ma.Ar                      | -                              | H&E                             |
| Kim et al., 2002             | ImageJ            | rat, proximal tibia          | manual              | -                           | Ad. content (Ad.Ar, T.Ar)             | Ad.Ar; $\Sigma$ Ad.Ar/T.Ar                                   | -                              | H&E                             |

**Table 2.2** | Description of the most used software for bone marrow histomorphometry.

| REFERENCES                          | SOFTWARE          | SPECIES, SAMPLE                  | AUTOMATIC OR MANUAL | OTHER METHODS                        | REPORTED PARAMETERS   | PROPOSED PARAMETERS  | OTHER MEASURES                       | STAINS (EMBEDDING)            |
|-------------------------------------|-------------------|----------------------------------|---------------------|--------------------------------------|---|--|--------------------------------------|-------------------------------|
| Bornstein et al., 2017              | ImageJ            | mouse, femur or tibia            | manual              | -                                    | Ad.V/Ma.V   | $\Sigma$ Ad.Ar/Ma.Ar                                       | bone standard histomorphometry       | H&E (plastic or paraffin) 20x |
| Yang et al., 2018                   | ImageJ            | rat, proximal tibia              | manual              | -                                    | Ad.N/T.Ar; Ad.Ar/T.Ar   | Ad.N/T.Ar; Ad.Ar/T.Ar                                      | -                                    | H&E                           |
| Costa et al., 2019                  | ImageJ            | mouse, distal femoral metaphysis | Automatic/manual    | OsteoMeasure                         | T.Ar adiposity, Ad.N/T.Ar, adiposity (%)                        | $\Sigma$ Ad.Ar/T.Ar; $\Sigma$ Ad.Ar/Ma.Ar; Ad.N/Ma.Ar      | -                                    | Von Kossa tetrachrome         |
| Beekman et al., 2019a               | OsteoidHisto      | human, biopsy                    | semi-automatic      | -                                    | Ad.V/TV; Ad.V/Ma.V AdDm AdN/Ma.Ar                               | $\Sigma$ Ad.Ar/T.Ar; $\Sigma$ Ad.Ar/Ma.Ar; AdDm; AdN/Ma.Ar | bone standard histomorphometry       | Goldner's Trichrome           |
| Beekman et al., 2019b               | OsteoidHisto      | mouse, tibia                     | semi-automatic      | -                                    | Ad.V/TV Ad.V/Ma.V AdDm AdDm                                     | $\Sigma$ Ad.Ar/T.Ar; $\Sigma$ Ad.Ar/Ma.Ar; AdDm; AdN/T.Ar  | bone standard histomorphometry       | calcein blue / TRAP           |
| Fan et al., 2017                    | Bioquant Osteo    | human, biopsy                    | semi-automatic      | blinded count                        | Ad.N, Ad. size,   | Ad.N/Ma.V; $\Sigma$ Ad.Ar/Ma.Ar                            | bone standard histomorphometry       | -                             |
| Chandra et al., 2014                | Bioquant Osteo    | rat, tibia                       | manual              | -                                    | Ad.N/TV   | Ad.N/T.Ar  | bone standard histomorphometry       | Goldner's trichrome           |
| Brennan et al., 2014                | Bioquant Osteo II | mouse, femur                     | no information      | -                                    | AV/TV   | $\Sigma$ Ad.Ar/Tar   | bone standard histomorphometry       | Goldner's Trichrome or TRAP   |
| Li et al., 2013a                    | Leica Q-win Plus  | rabbit, vertebrae                | no information      | -                                    | AdDm; Ad.N/Ma.Ar  | AdDm; Ad.N/Ma.Ar   | -                                    | Oil-Red-O                     |
| Li et al., 2013b                    | Leica Q-win Plus  | rabbit, femur                    | -                   | -                                    | AdDm; Ad.D; Ad.V/Ma.V   | Ad.Dm; Ad.N/Ma.Ar; $\Sigma$ Ad.Ar/Ma.Ar                    | -                                    | H&E                           |
| Chapter 3                           | MarrowQuant       | mouse, skeleton                  | semi-automatic      | osmium tetroxide stain with $\mu$ CT | T.Ar; Ma.Ar; Ad.N; Ad.Ar; $\Sigma$ Ad.Ar/Ma.Ar; AdV ( $\mu$ CT) | T.Ar; Ma.Ar; Ad.N; Ad.Ar; $\Sigma$ Ad.Ar/Ma.Ar; Ad.N/Ma.Ar | bone A, hematopoietic A, vascular A. | H&E (paraffin) 20x            |
| Rojas-Sutterlin et al., unpublished | MarrowQuant       | mouse, tibia                     | semi-automatic      | -                                    | T.Ar; Ma.Ar; Ad.Ar; $\Sigma$ Ad.Ar/Ma.Ar                        | T.Ar; Ma.Ar; Ad.N; Ad.Ar; $\Sigma$ Ad.Ar/Ma.Ar; Ad.N/Ma.Ar | hematopoietic A, vascular A.         | H&E (paraffin) 20x            |
| Styner et al., 2017                 | Metamorph         | mouse, femur                     | semi-automatic      | -                                    | Ad.Ar; Ad.N   | $\Sigma$ Ad.Ar/T.Ar; Ad.N/Ma.Ar; AdDm                      | -                                    | H&E                           |

Ad.: Adipocyte; AdDm: Adipocyte diameter; Ad.N: Adipocyte number; A: Area; Ma.: Marrow; Ma.Ar: Marrow Area; AV: Total Adipocyte volume; H&E: hematoxylin and eosin; TRAP: Tartrate-resistant acid phosphatase; TV: Total Tissue volume;  $\Sigma$ : summation;  $\mu$ CT: micro-computerized tomography.

## Chapter 2 – Methodologies of bone marrow adiposity research

### *Challenges and limitations*

Histomorphometric analysis is a very useful tool to determine the quality of bone and assess changes in the number and size of cells. One of the limitations is that histomorphometry is a time-consuming technique requiring microscopy, software and/or manual quantification. In addition, it is a technique that until now has relied on the interpretation of the single investigator, and therefore demands a solid quality control system. The detection of BMAd can be hampered by the close connection of adipocytes in yellow/adipocytic areas, making the separation and adequate counting of clustered adipocytes a big challenge, in particular if membranes are not intact. In mice, the number of adipocytes in long bones tends to be lower in sites of regulated BMAT, and thus separate adipocytes can be more easily discerned and counted in the red/hematopoietic marrow.

However, the distinction of adipocytes from small blood vessels can be a challenge, whether for manual quantification or automated algorithms, especially in the younger animals or in the context of marrow regeneration. Additional immunostains to discern microvasculature from adipocyte ghosts are thus highly recommended as a validation step. Moreover, one must keep in mind that histological sections are a cross-section of the bone/marrow organ and thus of the BMAd itself. In general, validation of automatic detection of adipocytes is not described, neither by presenting data on quality control measurements nor by comparison with a manual method. We therefore consider manual detection of adipocytes the gold standard for histomorphometry until automated software packages have been validated. Annotation and standardization of the quantified region, as well as reporting of the experimental parameters as detailed in the BMAS reporting guidelines (Table 2.1) cannot be emphasized enough. Additionally, correlation of histomorphometry findings with *ex vivo* or *in vivo* bone measurements of lipid content to calcified tissue constitutes a much-valued biological validation of findings. Finally, a recommendation on which bone may be considered as standard for reporting is premature, but we agree that choosing areas of transition between regulated and constitutive BMAT is most informative (e.g. tibia and/or caudal tail for mice).

### Ex Vivo Whole-Bone Imaging

Histological slicing and histomorphometry remain the gold standard for the *ex vivo* evaluation and characterization of biological tissues in general, and BMAT in particular, by measuring adipocyte cell size and cell number. However, histological assessment (sectioning, staining, imaging, and analysis) remains a challenging, time-consuming, and often costly technique (Silva et al., 2015). Moreover, spatial patterns as well as the spatial inter-relationship between different tissues within one sample (for example BMAT in relation to bone and vasculature) can be inaccurate or impossible. To overcome some of the limitations of 2D analyses, several 3D imaging techniques have emerged to quantify the morphometry, spatial distribution of BMAT and its inter-relationship with other tissues in the marrow.

#### *Contrast-enhanced microfocus computed tomography*

X-ray microfocus computed tomography ( $\mu$ CT) is a very powerful tool for 3D imaging of mineralized tissues (Neues and Epple, 2008). High-resolution  $\mu$ CT ( $<2\mu\text{m}$  voxel size) and nanoCT (down to 150nm (Salmon, 2007)) scans are achievable and a high field of view to voxel size ratio can be obtained (Kerckhofs et al., 2016). While one of the biggest advantages of  $\mu$ CT is its non-destructive character, a considerable limitation of this technology is its lack of specificity for soft tissues. Phase contrast  $\mu$ CT is a possible solution, as it can be used to, for example, enhance edges, which allows a better visualization of soft tissues (Ritman et al., 2011). Indeed, it provides information concerning changes in the phase of



an X-ray beam that passes through an object. Moreover, it uses monochromatic X-rays, resulting in accurate measures of the attenuation coefficient, and thus enabling quantitative  $\mu$ CT imaging. This technique requires, however, highly dedicated hard- and software, and is not readily available. In addition, to the best of our knowledge, phase contrast imaging has so far not been used to visualize BMAT. Therefore, the focus of this review is rather on desktop single energy, polychromatic absorption contrast-enhanced  $\mu$ CT (CE-CT) imaging. Although having its limitations in the cone-beam shape of the X-ray bundle and the lower X-ray flux compared to synchrotron  $\mu$ CT, scanning times down to 15 minutes for high-resolution imaging can be achieved nowadays. For this kind of CE-CT, typically, there are two kinds of contrast agents used for the visualization of soft tissues: perfusion contrast agents, mostly used for in vivo or ex vivo indirect imaging of vasculature, and contrast agents that bind to the tissues for ex vivo imaging, further referred to as contrast-enhancing staining agents (CESAs). Here, we will focus on CESAs, which have proven to allow CE-CT imaging of BMAT.

The introduction of CESAs has enabled contrast-enhanced CE-CT to become a very important tool in biomedical imaging. CESAs bind to tissues of interest, increasing the X-ray attenuation coefficient (De Bournonville et al., 2019). The very first reports on the use of CESAs for CE-CT imaging of soft tissues go back to only about a decade ago. Indeed, several groups (Johnson et al., 2006; Litzlbauer et al., 2006; Ribi et al., 2008) used osmium tetroxide ( $\text{OsO}_4$ ) on mouse embryos, pig lungs, and honeybees, respectively, to enable virtual 3D anatomical analyses using CE-CT. Although in these studies  $\text{OsO}_4$  was used for general tissue staining, it is well known for its specific binding to unsaturated lipids (Palade, 1951; Turello et al., 1984). Consequently, several years later, Scheller *et al.* reported the use of  $\text{OsO}_4$  for 3D CE-CT visualization of BMAT and quantification of its amount and distribution in long bones of mice using standard  $\mu$ CT (Scheller et al., 2014; Scheller et al., 2015) and, subsequently, ultrahigh-resolution  $\mu$ CT (Khoury et al., 2015).

$\text{OsO}_4$ -based BMAT characterization requires a two-step scanning protocol: first, bones are detached and thoroughly cleaned from soft tissues, fixed, and scanned to enable characterization of 3D calcified bone parameters. The fixed bones are subsequently decalcified and then stained with  $\text{OsO}_4$  for 48 hours (Scheller et al., 2014) or longer if the mouse models develop severe BMAT accumulation. Subsequently,  $\text{OsO}_4$ -stained bones are rescanned. These images provide 3D quantification of BMAT structural properties, such as adipocyte volume/total volume (Ad.V/TV), adipocyte volume/marrow volume (Ad.V/Ma.V), and adipocyte volume/bone volume (Ad.V/BV), which are quantified based on the amount of osmium-bound lipid. When combining  $\text{OsO}_4$  staining with high-resolution  $\mu$ CT imaging, individual adipocytes can be distinguished (Figure 2.2a, 2.2c and 2.2e) and a distribution of diameter can be calculated. When combined with image coordinate registration, this technique allows alignment of both the BMAT distribution and bone micro-architecture, as well as calculation of the distance of the BMAd from the bone surface (Coutel et al., 2018). Some studies have also used this approach to measure BMAd density (cells/ $\text{mm}^2$  Ma.V) (Xiao et al., 2014). The use of  $\text{OsO}_4$  for CE-CT-based BMAT visualization in mouse bones has quickly become widespread due to its compatibility with existing  $\mu$ CT infrastructure, ease of use, and reasonable cost (Balani et al., 2017; Liu et al., 2017; Styner et al., 2017; Yu et al., 2018). As with most techniques, a high level of standardization is needed for each step in the procedure (fixation, decalcification,  $\text{OsO}_4$  staining, imaging, and analysis). For example, insufficient decalcification can lead to problematic osmium penetration and staining (Metscher, 2009). Indeed, the limited tissue penetration capability makes staining of dense regions of adipocytes or larger bones problematic, restricting this technique primarily to whole bones in mice. Moreover,  $\text{OsO}_4$  staining is

## Chapter 2 – Methodologies of bone marrow adiposity research

highly toxic, needing careful handling within a fume hood and appropriate disposal (Makarovsky et al., 2007; Nakakoshi et al., 2011).

To overcome these limitations, a recent study by Kerckhofs *et al.* reported the simultaneous visualization of mineralized and soft tissue structures within bones (Figure 2.2f) utilizing Hafnium Wells-Dawson polyoxometalate (Hf-WD-POM) as CESA (Kerckhofs et al., 2018). For this technique, murine long bones are incubated in POM powder dissolved in phosphate buffered saline while shaking gently for 48-hours to five days. Samples are then scanned in the staining solution, or wrapped in parafilm and put in a sample holder for scanning. Thanks to the combination of the hydrophobic behaviour of adipocytes and the binding of Hf-WD-POM to the BM tissue, visualization of the adipocytes is possible. When combining this CESA with high-resolution scanning (about 2 $\mu$ m voxel size - maximum total image volume about 6 x 4.8 x 6 mm<sup>3</sup> -), BMAdS can be imaged at the single cell level (Figure 2.2b, 2.2d and 2.2f). This not only facilitates measurement of the volume fraction of BMAT within the bone (Ad.V), but also enables the quantification of the BMAd Number (Ad.N), density (Ad.N/TV), and Diameter (Ad.Dm). Additionally, with sufficient contrast, the vascular network can be discriminated from the other

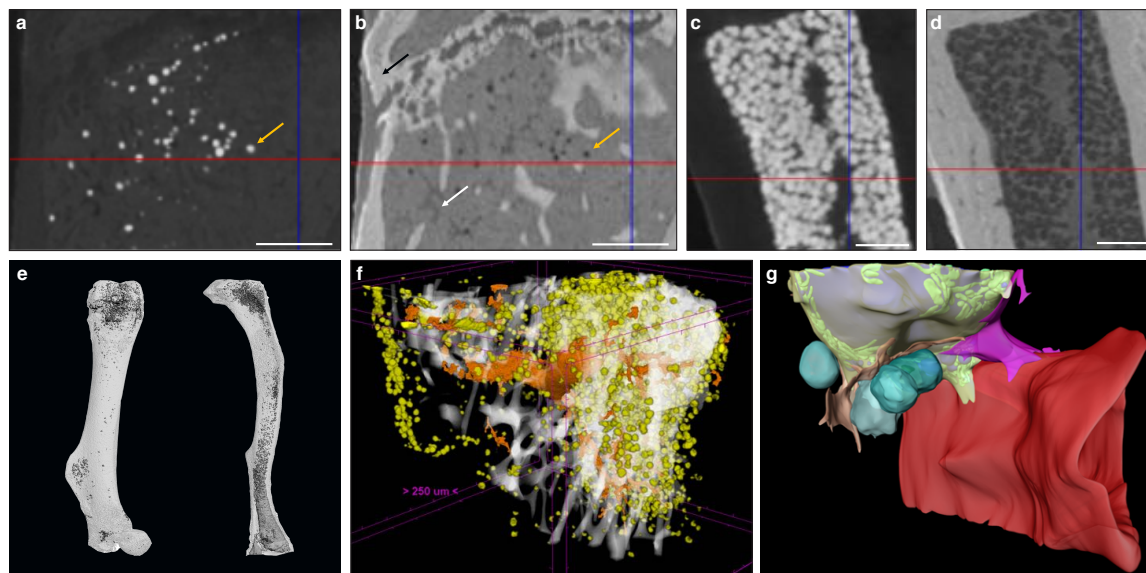


**Figure 2.2** | Zoom of a longitudinal CE-CT cross-section of the metaphysis of a murine tibia from a 16-week-old C57BL/6Rj male mouse fed ad libitum standard diet, using (a) osmium tetroxide and (b) Hf-WD POM staining, on the same sample. The orange arrows indicate the same adipocyte. The black arrow in (b) indicates the bone and the white arrow indicates a blood vessel. Zoom of a longitudinal CE-CT cross-section of the diaphysis of a murine long bone using (c) osmium tetroxide and (d) Hf-WD POM staining on the same sample. Scale bars are 250 $\mu$ m. 3D rendering of (e) an osmium tetroxide stained murine femur (left) and tibia (right) from an 11-week-old C57BL/6J male fed ad libitum standard diet at room temperature, where adipocytes are presented in dark grey and bone in light grey. f Hf-WD POM stained murine tibia from a 30-week-old C57BL/6Rj male mouse fed high fat diet for 22 weeks, (reprinted with permission from Kerckhofs et al. 2018), where white represents the bone, orange the blood vessels and yellow the marrow adipocytes. g 3D EM image of an adipocyte (reprinted with permission from Robles et al., 2019). Lipid is shown in grey, mitochondria in green, cytoplasm in semi-transparent yellow, vascular sinusoid in red, perivascular cells in pink and orange, and blood cells in turquoise. 3D: three-dimensional; CE-CT: contrast-enhanced computed tomography; EM: electron microscopy; Hf-WD POM: Hafnium Wells-Dawson polyoxometalate.

marrow tissues. This allows for full 3D blood vessel network assessment (i.e. branching and spatial distribution). Hence, Hf-WD POM-based CE-CT provides complementary data to standard histomorphometry, with enhanced 3D spatial information and inter-relation between different tissues in the BM compartment (Figure 2.2f). This was recently used to show that BMAT increased after menopause, and that increased BMAT was associated with osteoporosis and prevalent vertebral fractures (Beekman et al., 2018). It should be highlighted that Hf-WD POM is non-invasive and non-toxic, and does not interfere with subsequent histological processing and immunostaining. A limitation of Hf-WD POM, however, is that it is not yet commercially available, although it can be requested in the frame of a collaboration.

When making a direct comparison between Hf-WD POM and OsO<sub>4</sub> using high-resolution CE-CT, it was observed that both CESAs performed equally well for detecting BMAd (Figure 2.2). For locations with a low to medium BMAT amount, however, OsO<sub>4</sub> staining was more sensitive in visualizing the sparsely distributed adipocytes (Figure 2.2a-b). For medium to high BMAT content, OsO<sub>4</sub> tended to overestimate the adipocyte size due to high contrast difference between stained adipocytes and background, and thus contributed to the partial volume effect (Figure 2.2c-d). For this condition, Hf-WD POM allowed more accurate separation of individual adipocytes. Advantages and disadvantages of these *ex vivo* techniques are summarized in Table 2.3.

#### *Future challenges: 3D microscopy*

In recent years, standard microscopy techniques have also been optimized to gain 3D information about whole-bone cellular networks and nanoscale insight into the microenvironment of single cells. For example, tissue clearing strategies in skeletal tissues allow mapping of vascular networks and cell distributions in whole bones using light-sheet or two-photon microscopy (Greenbaum et al., 2017; Jing et al., 2018). Similarly, >50µm-thick section immunohistochemistry can provide *ex vivo* insight into cell localization in 3D via conventional confocal microscopy (Coutu et al., 2017). Though not yet published, we anticipate that clearing techniques described for marrow tissue will be used to provide novel information about BMAT localization and function. A key advantage relative to CT-based analyses is the ability to interrogate local cells and pathways that are defined based on expression of specific proteins and biomolecules using antibodies or genetically modified rodents.

At the nanoscale, focused ion beam scanning electron microscopy (EM), a form of serial EM that allows for 3D reconstructions at subcellular resolution, was recently applied to the BMAT adipocyte niche (Robles et al., 2019). This work builds upon previous 2D EM analyses of BMAT (Tavassoli, 1976) and has helped to define interactions of BMAT with surrounding cells at the endothelial interface, within the hematopoietic milieu, and at the bone surface (Figure 2.2g). The major limitation of all of these techniques is the need for specialized imaging equipment. In many instances, data handling and analysis paradigms, which require very sophisticated statistical analysis to correct for the boundaries imposed by the confined bone architecture (Gomariz et al., 2018), are also just beginning to emerge. In any case, the development of regularly revised common standards and the commitment to BMAS reporting guidelines, as specified in Table 2.1, will increase comparability and pave the way for the comparative studies necessary to determine future gold standards in this rapidly evolving field.

## Chapter 2 – Methodologies of bone marrow adiposity research

**Table 2.3** | Main quantitative parameters assessed when using ex vivo imaging techniques to explore bone marrow adipose tissue.

|               | PARAMETERS  | METHOD  | ADVANTAGES   | LIMITATIONS  |
|---------------|---|---|--|--|
| 2D TECHNIQUES | <b>Histomorphometry</b> <ul style="list-style-type: none"> <li>Adipocyte number (Ad.N)</li> <li>Adipocyte size (Ad.V)</li> <li>Adipocyte density (Ad.N/Ma.Ar)</li> <li>Spatial localization (2D)</li> </ul>                       | Resin, paraffin, or frozen sections (<5-10µm)   | <ul style="list-style-type: none"> <li>General availability</li> <li>Can be used in all species</li> <li>Pairs well with histological stains</li> </ul>  | <ul style="list-style-type: none"> <li>Slice/region bias</li> <li>Limited field of view</li> <li>Time consuming</li> <li>High cost</li> </ul>  |
|               | <b>µCT – Osmium</b> <ul style="list-style-type: none"> <li>BMAT volume (mm<sup>3</sup>)</li> <li>BMAT density (%)</li> <li>Adipocyte number* (Ad.N)</li> <li>Adipocyte size* (Ad.V)</li> <li>Spatial localization (3D)</li> </ul> | Whole bones or tissue samples, decalcified & stained in osmium tetroxide solution.<br><br>Samples imaged & analyzed with µ- or high-resolution CT | <ul style="list-style-type: none"> <li>Adapts existing CT infrastructure and analysis techniques</li> <li>Simple protocol</li> <li>Low cost</li> <li>Commercially available reagents</li> <li>Highly sensitive for sparse BMAds</li> </ul>   | <ul style="list-style-type: none"> <li>Poor penetration in large, or high adiposity samples</li> <li>Two-step scanning protocol for bone and BMAT analyses</li> <li>Overestimates Ad.Dm</li> <li>Highly toxic</li> </ul>   |
|               | <b>µCT – POM</b> <ul style="list-style-type: none"> <li>BMAT volume (mm<sup>3</sup>)</li> <li>BMAT density (%)</li> <li>Adipocyte number* (Ad.N)</li> <li>Adipocyte size* (Ad.V)</li> <li>Spatial localization (3D)</li> </ul>    | Whole bones or tissue samples are immersed in POM solution.<br><br>Samples imaged & analyzed with µ- or nanoCT.                                   | <ul style="list-style-type: none"> <li>Simultaneous visualization of bone, BMAT, and vessels in a single dataset*</li> <li>Adapts existing CT infrastructure and analysis techniques</li> <li>Simple staining protocol</li> <li>Non-invasive</li> <li>Accurate measure of Ad.Dm</li> </ul> | <ul style="list-style-type: none"> <li>High spatial and contrast resolution needed to discriminate blood vessel network</li> <li>Not yet commercially available</li> <li>Not very sensitive for sparsely BMAds</li> <li>Diffusion can take several days, depending on the sample size</li> </ul> |
| 3D TECHNIQUES | <b>FIB-SEM</b> <ul style="list-style-type: none"> <li>Ultrastructure</li> <li>Cell-cell interactions</li> </ul>   | 3D electron microscopy  | <ul style="list-style-type: none"> <li>Cellular and sub-cellular resolution of BMAd within niche</li> </ul>  | <ul style="list-style-type: none"> <li>Requires highly specialized equipment</li> <li>Time-consuming</li> <li>Limited field of view</li> <li>High cost</li> </ul>  |

\*High-resolution µCT only (<2µm resolution). Ad.Dm: Adipocyte diameter; Ad.N: Adipocyte number; Ad.V: Adipocyte volume; BMAd: bone marrow adipocyte; BMAT: bone marrow adipose tissue; FIB-SEM: Focused Ion Beam Scanning Electron Microscopy; POM: polyoxometalate; Ma.Ar: Marrow Area; µCT: micro-computed tomography.

## *In Vivo* Imaging

While *ex-vivo* techniques provide ample information of structures and allow for specific quantification of tissues, non-invasive imaging tools are essential when it comes to clinical studies so as to better understand the pathological processes that affect the BM *in situ*. To date, magnetic resonance imaging (MRI) is considered as the reference imaging modality to appraise *in vivo* BMA (Hu and Kan, 2013; Karampinos et al., 2018). This powerful imaging tool has been used in animals, for example to follow the effects of zoledronic acid treatment on marrow adipogenesis in ovariectomized rats (Li et al., 2014a), to quantify the decrease in BMAT volume in obese exercising mice (Styner et al., 2017), and to follow the progression of BMA in murine hematopoietic recovery (Chapter 3, Figure 2.3c and 2.3d). Due to their small size, such measurements are not straightforward in rodents, as they require very strong magnetic fields for meaningful BMA signal detection, and dual-energy  $\mu$ CT is a valid alternative. MRI techniques are primarily applied *in vivo* in humans (Figure 2.3a, 2.3b). Indeed, the growing interest in BMA in relation with postmenopausal osteoporosis, fractures, metabolic perturbations, as well as over- or undernutrition states, opens up potential exciting perspectives for clinicians (Paccou et al., 2015). However, the multiple interfaces between trabecular bone and bone marrow foster local magnetic inhomogeneities and challenge the accuracy and precision of BMAT quantification.

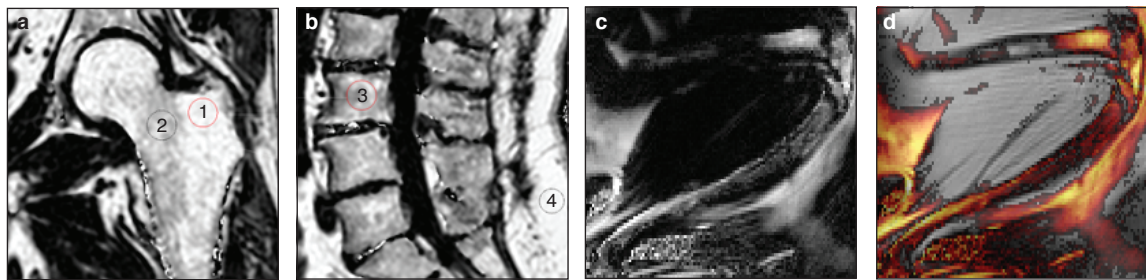


**Figure 2.3** | MRI of human and mouse bone marrow. **a-b.** Proton-density fat fraction (PDFF) maps generated using chemical shift encoding-based water-fat imaging from a commercially available sequence on a 3 Tesla magnetic resonance scanner. Coronal oblique acquisition of the left hip (**a**) and sagittal acquisition of the lumbar spine (**b**) of a 69-year-old woman with chronic lumbar and inguinal pain. Regions of interest can be drawn to assess bone marrow adiposity (1: 94%, 2: 77%, 3: 71%, 4: 96%) at different anatomical sites through the PDFF parameter. **c-d** A triple-point Dixon acquisition using a spin-echo based sequence with fat-water chemical shift was conducted on a 9.4 Tesla horizontal magnet, to assess BMAT *in vivo* at the peak of aplasia after irradiation and bone marrow transplant in an eight-week-old C57BL/6 female mice housed at room temperature fed ad libitum standard diet with antibiotics supplemented in the drinking water. The lower limb is shown as imaged in maximal flexion. Normalized fat content map (**c**) and fat content overlaid a magnitude image, red 10% - yellow 100% (**d**) show high BMAT content in the distal femur and also some BMAT in the proximal femur (horizontal, top of image) and throughout the tibia (diagonally across the image), in comparison to fat signal of surrounding extramedullary adipose tissue. BMAT: bone marrow adipose tissue; PDFF: proton-density fat fraction.

### *What can we measure?*

#### Main MR imaging biomarkers

The most relevant imaging biomarker used to quantitatively assess BMAT using MRI is the proton-density fat fraction (PDFF), which is the ratio of *unconfounded* fat signal to the sum of the *unconfounded* fat and water signals (Hu and Kan, 2013) (Reeder et al., 2011; Reeder et al., 2012; Hu and Kan, 2013) (Table 2.4). As a result, the main challenge and limitation with quantitative BMAT assessment using MRI is to

## Chapter 2 – Methodologies of bone marrow adiposity research

minimize the confounding factors to measure only signals coming from lipid protons. Interestingly, PDFF assessment of BMAT has benefited from technical developments in abdominal imaging. These technological improvements have been crucial for the emergence of reliable and non-invasive approaches to quantify adipose tissue in a standardized manner, especially through single-voxel proton spectroscopy ( $^1\text{H}$ -MRS) and chemical shift encoding-based water-fat imaging (WFI) techniques (Reeder et al., 2011).

The second most common quantitative parameter reported in the literature reflects BMAT fatty acid composition. This specific evaluation is a topic of growing interest, as saturated fatty acids may have deleterious effects on the osteoblast lineage and may play a role in multiple inflammatory processes along with certain polyunsaturated fatty acids, affecting bone health (Piño et al., 2019). Fat composition assessment can be performed through an expression of its degree of unsaturation or polyunsaturation, calculated respectively as the ratio of signal coming from the olefinic protons at 5.31 ppm or diallylic protons at 2.8 ppm on  $^1\text{H}$ -MRS acquisitions, to the sum of all lipid signals (Table 2.4), as discussed in detail in section below (Karampinos et al., 2018).

### Robustness of $^1\text{H}$ -MRS and WFI methodologies

When the main biases are taken into account, WFI sequences appear to be robust in quantifying PDFF against changes in experimental parameters, in good agreement with  $^1\text{H}$ -MRS ( $r=0.979$  reported by Li et al., 2017, and  $R^2=0.92$  by Ruschke et al., 2017), using calibration constructs (BM phantoms:  $R^2=0.97$ ; Gee et al., 2015), and in agreement with histology using excised lumbar vertebrae ( $r=0.72$ ; MacEwan et al., 2014). The intraclass correlation coefficients for repeatability and reproducibility of WFI were respectively 0.997 and 0.984 (Zhang et al., 2018), and the coefficient of variation in the quantification of PDFF varied from 0.69% to 1.70% (Aoki et al., 2016). Moreover, a negative correlation ( $r=-0.77$ ; Karampinos et al., 2015) was demonstrated between  $^1\text{H}$ -MRS-based PDFF and *ex vivo* biomechanical vertebral properties (failure load), highlighting the relevancy of this parameter in bone strength (Karampinos et al., 2015). The reproducibility of  $^1\text{H}$ -MRS is known to be excellent, especially when assessing the lumbar spine *in vivo*, with an average coefficient of variation of vertebral bone marrow content of 1.7% (Li et al., 2011; Karampinos et al., 2018). Although  $^1\text{H}$ -MRS has long been considered the gold standard (Li et al., 2011), WFI seems therefore to be a relevant and efficient alternative due to its ability to derive spatially resolved PDFF maps, with an absolute precision error of 1.7% between C3 and L5 vertebrae (Baum et al., 2015), and no significant differences with spectroscopic assessment in children (Ruschke et al., 2017) or in adults (Li et al., 2017).

With regard to BMAT composition, although similar values have been reported between measurements from high-resolution proton spectroscopy acquisitions on *ex vivo* specimen and *in vivo* imaging ( $R=0.61$ ; Li et al., 2017), the true BMAT unsaturation level is consistently underestimated in *in vivo* acquisitions because of the fewer visible peaks. As a result, Li et al. preferred the use of *pseudo*-unsaturation level to better discriminate the apparent BMAT composition assessment in *in vivo* studies from *ex vivo* measurements. This differentiation in terminology reflects well the need to bear in mind the technical limitations encountered when evaluating fat composition *in vivo*.

**Table 2.4** Main quantitative parameters assessed when using *in vivo* imaging techniques to explore bone marrow adipose tissue.

|                             | PARAMETER                          | DEFINITION  | PROPERTIES   | MAIN IMAGING TECHNIQUES   |                               | OUTCOME |
|-----------------------------|------------------------------------|---|--|---|-------------------------------|---------|
| MRI- or CT-based techniques | Bone marrow fat fraction (BMFF)    | Estimate of relative bone marrow fat content  | <ul style="list-style-type: none"><li>• Generic term</li><li>• Sensitive to experimental parameters when measured with MRI</li></ul>             | <ul style="list-style-type: none"><li>• Single-voxel proton spectroscopy</li><li>• Water-fat imaging</li><li>• Dual-energy CT</li></ul> | Marrow fat content            |         |
|                             | Signal fat fraction (SFF)          | Ratio of fat signal to the sum of the fat and water signals   | <ul style="list-style-type: none"><li>• Generic term</li><li>• Specific to MRI techniques</li><li>• Can be sensitive to MRI parameters</li></ul> | <ul style="list-style-type: none"><li>• Single-voxel proton spectroscopy</li><li>• Water-fat imaging</li></ul>                          |                               |         |
| MRI-based techniques        | Proton-density fat fraction (PDFF) | Ratio of <i>unconfounded</i> fat signal to the sum of the <i>unconfounded</i> fat and water signals | <ul style="list-style-type: none"><li>• Unconfounded imaging biomarker</li><li>• Insensitive to MRI parameters</li></ul>                         | <ul style="list-style-type: none"><li>• Single-voxel proton spectroscopy</li><li>• Water-fat imaging</li></ul>                          | Marrow fatty acid composition |         |
|                             | Degree of lipid unsaturation       | Ratio of signal coming from unsaturated lipids to the sum of all lipid signals                      | <ul style="list-style-type: none"><li>• Olefinic protons (5.31 ppm) are often used as an estimate of unsaturated lipids</li></ul>                | <ul style="list-style-type: none"><li>• Single-voxel proton spectroscopy</li></ul>  |                               |         |

BMFF: bone marrow fat fraction; CT: computed tomography; MRI: magnetic resonance imaging; PDFF: proton density fat fraction; SFF: signal fat fraction.



## Chapter 2 – Methodologies of bone marrow adiposity research

### *Towards a better standardization of MRI techniques*

Because  $^1\text{H}$ -MRS and WFI can be performed in most clinical facilities, their main technical limitations must be taken into account when assessing *in vivo* BMAT. A better standardization of the methodologies used to quantitatively assess BMAT would increase the accuracy of the reported PDFF in the literature, as well as the relevancy of inter-study comparisons.

#### Single-voxel proton spectroscopy

Based on the frequency shift which exists between molecular groups, signals from water and lipid protons can be discriminated in a defined voxel of interest through  $^1\text{H}$ -MRS. However, although the area under each peak of the acquired spectrum is related to the number of protons of a specific chemical moiety, the MRS acquisition and post-processing analysis to calculate PDFF needs to consider the following confounding effects:

First, the water and fat components of BMAT have different  $T_2$  relaxation times. Therefore, in the absence of any  $T_2$ -correction, the calculated signal fat fraction from  $^1\text{H}$ -MRS acquisitions is  $T_2$ -weighted, depends on sequence parameters and overestimates the true PDFF. An  $^1\text{H}$ -MRS acquisition at different echo times combined with a  $T_2$  correction can removed  $T_2$ -weighting effects (Karampinos et al., 2014; Dieckmeyer et al., 2015).

Second, even though initial  $^1\text{H}$ -MRS studies mainly considered the methylene group peak at 1.3 ppm to calculate bone marrow fat fraction or lipid/water ratio, adipose tissue has a complex spectrum made of multiple peaks. An oversimplification of the model used may reduce the accuracy of the qualitative and quantitative fat assessment. However, the trabecular microarchitecture promotes broad spectral peaks which make peak fitting challenging (Karampinos et al., 2018). Nevertheless, constrained peak fitting methodologies have been depicted and performed successfully at the hip and lumbar spine (Karampinos et al., 2014; Dieckmeyer et al., 2015).

Third, the short  $T_1$  value of bone marrow fat compared to water induces a relative amplification of the measured signal. PDFF calculations might be subsequently biased if  $T_1$  effects are not minimized. This effect can be minimized by using long repetition times for  $^1\text{H}$ -MRS acquisitions (Liu et al., 2007; Reeder et al., 2011; Hu et al., 2012; Karampinos et al., 2018).

Finally, the choice of the sequence mode is also of importance and depends on the employed echo times. By lowering J-coupling effects and being able to acquire spectra using shorter echo times, stimulated echo acquisition mode (STEAM) might offer a more accurate precise BMAT quantification compared to point-resolved spectroscopy (PRESS) sequences, despite its relatively noisier sensitivity (Karampinos et al., 2018).

The consideration of the above confounding effects is critical for assuring the robustness of MRS-based PDFF measurements across imaging protocols and imaging platforms, and essential towards the standardization of MRS-based PDFF measurements.



### Water-fat imaging

#### *Dedicated WFI techniques for BMAT assessment*

WFI techniques share comparable confounding factors with  $^1\text{H}$ -MRS: there is a need for  $T_2^*$  decay correction and  $T_1$  bias minimization, as well as a consideration of the multi-peak spectral characteristics of fat.

Indeed, due to the complex bone microarchitecture, the multiple interfaces between trabeculae and bone marrow induce an important but differential  $T_2^*$ -shortening effect affecting both water and fat.  $T_2^*$  decay effects have therefore to be considered in the estimation of PDFF based on WFI. Despite its theoretical justification, a dual- $T_2^*$  decay correction adjusting both water and fat relaxation times provides accurate bone marrow fat fractions at a nominal fat fraction close to 50% but noisy PDFF maps were reported in the spine in regions with lower values (Karampinos et al., 2015). Therefore, a single  $T_2^*$  decay model should be at least adopted in BMAT WFI (Karampinos et al., 2018).

Regarding the  $T_1$ -effect, the relative signal amplification can be easily lessened by using low flip angles or predetermined calibration values on WFI acquisitions (Liu et al., 2007; Reeder et al., 2011; Hu et al., 2012; Karampinos et al., 2018).

Finally, concerning the multi-peak spectral characteristics of fat, one direct consequence in WFI that illustrates an oversimplification of the model used is the “grayish” appearance of adipose tissues on water-only images generated from WFI reconstructions considering a single fat peak. This residual fatty signal may come from an incomplete discrimination of fat and water signals, especially between olefinic fat protons and water (Yu et al., 2008). Although this simplification is acceptable for most clinical applications, a more advanced modeling of the fat spectrum is necessary for a quantitative purpose.

#### *Commercially available WFI solutions*

As mentioned above, the methodological improvements of fat quantification using MRI emerged mainly from abdominal imaging. Most MRI vendors have played an active role in the development of these sequences. Although these commercial quantitative WFI solutions aim to quantify liver PDFF, these techniques may be an easier and interesting alternative to  $^1\text{H}$ -MRS in quantifying BMAT. An approximation with the multi-peak liver fat spectrum can indeed be considered, as only a negligible difference between the total signal fat from the 3 main peaks was reported when comparing the proximal femoral bone marrow and the liver (87% versus 90% respectively) (Karampinos et al., 2014; Le Ster et al., 2016; Karampinos et al., 2018). In addition, these sequences implement de facto a  $T_2^*$  decay correction, and because the  $T_1$ -effect can be simply lowered through a low flip angle, these solutions might be performed for BMAT PDFF assessment.

#### *Other technical considerations*

Other confounding factors may also be taken into account, such as noise-related bias (especially when using complex-based methods), eddy currents effects, gradient timing mis-registrations, phase errors in WFI and correction of J-coupling effects and chemical shift displacement effects in  $^1\text{H}$ -MRS (Hu et al., 2012; Karampinos et al., 2014; Ruschke et al., 2017). Their description goes beyond the purpose of this review, but they are fundamental for the development of future techniques.

## Chapter 2 – Methodologies of bone marrow adiposity research

### *Current challenges when imaging in vivo BMAT*

A more accurate description of BMAT fatty acid composition

Reporting of BMAT fatty acid composition through an expression of its degree of unsaturation constitutes the second most common quantitative parameter provided in the literature after PDFF-based quantification of total BMAT. Currently, only <sup>1</sup>H-MRS can reliably assess BMAT composition.

However, contrary to PDFF assessment, there is not sufficient literature on the methodological considerations that should be followed in imaging studies. The importance of STEAM acquisitions over PRESS when assessing BMAT composition has been nevertheless highlighted, as a low reproducibility of unsaturation level measurements has been reported using the latter, with a reported coefficient of variation of 10.7% (Li et al., 2011).

Moreover, the proximity and partial overlap of the olefinic peak with the water peak (present at 4.7 ppm) reduce the robustness of the peak fitting process. As a result, in addition to the previously described technical considerations, postprocessing the spectra for this specific purpose is challenging, especially in young adults. Areas with low fat content, more frequently encountered in red bone marrow, limits the accuracy and precision of the reported measurements (Karampinos et al., 2018). The extraction of BMAT unsaturation levels is subsequently less prone to variations in yellow bone marrow or red marrow with elevated fat content.

Consequently, there is an urge to standardize and improve the reliability of this potential biomarker, as the degree of unsaturation of BMAT might have clinical implications, such as its potential role in the occurrence of fragility fractures (Yeung et al., 2005; Patsch et al., 2013).

A better depiction of physiological values

To date, studies performed in healthy subjects have allowed for the description of physiological variations, especially in the spine. In children, WFI showed a decrease in PDFF measurements from the lumbar to the cervical spine, with a natural logarithmic increase with age but without sex difference (Ruschke et al., 2017). However, in adults, sex-related variations in addition to age-dependence of PDFF have been reported in the spine (Baum et al., 2015; Dieckmeyer et al., 2015). Regarding BMAT composition, differences in the degree of saturation have also been observed between adult males and females, with unsaturated lipids being higher in women (Maciel et al., 2017).

Nonetheless, even though these physiological variations are critical for a better understanding of BMAT physiology, data is still insufficient in the literature to determine the exact normal values by age and gender, primarily due to the lack of standardization in methods used to assess BMAT.

### *Alternatives to <sup>1</sup>H-MRS and WFI*

Diffusion weighted-imaging, relaxometry, texture analysis, direct signal intensity and dynamic contrast-enhanced imaging are alternative tools that have been performed to assess bone marrow adiposity. Although they provide interesting information, such as functional parameters related to bone marrow vascularization (Budzik et al., 2014), these MRI techniques have not yet reached a consensus due to the insufficient number of relevant publications.

On the contrary, dual-energy computed tomography (DECT) is an emergent technique which may become a powerful alternative to MRI techniques as it can provide quantitative parameters representing

both mineral and organic bone components (Goodsitt and Rosenthal, 1987). Consequently, whereas conventional single-energy quantitative computed tomography methods underestimate volumetric BMD measurements, DECT can correct for BMAT, resulting in more accurate densitometric measurements (Laval-Jeantet et al., 1986; Arentsen et al., 2017) (Rosenthal et al., 1989). Furthermore, BMAT content can be explored reliably, as good correlations have been reported with WFI and histology on cadavers (Arentsen et al., 2015; Magome et al., 2016), and  $^1\text{H}$ -MRS *in vivo* (Bredella et al., 2015). Potential interesting applications exist in oncology, to follow marrow fat expansion and BMD involution in patients after chemotherapy or radiotherapy (Hui et al., 2015). The main limitations of this modality are the radiation exposure, the need for prior phantom calibration, and the lack of standardization and data regarding reproducibility between different scanners and manufacturers.

In summary, MRI constitutes the current gold standard for *in vivo* imaging of BMAT in a clinical research setting, with current acquisition methods allowing for inter-center comparability. The field would however benefit from increased standardization, both in terms of reporting of confounding factors of the measured subjects as recommended in Table 2.1 and in terms of definition of standard sites of measurements, in order to increase comparability and to establish physiological reference ranges in humans and possibly larger mammals. The use of MRI for mouse models is only starting, due to the need for very strong magnetic fields for meaningful BMA signal detection; dual-energy  $\mu\text{CT}$  is a valid alternative for murine *in vivo* imaging.

## From Cell Isolation to In Vitro Modulation

Bone marrow adipocytes exist in a complex microenvironment within the bone, embedded within the marrow tissue where access to live cells for functional analysis is not trivial. Complementary to the above discussed challenges associated to BMAd imaging within their native environment, *in vitro* systems and *ex vivo* assays are crucial for understanding of the BMAd and its subtypes at the cellular level. The difficulty in isolating and handling primary mature adipocytes from the BM has led to the use of *in vitro* adipogenic differentiation assays from BM stromal cells as a surrogate method to study BMAd, an approach widely used in the field of peripheral adipocyte biology. This approach relies on the isolation of a stromal vascular fraction (SVF) from adipose tissue which is then plated and expanded in tissue culture plastic. The resulting adherent monolayer of stromal cells isolated from the BM, the so-called bone marrow stromal cell (BMSC) fraction, acquires the phenotype of multilocular and sometimes fully mature unilocular adipocytes in the presence of specific differentiation cocktails in standard 2D cultures. Mature BMAds, which *in vivo* develop only after birth (Bianco and Robey, 2015), most likely originate from a specific subset of progenitor cells present within the BMSC fraction. This biological sequence thus supports, in part, the use of differentiated BMSCs to model BM adipogenesis. *In vitro* differentiation assays, however, reveal a cellular response to chemical stimuli resulting in a sum of specific phenotypes which describe *in vitro* plasticity, but do not necessarily reflect their native *in vivo* differentiation potential. The *in vitro* plasticity of BMSCs is in fact often larger than the plasticity revealed by *in vivo* readouts in native or injury-repair conditions, highlighting the importance of complementary *in vitro* assays and *in vivo* readouts to establish cell fate mapping within the BM, as described below and extensively reviewed elsewhere (Bianco and Gehron Robey, 2000; Kassem and Bianco, 2015). The sections below summarize key challenges and practical considerations to minimize variability and increase comparability in future BMAT cell-based studies, whether based on the isolation of primary BMAds or *in vitro* adipogenesis from BMSCs.

## Chapter 2 – Methodologies of bone marrow adiposity research

### *BMAT: Location and Isolation*

The BM is a soft tissue within the medullary cavity of compact bone. A mixture of hematopoietic precursors and differentiated cells, adipocytic cells, stromal cells, blood vessels, and nerve fibers occupy the marrow space within a complex network of extracellular matrix. Several techniques to isolate BMAT have been developed, all of which require invasive procedures to extract different populations from the encompassing bone.

In juvenile (age 8-12-week-old) mice, yellow/adipocytic marrow is present essentially in the distal tibia (filling up about one third of the total shaft length), the tail vertebrae and phalanx. Of the mouse strains systematically compared, BMAT is maximal in these locations in C3H/HeJ mice, and minimal in C57BL/6J mice (Scheller et al., 2015). Older mice show a progressive increase in BMAT from distal to proximal, gradually gaining mature adipocytes in most skeletal sites of red/hematopoietic marrow. BMAT development and progression varies with strain and gender (Hardouin et al., 2016). Sites of murine BMAT for isolation in steady-state are thus small, and obtaining sufficient number of cells for cell sorting or cell culture purposes requires in most cases pooling samples from several animals.

It is important to note, as discussed in the *in vivo* modulation and *in vivo* tracing sections, that there may be differences in developmental origin according to the site of BMAT isolation. Due to the high degree of yellow/adipocytic marrow in the distal tibia, which also contains less trabecular bone than the caudal vertebrae, isolation of intact BMAT is relatively straightforward from the tibia after section at the epiphyses followed by gentle flushing or centrifugation. Contrarily, enzymatic digestion or mechanical disruption provides a higher yield of primary adipocytes from the tail due to the high number of caudal vertebrae and the predictable yellow/adipocytic marrow transition in the murine tail from the non-weight bearing segments (O.N., J.T., B.P., E.S., personal communication). It is particularly important to note, however, that the fibrous tissue surrounding tail vertebrae is very rich in subcutaneous and periosteal adipocytes which require extensive mechanical removal or enzymatic digestion prior to isolation of BMAds to avoid contamination from subcutaneous adipocytes. One should also be aware that crushing bones can result in high cell death of BMAds and BMSCs, and it is thus to be avoided. Extraction of the intact BM plug or gentle mechanical disruption of the bone by fragmentation with a scalpel or scissors is thus preferred. Alternatively, a disrupted marrow plug can be obtained from smaller bones by removing the epiphysis and placing the open shaft in a qPCR tube with a pierced bottom inside an Eppendorf tube containing a small amount of media (e.g. 200µl), then gently centrifuging (e.g. 1 second at 500g). BMAd markers are present in the top buoyant layer, while hematopoietic markers are only present in the pellet fraction upon RNA transcription analysis (P.B., personal communication).

The long bones of mice are of similar size than human iliac crest biopsies, also called trephine biopsies, which involve the spongy bone and are performed for diagnostic purposes in hematology (1-2cm long and 0.2-0.4cm in diameter). Isolation and mounting approaches are thus often appropriate for both murine and human samples. Bone marrow aspirates are in most instances performed in parallel to trephine biopsies. In pediatric practice, BM aspirates are often performed from the sternum. Either are excellent sources of BMAT for research purposes after appropriate ethical approval. Debris from hip- or knee-replacement surgeries, including limb amputations, as well as spine neurosurgery also provide material rich in BMAds, as these are skeletal sites of abundant yellow/adipocytic marrow in the human adult.

Due to physiological BMAT specific variations according to species, strain, age, gender and skeletal site, as well as variations imposed by the isolation technique (flushing, spin-down, direct collagenase digestion, other enzymatic digestion), it is extremely important that researchers detail these parameters and indicate yield of primary BMAd or BMSC populations to favor comparisons across groups. Future efforts of the field should include evidence-based recommendations on extraction protocols that best preserve the heterogeneity of BMAd and their precursors. Other factors that may influence BMAT quality, and therefore yield, are related to body weight, bone weight or length and presence of metabolic perturbations or disease. BMAT obtained from human samples may be normalized to weight ( $\mu\text{g}$ ) of tissue. Weight-based normalization remains however challenging for the small murine samples, where normalization per bone or “per leg” (e.g. tibia and femur) is standard (Colvin et al., 2004).

### *Mature BMAds: Isolation and Culture*

Isolation of primary mature BMAds has been done to high purity by multiple gentle centrifugation steps (Poloni et al., 2013; Mattiucci et al., 2018a; Fan et al., 2017; Hozumi et al., 2010) and may include enzymatic digestion to aid dissociation of BMAds from their surrounding connective tissue. BMAds, just like visceral adipocytes, are fragile cells that are very sensitive to the strains of handling and temperature gradients. Samples must be manipulated gently and typically at 17-37°C to avoid lipid droplets from bursting. Generally, BMAd numbers obtained from murine bones are low due to the small volumes and their affinity to plastic and proneness to floatation or bursting, which encumbers handling. Cell counting of mature adipocytes by hemocytometer or flow cytometry is not representative of the sample at hand, and quality controls for purity and viability need to be devised through other methods including, for example, immunofluorescence for adipocyte yield and quantification of hematopoietic cell contamination (e.g. DAPI, phalloidin, LipidTox-DR and anti-CD45) or nuclei counting coupled to ceiling culture for quantification of yield of viable mature adipocytes. For claims on purified BMAds, especially those that refer to population based transcriptional analysis or proteomics/lipidomics, it is paramount that researchers specify the degree of hematopoietic and undifferentiated BMA cell contamination in both mouse and human BMAT. Single cell RNA sequencing techniques will facilitate BMAT studies, albeit at a high cost.

The possibility of fluorescence activated cell sorting (FACS)-based purification of mature adipocytes for downstream studies has been recently described for extramedullary adipocytes, based on forward/side scatter light signal and viability ensured by manual adjustments to the sorting pressure (Hagberg et al., 2018). It is to be demonstrated whether this approach may be compatible with primary BMAd isolation.

Regardless of the isolation approach, a large number of primary BMAds must be initially isolated for most downstream assays (see section on BMAd assessment *in vitro*). On successful isolation of mature BMAds, their culture is delicate and short-lived. Ceiling culture in 2D allows for maintenance of BMAds for about one week (Figure 2.4e), after which de-lipidation is often observed. To avoid de-lipidation, irradiation of the cells has proven to be technically beneficial prior to culture (Mattiucci et al., 2018a). The recent description of protective 3D BMAd cultures in engineered devices or silk scaffolds holds great promise to recapitulate important clues for their behavior *in vivo* (Torisawa et al., 2014; Bourguine et al., 2018; Fairfield et al., 2019), but raises new challenges to develop efficient cell extraction protocols for endpoint analysis and 3D imaging techniques compatible with these set-ups.

## Chapter 2 – Methodologies of bone marrow adiposity research

### BMA<sub>d</sub> Progenitors: Isolation, Culture, and Modulation In Vitro

Mature BMA<sub>d</sub>s coexist hand-in-hand with their immature progenitors, which constitute a subset of the total BMSC fraction. The BMSC fraction has been defined by either (i) exclusion of endothelial and hematopoietic markers (typically CD31 to exclude endothelial components, CD45 to exclude hematopoietic components, and either murine Ter119 or human Glycophorine A to exclude nucleated erythroid lineage cells which lost CD45 expression, as discussed in (Boulais et al., 2018), or (ii) by adherence and expansion in tissue culture plastic. Specific subpopulations with functionally validated *in vivo* stem cell or progenitor function, the so-called skeletal stem cells (SSCs) and their downstream committed or partially committed stromal, bone and cartilage progenitors have been recently described in mouse and human BM (Worthley et al., 2015; Chan et al., 2018). They present *in vitro* adipogenic potential and different degrees of *in vivo* adipogenesis, with human CD146 constituting the best functionally characterized marker for prospective isolation of SSCs (Tormin et al., 2011; Serafini et al., 2014). Other skeletal multi-potent populations have been identified within the BM, including P $\alpha$ S (CD45<sup>-</sup> Ter119<sup>-</sup> PDGFR $\alpha$ <sup>+</sup> Sca1<sup>+</sup>) (Houlihan et al., 2012; Li et al., 2014b), although care must be taken when defining clonal multi-potency (Serafini et al., 2014; Bianco and Robey, 2015). Specific markers to prospectively isolate intermediate steps within the stromal to adipocyte commitment axis have also recently been identified in mice by Ambrosi et al. Namely, a tri-potent bone/cartilage/adipocytic perivascular CD45<sup>-</sup> CD31<sup>-</sup> Sca1<sup>+</sup> CD24<sup>+</sup> stem-cell like population, a CD45<sup>-</sup> CD31<sup>-</sup> Sca1<sup>+</sup> CD24<sup>-</sup> adipocytic progenitor population and a more mature CD45<sup>-</sup> CD31<sup>-</sup> Sca1<sup>-</sup> Zfp423<sup>+</sup> BMA<sub>d</sub> precursor population were identified in the context of aging, high-fat diet (HFD) induced obesity and bone regeneration (Ambrosi et al., 2017). No equivalent adipocytic differentiation hierarchy has yet been described in the human BM.

Due to the difficulty in isolating and expanding highly purified BMA<sub>d</sub> progenitors in mice, and to the lack of specific prospective BMA<sub>d</sub> progenitor markers in human BM, most studies to date have used unfractionated murine BMSCs, or *in vitro* expanded human BMSCs complying with International Society for Cellular Therapy (ISCT) standards (Dominici et al., 2006) to produce *in vitro* differentiated BMA<sub>d</sub>s for functional studies. ISCT standards provide a minimal set of surface markers and functional assays to validate human BMSC homogeneity. Standardized downstream functional assays have been proposed by the FDA (Robey et al., 2015; Tanavde et al., 2015; Arcidiacono et al., 2018). BMSC cultures rely on the rapid adherence of the cells to the culture dish, which allows exclusion of most hematopoietic cells from the culture. Nonetheless, passaging and sometimes sorting are necessary to eliminate macrophage contamination. As for primary isolated BMA<sub>d</sub>s and to maximize comparability across studies, it is paramount to detail the source of BMSCs (gender, age, strain if applicable, metabolic diseases, skeletal location) and the method of isolation, such as specific enzymatic (e.g. collagenase-1, -2, -4, a combination thereof, trypsin) or mechanical dissociation as well as the specific expansion protocol, whose heterogeneity may explain some disparities in the field (summarized in Table 2.5, BMAS reporting guidelines as summarized in Table 2.1), (Nagasawa et al., 2011). It is equally important to include quantification of contamination with hematopoietic or endothelial cells, and, specifically for BMSC populations, and to quantify the overall progenitor function of the primary isolate through fibroblastic colony forming unit assays (CFU-F) prior to adipocytic differentiation.

**Table 2.5** Variations in mouse BMSC isolation protocols.

| SAMPLES   | ISOLATION MEDIUM   | RBC LYSIS               | ENZYMATIC DIGESTION   | DEPLETION / ENRICHMENT            | APPLICATION    | REFERENCE                                    |
|---|--|-------------------------|---|-----------------------------------|----------------|--|
| Flushed BM  | DMEM/F12, 20% FCS, P/S, 2mM L-glutamine, 0.1mM AA, 3mM sodium pyruvate | -                       | -   | -                                 | Cell culture   | Sreejit et al., 2012                         |
|   | PBS, 2%FCS, 2mM EDTA   | -                       | 3mg/ml collagenase (col.) I + 4mg/ml Dispase (15 min 37°C)                      | -                                 | Cell culture   | Suire et al., 2012                           |
|   | Leibovitz's L-15 medium, 1mg/ml BSA, 10mM HEPES, 1% P/S                | 0.8% NH <sub>4</sub> Cl | 0.005% trypsin + 0.002% EDTA + 0.25mg/ml col. IV (4min 37°C)                    | anti-CD45, Nestin-GFP+ FACS       | Flow cytometry | Mendez-Ferrer et al., 2010                   |
|   | HBSS, 2%FBS  | -                       | DNase I + col. IV <i>or</i> + liberase <sup>DL</sup> (15 <i>or</i> 20 min 37°C) | -                                 | Flow cytometry | Ding et al., 2012 ; Zhou et al., 2017        |
|   | DMEM, 15% FBS, 2mM L-Glutamine, 1% P/S, 3.7g/l NaHCO <sub>3</sub>      | -                       | -   | -                                 | Cell culture   | Soleimani et al., 2009                       |
|   | $\alpha$ -MEM, 10% FBS, 1% P/S   | -                       | -   | -                                 | Cell culture   | Sui et al., 2016                             |
|   | $\alpha$ -MEM, 15% FBS, 1% P/S, 2.2/l NaHCO <sub>3</sub>               | -                       | -   | -                                 | Cell culture   | Huang et al., 2015                           |
|   | $\alpha$ -MEM  | -                       | -   | -                                 | Cell culture   | Robey et al., 2014; Ko et al., 2016          |
|   | RPMI-1640, 10% FBS, 1% P/S   | -                       | -   | -                                 | Cell culture   | Abdallah et al., 2018                        |
|   | -  | -                       | Trypsin (2 min 37°C)  | -                                 | Cell culture   | Yu et al., 2018                              |
| Centrifuged BM  | Long term medium   | -                       | -   | -                                 | Cell culture   | Calvi et al., 2003                           |
|   | RPMI-1640, 20% FBS, 2mM glutamine, 1% P/S                              | -                       | -   | -                                 | Cell culture   | Caroti et al., 2017                          |
|   | N/A  | RBC lysis buffer        | -   | -                                 | BMAd isolation | Fan et al., 2017                             |
| Crushed long bones<br>Flushed & cut long bones<br>Cut & washed long bones<br>Cut long bones | N/A  | -                       | -   | -                                 | Cell culture   | Fairfield et al., 2019, Peister et al., 2004 |
|   | PBS  | -                       | col. (20 min 37°C)  | -                                 | Flow cytometry | Kusumbe et al., 2016                         |
|   | $\alpha$ -MEM, 10% FBS   | -                       | 1mg/ml col. II (1-2 h 37°C)   | -                                 | Cell culture   | Zhu et al., 2010                             |
|   | DMEM   | H <sub>2</sub> O 6 sec  | 0.2% col. (1 h 37°C)  | -                                 | Flow cytometry | Houlihan et al., 2012                        |
|   | N/A  | -                       | 5% col.   | Anti-CD45, anti-Ter119, anti-CD31 | Cell Culture   | Tencerova et al., 2018                       |
|   | PBS, 20% FBS   | ACK                     | 0.5% col. II (1 h 37°C)   | -                                 | Flow cytometry | Ambrosi et al., 2017                         |

BSA: bovine serum albumin; Col.: Collagenase; DMEM: dulbecco's modified eagle medium; FBS: fetal bovine serum; RBC: red blood cell; RPMI: L-Glutamine, Phenol Red, Reduced Serum; P/S: penicillin/streptomycin.

**Table 2.6** | Variability of *in vitro* murine BMSC adipogenic differentiation protocols.

| REFERENCES:                                | Sreejit et al., 2012 | Yu et al., 2018  | Abdalian et al., 2018 | Zhu et al., 2010 | Fan et al., 2017 / Fairfield et al., 2019 | Ambrosi et al., 2017                                 |
|--|----------------------|------------------|-----------------------|------------------|---|--|
| <b>MAINTENANCE</b>                         |                      |                  |                       |                  |   |  |
| medium                                     | DMEM:F12             | $\alpha$ -MEM    | RPMI                  | $\alpha$ -MEM    | $\alpha$ -MEM or DMEM                     | 60% DMEM low Glc: 40%MCDB                            |
| serum                                      | 20% FBS              | 10% FBS          | 10% FBS               | 10% FBS          | 20% or 10% FBS                            | 2% FBS   |
| other                                      | 0.1mM NEAA           | 200 $\mu$ M NEAA |                       |                  |   | ITS, linoleic acid, dexam, AA, EGF, LIF, PDGFB, bFGF |
| <b>ADIPOGENIC</b>                          |                      |                  |                       |                  |   |  |
| medium                                     | DMEM:F12             | $\alpha$ -MEM    | DMEM                  | $\alpha$ -MEM    | $\alpha$ -MEM or DMEM                     | 60% DMEM low Glc: 40%MCDB                            |
| serum                                      | 20% FBS              | 10% FBS          | 9% horse serum        | 10% FBS          | 20% or 10% FBS                            | 2% FBS   |
| other                                      |                      | 200 $\mu$ M NEAA |                       |                  |   |  |
| IBMX ( $\mu$ M)                            | 500                  | 500              | 450                   | 0.5              | 500                                       | 0.5  |
| Dexamethasone or Hydrocortisone ( $\mu$ M) | 1                    | 0.5              | 0.25                  | 1                | 1   | 1  |
| Indomethacine ( $\mu$ M)                   | 100                  | 60               |                       |                  |   | 50   |
| Insulin ( $\mu$ g/ml)                      | 5                    |                  | 5                     | 0.01             | 10  | 5  |
| Rosiglitazone ( $\mu$ M)                   |                      |                  | 1                     |                  | 1   | 1  |
| T3 (nM)                                    |                      |                  |                       |                  |   | 1  |
| Differentiation time                       | 2 weeks              | 3 weeks          | 12 days               | 2 weeks          | 2-4 days                                  | 48h  |

NEAA: Non-essential amino acids, dexam : dexamethasone, ITS: insulin-transferrin-selenium mix, AA: L-ascorbic acid 2-phosphate, EGF: epidermal growth factor, LIF: leukemia inhibitory factor, PDGFB: platelet-derived growth factor BB, bFGF: basic fibroblast growth factor.



Induction of adipogenesis from BMSCs *in vitro* has included a variety of inducers in standard 2D culture conditions, as summarized for primary murine samples in Table 2.6. Most differentiation techniques are based on methods developed for murine extramedullary pre/adipocytes (e.g. 3T3L1) or BMSCs primed for adipogenic differentiation (such as C3H10T1/2 or OP9). The common denominator includes a combination of the corticosteroid dexamethasone, which ultimately induces master transcriptional regulator of adipogenesis C/EBP- $\alpha$ , and phosphodiesterase inhibitor isobutylmethylxanthine (IBMX), which leads to cAMP accumulation, protein kinase A activation and thus PPAR- $\gamma$  expression. The cocktail is classically accompanied by insulin exposure, whether from the serum or exogenously administered. Thus, the acronym “DMI” cocktail for Dexamethasone, IBMX and insulin (Scott et al., 2011). In addition, adipogenesis can be further boosted through the use of COX inhibitor indomethacin or PPAR- $\gamma$  agonist rosiglitazone. Of note, the mechanical properties of the substrate are also determinant for BMSC differentiation, and even dominant to exogenous biochemical signaling (Gobaa et al., 2015), with softer matrixes favoring adipogenesis. The role of extracellular matrix components in this context, and its rate of degradation, has been however largely understudied in this context.

### BMA<sub>d</sub> Differentiation Assessment: *In vitro* Assays and Applications

Multiple different cell types have the ability to accumulate lipid droplets, and thus we must evaluate the criteria with which we distinguish BMAd<sub>s</sub> from other cells of the BM. In the context of extramedullary stromal differentiation, some groups have adopted the criteria of presence of at least four lipid droplets to define an adipocyte (Gubelmann et al., 2014). This is especially useful as a threshold in imaging techniques where lipid droplets are visible (Figure 2.4a, 2.4c, 2.4e). As such, each investigator should critically evaluate what threshold is used as a definition.

Adipocytic differentiation is not completely efficient from primary BMSCs obtained on isolation, and the heterogeneity in cultures is well known (Whitfield et al., 2013). This may be due to undetected heterogeneity of the initial BMSC population and adipocyte progenitors therein, to paracrine signaling cues in the culture, or, possibly, to presence of stromal cells that actively inhibit adipogenesis as recently described for CD142<sup>+</sup> SVF cells in murine extramedullary adipogenesis (Schwalie et al., 2018). Moreover, as discussed above, *in vitro* differentiation potential may not faithfully reflect *in vivo* potential. Stringent *in vivo* assays in the form of heterotopic marrow formation by *in vivo* transplant in permissive conditions should thus be the norm to reveal the true lineage potential (Friedenstein et al., 1968; Sacchetti et al., 2007; Serafini et al., 2014). Researchers must therefore rely on genetically modified mouse models with differential donor/recipient marker expression, or, in the case of human samples, in xenotransplants into immune-deficient mice with species-specific surface marker, Alu sequence or mitochondrial DNA detection to determine donor versus host BMAd<sub>s</sub>.

Upon isolation and culture or differentiation *in vitro*, assessment of BMAd maturation relies on the definition of the BMSC-to-BMAd axis and on established or forthcoming readouts. Classical biochemical techniques (including western blot, real-time qPCR, flow cytometry, RNA sequencing, lipidomics) require relatively large cell numbers, thereby limiting assay performance for BMAd<sub>s</sub>. Importantly, the cells on each extreme of the maturation spectrum vary greatly, as simply illustrated by the morphological changes when comparing the spindle-shaped BMSCs with large lipid-filled BMAd<sub>s</sub> (Figure 2.4). This must be accounted for in the selection of suitable references, such as reference genes for RT-qPCR that do not change upon adipocytic differentiation. Thus, cytoskeletal or metabolic genes must strictly be avoided as reference genes, while at least two early/mid- (PPAR $\gamma$ , CEBP $\alpha$ ) and two late- (ADIPOQ, GLUT4, FABP4, LPL, PLIN1) stage markers should be quantified as genes of interest to cover the

## Chapter 2 – Methodologies of bone marrow adiposity research

adipocytic maturation spectrum. The stability of reference genes needs to be demonstrated upon differentiation in every experimental setting, but others have identified good reference gene in the context of adipocytic differentiation from peripheral stromal cultures human and rodent studies (Krautgasser et al., 2019; Santos et al., 2016).

*In vitro* microscopy-based readouts classically detect lipid droplet formation with fluorescent dyes (e.g. Nile Red, ORO, BODIPY) (Figure 2.4f), or use of cells from fluorescently-tagged reporter mice (e.g. tdTomato, RFP, GFP as extensively reviewed here). Whether for microscopy or flow cytometric applications, careful interpretation of results is required, as most mature BMAdS will be lost on liquid handling, and care must be taken not to count lipid vacuoles from broken cells as BMAdS. More recently, label-free techniques such as digital holographic microscopy (Figure 2.4b) or Raman-based microspectroscopy have been developed for *in vitro* BMAd cultures with high resolution and potentially improved performance over classical techniques (Smus et al., 2015; Campos et al., 2018). By preventing staining and liquid-handling biases, these methods provide additional information on lipid content along with quantification of morphological parameters. Additionally, microspectroscopy holds the promise to reveal information on chemical composition at the single cell level, which may reveal physiologically relevant heterogeneity.

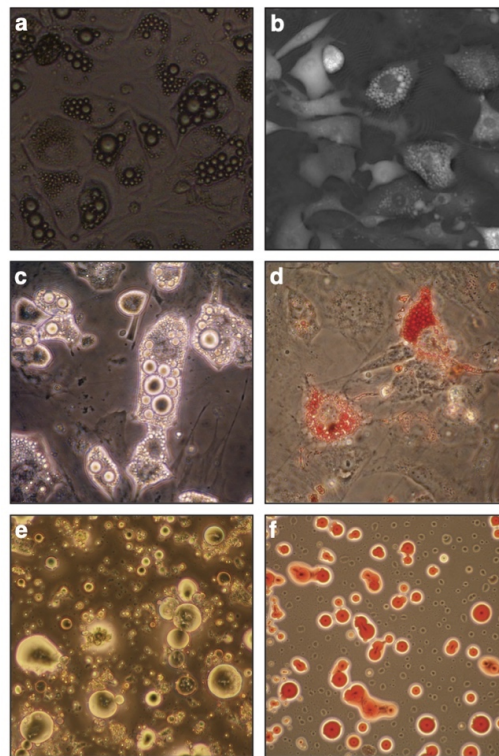


**Figure 2.4** | *In vitro* differentiation. **a** Bright field image (objective 10x) of OP9 cells differentiated in presence of serum, dexamethasone, insulin and IBMX (DMI cocktail) for 6 days and **b**, Digital Holographic Microscopy (DHM) image of OP9 cells differentiated in DMI for 7 days. **c-d** Primary murine BMSC after *in vitro* differentiation in similar conditions imaged by light-transmission microscopy, where lipid droplets show a high refractive index (**c**) or stained with neutral lipid oil-soluble colorant Oil Red O (**d**). **e-f** Primary murine BMAdS from 2-month-old FVB female mice as seen by light-transmission microscopy (**e**) or stained with Oil Red O (**f**). BMAd: bone marrow adipocyte; BMSC: bone marrow stromal cell. DHM: digital holographic microscopy

## Challenges in Cell-based Assays

Isolation of primary BMAd remains challenging in both mouse and human. *In vitro* BMSC or BMAd precursor differentiation provides a valid alternative for studying the role of BMAd in cell-based assays, although potential differences with *in vivo* differentiated BMAd should always be acknowledged. This presents a challenge for normalization with age-matched control groups where the BMAd do not undergo similar changes. For appropriate normalization, it is thus important to account for both cell number and tissue weight, with pooling of control group mice to reach similar levels of BMAd isolation from the experimental and control groups for appropriate comparisons. For both primary BMAd and BMSCs, the cell mixtures obtained are highly dependent on the source and handling, and thus gender, age, skeletal location, metabolic perturbations, as well extraction and culture methods should be thoroughly described as detailed in the recommended BMAS reporting guidelines (Table 2.1). With the application of *in vivo* BMA induction protocols (reviewed in Tables 2.7 and 2.8), BMAd are modulated in cell size, number, and phenotypic/functional properties. Additionally, measures of BMAd purity and BMSC CFU-F progenitor function should be reported to increase comparability of results across different researchers. It is imperative that as the BMA field matures, so must the publication of consensus protocols as well as definitions for both BMAd and BMSC isolation and differentiation.

*In vivo* BMAT modulation

## In vivo lineage Tracing

It is now well accepted that BMAd differentiate from a small number of radioresistant mesenchymal progenitor cells that reside in the bone marrow. The ability to identify these early progenitor cells, more mature precursor cells, mature marrow adipocytes, and other mesenchymal lineage derived cells (e.g. osteoblasts), has been accomplished by the advent of modern lineage tracing using relatively specific Cre-drivers and fluorescent reporters (Kalajzic et al., 2008; Mizoguchi et al., 2014; Zhou et al., 2014; Worthley et al., 2015; Ambrosi et al., 2017; Horowitz et al., 2017; Yu et al., 2018). This approach has the added benefit of being able to compare marrow adipocytes to white, brown, and beige adipocytes, and adipocytes in different anatomical locations *in vivo*.

Today's lineage tracing consistently depends on the Cre/Lox system (Kretzschmar and Watt, 2012). In the standard Cre/Lox system, Cre recombinase is expressed under the control of a tissue-specific promoter to permanently activate a reporter gene that functions to mark the original Cre-expressing cell population and all daughter cells that develop. Therefore, it is paramount that one has a detailed understanding of the Cre driver's spatiotemporal expression. Lack of this understanding can result in false interpretations of the origin of the cells. As an example, *Pdgfra-cre* traces all the adipocytes in white adipose tissue, but within the bone marrow, it traces about 50% of the adipocytes (Horowitz et al., 2017). By contrast, *Prx1-cre* traces all marrow adipocytes (Horowitz et al., 2017). It also traces posterior subcutaneous white adipose tissue, including beige adipocyte precursors, as the mesenchymal origin of this depot gets recombined during limb development. In contrast, *Prx1* does not trace the majority of brown adipocytes or any visceral adipocytes (Sanchez-Gurmaches et al., 2015). Thus, it is useful because of its relative specificity, especially compared to *Adiponectin-cre*, which traces all adipocytes including marrow adipocytes (Figure 2.5a), and a range of BMSC precursors (Mukohira et al., 2019b). Another advantage to this system are inducible Cres. As an example, *Prx1-ER-cre*, where Cre expression is activated in Prx1 positive cells by tamoxifen injection. These types of constructs allow for the timed induction of the reporter. A caveat to be considered when using tamoxifen and ER-inducible cre-drivers, however, is that the dose of tamoxifen required to efficiently activate Cre expression can be 100-1,000 times greater

## Chapter 2 – Methodologies of bone marrow adiposity research

than required to activate estrogen receptors. A single dose of tamoxifen is reported to have irreversible effects on the uterus. Furthermore, tamoxifen crosses the blood brain barrier to regulate energy metabolism, is a potent immune modulator in mice, and can induce bone marrow failure (Hammad et al., 2018; Perry et al., 2005; Ye et al., 2015). Investigators who choose to use tamoxifen in spite of its potent estrogen receptor-mediated actions, should be advised to include a no treatment control as well as a tamoxifen-treated/no Cre control. Equally important is the nature of the reporter gene used. For example, adipocytes possess little cytoplasm relative to other cell types, therefore cytoplasmic reporters such as LacZ are not optimal for tracing adipocytes. Instead, membrane-targeted reporters such as mT/mG (membrane Tomato/membrane GFP) provide superior results (Soriano, 1999; Muzumdar et al., 2007). For extensive discussions on this topic see Jeffery et al. (Jeffery et al., 2014) and Sanchez-Gurmaches et al. (Sanchez-Gurmaches et al., 2016).

Once the Cre-reporter has been selected, which will be dictated by the demands of the experiment, either an *ex-vivo* or *in situ* approach can be taken.

The *ex-vivo* approach involves dissecting out the femur, cutting off the femoral head and removing the distal epiphysis above the growth plate. A 20-gauge needle can then be inserted down the medullary canal (from proximal to distal), and punching out the needle through the distal growth plate. Because the distal growth plate is intact this causes the bone marrow to fill the needle. The needle is then attached to a syringe and the marrow plug can then be deposited on a microscope slide by depressing the barrel of the syringe. The adipocytes in the marrow plug can then be prepared for imaging by confocal microscopy. Femora are preferred for this technique because they are fairly uniformly cylindrical along the length of the bone making them amenable to boring.

*Advantages:* 1) This is a straight forward simple method that requires no specialized equipment, with the exception of the confocal microscope; 2) The method is rapid. It avoids the requirement of decalcification or sectioning; 3) Using mT/mG reporter mice, in addition to tracing mature marrow adipocytes, will show whether marrow adipocyte precursors (GFP<sup>+</sup>) expressed the gene of interest; 4) The marrow adipocytes, in the marrow plug, can be stained with a fluorescent lipophilic dye (i.e. LipidTOX) allowing for easy identification of the mature adipocytes. This also allows for better determination of cell counts and size. This approach can be combined with immunofluorescence to co-stain for other cell markers if desired.

*Challenges:* 1) Because adult mice (C57BL/6 background) have few marrow adipocytes in the femur, induction of marrow adipogenesis is recommended. However, the choice of which induction protocol to be used (x-irradiation, high fat diet feeding, feeding with a methionine restricted diet or a rosiglitazone containing diet, see Tables 2.7-2.8) will depend on the experimental design; 2) The femoral medullary canal in adult mice is the only site sufficiently large to collect a workable bone marrow plug; 3) Because the cells are removed from the marrow their anatomical location, especially as it relates to trabecular bone and the endosteum is lost.

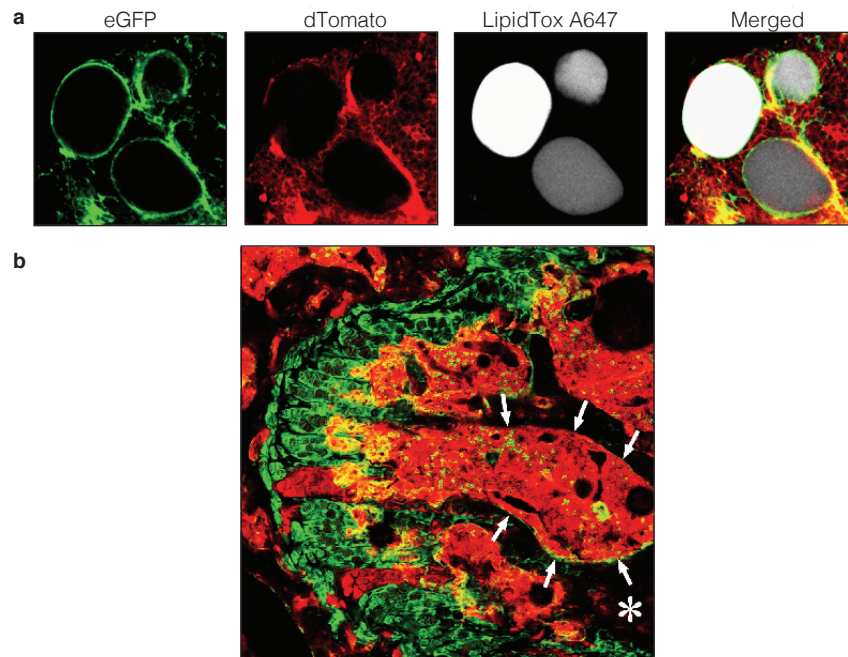


**Figure 2.5** | Lineage tracing of BMAd and BMSCs. **a** *Adiponectin-cre:mT/mG* mice received a single dose of x-irradiation (1000 rads) to induce bone marrow adipogenesis. Following irradiation, the mice were reconstituted by an i.v. injection of 106 syngeneic bone marrow cells to prevent radiation induced bone marrow damage. Bone marrow was collected from the femur as an intact plug, stained with LipidTox (fluorescent lipophilic dye), and marrow adipocytes visualized by confocal microscopy. Greater than 95% of the cells were eGFP<sup>+</sup> indicating they were traced by expression of Adiponectin. **b** The femur from *Twist-2-cre:mT/mG* mice was isolated, the femoral head removed and the bone fixed in 4% paraformaldehyde overnight. The bones were then immersed in 30% sucrose for 3-4 days, then placed in OCT, and frozen. 5-10μm thick-sections were imaged by confocal microscopy. Columns of growth plate cartilage cells were eGFP<sup>+</sup>. In the bone marrow (outlined by arrows and appearing red), a small number of eGFP<sup>+</sup> cells can be seen. In addition, approximately 50% of osteocytes (\* denotes bone, appearing black) were also eGFP<sup>+</sup>. Cells that were eGFP<sup>+</sup> were traced by the expression of Twist-2. BMAd: bone marrow adipocytes; BMSC: bone marrow stromal cells; eGFP: enhanced green fluorescent protein.

The second, *in situ*, approach maintains anatomical location with respect to the growth plate and endosteum, but by maintaining the calcified bone matrix, introduces its own complications. Although the *in situ* approach involves collecting fresh femurs, from that point, the method varies significantly from investigator to investigator. The bones can be fixed in paraformaldehyde overnight and then given a partial decalcification in EDTA, sucrose incubation follows, and then embedding in either a cryomedia or carboxymethyl cellulose, followed by frozen sectioning (Figure 2.5b). Some of the best images have been acquired using a tape-transfer system and cutting 10-30μm sections (Kalajzic et al., 2008; Mizoguchi et al., 2014; Zhou et al., 2014; Worthley et al., 2015). Other investigators have even used paraffin embedding instead of frozen sections, although this necessitates the use of antibodies, even in fluorescence reporter mice (Ambrosi et al., 2017). After sectioning, the tissue can then be stained with the desired antibody-conjugate (direct i.e. GFP, or indirect using a secondary fluorescent antibody or

## Chapter 2 – Methodologies of bone marrow adiposity research

biotin-avidin conjugate), and imaged by fluorescence or confocal microscopy. However, the fixation and decalcification can vary greatly from investigator to investigator, including some who use no fixation and rapid freezing (Mizoguchi et al., 2014). In addition, to immunofluorescent staining, transient fluorescent reporter mice (e.g. *Zfp423-EGFP*) or Cre/Lox lineage tracing fluorescent reporter mice can be used.

*Advantages:* 1) The major advantage to this method is that it allows for direct visualization of the cells within intact bone. Thus, the spatial relationship between marrow adipocytes, other cells, and bone is maintained; 2) Using *mT/mG* reporter mice can be a significant advantage; 3) Mature marrow adipocytes can be imaged.

*Challenges:* 1) This method requires expertise and experience in bone histology and specialized histologic equipment (e.g. tungsten-carbide knives to section bone); 2) Sectioning small bones (e.g. distal tibia and caudal vertebrae) can be difficult; 3) Difficulties using the tape-transfer systems have been reported; 4) The embedding techniques and section preparation often exclude the combined use of lipid-tracing dyes.

It is clear that great progress in lineage tracing of marrow adipocytes has been made during the last few years, due to advances such as the Cre/Lox system. Our ability to delineate cells in the bone marrow adipocyte lineage will only get better with the advent of more specific Cre-drivers and more robust reporters. Refinements in our ability to process bone to make it more accessible to these methods will result in an even better understanding of the lineage, how it relates to other mesenchymal lineage cells, and the myriad of other cells in bone marrow.

### In vivo modulation of BMA

BMAT is a complex and dynamic depot that is highly regulated and can affect the function of other tissues/organs. Whether presence of BMAT is necessary for normal physiological responses is still controversial. While some studies have shown that BMAT is negatively influencing bone mass, a study in BMAT-deficient *Kit<sup>W<sup>W</sup>/W<sup>-v</sup></sup>* (BMAT<sup>-/-</sup>) mice suggested that the absence of BMAT did not have any relevant effect on ovariectomy-induced bone loss (Iwaniec et al., 2013). However, a recent study in BMAT<sup>-/-</sup> male mice has shown that absence of BMAT exacerbated bone loss during hindlimb unloading (Keune et al., 2017).

The expandability of BMAT is regulated by nutritional and environmental factors, aging, endocrine signals, and pharmacological agents. Here, we critically summarize experimental models used to study *in vivo* regulation of BMAT development and function.

### Nutritional and environmental interventions

In C57BL/6J mice, a strain susceptible to obesity and diabetes, HFD feeding induces also BMAT expansion (Doucette et al., 2015; Scheller et al., 2016). When diet-induced obesity (DIO) is reversed by switching to normal chow diet (NCD) to mimic weight loss, the HFD-induced BMAT recedes (Scheller et al., 2016). Some of these alterations are microbiota-dependent (Luo et al., 2015). The alterations induced by the HFD on BMAT gene expression differ from that observed in peripheral adipose tissues. In contrast to visceral white adipose tissue (WAT), pro-inflammatory gene expression was decreased while the expression of genes of the insulin signaling pathway increased in BMAT of HFD-fed mice, suggesting a differential metabolic regulation of BMAT adipocytes (Tencerova et al., 2018). Walji et al. (2016) used microfibril-associated glycoprotein-1 (MAGP1) deficient (*Mfap2<sup>-/-</sup>*) mice that develop adult-onset obesity that precedes insulin resistance. In these mice, BMAT increased relative to WT mice

coincident with the development of insulin resistance, and not with excess peripheral adiposity, hyperglycemia, change in trabecular bone volume or hematopoiesis.

Exercise is a life-style intervention proposed to prevent/counteract obesity-associated BMAT expansion (Table 2.7). Voluntary wheel running in C57BL/6 fed NCD or HFD demonstrated that exercise prevented the increase in BMAT acquisition (Styner et al., 2014). Styner et al. (2015) found that exercise (alone or in combination with rosiglitazone) reduced BMAT volume and upregulated UCP1 expression in whole tibia (Table 2.8). Exercise can also reverse the increase of BMAT observed in previously obese animals (HFD-fed for 3 months) by decreasing both adipocyte number and size (Styner et al., 2017). Exercise was associated with higher trabecular and cortical bone quantity in lean and obese mice, but HFD itself did not influence bone quantity. Importantly, a recent study, also provided evidence that physical exercise modulates vertebral BMAT in humans (Belavy et al., 2018).

The differential *in vivo* regulation of BMAT by nutritional status also occurs in animal models of caloric restriction (CR). In contrast to what is observed in visceral or subcutaneous WAT, BMAT is preserved or even increased in states of CR (Devlin et al., 2010;Cawthorn et al., 2016;Devlin et al., 2016;Scheller et al., 2019) (Tables 2.7-2.8). Indeed, CR (30%) in young growing mice alters bone formation, but despite having a lower body weight and body fat percentage, they exhibit a dramatic increase in BMAT (Devlin et al., 2010). In patients with anorexia nervosa, CR is also associated with increased BMAT (Mayo-Smith et al., 1989;Bredella et al., 2009). However, in New Zealand rabbits moderate or extensive CR did not cause BMAT expansion (Cawthorn et al., 2016). It has been suggested that the increase in BMAT is especially prominent when nutrient deprivation occurs during periods of skeletal growth, such as childhood or adolescence (Scheller et al., 2019). This period of rapid skeletal growth may already be poised for BMAT development as this is also a time of rapid baseline BMAT accumulation (Moore and Dawson, 1990).

The expansion of BMAT during CR has also been associated with changes in several neuroendocrine factors that are modulated in response to energy deprivation. The decrease in leptin that occurs during CR-induced weight loss may account for the increased BMAT. Indeed, BMAT is increased in leptin-deficient *ob/ob* mice (Hamrick et al., 2004), and subcutaneous leptin treatment induces loss of BMAT adipocytes and increases bone formation in these mice (Hamrick et al., 2005). Moreover, peripheral leptin therapy is effective in reversing the increased BMAT observed in type 1 diabetic mice and CR models, but does not stop the bone loss that occurs concomitantly (Motyl and McCabe, 2009;Devlin et al., 2016) (Table 2.8). Furthermore, central injections of leptin into the ventromedial hypothalamus (VMH) of Sprague-Dawley rats, as well as leptin gene therapy (intraventricular administration of recombinant adeno-associated virus (rAAV)-leptin gene) to *ob/ob* mice also reduced BMAT (Hamrick et al., 2007;Lindenmaier et al., 2016). Interestingly, mice with selective deletion of the leptin receptor (*Lepr*) in limb bone marrow stromal cells (*Prx1-Cre;Lepr<sup>fl/fl</sup>* mice) exhibited normal body mass and hematopoiesis, but have decreased BMAT, and increased osteogenesis (Yue et al., 2016). Moreover, *Prx1-Cre;Lepr<sup>fl/fl</sup>* mice were protected from the HFD-increases in BMAT and reductions in osteogenesis. It therefore appears that hypothalamic and peripheral leptin signaling may have different or multiple effects on adipogenesis within bone marrow.

**Table 2.7** | *In vivo* modulation of bone marrow adipose tissue by dietary and environmental factors

|  |  |  |  |
|--|--|--|--|
| High fat diet<br>(45% to 60%)  | C57BL/6J mice  | ↑ BMAT<br>↔ or ↓ Bone mass<br>(O, $\mu$ CT)                                    | Doucette et al., 2015<br>Scheller et al., 2016<br>Tencerova et al., 2018 |
| Physical exercise<br>(voluntary exercise wheel in NCD and<br>HFD mice) | C57BL/6 mice   | ↓ BMAT volume in NCD and HFD-<br>fed mice.<br>↑ Bone mass<br>(O, $\mu$ CT)     | Styner et al., 2014<br>Styner et al., 2017                               |
| Caloric restriction (CR)   | C57BL/6J mice<br>(CR: 30% of NCD)<br>New Zealand White<br>rabbits<br>(CR: Moderate (30%)<br>or extensive (50-70%)) | ↑ BMAT volume<br>(H, MR)<br><br>↔ BMAT volume<br>(O, $\mu$ CT, H)              | Devlin et al., 2010<br><br>Cawthorn et al., 2016                         |
| Acute fasting (48 h)   | Sprague-Dawley rats  | BMAT adipocytes size:<br>↓ proximal tibia<br>↔ tail vertebrae<br>(O, $\mu$ CT) | Scheller et al., 2018  |
| Cold exposure (4 °C)   | C57BL/6J<br>C3H/He   | ↓ rBMAT ↔ cBMAT<br>(O, $\mu$ CT)   | Scheller et al., 2015  |
| CLA +FO supplementation  | C57BL/6 mice   | ↓ BMAT<br>(H)  | Halade et al., 2011  |
| Dietary methionine restriction   | C57BL/6J mice  | ↑ BMAT<br>(O, $\mu$ CT)  | Plummer et al., 2017   |

↓Decrease; ↑Increase; ↔No change; BW: body weight; CLA: conjugated linoleic acid; FO: fish oil; HFD: high fat diet; O: Osmium tetroxide staining; BMAT: bone marrow adipose tissue; NCD: normal chow diet; rBMAT: regulated BMAT; cBMAT: constitutive BMAT.



*Aging*

Increased BMAT is also observed during aging, and has been negatively correlated with bone health, and sometimes precipitates impaired hematopoiesis in animals (Takeshita et al., 2014; Ambrosi et al., 2017) and humans (Justesen et al., 2001; Tuljapurkar et al., 2011; Bani Hassan et al., 2018). Dietary strategies have also been proposed to counteract the increased BMAT associated with aging, and combination of conjugated linoleic acid with fish oil can decrease age-associated BMAT in C57BL/6J mice (Halade et al., 2011). Dietary methionine restriction (MR) increases longevity in rodent models, however MR promotes BMAT accumulation in contrast to WAT reduction (Plummer et al., 2017).

*Endocrine Regulation*

From an endocrine perspective, bone and BMAT metabolism are tightly linked and therefore BMAT is under extensive hormonal regulation. First of all, already a long time ago it has been observed that ovariectomy increases BMAT in animals (Martin and Zissimos, 1991) and ovariectomy is now commonly used to induce BMAT in animal models. These observations have been extended to humans, as BMAT increases during aging and this increase is accelerated in women around the time of menopause (Baum et al., 2018). Postmenopausal hormonal replacement therapy with estradiol, both long term (1 year) and short term (two weeks) decreases BMAT in women (Syed et al., 2008; Limonard et al., 2015), showing that indeed estradiol is an important regulator of BMAT. At the same time that estradiol secretion by the ovaries ceases, compensatory follicle stimulating hormone (FSH) secretion by the pituitary gland increases. In addition to the effect of hormonal replacement therapy, also FSH blocking therapy has been shown to decrease BMA in mice (Liu et al., 2017). In addition to gonadal hormones, glucocorticoids have a profound effect on adipose metabolism and this also holds true for bone marrow adiposity. Cushing's disease, defined by increased adrenocorticotrophic hormone (ACTH) production by a pituitary adenoma and therefore hypercortisolemia, increases BMAT and this reverses again following surgical cure by removal of the pituitary adenoma (Maurice et al., 2018). Also, long-term glucocorticoid treatment leads to increased BMAT (Li et al., 2013b) and can be used to induce BMAT in animal models. Finally, parathyroid hormone, an important regulator of bone metabolism and potent osteoanabolic drug, also has an effect on BMA. Teriparatide treatment in osteopenic women reduces BMAT (Yang et al., 2016) and animal studies showed that this effect can be recapitulated by genetic deletion of the parathyroid hormone receptor in skeletal stromal cells (Fan et al., 2017). Interestingly, additional studies from the Rosen lab showed that the effect of PTH is not only on the differentiation of the SSC into the adipocytic lineage, but that PTH can also induce lipolysis in BM adipocytes (Maridas et al., 2019). In addition, growth hormone (GH) is an important regulator of skeletal growth and growth hormone deficiency or resistance has been associated with changes in BMAT. In growing rats, hypophysectomy dramatically increases BMAT and this could not be reversed by treatment with either estradiol, thyroid hormone, cortisol or Insulin Growth Factor-1 (IGF-1), but was completely reversed by treatment with GH (Menagh et al., JBMR 2010). In healthy, premenopausal women, vertebral BMAT measured with <sup>1</sup>H-MRS was inversely associated with IGF-1 concentrations, but not stimulated GH concentrations (Bredella et al Obesity 2011). However, treatment with recombinant GH for 6 months in premenopausal obese women, did not change BMAT, although there was a significant difference between the GH treated and placebo treated groups due to the decrease in BMAT in the placebo group (Bredella et al Bone 2014). Therefore, the role of GH in the regulation of BMAT in adult humans remains uncertain and studies in children during growth have not been performed.

## Chapter 2 – Methodologies of bone marrow adiposity research

BMAT is not only regulated by hormones, but also acts as an important endocrine organ itself. Cawthorn et al. (2014) found that increased BMAT significantly contributes to the higher circulating adiponectin levels during CR. Moreover, studies in Ocn-Wnt10b mice, which resist BMAT expansion during CR, demonstrated that increased BMAT is required for the elevated circulating adiponectin in this condition. Furthermore, BMAT and adiponectin levels increase in patients undergoing therapy for ovarian or endometrial cancer, despite no change in total fat mass (Cawthorn et al., 2014). Increased adiponectin levels and BMAT volume were also observed in DIO WT (C57BL/6J) mice treated with Rosiglitazone. However, female Ocn-Wnt10b mice treated with Rosiglitazone had mildly blunted hyperadiponectinemia (Sulston et al., 2016) while males did not, suggesting a sex-specific response.

### *Pharmacological modulation*

Several drugs also regulate BMAT. PPAR $\gamma$  is a master transcription factor for adipocyte differentiation, and treatment with the insulin-sensitizing drugs thiazolidinediones (TZDs), which are PPAR $\gamma$  agonists, affects marrow adiposity. As shown in Table 2.8, treatment with several PPAR $\gamma$  agonists such as Rosiglitazone and Troglitazone enhanced BMAT in different animal models (Tornvig et al., 2001; Lazarenko et al., 2007). However, the effects of TZDs on BMAT seem to be strain-specific (Ackert-Bicknell et al., 2009) and age-dependent, favoring BMAT accumulation in older mice rather than in young-growing animals (Lazarenko et al., 2007). In ovariectomized (OVX) rats, treatment with rosiglitazone (BRL49653) exacerbated bone loss and increased BMAT (Sottile et al., 2004). On the other hand, several studies have shown that treatment with PPAR $\gamma$  agonists increased BMAT without affecting trabecular bone volume, suggesting that adipogenesis and osteogenesis can be regulated independently *in vivo* (Tornvig et al., 2001). Similarly, netoglitazone administered to 6-month-old C57BL/6 mice had a strong adipogenic induction with no change in the trabecular architecture and modest decreases in cortical bone mineralization (Lazarenko et al., 2006). In contrast, a reduction in BMAT has been observed in all studies administering PPAR $\gamma$  antagonists after chemo/radiotherapy, which are potent inducers of BMAT (Table 2.7) (Botolin and McCabe, 2006; Naveiras et al., 2009; Duque et al., 2013; Zhu et al., 2013; Lu et al., 2016; Sato et al., 2016). Moreover, genetic models of PPAR $\gamma$  loss show a pronounced increase in bone mass with extramedullary hematopoiesis (Cock et al., 2004; Wilson et al., 2018). The effects of BMAT in the recovering of hematopoietic compartment seem apparently contradictory, possibly due to the differential effects of distinct BMAT subtypes and differentiation stages in hematopoietic progenitor support (reviewed in Mattiucci et al., 2018b; Cuminetti and Arranz, 2019). Methodologically, it is to be noted that although effective in reducing BMAT, the most commonly used PPAR $\gamma$  “antagonist” for *in vivo* experimentation, Bisphenol A Diglycidyl Ether (BADGE), has partial PPAR $\gamma$  agonist effects and is a potential endocrine disruptor receptor anti-androgenic and pro-estrogenic properties (Seimandi et al., 2005; Desdoits-Lethimonier et al., 2017; van Leeuwen et al., 2019). It is therefore recommended that future *in vivo* studies use a more specific PPAR $\gamma$  antagonist such as GW9662 (Sato et al., 2016).

BMAT thus accumulates following hematopoietic marrow ablation. A wave of BMAT precedes hematopoietic repopulation and peaks from 2-3 weeks after whole-body radiation depending on dose and recipient characteristics (700-1000 Gy) (Naveiras et al., 2009; Horowitz et al., 2017). BMAT is then lost and the timing of recovery depends on the radiation dose and on the number of hematopoietic cells used for the rescue. Sublethal models which do not require hematopoietic rescue have also been developed with 5-fluorouracil or cytarabine treatments (Zhu et al., 2013; Lu et al., 2016). Both radiation and chemotherapeutic treatments induce dramatic increases in BMAT also in patients (Bolan et al., 2013; Cawthorn et al., 2014), whereas certain disorders of inefficient hematopoiesis (e.g. W/W<sup>v</sup> mice) are

associated with greatly reduced BMAT and a modified lipid composition of the stroma (Geissler and Russell, 1983; Potter and Wright, 1980). The biological implications of BMAT in neoplastic progression within the BM microenvironment are only beginning to unravel (Chen et al., 2010; Wang et al., 2017; Boyd et al., 2017; Cahu et al., 2017; Lu et al., 2018).

### *Sympathetic regulation*

A very important issue when studying the *in vivo* modulation of BMAT is to consider the region-specific variation in the properties of the skeletal adipocytes, as already discussed in the BMAT isolation section. The studies of Scheller et al. (2015) in mice strongly support the existence of a constitutive (cBMAT) and a regulated (rBMAT) depot. cBMAT is in the distal long bones fills the medullary canal from the tibia-fibular junction into the malleolus and caudal vertebrae, histologically resembles WAT, appears rapidly in the early postnatal period, does not usually respond to stimuli or pathophysiological changes (Horowitz et al, Adipocyte 2017), though it can reduced over several months with thermoneutrality (Huggins and Blocksom, 1936). In contrast, rBMAT is situated in the proximal regions of long bones and in spinal vertebrae, develops after cBMAT, and is interspersed with hematopoietic cells. rBMAT increases or decreases in various conditions (DIO, aging, CR, etc.) (Suchacki and Cawthorn, 2018).

The study of Scheller et al. (2015) also revealed that knockout of PTRF (Ptrf<sup>-/-</sup> mice, a model of congenital generalized lipodystrophy 4) selectively inhibits formation of rBMAT adipocytes without affecting cBMAT, which could be one step towards generation of a genetic model of rBMAT ablation (Scheller et al., 2015).

The lack of response of BMAT adipocytes to lipolysis during energy deprivation has been attributed to resistance to  $\beta$ -adrenergic stimulation, but this effect also shows region-specific differences. Acute fasting (48 h) decreases cell size of BMAT adipocytes within the proximal tibia but not within the tail vertebrae in Sprague-Dawley rats (Scheller et al., 2019). Moreover, BMAT from distal tibia and tail vertebrae of these rats resist  $\beta$ -adrenergic-induced phosphorylation of HSL and/or perilipin, which are required for stimulation of lipolysis. Furthermore, treatment of C3H/HeJ mice with CL316,243, a  $\beta$ 3-AR agonist, caused remodeling/beigeing of WAT, but only moderate remodeling of lipid droplets in BMAT of proximal tibia without affecting mid or distal tibia (Table 2.8). Furthermore,  $\beta$ -adrenergic stimulation through cold exposure shows lipolytic response by rBMAT (decreased rBMAT in the tibial epiphysis and in the proximal tibia) while cBMAT remained unchanged (Scheller et al., 2015). Therefore, these data suggest that the lipolytic response to  $\beta$ -adrenergic stimulation is more pronounced in rBMAT than in cBMAT (Scheller et al., 2019).

Another important factor to take into account when designing and interpreting studies about *in vivo* BMAT regulation is the effect of housing temperature. Most of the studies in mouse models are performed at room temperature (RT, around 22°C), which is below the thermoneutral temperature for mice (around 32°C). Therefore, RT housing can increase non-shivering thermogenesis by the sympathetic outflow and the activation of UCP1 in BAT (Cannon and Nedergaard, 2011; Iwaniec et al., 2016) showed that thermoneutral housing not only reduces UCP1 expression in BAT, but also increase BMAT and the percentage of body fat as compared with RT-housed mice. Therefore, the mild cold stress induced by RT-housing could be a non-considered confounding factor in mice studies.

## Chapter 2 – Methodologies of bone marrow adiposity research

### In vivo modulation challenges

All these studies have demonstrated that BMAT expansion accompanies metabolic dysfunction. However, many physiopathological changes take place in these processes, and dissecting the role of BMAT expansion from the role of peripheral adipocytes and other metabolic perturbations make mechanistic studies a challenge. Furthermore, the divergent BMAT responses to different strains/species suggest the existence of a strong genetic background effect, which should be considered when designing studies, highlighting once more the importance of adhering to the BMAS minimal reporting guidelines when communicating results (see Table 2.1). Possibly, standard *in vivo* experimental conditions need to be defined for inter-laboratory comparisons. As we continue to identify the physiological processes that underlie the formation of BMAT and the environmental and genetic cues that control its accumulation, it is becoming increasingly evident that BMAT may be heterogenous.

Finally, in spite of their limitations, wider use of available genetic models of non-selective BMAT depletion (e.g. *Ptrf*<sup>-/-</sup>, *W/W<sup>v</sup>*), which have lesser metabolic phenotypes than severely lipodystrophic mice (e.g. *A-ZIP/F*), should advance the field until models of highly-specific BMAT depletion can be developed. Furthermore, it is paramount to consider that the BMA, bone, vascular and hematopoietic compartments are tightly interlinked within the BM, such that *in vivo* analysis requires functional measurements of all four compartments to reach mechanistic conclusions.

### Biobanking

The BMAS Working Group on Biobanking has the ambition to generate standardized approaches towards isolation, characterization and long-term storage of tissues/cells related to BMA and their associated data and annotations. Although difficult to achieve due to several challenges (see below), creating minimal standards to isolate and characterize BMAdS as well as freezing protocols for long-term storage should significantly reduce variability in outcomes between studies and laboratories. This is especially important to ensure viability and conservation of heterogeneity in cell-based assays, and to ensure sample stability for chemical analysis including mass spectrometry. Most importantly, unified biobanking standards along with the protection of associated data will enable responsible use and exchange of samples for comparative and larger-scale studies. Ultimately, the field will benefit from improved applicability of animal and human BMA-related samples, which may better facilitate the discovery of novel therapeutics to target BMA.

In a complementary fashion to the BMAS Working Group in Methodologies, one of the foci of the BMAS Biobanking Working Group will be to congregate methodologies related to the collection, freezing/thawing and long-term storage of BMAdS. Additional aspects of biobanking that the working group will scrutinize are privacy regulations regarding participants/patients, data protection and ethical guidelines to facilitate collaborative efforts. Main challenges towards this objective are briefly introduced below.

**Table 2.8** | *In vivo* modulation of bone marrow adipose tissue by hormonal and pharmacological treatments in animal models.

| IN VIVO INTERVENTION  | ANIMAL MODEL<br>(ROUTE OF ADMINISTRATION)   | OUTCOMES<br>(ASSAYS)  | REFERENCES   |
|---|---|---|--|
| Leptin  | <i>ob/ob</i> mice<br>(s.c. osmotic pumps)   | ↓ BMAT volume, ↑ bone formation<br>(H-t)  | Hamrick et al., 2005   |
|   | Type 1 Diabetic mice<br>(s.c. osmotic pumps)  | ↓ Adipocyte number, ↔ bone mass loss<br>(H, $\mu$ CT)   | Moryl and McCabe, 2009   |
|   | C57BL/6J mice<br>(s.c.)   | ↓ BMAT formation induced by CR, ↔ BMD<br>(O, $\mu$ CT, H)   | Devlin et al., 2016  |
|   | Sprague-Dawley rats<br>(VMH injection)  | ↓ number of BMAT adipocytes<br>(H-t)  | Hamrick et al., 2007   |
|   | <i>ob/ob</i> mice<br>(rAAV-Lep, i.c.v.)   | ↓ BMAT, ↑ bone formation<br>(H-f)   | Lindenmaier et al., 2016   |
| Orchidectomy  | C57BL/6J mice   | ↑ BMAT<br>(H-f)   | Sui et al., 2016   |
| PPAR $\gamma$ Agonists<br>Rosiglitazone<br>Ovariectomy (OVX)<br>OVX + Rosiglitazone | Wistar rats<br>(gavage)   | ↔ Ad.Ar./M.Ar., ↑ Ad.Ar./M.Ar., ↑ Ad.Ar./M.Ar.<br>(H-t)   | Sottile et al., 2004   |
| Troglitazone  | ApoE <sup>-/-</sup> mice<br>(mixed with diet)   | ↑ BMAT (Ad.Ar./M.Ar.)<br>(H-t)  | Tornvig et al., 2001   |
| Rosiglitazone   | C57BL/6J mice   | C57BL/6J: ↑ BMAT (adipocyte number) (H-t)   | Lazarenko et al., 2007   |
|   | C57BL/6J mice + Exercise<br><br>C57BL/6J mice<br>C3H/HeJ mice<br>DBA/2J mice<br>A/J mice<br><br>Diabetic yellow agouti <i>Avy/a</i><br><br>Ocn-Wnt10b mice<br>(mixed with diet) | <i>Exercise</i> : ↓ BMAT-induced by rosiglitazone (O, $\mu$ CT)<br><br>C57BL/6J: ↑↑ BMAT (H-f)<br>C3H/HeJ: ↑ BMAT (H-f)<br>DBA/2J: ↔ BMAT (H-f)<br>A/J: ↔ BMAT (H-f)<br><br>↑ BAT/WAT gene expression in marrow of C57BL/6 mice,<br>not increase BAT genes in diabetic mice (H-t, RT-PCR)<br><br>↓ BMAT <i>vs.</i> WT (O, $\mu$ CT) | Styner et al., 2015<br>Ackert-Bicknell et al., 2009<br><br>Krings et al., 2012<br>Sulston et al., 2016 |

**Table 2.8** | *In vivo* modulation of bone marrow adipose tissue by hormonal and pharmacological treatments in animal models.

| IN VIVO INTERVENTION   | ANIMAL MODEL<br>(ROUTE OF ADMINISTRATION)                        | OUTCOMES<br>(ASSAYS)   | REFERENCES                                |
|--|--|--|---|
| PPAR $\gamma$ Antagonists<br>Bisphenol A Diglycidil Ether, BADGE (partial antagonist properties) | BALB/c (streptozotocin-induced diabetes)                         | ↓ BMAT, ↔ BMD  | Botolin et al., 2006                      |
|  | male C57BL/6j mice   | ↓ BMAT, ↑ BMD  | Duque et al., 2013                        |
|  | C57BL/6j mice + lethal irradiation<br>C57BL/6j mice + cytarabine | ↓ BMAT, ↑ hematopoietic recovery   | Naveiras et al., 2009<br>Zhu et al., 2013 |
| GW9662 (pure antagonist)   | C57BL/6j mice + high fat diet (35%)<br>(i.p.)                    | ↔ BMAT, rescue BMD<br>(H-t, $\mu$ CT, IF, RT-PCR)  | Luo et al., 2015                          |
|  | C57BL/6 into C.B10-immune BM aplasia<br>(i.p.)                   | ↓ BMAT, ↑ hematopoietic recovery<br>(IF, RT-PCR)   | Sato et al., 2016                         |
| B-3 Adrenergic agonists<br>Isoproterenol or CL316,243  | Sprague-Dawley rats<br>(i.p.)                                    | BMAT from distal tibia and tail vertebrae resists $\beta$ -adrenergic-induced lipolysis      | Scheller et al., 2019                     |
|  | C3H/HeJ mice<br>(i.p.)   | Moderate lipid droplet remodeling of BMAT adipocytes<br>(proximal tibia); (O, $\mu$ CT, IHC) |   |
| Dexamethasone  | C57BL/6j mice<br>(i.p.)  | ↑ BMAT, ↓ BMD<br>(H-f, $\mu$ CT)   | Li et al., 2013                           |
| Lethal irradiation + BM Transplantation  | FVB  | ↑ BMAT   | Naveiras et al., 2009                     |
|  |  | ↔ BMAT, ↑ BMD in “fatless” FVB.A-ZIP/F<br>(H-f, $\mu$ CT)                                    |   |
|  | C57BL/6j mice  | ↑ BMAd/MAr<br>↑ Ad. number and size<br>(MQ-t, f <sub>st,sp</sub> & MRI-f)                    | Chapter 3                                 |
|  | Beagle dogs  | ↑ BMAT<br>(H-t, hu r)  | Calvo et al., 1976                        |

↓ Decrease; ↑ Increase; ↔ No change; BAT: brown adipose tissue; BMAT: bone marrow adipose tissue; BMD: bone mineral density; f: femur; H: histomorphometry; hu: humerus; IF: immunofluorescence; IHC: immunohistochemistry; i.p.: intraperitoneal; O: Osmium tetroxide staining; r: radius; st: sternum, sp: spine; t: tibia; WAT: white adipose tissue; rAAV

### Isolation of BMAds

Different types of materials have been and will be employed to study BMA, including BM aspirates, biopsies, specific cell types, BM plasma fraction, etc. After having defined these, recommended standard procedures are required regarding BMA isolation, processing and characterization. For example, isolation protocols vary substantially between laboratories (digestion with collagenase or other enzymes, incubation times, etc.). In addition, it is important to distinguish protocols for animal studies versus human materials as BMA is different in composition, location, metabolism and regulation. For human bone marrow-related samples, recommended patient screening should be additionally established (HIV, Hepatitis B and C virus). Finally, minimal standards should also be established for sample annotation, which should include description of the site of collection, method of collection and isolation, including time and type of digestion, time from collection to freezing, etc.

### Characterization of BMAds

One of the biggest challenges is to define a healthy control set, especially for human samples (see Table 1). What is regarded as normal population and a standard site of collection and how do we define this? What is the minimal set of parameters required to define such a set? One solution is to propose a minimal set of specific surface molecules, gene expression markers and/or other biomarkers (e.g. lipid profiles) to facilitate comparisons and thus also multicenter studies. Some specific markers have been proposed (adipokine markers, absence of hematopoietic, endothelial and hematopoietic markers) but additional species-specific markers are needed to be able to characterize BMAds in a uniform and reliable fashion.

### Long-term storage of BMA-related samples

To date it has proven impossible to freeze BMAds, and the only access point to retrospective samples relies on the identification of adipocyte ghosts in paraffin blocks. Tissue samples containing adipocytes are being collected but these require purification and/or digestion steps before freezing. On the other hand, storage of precursor cells (SSCs) may poorly reflect the BMA situation at the time of isolation, most often due to cellular expansion (and deviation) *in vitro* before or after freezing. In order to create as much homogeneity as possibly, it is vital to define freezing and thawing procedures employed with a minimum of interfering steps as well as viability and cell growth/differentiation characteristics of previously stored BMA samples. Non-frozen samples, including paraffin blocks, may pose less issues, but still homogeneity in tissue processing and database management are required to optimize storage and exchange of samples.

### Ethical issues and data protection

With the installment of the General Data Protection Regulation (GDPR) in 2018 (EU GDPR Portal (website), accessed August 27, 2019, <http://eugdpr.org>) the protection of people and data has become more stringent. Trying to come up with a standardized procedure towards biobanking will face challenges, including different national regulations, institutionalized rules, etc. Ethical guidelines varying between countries should be dealt with to assess the possibility to generalize ethical topics into one document for samples to be collected in the future. Related to this, a general template for informed consent and awareness of mutual use of obtained samples by all involved may improve standardization and the possibility to share samples, which is especially relevant in the context of rare diseases. A BMAS consortium-wide material transfer agreement may be instrumental for this.

## Chapter 2 – Methodologies of bone marrow adiposity research

Issues related to data protection include the assurance that participant/patient data remains anonymous at all costs. Although the consciousness around this subject is increasing, the working group will assess these issues in detail and will aim to propose a comprehensive recommended protocol to safeguard anonymity and data protection that originates from any of the laboratories. Data obtained in the EU often cannot be stored on servers outside the EU and similar regulations may apply to different continents as well. Therefore, a robust data management plan needs to be installed that can explore and potentially overcome challenges such as decentralized storage of samples and associated files.

In conclusion, biobanking and methodological challenges are tightly linked. Minimal standards and international overarching ethical guidelines for BMA sample collection and data protection will be critical to increase the quality of fundamental and multicenter clinical studies, and interpret with greater confidence the outcome and impact of BMA research within the next few years.

## Conclusion

Specific methodologies for the study of BMA have been developed in the last decade, paralleling the increasing interest in the field. Gold standard methodologies currently exist for the assessment of BMA *ex vivo*, *in vivo* and *in vitro* (e.g. histomorphometry and OsO<sub>4</sub>-3D contrast-enhanced  $\mu$ CT for *ex vivo*, WFI and <sup>1</sup>H-MRS MRI sequences for *in vivo* studies, lipid-dye-based and RT-qPCR-based assessment for assessment of *in vitro* BM adipogenesis) and emerging techniques may soon come to complement or substitute these gold standards (i.e. digital pathology algorithms for histomorphometry, POM-based contrast-enhanced CT for *ex vivo* imaging, dual energy CT for *in vivo* imaging as well as more reproducible parameters for *in vivo* MRI spectroscopy, label-free or 3D microscopy and microspectroscopy for *in vitro* imaging, or 3D adipose organoids for *in vitro* cultures).

However, great challenges still remain. First, given the inherent fragility of BMAd and their difficult access within the bone, protocols for extraction, *ex vivo* handling, and *in vitro* culture/differentiation of BMAd or BMSC progenitors vary greatly. Thus, recommended standardized protocols for *in vivo* modulation and extraction, minimal standards for BMAd purity assessment, and standardization of method-specific thresholds for BMA detection would greatly increase inter-study comparison and multi-site collaborations. Second, given the number of factors that affect BMA mass, and possibly type (e.g. skeletal location, gender, age, strain, nutritional status, metabolic state, exercise, ambient temperature, isolation technique), great attention needs to be paid in careful annotation and reporting of these confounding factors for all BMA scientific output. Third, in order to move forward the functional understanding of BMA, tools for the specific ablation of BMAd are urgently needed to uncouple the local BMA-effects from the metabolic effects of systemic lipodystrophy.

The BMAS Working Group in Methodologies and the collaborative BMAS community at large present the opportunity to reach methodological consensus guidelines and propose minimal standards that would strengthen the quality of our scientific output, increase comparability and prepare the field for multi-site preclinical and clinical studies which can pave the way to sound clinical translation. As a first step,



## Chapter 2 | Methodologies of bone marrow adiposity research

incorporation of the BMAS nomenclature (Bravenboer et al., 2019) and adherence to the methodology reporting guidelines presented here (Table 1) will ensure a common language for our community.

### Author contributions

J. T., A.V.G. and O.N. conceptualized the manuscript, coordinated the writing and edited the sections. J.T., B.P., R.L. and P.B. mounted the manuscript and tables. R.L., N.B, J.T. and A.V.G. wrote the histomorphometry section. G.K., E.D. and E.S. wrote the ex vivo imaging section. S.B. and D.K. wrote the in vivo imaging section. J.T., S.B.C, B.P, A.P., P.B. and O.N. wrote the in vitro section. M.J.M-A., J.F., A.V.G. and O.N. wrote the in vivo modulation section. J.F., M.S.R., C.J.R. and M.H. wrote the *in vivo* reporter section. O.N and B.E. wrote the biobanking section. All authors edited and approved the final version of the manuscript.

### Competing Interests Statement

A.V. and O.N. are co-chairs and J.T. is coordinator of the BMAS Working Group in methodologies. B.P., B.E, C.J.R., E.D. and O.N. are members of the BMAS Executive Board. A.V.G., D.K., E.S., G.K. and M.H. are members of the BMAS Scientific Board.

### Acknowledgements

The BMA2017 annual meeting to constitute BMAS and its Working Groups was funded by Swiss National Science Foundation (SNSF) grant 31CO30\_173949. O.N. and J.T were founded by SNSF grants PP00P3\_183725 and PP00P3\_176990 and the Anna Fuller Fund. M.J.M-A. was founded by grant BFU2015-65937-R (MINECO/FEDER, Government of Spain). This work was supported by Université de Nantes, Région Pays de Loire and Société Française de Rhumatologie (S.B.C).

A special thank you to William Cawthorn, University of Edinburgh, for help on aligning this manuscript with the BMAS nomenclature position paper (in preparation). We thank Giulia Frangi, Université de Nantes for contributing to compilation of data for Tables 2.5 and 2.6, Vasco Campos, EPFL, for the Digital Holographic Microscopy image on Figure 2.4, and Mara Riminucci, Sapienza University of Rome, for kindly providing the histological images for Figures 2.1 and 2.4. We acknowledge the Medical Research Council (CDA: MR/P02209X/1) grant to Anjali Kusumbe, University of Oxford for providing the immunofluorescent staining in Figure 2.1.



## **CHAPTER 3**

### **Quantitative imaging of the bone marrow**



*This work is part of a manuscript in preparation, entitled*

## **MarrowQuant: Semi-Automated digital pathology quantification tool for histological bone marrow sections**

Josefine Tratwal<sup>1</sup>, Ibrahim Bekri<sup>1</sup>, Chiheb Boussema<sup>1</sup>, Nicolas Kunz<sup>2</sup>, Teresa Koliqi<sup>1</sup>, Shanti Rojas-Sutterlin<sup>1</sup>, Frédérica Schyrr<sup>1</sup>, Daniel N. Tavakol<sup>1</sup>, Vasco Campos<sup>1</sup>, Erica L. Scheller<sup>3</sup>, Rossella Sarro<sup>4</sup>, Carmen Bárcena<sup>5</sup>, Bettina Bisig<sup>4</sup>, Valentina Nardi<sup>6</sup>, Laurence De Leval<sup>4</sup>, Olivier Burri<sup>7</sup>, Olaia Naveiras<sup>1,8</sup>

<sup>1</sup>Laboratory of Regenerative Hematopoiesis, Institute of Bioengineering and Institute for Experimental Cancer Research, Ecole polytechnique fédérale de Lausanne, Lausanne, Switzerland

<sup>2</sup>Animal Imaging and Technology Core, Center for Biomedical Imaging, Ecole polytechnique fédérale de Lausanne, Lausanne, Switzerland

<sup>3</sup>Division of Bone and Mineral Diseases, Department of Internal Medicine, Washington University, Saint Louis, MO, USA

<sup>4</sup>University Institute of Pathology, Clinical Pathology Service, Centre hospitalier universitaire vaudois, Lausanne, Switzerland

<sup>5</sup>Department of Pathology, University Hospital 12 de Octubre, Madrid, Spain

<sup>6</sup>Department of Pathology, Massachusetts General Hospital, Harvard Medical School, Boston, USA

<sup>7</sup>Bioimaging and Optics Core Facility, Ecole polytechnique fédérale de Lausanne, Lausanne, Switzerland

<sup>8</sup>Department of Oncology, Hematology Service, Centre hospitalier universitaire vaudois, Lausanne, Switzerland

Corresponding author: Olaia Naveiras

## Preface

The work in this chapter started as a side project, as most are wont to do. Having taken it upon myself as one of my first missions on arrival in the lab, to dissect multiple whole mouse skeletons in order to see the transitions of red to yellow marrow, it was only natural for Olaia to ask me to find or develop a tool to quantify it. Not having located something available to my satisfaction, I embarked on the later. With my minimal knowledge of image processing or anything related to software development, I was immensely lucky to have a talented bachelor student, **Chiheb Boussema**, join me in this quest. We would work together closely and laboriously to iterate and re-iterate the code to near-perfection that he developed for detection of bone marrow compartments in histological sections of murine bones. In collaboration and under the steady guidance of **Olivier Burri** from the Bioimaging and Optics Core Facility (with help also from **Romain Guiet**), we established a first version of the quantification tool described in this chapter. The students that followed Chiheb, namely **Teresa Koloqi** and **Ibrahim Bekri**, arduously worked to improve the next versions of the code, to bring it to a working condition that could be shared with the community. It is a great pleasure to receive requests from labs across the world asking to use it, and having come to the point where we can finally share what will hopefully become a useful tool to the bone marrow adiposity community and beyond. While Teresa and I were eager to develop the tool for human trephine biopsies, it became clear that the samples varied too greatly from those of mouse for proper detection, and it would require in depth analysis and changes to the code. It is gratifying to know that this is now being undertaken as a PhD project by Rita Sarki.

The realization of this tool would not have been possible without the expertise of **Bettina Bisig**, **Rossella Sarro**, and the support of **Laurence De Leval** from the Pathology Department at the Centre hospitalier universitaire vaudois, as well as **Carmen Bárcena** in Spain and **Valentina Nardi** in Massachusetts. I am humbled by their wisdom, incredible kindness, and generosity that know no bounds. It has been my honor to have the opportunity to discuss fundamental questions and to receive their invaluable feedback for the project.

The amount of bone marrow transplants, bone dissections, tissue processing, sectioning, slide scans, and quantifications that accompany this project are immense. Therefore, I am grateful to any help that I had from Shanti, Vasco, Aurélien, Frédérica, and Naveed along the way – be it in preforming a transplant or a blood sampling or changing decalcification solutions and performing quantifications, those times when I had another experiment running in parallel. We were also lucky to have the opportunity to test our plugin on sections processed with a different protocol in another lab, and for that I thank **Erica Scheller** for her generosity and readiness to provide the samples.

The team of the Histology Core Facility require particular acknowledgement for the patience of developing new protocols for bone (that aren't always straight-forward) with the expertise of **Jessica Dessimoz** and the technical help of **Gianni Mancini**, **Agnès Hautier** and **Nathalie Müller**.

**Graham Knott** and **Stéphanie Rosset** from the Bioelectron Microscopy Core Facility were especially kind to provide materials and help with the osmium staining of the bones. **Roy Combe** from the Phenotyping Unit was also very supportive with initiating me into  $\mu$ CT, always doing his best to find answers to my many questions.

Incredibly, **Nicolas Kunz** who worked at the Center for Biomedical Imaging, was offered his time and talent generously to for a first attempt and visualizing the BM by Magnetic Resonance Imaging (MRI) in mice. This is an incredible undertaking knowing the size of a murine bone that is no more than two centimeters long and a few millimeters wide with the marrow cavity that is to be detected even smaller. This falls just barely within the sensitivity of a 14.1 or 9.4 Tesla MRI machine. This was Nicolas' first time imaging murine bones and I thank him for his faith and commitment to the project. There were many times when it seemed we were fighting against the limits but with Nicolas' trust and perseverance, we managed to reach our dream after three years of unwavering effort. Being able to work with Nicolas was a true joy and one of the most positive experiences of my doctorate, for which I am very grateful. The sequence that we developed is a powerful tool for *in vivo* temporal quantification of marrow adipose tissue changes, that I hope others in the lab will be able to make good use of in the years to come.

Bringing together the methods described above, **this chapter aims to** provide robust, reliable, and reproducible ways in which to quantify changes in BMA in the mouse skeleton. First, we describe the novel digital pathology tool for detection and quantification in histological hematoxylin and eosin stained paraffin sections of murine bones. We validate the developed tool by comparison to assessment of hematopoiesis by the pathologists, and by comparison to bone and adipocytic volume through  $\mu$ CT measurements coupled to osmium-tetroxide stains of decalcified bones. We then apply the tool in a homeostasis setting of the standard C57BL6/J female juvenile mouse as well as with increasing BMA in age. We also use it to quantify changes in the marrow compartments in the setting of irradiation- and transplantation induced aplasia. We are able to draw similarities between the quantification of these changes with those observed in the same setting with MRI measurements. These quantifications also allow us to observe whether a reciprocity exists between any of the BM compartments.

## Introduction

Bone marrow adipocytes (BMAds) were long considered as passive fillers of the marrow cavity, but have relatively recently accepted as occupying an important role within the bone marrow microenvironment in health and disease, while also contributing to whole-body energy homeostasis (Scheller and Rosen, 2014, Scheller et al. 2016).

At birth, the murine and human skeleton is entirely hematopoietic. BMAds appear shortly thereafter and increase throughout juvenile development in a centripetal fashion as the skeleton matures (Kricun et al. 1985). This reciprocal relationship between adipocytic and hematopoietic content has been known since the enunciation of the “Neumann” law in 1902, describing the age-driven adipocytic conversion of the marrow on distal bones. In humans, adipocytes become the most abundant cellular component in the adult BM. In mice, age-dependent adipocytic conversion of the marrow is highly strain-dependent (Scheller et al. 2015). Notably, the C57BL/6 murine strain, which constitutes the most widely used model for experimental hematopoiesis, presents the lowest degree of BM adipocyte content upon homeostatic skeletal maturation. A massive adipocytic conversion upon hematopoietic ablation (e.g. after chemo- or radiotherapy) has however, been described in humans and across different mouse strains. The BM is thus heterogeneous depending on specific skeletal location and age. Indeed, due to the macroscopic coloration of the predominant cell types, the marrow has been broadly categorized as hematopoietic/red or adipocytic/yellow marrow (Neumann, 1882).

At the single-cell level, however, BMAd heterogeneity was first described by the terms “labile” and “stable”. These terms were coined upon the discovery that performic acid Schiff (PFAS) positive and negative stains respectively differentiate “labile” BMAds interspersed within the hematopoietic red BM, which respond to hematopoietic demand (PFAS positive) from “stable” BMAds comprising the non-hematopoietic yellow BM of the distal long bones (PFAS negative) (Neumann, 1882; Tavassoli, 1976; Scheller et al., 2015). The integration of macroscopic characteristics and single-cell response at the tissue level resulted on the terms regulated Bone Marrow Adiposity (rBMA) and constitutive BMA (cBMA), and prompted further investigation on differential skeletal distribution, cell size and relative lipid composition. Mechanistically, specific loss of rBMA with conservation of cMAT has been described in the long bones upon cold exposure, and in lipodystrophic *Ptfr* knock-out mice, while an overall loss of BMAds is characteristic of c-kit mutant *W/W<sup>v</sup>* mice (Scheller et al., 2015; Iwanec et. al, 2013; Keune et al. 2015; Scheller et al. 2015).

The association between increased vertebral fracture risk and BMA in humans, as well as hematopoietic stem cell quiescence and BMA has prompted increased interest in marrow adiposity. Adipocytic conversion of the marrow has been associated to increased vertebral fracture risk in humans, although a cause-effect relationship is not clearly established (Schwartz et al. 2015). While mature BMAds generally induce hematopoietic stem cell quiescence in human and mice, BMAd precursors and their adiponectin-



expressing immature counterparts support hematopoietic expansion in vitro and in vivo (Zhou et al. 2017; Mattiucci et al. 2018; Naveiras et al. 2009; Ambrosi et al. 2017; Spindler et al. 2014; Ding et al. 2012; Ding and Morrison, 2013; Méndez-Ferrer, 2010; Nakamura et al., 2017). In mouse models and patients suffering acute BM failure or receiving chemo- or radiotherapy, a rapid and massive adipocytic infiltration of the BM takes place (red-to-yellow transition). Following the treatment with intensive chemotherapy, sometimes followed by hematopoietic stem cell transplantation, hematopoietic recovery ensues when BMAd recede and functional hematopoiesis is restored (yellow-to-red transition). In the clinic, hematopoietic activity is assessed by pathologists' scoring of BM cellularity in trephine bone biopsies of the iliac crest, and is functionally correlated with circulating blood cell counts. In vivo, contrast-enhanced (CE) osmium tetroxide (OsO<sub>4</sub>) lipid staining coupled to micro-computerized tomography ( $\mu$ CT) is used in rodents, while magnetic resonance imaging (MRI) fat-to-water ratio is used in humans as Gold Standard for quantification of marrow adiposity in the research setting. However, although highly informative, especially on higher resolution such as nano-CT, some labs may not have access to this method due to the high cost and toxicity of sample preparation. Accessibility to CE micro/nanoCT and/or MRI expertise can be, thus, limited outside of clinical laboratories or specific research settings,

We set out to develop a tool which could provide quantitative information on BMA with means accessible to all laboratories. Histological information obtained from hematoxylin-and-eosin (H&E) stained paraffin sections has long been the standard method to provide information on the architecture of biological samples. While the bone/marrow is a particularly difficult organ to work with, in part due to the soft hard tissue that are juxtaposed to one another, the overall analysis of its multiple components (bone, blood, adipocytes) provides important information to understand its physiopathology. Available histomorphometric analysis programs usually specialize in detecting individual components, and either require targeted staining protocols to detect specific components within the bone fraction, or use less adapted tools from the extramedullary adipose field to quantify the BMAd fraction (Radzilo et al. 2010; Keune et al., 2017; Iwaniec et al. 2013; Beekman et al. 2017; Styner et al., 2017; Costa et al., 2019; Syed et al., 2008; Lee et al., 2018; Devlin et al., 2010; Bornstein et al., 2017; Wessling-Perry et al., 2017; Yang et al., 2018; Li et al., 2016). In order to reduce inter-observer variability and to quantify sections of entire bones rather than representative fields of view, automation and standardization of methods are key. We have developed a semi-automated digital pathology ImageJ/Fiji plugin compatible with QuPath, named MarrowQuant, which subdivides and quantifies the total marrow area (Ma.Ar) in H&E stained, paraffin-embedded mid sections of mouse bones. The plugin subclassifies Ma.Ar into four actively detected compartments: bone, the hematopoietic, the adipocytic, and the interstitial/microvascular compartments, as well as an "undetected" area, when present. Then, MarrowQuant provides upon segmentation a BM Ad.Ar and size distribution for individual adipocytes, both in the context of BMAd and of extramedullary adipocytes. MarrowQuant thus provides absolute and relative areas for discrete BM compartments, thus calculating the hematopoietic cellularity and adiposity on H&E stained paraffin sections from murine whole-bones sections and, preliminarily, from human bone trephine biopsies. Additionally, the stand-alone AdipoQuant plugin quantifies relative number and performs adipocyte ghost size fragmentation on H&E-stained extramedullary adipose tissue.

Our software is thus complementary to other available plugins in that, together with more classically reported values for individual adipocytes or bone components, it provides quantification of hematopoietic cellularity while providing overall architectural segmentation of the BM space. We predict

## Chapter 3 | Quantitative imaging of the bone marrow

MarrowQuant will be a valuable addition to the rapidly evolving Digital Pathology field for use in a fundamental or, possibly, clinical research setting.

## Results

### Digital plugin

Based on a combination of color and texture of whole-bone H&E stained paraffin-sections as compared to background, *MarrowQuant* performs the segmentation and area quantification of four actively detected compartments in bone sections (i) the cortical and trabecular bone, (ii) the nucleated/hematopoietic cells, (iii) the BM adiposity, based on adipocyte ghost detection, and (iv) the interstitium/microvasculature, which recognizes both red blood cells and the eosinophilic protein or serous infiltrate that fills the remaining marrow space. If present, areas within the marrow space that are not recognized as any of the above will be categorized and shown as “Undetected area”. The total marrow area (see “Image processing logic” for definitions) is then used as denominator to calculate the percentage of each of the detected areas. From the adipocyte ghost segmentation, *MarrowQuant* additionally approximates the adipocyte count and size distribution. This function can be also applied to extramedullary adipose tissue sections with the stand-alone *AdipoQuant* script that runs directly through Fiji. The *MarrowQuant* plugin for bone sections operates through QuPath using Fiji as an extension, thus allowing the user to work with a more intuitive interface.

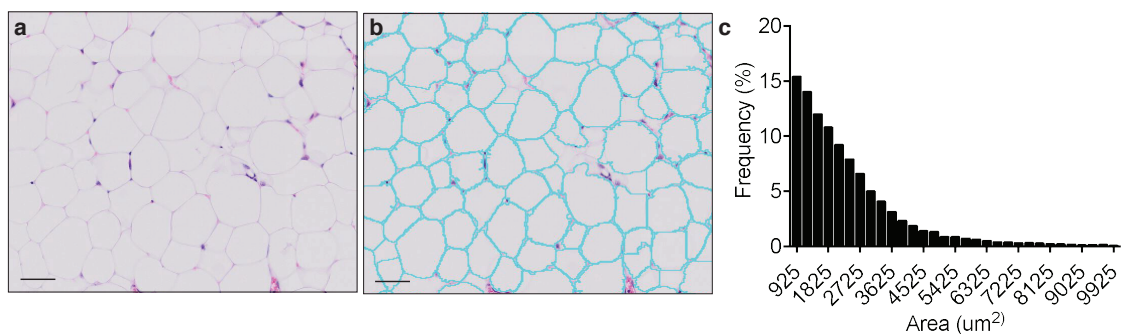
#### *Image processing logic*

Image files from total slide scans acquired at 20x magnification (VSI format or extracted TIFF files) are directly loaded into QuPath or opened with ImageJ for processing. Firstly, and prior to image processing, the user must manually identify the region of interest (ROI) to be analyzed, denoted as “Tissue Boundaries”. The magnetic wand tool in QuPath greatly simplifies this step. The user may also classify at this step regions that should be excluded from processing as “Artefacts”. In our dataset, we excluded at this step fixation artefacts which are common upon retraction of the marrow tissue from the endosteum. We also systematically excluded the retraction artefact that creates a central vein lumen. Secondly, a representative small area within the Tissue Boundaries must be defined as “Background” and will serve as a reference background correction factor for the whole ROI. These regions are selected manually by the user with built-in drawing tools in QuPath and assigned the corresponding annotation class. Preset parameters for adipocyte ghost circularity, roundness, and size are defined, but may be changed by the user depending on their application (e.g. tissues of different origin).

#### Extramedullary adipocyte quantification with AdipoQuant

As suggested by the opposing effects of adipocyte hyperplasia and adipocyte hypertrophy, the measurement of adipocyte size and number has become relevant in the context of multiple patho/physiological conditions (Shao et al., 2018; Lu et al., 2018). We thus developed AdipoCount to provide the adipocyte detection function as a stand-alone plugin which detects the total area covered by adipocyte ghosts and identifies individual adipocyte ghosts through recognition of the remaining

membranes, providing a fragmentation size distribution count which can be applied to extramedullary tissues (Figure 3.1). Of note, adipocytes can only be identified as lipid ghosts in H&E images, as the lipid content in the vacuoles is dissolved on the alcohols used for the processing. Changes in relative adipocyte size of a whole adipose tissue may be thus quantified with the *AdipoCount* script directly in Fiji, without the need to install QuPath for the full *MarrowQuant* plugin. The user must manually outline “Tissue Boundaries”, unwanted “Artifacts”, and the “Background” as described above. Not drawing any “Tissue Boundaries” will result in the plugin analyzing the entire image. A .txt file is generated upon processing which lists the adipocyte ghost fragmentation count and size. The tool relies on identification of intact, clearly H&E stained membranes for the most reliable generation of a watershed algorithm that fragments the mask. Therefore, a reliable size distribution is highly dependent on the quality of sample preparation (including staining, sectioning, and image acquisition).



**Figure 3.1** | Extramedullary adipocyte fragmentation as performed by *AdipoQuant*. **a** unprocessed image, **b** adipocyte ghost membrane detection and fragmentation (cyan), **c** adipocyte size fragmentation distribution. Scale bars are 50 $\mu$ m.

#### Bone marrow quantification with *MarrowQuant*

Following the initial manual steps performed by the user in setting “Tissue Boundaries”, excluding “Artifacts”, and defining the “Background” within the QuPath environment as described above, the full *MarrowQuant* plugin first identifies the bone compartment within the given “Tissue Boundaries”. The bone mask is then subtracted to generate the total area of interest that we define as the “Total Marrow Area”. Within the “Total Marrow Area”, nucleated cells are first detected to generate the “BM Hematopoietic Cellularity” mask. A watershed mask then detects and defines adipocyte ghosts by their intact cell membranes in the remaining area to generate the “BM Adiposity” mask. Finally, both the serous infiltrate and the red blood cells, located either within the microvasculature or dispersed across the marrow space, are detected based on their eosinophilic properties to define the “Interstitium/microvasculature” mask. The remaining area within the “Total Marrow Area”, if any, is then quantified as “Undetected Area”. The five masks are mutually exclusive in the priority order specified above. Thus, *MarrowQuant* segments the marrow space to provide an output of four compartments, plus the remaining undetected area when applicable, and after excluding the “Bone” mask uses the “Total Marrow Area” as denominator to calculate the “percent BM Hematopoietic Cellularity”, as well as the “percent BM Adiposity”. Derived parameters are then the adipocyte size fragmentation distribution, and the ratio of hematopoietic area over the hematopoietic and adipocytic areas combined. A mask output for the four defined compartments overlaid on the original image (Figure 3.2) lets the user confirm the results.

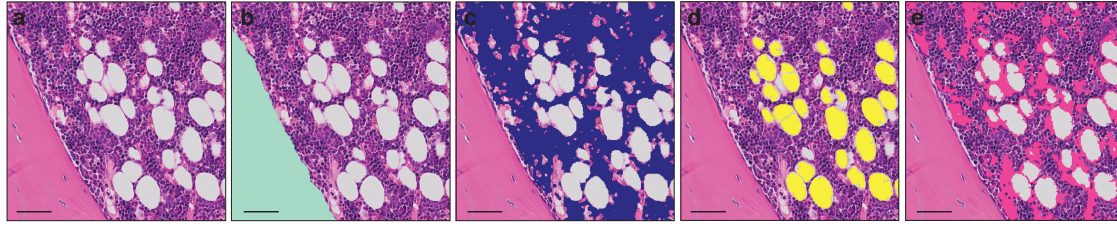


**Figure 3.2** | Masks of bone marrow compartment areas detected by MarrowQuant. **a** Unprocessed H&E image, **b** bone detection (green), **c** nucleated cell detection (violet), **d** adipocyte ghost detection (yellow), **e** interstitium and microvasculature (pink). Scale bars are 50 $\mu$ m.

### Comparison with gold standards

MicroCT is an established technique used to quantify changes in bone mineral density and bone architecture. It is now widely used in the field of BM adiposity for lipid detection. *Ex vivo* CT imaging of the native bone when it is combined with a second CT acquisition after bone has been decalcified and stained with the highly lipophilic dye OsO<sub>4</sub>. This procedure is usually referred to as OsO<sub>4</sub> contrast enhanced microCT or OsO<sub>4</sub>-CE- $\mu$ CT. We thus compared the volumetric assessment of lipid content via OsO<sub>4</sub>-CE- $\mu$ CT in C57BL/6 murine long bones to the MarrowQuant two-dimensional assessment of BM adipocyte area in mid-bone sections (Figure 3a, 3b). Importantly, mid-bone sections were defined by a complete bone silhouette plus the presence of the distal marrow space in the mid-sagittal tibial sections, and the femoral head marrow space in mid-longitudinal sections of the femur. Quantification of contralateral bones (right versus left) with the two techniques over a range of percentage adiposity spanning from 0% – 64% indicates a high correlation ( $R^2=0.81$ ) despite the comparison of a volumetric with a two-dimensional assessment.

Hematopoietic cellularity, often simply referred to as marrow “cellularity”, is the assessment by trained pathologists of the percentage hematopoietic content within the marrow. This assessment is often complementary to molecular and cytogenetic techniques for establishing the diagnosis of certain hematological disorders characterized by either hypercellularity (e.g. myeloproliferative neoplasias) or hypocellularity (e.g. hypoplastic bone marrow failure syndromes), or to follow disease progression and response to treatment. A common example is the evaluation of leukemic response to treatment after myeloablative chemotherapy. Of note, in the clinical diagnostic setting, values for normal cellularity of standard trephine biopsies from the pelvic bone in humans are corrected for age such that normal, age-adjusted cellularity is described by the formula: 100% - age (years).

While studying a “training-set” of 79 images from murine marrow spanning pathologist evaluated cellularities of 0% to 100%, which was used to set up the MarrowQuant code, we noticed that pathologists seem to subconsciously exclude the vascular space to estimate cellularity. As our program presently does not distinguish between the interstitium and microvasculature, we propose two general calculations to estimate cellularity depending on the type of sample, and therefore the biological context. These two calculations can be presented as the equations below.

$$ratio = \frac{hematopoietic\ area}{(hematopoietic+adipocytic)\ area} \quad (\text{Equation 3.1})$$

$$percent = \frac{hematopoietic\ area}{total\ area\ of\ interest} \quad (\text{Equation 3.2})$$

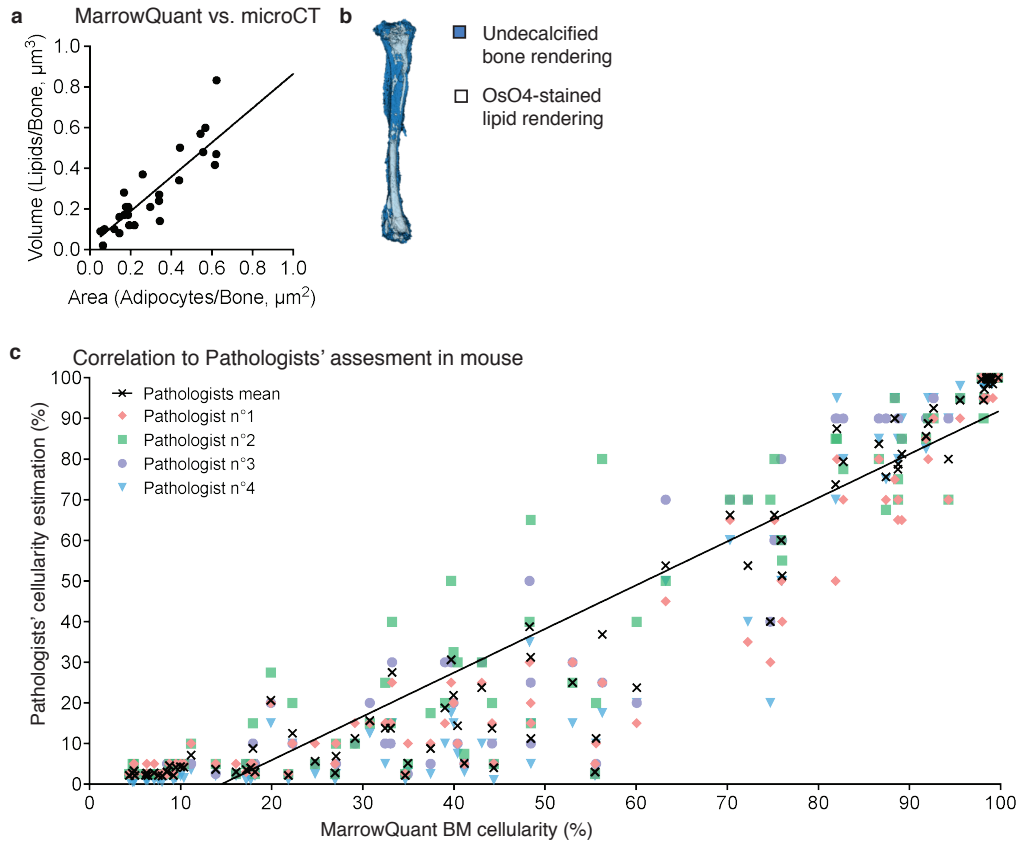


**Figure 3.3** | Correlation to Gold Standards. **a** MarrowQuant versus osmium-tetroxide contrast-enhanced micro-CT measurements ( $n=27$  bones,  $R^2=0.80$ ). **b** micro-CT rendering (white: osmium-tetroxide stained lipids; blue: undecalcified bone). **c** MarrowQuant nucleated cell percentage (Equation 3.2) versus Pathologists' cellularity assessment (Pathologists  $n=4$ , images  $n=79$ ,  $R^2=0.95$ ). microCT: micro-computed tomography.

We find that BM sections of high cellularity, where the BM cavity is mostly taken up by hematopoietic cells, or in sections of high adiposity where hematopoietic cells are interspersed within an adipocytic marrow, Equation 3.1 (that we define as a ratio of hematopoietic area to the combined hematopoietic and adipocytic area) best fits the pathologists' estimate of the hematopoietic content. This calculation excludes the area taken up by blood vessels centrally. In images of bones with intermediate states of adiposity, especially in cases of aplasia when lesions of blood vessels typically occur and their hemorrhagic components disperses within a large part of the marrow space, Equation 3.2 (a percentage hematopoietic area of the total area of interest) is applied to account for the hemorrhage and as such regarding the total marrow space.

MarrowQuant computes both equations and they have a high correlation with pathologists' evaluations when applying either calculation to the training-set of images. While Equation 3.1 ratio (Supplementary Figure A1.1a, Appendix A,  $R^2=0.91$ ) strongly agrees on the high cellularity cases, there is a discrepancy on mid- to low cellularity samples. Equation 3.2 becomes more robust in determining the % BM cellularity in these intermediate cellularity and hemorrhagic cases (Figure 3.3c,  $R^2=0.95$ ) as the calculation takes into account all components of the marrow space (Total Marrow Area as denominator). However,

## Chapter 3 | Quantitative imaging of the bone marrow

(as opposed to pathologists' evaluations) BM cellularity calculated with Equation 3.2 never reaches 100% precisely because it takes into account the entirety of the marrow space. In highly hematopoietic samples pathologists seem to make a subconscious switch to use Equation 3.1 instead. Despite these context-dependent choices on denominator for the pathologist Gold Standard assessment, MarrowQuant is robust and precise in delivering the percentage area of a compartment relative to the total marrow space (as a combination of all compartments). Reproducibility was assessed on a separate validation-set of images (n=59 Supplementary Figure A1.1b, Appendix A).

### Applications

We hypothesize that quantification of BM components as a first architectural assessment of BM regeneration may provide valuable information on homeostatic states and disease progression. The C57BL/6 mouse constitutes the most widely used animal model in experimental hematopoiesis. Its skeleton is often assumed to be homogeneously hematopoietic, whereas it has now been well-described that BMAd is interspersed within specific regions of the marrow (Naveiras et al. 2009; Scheller et al. 2015).

#### *Homeostasis*

Here we provide for the first time a quantitative BMA skeletal map of the homeostatic C57BL/6 eight week-old female mouse, which reveals a transition of low adiposity (high cellularity) red BM to high adiposity (low cellularity) yellow BM in the proximal to distal regions of the skeleton (Figure 3.4). This transition is most notable in the proximal-to-distal tibia, and the first caudal vertebrae of the tail (Supplementary Figure A1.2). The extremities of the skeleton such as the metatarsals or caudal tail vertebrae (e.g. Cd5,  $62\pm6\%$  adiposity) are highly adipocytic whereas the axial skeleton such as the sternum ( $1.0\pm0.5\%$  adiposity) and thoracic/lumbar vertebrae are almost entirely hematopoietic. These gradients of red and yellow marrow have also been reported in human, where the adult skeleton is nearly completely adipocytic. Location-specific BM adiposity may be explained from the perspective of skeletal development, musculoskeletal forces, and temperature gradients (Tavassoli and Yoffey, 1983).

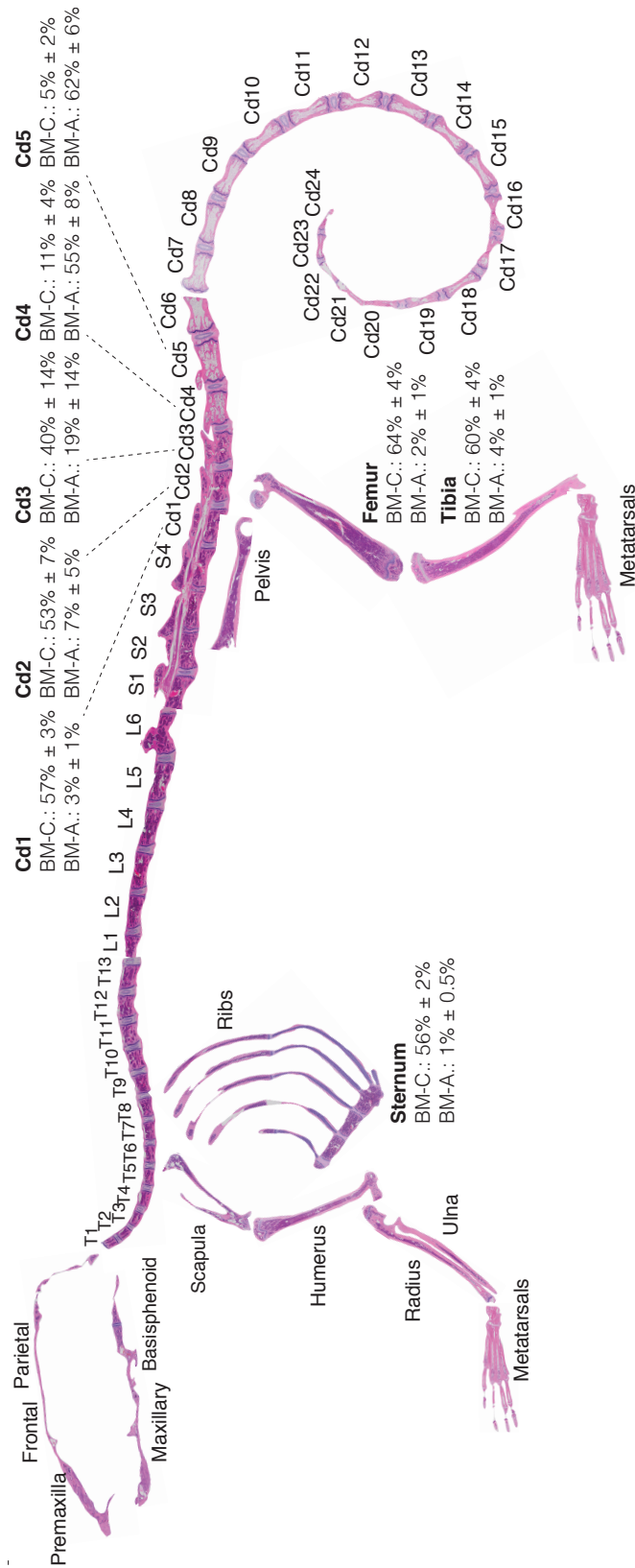


**Figure 3.4** | Red-to-yellow marrow transition in homeostasis. Eight-week old C57BL/6 reconstructed skeletal map locates the red-to-yellow marrow transition in the first caudal vertebrae and proximal-to-distal tibia approximately at the site of the fibular insertion. Percentages of MarrowQuant cellularity (BM-C) and adiposity (BM-A) are shown for select bones (femur n=6, tibia n=6, sternum n=10, tail n=6, all are mean  $\pm$  s.d. T: thoracic; L: lumbar; S: sacral; Cd: caudal (vertebrae)).



*Age*

BMA has been described to increase with age, which may in part be attributed to the terminal differentiation and depletion of BMAd precursors, and in part to the potential protective function assigned to mature BMAds of surrounding cells such as HSCs. In C57BL/6 mice, significant differences in BM adiposity are seen between eight weeks and 18 months of age (Figure 3.5a, 3.5b). The femurs of juvenile mice at eight weeks of age contain relatively few BMAds ( $2 \pm 1\%$ ) that are mostly located at the distal site. With age, BMA in this region increases slightly to  $4 \pm 2\%$  adiposity ( $P=0.03$ ) and also appears in the proximal femur (Figure 3.5a, 3.5c). While the distal tibia already contains BMAds at an early age with  $4 \pm 1\%$  adiposity at eight weeks old, BMA expands further up the BM cavity, especially at the epiphysis of the proximal tibia to  $31 \pm 14\%$  ( $P=0.01$ ) at 18 months old (Figure 3.5b, 3.5d). BMAd size fragmentation distributions of the distal versus proximal tibia in homeostasis (eight week-old C57BL/6 females) shows the distribution shifted toward larger adipocyte size on the distal tibia (Figure 3.5e) as has been previously reported (Scheller et al., 2015). Aged mice (18 month-old C57B6 females) have a similar distribution of BMAd size fragmentation of the proximal and distal tibia with comparatively larger sizes in the proximal tibia with regard to the young animals (Figure 3.5f). Interestingly, other strains such as the C3H, with high bone mass, or NSG, that are prone to obesity, have higher BMA than the C57BL/6 strain.

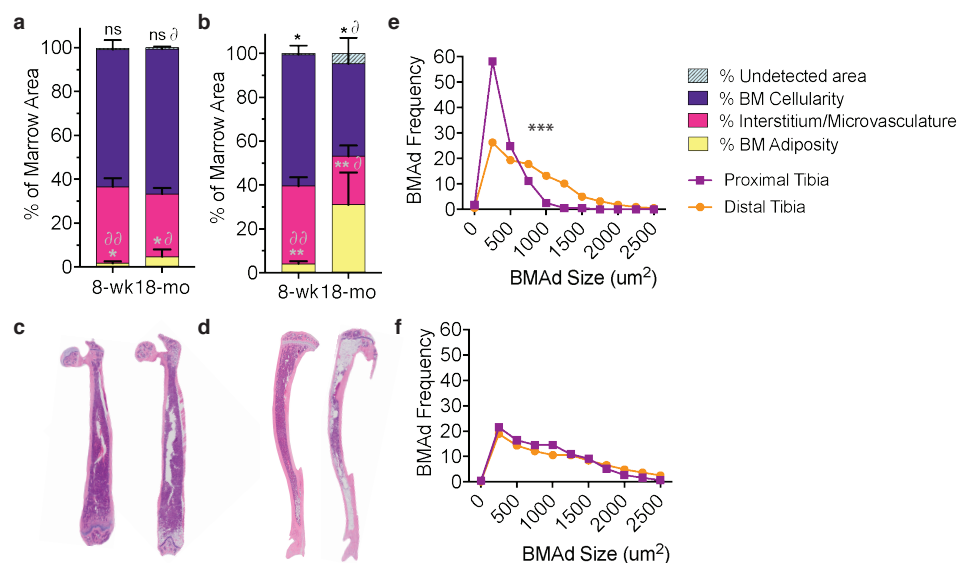


**Figure 3.5** | Red-to-yellow transition with aging. MarrowQuant results of (a) femurs (n=3) and (b) tibiae (n=3) from eight week-old and 18 month-old C57BL/6 females with representative images of femurs (c) and tibiae (d). Error bars represent mean  $\pm$  s.d. P-values indicated for purple hematopoietic compartment and yellow adipocytic compartment are \* $P<0.05$ , \*\* $P<0.01$ . e BMAd fragmentation distribution of the proximal (purple) and distal (orange) eight week-old tibia (n=10) versus (f) the 18 month-old tibia (n=3). BMAd: bone marrow adipocyte.

*Stress hematopoiesis*

In pathophysiological circumstances such as in osteoporosis, anorexia, or obesity, the marrow becomes infiltrated with adipocytes. Particularly in stress hematopoiesis such as the aplasia associated to hematopoietic failure, the plasticity of the marrow becomes very apparent. In the timespan of several weeks, the marrow undergoes a rapid red-to-yellow conversion. To overcome malignant hematopoiesis,



the BM is ablated with radio- or chemotherapy followed by BM transplantation. In our lethal irradiation model, the marrow initially becomes necrotic and highly hemorrhagic due to the breakage of the sinusoidal wall (day 4-10 post-transplant) and release of red blood cells (RBCs) and serous infiltrate. During this time, circulating white blood cells and platelets are reduced 10-fold (data unpublished). Shortly thereafter BMAds begin to occupy the marrow space such that the BM reaches peak adiposity at day 15-20 post-transplant (Figure 3.6). With revascularization, the new hematopoietic system starts to recover around day 25 post-transplant with circulating blood levels exiting severe thrombo- and neutropenia ( $<200$  cells/ $\mu$ l and  $<0.5$  cells/ $\mu$ l respectively). Over the next several weeks, blood counts increase and eventually return to normal levels of functional hematopoiesis (Supplementary Figure A1.3). Importantly, the overall peak of aplasia and time of recovery in this model closely resembles that observed in patients undergoing HSC transplantation (Schmitz et al., 2002; Dominietto et al., 2002).

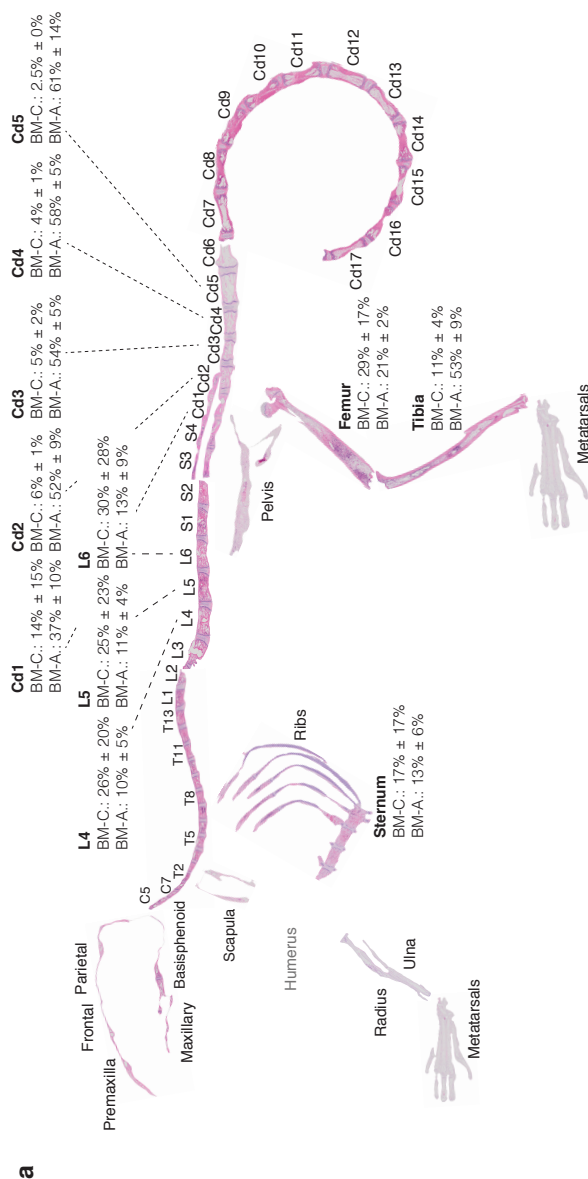


**Figure 3.6** | Red-to-yellow-to-red transition in bone marrow aplasia and hematopoietic recovery. **a** Skeletal map of an eight-week old C57Bl/6 female mouse 17 days post-lethal irradiation and total BM transplantation. Percentages of MarrowQuant cellularity and adiposity is shown for select bones (femur, n=3; tibia, n=10; sternum, n=3; tail, n=4, all error bars represent mean  $\pm$  s.d).

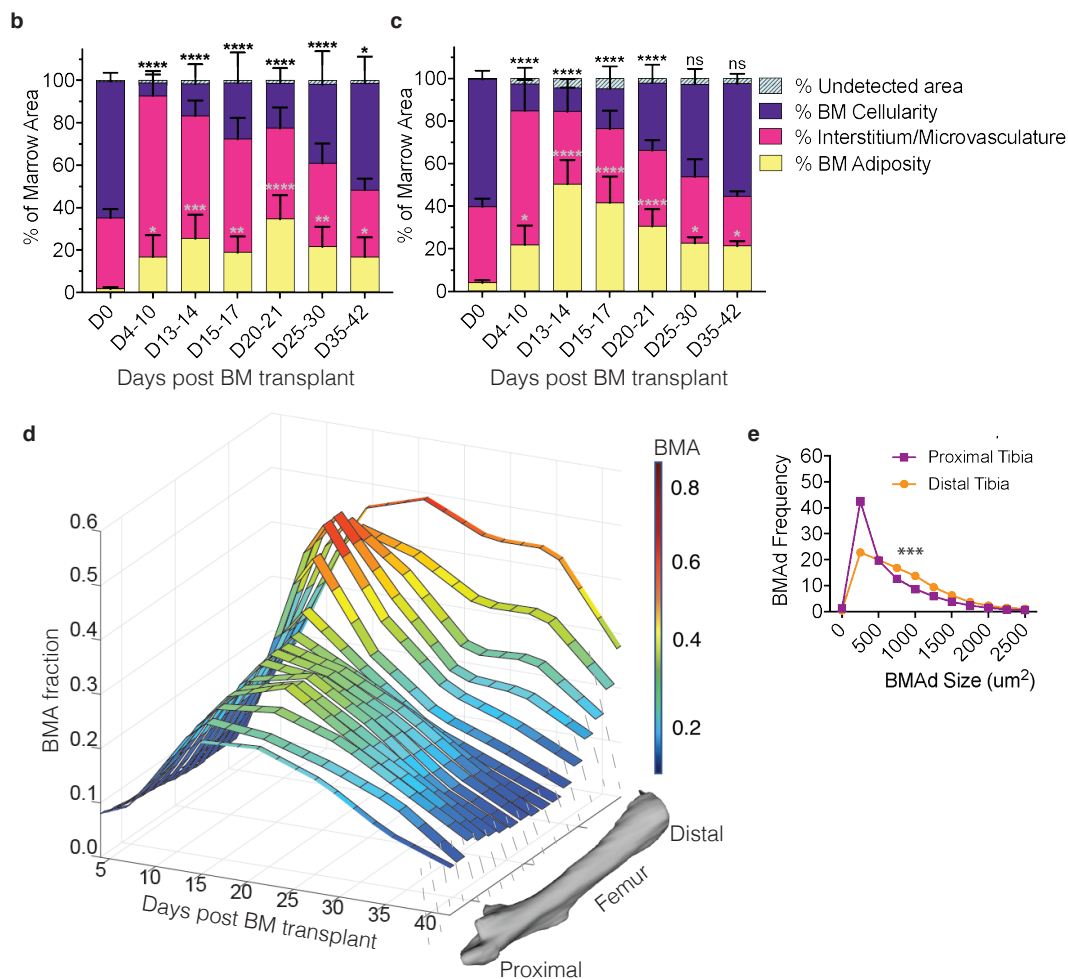


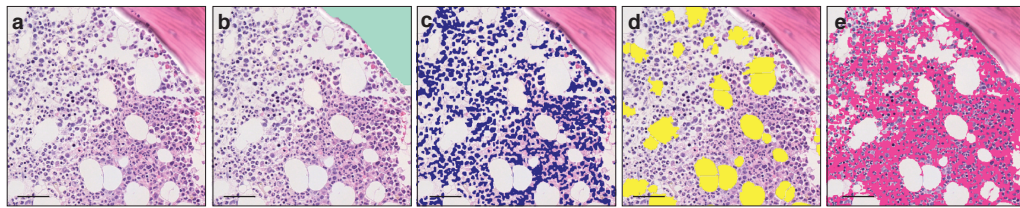
**Figure 3.6** | Red-to-yellow-to-red transition in bone marrow aplasia and hematopoietic recovery. MarrowQuant results for quantifications of (b) femurs and (c) tibiae in hematopoietic recovery. d changes in BMA fraction measured by MRI after lethal irradiation and total BM transplant as a time-course of recovery in the whole femur *in vivo*. e BMAd size fragmentation distribution in the proximal and distal tibia at peak of aplasia on days 17-20 from MarrowQuant measurements extracted from (c),  $n=10$ . All error bars represent mean  $\pm$  s.d. BM: bone marrow; BMA: bone marrow adiposity; BMAd: bone marrow adipocyte; MRI: magnetic resonance imaging.

Examination of the C57BL/6 skeleton at murine peak of aplasia shows that myeloablation renders the entire skeleton of the C57BL/6 eight week-old female mouse non-hematopoietic and highly adipocytic (Figure 3.6a). Changes in BMAd size fragmentation of lethally irradiated mice as compared to homeostatic C57BL/6 eight week-old females, indicates a shift toward more and larger BMAds in the proximal tibia (Figure 3.5e and 3.6e). The increase in number and size signifies hypertrophy and hyperplasia of the labile BMAds at the peak of aplasia putatively originating from a differentiation of skeletal stromal/stem cells or pre-BMAds. However, a small change in size fragmentation of the stable BMAds in the distal tibia suggests that these could also be undergoing regulation. A similar red-to-yellow-to-red conversion occurs in the femur during the time of aplasia. Just as with CE- $\mu$ CT in homeostasis, we set to validate these findings with MRI as an available tool for Gold Standard measurements of BMA. This is to our knowledge the first BMA quantification performed in murine limb

bones, which was possible through access to a 9.4 Tesla magnet for small animal imaging. We chose MRI *in vivo* imaging as an alternative to *ex vivo* imaging because repetitive imaging allows for a very significant reduction on the number of animals required to study the kinetics of marrow recovery, as compared to the *ex vivo* terminal experiments. MRI analysis validated the time course of marrow recovery in the femurs of mice undergoing lethal irradiation followed by HSC transplantation, as compared to *MarrowQuant* quantification of full bone mid-longitudinal sections (Figure 3.6d). Additionally, MRI analysis could also reveal that the proximal femur appears to recover more rapidly than the distal portion, which already contains some BMAd during homeostasis (stable/constitutive BMAd). In conclusion, volumetric measurements by MRI show a progression of fat signal that corresponds to the bidimensional quantification of adipocyte ghosts observed on histology with one of the most commonly used techniques to estimate fat content of a tissue (Glover, 1991).

### Human samples

*MarrowQuant* has been developed for quantification of mouse bone H&E stained paraffin sections and is also able to detect BM compartments in human trephine biopsies (Figure 3.7). Due to the different nature of human biopsies compared to mouse samples, several parameters of the plugin must still be optimized to obtain accurate and reliable measurements.



Diagnosis: Acute myeloid leukemia with macrophage activation syndrome

**Figure 3.7** | Application in human samples. a MarrowQuant detects BM compartments in human trephine biopsies that complements disease state and pathologists' diagnosis. Scale bars are 50µm.

While samples analyzed from mice have the entire bone encompassing the marrow still intact, trephine biopsies although similar in size (roughly 2cm long and 5mm in diameter) also have trabecular bone but not the cortical bone encompassing the marrow. Cells are larger in general thus presenting a different texture to stained mouse sections and may also present with a larger degree of serous infiltrate that is not detectable with the current version of *MarrowQuant*. Initial correlations, however indicate promising results (pathologists n=2, images n=37,  $R^2=0.93$ , data not shown).

## Conclusion

While standard practices of evaluating BM cellularity in the field of hematology have existed for many years, the field of bone marrow adiposity is newly emerging and thus methods of quantification are currently being defined. Classical methods such as histomorphometry reveal abundant information about a specimen but automatization of not only sample preparation but also quantification is required to

## Chapter 3 | Quantitative imaging of the bone marrow

increase accuracy, comparability, and reproducibility of results. This is rapidly developing in clinical and experimental pathophysiology with image-analysis programs emerging for quantification and detection of specific cell types related to disease progression. Classical histomorphometry in combination with fluorescent staining, has the possibility to reveal as much information of cells in highly multiplexed images as conventional flow cytometry analyses. Eventually such tools may supplement and become routinely integrated in current diagnostics.

### General and hematopoietic detection

*MarronQuant* relies on the user's definition of a region of interest and artifacts that may arise from sample processing (such as fixation retractions). High-quality stained sections provide best results as the tool relies on intact adipocyte membranes and an even staining coloration for quantification. Image acquisition is also an important initial aspect of preparation as the tool relies on background identification, and therefore stitched images should not show a gradient that would produce an uneven shade of the background and influence subsequent processing steps. Despite these measures that must be accounted for on setup, the automation of image quantification with *MarronQuant* means that numerous samples can be batch processed. While the automated quantification takes up to four times longer than a pathologists' assessment of BM cellularity (four minutes versus one minute per image), it provides information on several BM compartments at once that the human eye may not be able to estimate in parallel. Apart from initial setup, human biases are eliminated and area values are given in absolute terms. Thus, *MarronQuant* does not provide a regional gradient of cellularity or adiposity within the whole organ (such as for example in the case of hematopoietic recovery post-aplasia with first loci of hematopoiesis appearing), nor does it provide a fine evaluation of what the cellularity means like a cytology report would provide. Despite discordances in mid-cellularity regions, *MarronQuant* cellularity calculation falls within the range of pathologists' estimations. As such, the potential value to the clinic lies in the standardization of evaluations, and automation for research laboratories is also pertinent.

### *Adipocyte detection*

In our hands, the adipocyte-only detection function of *AdipoQuant* is somewhat more convenient to apply on extramedullary tissue than other current open-source softwares developed specifically for white adipose tissue. Although the number of adipocytes obtained are similar, the area identified by *MarronQuant* seems truer to size in that the fragmentation of the adipocytes lies clearly on the membranes and not within the adipocyte itself when compared to Adiposoftware. Identifying an area of interest before quantification also allows the user to quantify whole tissue sections and eliminating regions that may be irrelevant for a particular analysis (such as vasculature) and therefore obtain a result without additional fragmentations of areas that do not consist of adipocytes. One caveat is that adipocyte size fragmentation is a comparative measure and *MarronQuant* may hyper- or hypo-fragment adipocytes where membranes are not clear when Adiposoftware more frequently does not. This goes in hand with the detection of false positive adipocytes (Supplementary Figure A1.4, Appendix A), however, this does not contribute significantly to the overall size fragmentation distribution of the adipocytic area (data not shown). When membranes are intact, as is more often the case with extramedullary adipose tissue due to the nature of the samples, it is a negligible factor. However, for BM sections this will be largely dependent on the quality of the sample and absolute values must be interpreted with caution. Thus, while Adiposoftware may give a more accurate total adipocyte count, *MarronQuant* will be truer to the total adipocytic area and

distribution. Importantly, histological tissue sectioning provides only a segmentation and therefore an estimate of adipocyte size but is comparable to whole volumetric measurements with other methods.

### *Inherent errors*

While megakaryocytes may contribute to bone area due to their large cytoplasm and similar staining color, this does not affect the total bone area significantly (data not shown). Similarly, osteoblasts or bone lining cells that have a similar color and texture to the nucleated cells that make up the hematopoietic mask, are included in the hematopoietic area (Supplementary Figure A1.4, Appendix A). If this has importance for the user, the cells lining the endosteum may be excluded from the region of interest (or included as artifacts) initially. The interstitium/microvasculature is well detected by MarrowQuant but may be slightly problematic in specific cases such as on hemorrhage with leakage of vessels if most red blood cells and/or serous infiltrate does not remain to fill the space upon tissue fixation. In these cases empty spaces must be taken as artefacts in order for them not to be counted as adipocytes, thus changing the total area of interest. Depending on the section of a bone in general, it may be cut through the central sinusoid that then fills a large proportion of the marrow cavity and thereby also influences the total area of interest (that includes all compartments). These are examples of issues that the user should be familiar with and aware of when presenting results.

### *Human application*

The most important difference between human and mouse samples that affect *MarrowQuant* results lies in the fact that hematopoietic nuclei are less densely packed in human tissue. The cytosolic space of mouse hematopoietic cells is relatively small in histological sections and therefore not an issue for *MarrowQuant* that currently only recognizes the nuclei as the hematopoietic compartment. In human samples, where the cytosolic space is comparatively larger, it will be necessary to include the cytosolic space when trying to assess the cellularity. This raises new technical questions outside of the scope of this paper on how to segment the hematopoietic compartment in human samples to overcome this issue. Other less problematic processing issues come from visible color differences between mouse and human samples. The duller stain of the human samples has consequences on the efficiency for the thresholding methods used in the code and can sometimes result in mis-segmentation. The observed color difference may be due to the nature of the samples, the preparation and staining protocols, and subsequent storage of slides before image acquisition. The method for decalcification of the bone is different which may influence bone staining. Additionally, human slides were imaged weeks after staining whereas mouse image were scanned days after staining. These points could explain the observed color alteration in human samples. Thus, technical adaptations are still needed for an improved quantification of human BM.

## Outlook

The semi-automated digital pathology tool for QuPath or ImageJ, quantifies four detectable BM compartments (adipocytic, hematopoietic, bone, interstitium/microvasculature) and the remaining undetected area, if any, on H&E stained paraffin sections of whole intact murine bones. H&E is one of the most common and routinely performed histological stains. While paraffin sections present only one slice of the whole organ, in our experimental setup with bones of C57BL/6 mice, the quantification correlates highly with expert pathologist evaluations in H&E and volumetric quantifications of the contralateral whole bone by microCT combined with osmium-tetroxide staining. Moreover, we were able

## Chapter 3 | Quantitative imaging of the bone marrow

to apply the non-invasive technique of MRI to follow changes in fat signal on hematopoietic recovery that corresponds to histological assessment with MarrowQuant and blood recovery. In addition, MarrowQuant provides a size fragmentation distribution of adipocytes and thus may additionally be applied to H&E sections of extramedullary white (omental or inguinal) adipose tissue.

Future iterations of the tool applied to human samples will incorporate machine learning methods to overcome the hurdles of the distinct morphology of human tissue and detection of specific cells (e.g. macrophages and megakaryocytes with large cytoplasm, immune cells). While we also aspire to separate the extravascular marrow space (interstitium) from the vascular space (microvasculature), our technology does not currently allow for that. Close collaboration with clinical pathologists will help to further develop this tool for human application.

## Methods

### Mice

Eight-week old C57BL/6J were purchased from Charles River Laboratories International and maintained at the Center for Studying Living System (CAV) at the EPFL in microisolator cages. Mice were provided continuously with sterile food and water ad libitum, and bedding. In vivo procedures were carried out in accordance with the Swiss law after approval from the local authorities (Service Vétérinaire de l'Etat de Vaud) and experiments were designed according to the ARRIVE guidelines.

### Human samples

Images of human bone marrow H&E stained paraffin sections from diagnostic samples of patients undergoing treatment for acute myeloid leukemia were received for analysis as blinded images from the Centre Hospitalier Universitaire Vaudois (CHUV). The trephine biopsies were processed for standard pathology diagnosis and H&E stained paraffin sections were scanned using a 20x objective. This work was performed under the approval of the local ethical authorities (CER-VD).

### Bone marrow transplantation

Eight week-old female C57BL/6 mice were lethally irradiated with a total 850 rad dose in a X-ray radiator (RS-2000, RAD SOURCE) 24 hours before transplant. The dose was split in two doses of 425 rads separated by a 4-hour interval. Total bone marrow cells were isolated from crushed bone marrow of eight week-old female C57BL/6J donor mice in phosphate buffered saline (PBS, Life Technologies 10010056) solution with 1mM EDTA (Thermo Fisher Scientific 15575020). Total BM cells for transplantations by S.R.S were obtained by flushing instead of crushing. Red blood cells were removed by incubation with ice-cold lysis buffer (BioLegend) for 30 seconds. Samples were filtered through a 70µm cell strainer (Sigma Aldrich CLS431751) and centrifuged at 300g for 10 minutes at 4°C. Recipient mice were injected with 125,000 donor cells via tail-vein injection. For at least two weeks after lethal

irradiation mice were treated with paracetamol and antibiotics in the form of 30mg of Enrofloxacin (300µl of Baytril 10% solution, 100mg/ml, Bayer) and 5mg of Amoxicillin (100µl of Amoxi-Mepha 200mg/4ml, Mepha Pharma AG) as well as 500mg of Paracetamol (Dafalgan®) to 250ml of drinking water protected from light. Peripheral blood was collected to assess blood recovery (blood volume 50µl) and analyzed by standard veterinarian blood cell counter (ABC™). Mice were sacrificed by CO<sub>2</sub> inhalation.

### Magnetic Resonance Imaging

All experiments were conducted on a 9.4T/26cm horizontal magnet (Agilent/Varian) using a home-built quadrature transceiver of 20mm diameter loops (Figure A3.1, Supplementary 3, Appendix A). Animals were anesthetized with 1.5% of isoflurane, respiration and temperature were monitored during the whole study. Animals were placed on their side and the leg was immobilized in a contracted position. A triple point Dixon acquisition (Glover, 1991) was performed using a spin-echo based sequence ( $t_e=9\text{ms}$ ,  $t_r=1.5\text{s}$ ) with ten coronal slices of 0.8 mm on a FOV 25x20 mm<sup>2</sup> (acq. Matrix 192x128). Dixon's technique in combination with a spin-echo based sequence minimized signal loss of the marrow due to bone magnetic susceptibility. Three acquisitions were performed with the echo acquisition shifted 0, 0.4 and 0.8 ms corresponding to the fat-water chemical shift of 1250Hz at 9.4T. Images were reconstructed using a homebuilt Matlab script to extract water and fat maps. Phase unwrapping was performed using a toolbox from Matlab file exchange (Ghiglia and Pritt, 1998). At the end of the MR acquisitions, animals were sacrificed, tibia and femur were dissected to conduct histology and validate MR Dixon acquisitions.

### Histology

Bones were extracted, and cleaned of soft tissue. Long bones and cranium were placed loosely in histology cassettes while spine (including tail) and paws were placed in histology cassettes (Simport M505-11) with sponges (Simport M476-1). Bones were fixed for 24 hours at room temperature in 10% neutral buffered formalin (VWR 11699404), then rinsed three times with phosphate buffered saline (1x PBS) solution. Bones were decalcified in 20% sodium-citrate (Sigma Aldrich 71405) and formic acid (ROTH 4724.3) solution (v/v) for 30-36h or in 0.4M EDTA pH 7.4 (Sigma Aldrich 607-429-00-8) for two weeks (solution changed every three days) at room temperature. Bones were washed three times in PBS or under running tap water for two hours before transferring to 70% ethanol (Reactolab 96170). The tissues were submitted for stepwise dehydration and embedded in paraffin blocks for sectioning at 3-4µm thickness with a rotary microtome (RM, Leica microsystems). After floating on a water bath to flatten, sections were mounted on glass slides (Superfrost+ slides, Menzel gläser). Paraffin sections were stained with Hematoxylin and eosine (H&E) using the Tissue-Tek Prisma automate (Sakura) and permanently mounted using the Tissue-Tek glas G2-coverslipper (Sakura) to assess morphology.

### Image acquisition and processing

Whole-slide images were acquired with an automated slide scanner (Olympus VS120-SL) at 20x magnification with focus points along the total area of interest or using the in-situ focus mode using the accompanying software (Olympus VS-ASW L100 2.9). VSI files obtained from scanning were directly loaded into QuPath for analysis on Windows or Mac operating systems. Extracted TIFF files were also used for analysis. Parameters are pre-set but adjustable by the user if deemed necessary (see tutorial). The software workflow follows basic morphological operations, color deconvolutions, thresholding,

## Chapter 3 | Quantitative imaging of the bone marrow

smoothing operations and watershed as annotated in the code provided as open source and described in the technical guidelines. When accounting for pre-processing steps such as the drawing of the regions of interests as well as the segmentation process, it typically takes around ten minutes in order to obtain MarrowQuant outputs for an image with a sample of a mouse bone. Technical details are annotated in the code and details on download, installation and use of the plugin with the Fiji and QuPath softwares are given in the tutorial (Supplementary 2, Appendix B).

### MicroCT

Fixed bones were scanned for reconstruction of undecalcified bone. Samples were placed in an Eppendorf tube with PBS and scanned using a Quantum X-Ray Micro-CT Scanner (Perkin Elmer Quantum) at 90kV, 160 $\mu$ A, CT 160, live 80 and field of view (voxel size) 20 $\mu$ m<sup>2</sup> at setting Fine for two minutes per sample. A hydroxyapatite phantom was included as control. The software suite provided by the manufacturer was used for image acquisition and reconstruction. Bones were then processed further with formic acid decalcification and osmium tetroxide staining.

#### *Osmium Tetroxide Staining*

Decalcified bones were rinsed in distilled water. Osmium tetroxide solution was prepared fresh (1% osmium tetroxide (Electron Microscopy Sciences 19110), 2.5% dichromate potassium solution (VWR 1.04864.0500)) and samples stained in 20ml glass scintillation vials (Electron Microscopy Sciences 7632) in 2ml of solution at room temperature for 48 hours. Bones were washed with distilled water three times and transferred to Eppendorf tubes with distilled water for microCT acquisition as done previously. Quantifications were done on the Analyzer 10.0 software (Analyze Direct, Inc.).

#### Competing Interests Statement

The authors declare that the research was conducted in the absence of any commercial or financial relationships that could be construed as a potential conflict of interest.

#### Author Contributions

O.N. and J.T. conceived ideas, designed experiments, analyzed results and wrote the manuscript. J.T. performed all experiments and analyses unless otherwise stated. C.B. and O.B. designed the code. I.B., T.K., and O.B. edited the code to the final version. I.B. and F.S. performed histological quantifications. Pathologists B.B., R.S., V.N., L.D.V., and C.B. evaluated histological sections for hematopoietic cellularity and provided valuable feedback and discussions. N.K. performed MR imaging and analyses. D.N.T. contributed to microCT analysis and blood recovery curves. S.R.S., F.S., D.N.T. and V.C. contributed to specific transplants and histological mounting/analysis. E.L.S. provided slides and discussions on histology. O.N. initiated the project. All authors edited and reviewed the final manuscript.

#### Funding

O.N. and lab members were supported by the Machaon Foundation, the Dr. Henri Dubois-Ferrière Dinu Lipatti Leukemia Foundation, the Fondation Pierre Mercier pour la science, and Swiss National Science Foundation (SNF/SNSF) Professorship grants PP00P3\_144857 and PP00P3\_176990. N.K. was funded by the Leenards and Jeantet foundation.



### Acknowledgments

We thank members of the Center for the Study of Living Systems at EPFL for animal care, the EPFL Electron Microscopy Facility, namely Graham Knott and Stephanie Rosset for providing osmium and solution preparation, and the EPFL Phenogenomics Unit and E. Meylan for flexibility and assistance on microCT imaging. We thank the Center for Biomedical Imaging Animal veterinarians for their kind help during experiments. The histology data was performed at or with the help of the EPFL Histology Core Facility, notably Dr. Jessica Sordet-Dessimoz. We are grateful to Frédéric Schütz from the Swiss Institute of Bioinformatics for valuable statistical guidance, and to Teresa Didonna and Bart Deplancke for feedback on the beta version of AdipoQuant.



## **CHAPTER 4**

***In vitro* model of bone marrow adipocyte subtypes**



*This work is part of a manuscript in preparation, entitled*

## ***In vitro* model of bone marrow adipocyte subtypes with distinct lipid signatures at the single droplet level**

Josefine Tratwal<sup>1\*</sup>, Guillaume Falgayrac<sup>2\*</sup>, Alexandrine During<sup>2</sup>, Nicolas Bertheaume<sup>2</sup>, Jonathan Paz Montoya<sup>3</sup>, Naveed D. Tavakol<sup>1</sup>, Vasco Campos<sup>1</sup>, Pernille Yde Rainer<sup>4</sup>, Ludovic Duponchel<sup>5</sup>, Olaia Naveiras<sup>1,6</sup>

<sup>1</sup> Laboratory of Regenerative Hematopoiesis, Ecole Polytechnique Fédérale de Lausanne (EPFL), Lausanne, Switzerland

<sup>2</sup> PMOI, EA4490, EA-Physiopathologie des Maladies Osseuses Inflammatoires, Université de Lille, Université du Littoral Côte d'Opale, Lille, France

<sup>3</sup> Proteomics Core Facility, Ecole Polytechnique Fédérale de Lausanne (EPFL), Lausanne, Switzerland

<sup>4</sup> Laboratory of Systems Biology and Genetics, Ecole Polytechnique Fédérale de Lausanne (EPFL), Lausanne, Switzerland

<sup>5</sup> UMR 8516, Laboratoire de Spectrochimie Infrarouge et Raman, Ecole Polytechnique Universitaire de Lille, Lille, France

<sup>6</sup> Hematology Service, Departments of Oncology and Laboratory Medicine, Centre Hospitalier Universitaire Vaudois (CHUV), Lausanne, Switzerland

\* Equal author contribution.

Corresponding Author: Olaia Naveiras

## Preface

This chapter brings together biology and engineering in an example of what can come of a beautiful international collaboration. It started at a BMA kick-off meeting in 2017 where **Olaia Naveiras**, **Guillaume Penel**, and Guillaume Falgayrac discussed the possibility of applying Raman microspectroscopy to study the lipid composition of bone marrow adipocytes. It seemed to me at the time almost too simple to bear fruit. Of course, it was **Guillaume Falgayrac** from the *University of Lille* who would apply his technical expertise and diligence to analyze thousands of lipid droplets that made their way from Lausanne to Lille. At the same time a student landed in the lab, **Naveed Tavakol**, who would perform many of the differentiation protocols.

It was always interesting to discuss the project with Guillaume and to understand it from the engineer and biologist's perspective. It was through many Skype sessions that we were able to piece together the beginning of a manuscript. Along came **Alexandrine During** who would bridge the gap, willing to perform HPLC analysis on our samples. Early results were positive, encouraging us to perform RT-qPCR, for which **Aurélien Oggier** in our lab was an incredible help. **Vasco Campos** also lent his expertise for the co-culture assays and provided material for **Pernille Yde Rainer** who was understanding and kind enough to perform RNA-seq analysis days before a meeting.

The road has been long afterall, and for me it started in my early days at EPFL long before that initial meeting as I started collecting patient marrow aspirates, carefully isolating the oil fraction of the scarce bone marrow adipocytes. This tie to the hospital was encouraging and is what often motivates me. Fortunately, or unfortunately, the mouse model is a strong contender for experiments as human samples are relatively rare and precious. I was able to isolate oil from the distal tibia of mice and convince **Jonathan Paz Montoya** to perform mass spectrometric analysis on this and one human sample. Over the years I have scraped together any bone marrow adipocyte oil samples I could for subsequent lipid analysis.

**This chapter aims** to highlight differences in BM adipocytes on the population, single cell, and single droplet with regard to lipid composition and on the hematopoietic support capacity in culture.

## Introduction

Bone marrow adipocytes (BMAds) make up an intriguing adipose depot contained within the bone marrow cavity of vertebrate animals (Craft and Scheller 2017). While two subtypes of BMAds with distinct properties are known to exist, much about their nature remains elusive. The distal parts of the skeleton predominantly house the adipocytic or yellow marrow made up of the so-called stable or constitutive BMAds (cBMAds) that appear just around birth, while proximal locations of the skeleton contain the labile or regulated BMAds (rBMAds) interspersed within hematopoietic or red marrow (Kricun et al. 1985, Scheller et al. 2015). While rBMAds are smaller in size and respond readily to induction of BMA such as high fat diet caloric restriction and lipolytic stimuli including phenylhydrazine or beta3-adrenergic activation through environmental factors or pharmacologically, it is argued that cBMAds do not (Doucette et al. 2015; Scheller et al., 2016; Tencerova et al., 2018; Thouzeau et al., 1997; Cawthorn et al., 2014; Tavassoli et al., 1974; Scheller et al., 2015; Scheller et al., 2019), (Scheller et al. 2015; Scheller et al., 2019; Craft and Scheller 2017; Horowitz et al., 2017).

The international BMA community is adamantly working towards characterizing the different BMAds and their origin within the skeleton. While concrete definitions are being established and true BMAD classification markers are yet unidentified, the gold standard for classifying the two known types of BMAds is by the composition of their lipid content (Chapter 2; Tratwal et al., 2020). The first reports by Mehdi Tavassoli showed that the yellow marrow from the os calcis of rabbits was high in the unsaturated palmitoleic acid (16:1), whereas fatty acid composition of the red marrow of the vertebrae was richest in saturated palmitic acid (16:0). Congruently <sup>1</sup>H-MRS and gas chromatographic data from human subjects consistently showed that BMAT from sites of red marrow has highly saturated lipid content compared to the mostly unsaturated lipids detected at yellow marrow sites (Ren et al. 2008, Scheller et al. 2015). Primary cBMAds from rat tail vertebrae and distal tibia were likewise shown to contain a higher proportion of unsaturated fatty acids as measured by unsaturation ratio of 16:1n-7/16:0 and 18:1n-9/18:0, compared to the rBMAds isolated from lumbar vertebrae or femur plus proximal tibia (Scheller et al. 2015). From murine samples, it is considerably more challenging to obtain sufficient BMAT samples due to the size of the animal as well as the amount of BMAT present in the bones. To our knowledge, the lipid composition of murine BMAds has not been described to date. However, it seems there is a conservation of the differences in the fatty acid unsaturation ratio (16:1n-7/16:0) and saturation index (18:0/18:1n-9), at least from rat- to rabbit- to human, between BMAT of red and yellow marrow.

In a model of congenital generalized lipodystrophy (CGL) that is marked by partial or complete loss of adipose tissue *Ptrf*<sup>-/-</sup> mice have BMAT only in the tail vertebrae and very distal tibia with a loss of BMAds at- and proximal of the tibia-fibula junction (Hayashi et al. 2009, Liu et al. 2008, Ding et al. 2014, Scheller et al. 2015). This is accompanied by a small increase in cortical bone mineral content in adult male mice and a large increase in trabecular number and cortical bone mineral content in females (Scheller et al. 2015). *PTRF* encodes for cavin-1 which is a protein required for the formation of caveolae and formation

of caveolins (Thorn et al. 2003, Hill et al. 2008, Liu and Pilch et al. 2008). These results point toward differential regulation of lipid droplet (LD) formation in red and yellow marrow, but to what extent this is due to divergent transcriptional programs or part of a stabilization of the adipocytic differentiation program remains to be determined. Isolation of BM stroma for differentiation and analyses of BMAd *in vitro* to study these processes in mouse models is challenging due to the amount of material obtained from one bone (let alone the distal portion of the tibia alone). This is compounded by the fact that the defining surface markers that would aid in purification of BMAd progenitor populations from homeostatic mice are still not clearly defined or do not discriminate between the labile and stable BMAd (Ambrosi et al. 2017).

A promising alternative to primary cells for *in vitro* studies is the multipotent bone-marrow derived non-clonal OP9 stromal cell line (Gao et al. 2010, Naveiras, 2008). It is originally derived from the calvaria of newborn osteopetrotic mice ((C57BL/6xC3H)F<sub>2</sub>-op/op) deficient in macrophage colony-stimulating factor (M-CSF), useful for studies of hematopoietic cell development and differentiation that is sensitive to M-CSF (Nakano et al. 1994, Takakura et al. 1996). OP9 cells have been described as preadipocytes capable of readily differentiating to adipocytes, and express the transcriptional activators CCAAT/enhancer binding proteins (C/EBP)  $\alpha$  and  $\beta$ , together with the master regulator of adipocyte differentiation peroxisome proliferator activated receptor- $\gamma$  (PPAR $\gamma$ ), and perilipin (PLIN), a phosphoprotein associated with the surface of lipid droplets (Wollins et al. 2006). Thanks to their multipotency, hematopoietic support-, and adipocytic differentiation capacities, these cells are optimal for *in vitro* studies on BM adipogenesis. Due to their non-clonal nature and inherent heterogeneity, it would be of interest to study the differentiating OP9 cells at the single cell level. Established assays such as single-cell RNA sequencing provide the potential for powerful gene expression analysis (Tratwal et al., 2020). Caveats in this rapidly-evolving field are dominated by the importance of cell preparation, which is especially cumbersome with fragile lipid-filled adipocytes. More recently a high-throughput image quantification platform of adipocytic differentiation by lipid droplet accumulation has been developed requiring minimal handling to avoid perturbation of the culture (Campos et al., 2018). While not limited by end-point analysis or introduction of handling or preparation biases, this technique does not provide information on the molecular composition of the cells. Techniques capable of combining manipulation-free, label-free single-cell imaging with analysis of molecular composition are thus of great interest to the field of adipogenesis.

Raman microspectroscopy is a powerful technique attracting growing interest in a variety of scientific disciplines. The Raman effect originates from the inelastic or non-linear scattering of photons with vibrational energy gained by a molecule from the shift in energy of the incident photons, and thus can directly probe vibration states in molecules (Jones et al. 2019). This vibrational spectroscopic technique combines multiple advantages for the characterization of cells such as differentiated osteocytes and lipid accumulation in adipocytes or translocation of lipids within macrophages in culture (Ghali et al. 2015, Stiebing et al. 2017). It is a label-free method, non-invasive and does not require specific sample preparation, with a sub-cellular resolution on the scale of  $\sim 1\mu\text{m}$ . Raman microspectroscopy provides the molecular composition with spatial data, where standard methods provide bulk information (e.g. mass spectroscopic and chromatographic methods). Therefore, OP9 adipocytic differentiation in minimal or standard conditions, combined with lipid profiling by Raman microspectroscopy would make for a powerful tool to aid in the understanding of BM adipogenesis.



We set out to further characterize the OP9 stromal cells and OP9 differentiated adipocytes (whether spontaneously or through induction of the adipogenic differentiation program) by their gene expression and lipid profiles to draw a comparison with that currently known for primary BMAd. Additionally, to test the interaction with a hematopoietic component, we assessed the hematopoietic support of OP9 cells from these conditions in short-term co-cultures with hematopoietic stem and progenitor cells (HSPCs). We hypothesized that the OP9-derived adipocytes that develop upon simple serum induction may resemble labile/regulated BMAd in their lipid composition and hematopoietic support capacity, while OP9-derived adipocytes generated from full biochemical induction of the adipogenic differentiation program may better resemble stable/constitutive BMAd.

## Results

### Differentiating OP9 cells resemble primary BMAd

Mass-spectrometric analysis revealed similar lipid profiles for primary isolated murine and human BMAd from highly adipocytic regions of the marrow, with triacylglycerols (TAGs) as the most abundant lipid species (Figure 4.1). For human BMAd, primary oil samples were collected from human tibial plates as the floating layer during the first centrifugation steps for the preparation of bone fragments for clinical grafting (Figure 4.1a). For murine samples, distal tibiae were first carefully flushed and then centrifuged to obtain the oil sample by flotation (Figure 4.1b). Although similar lipid profiles are observed in the two species, the minor differences observed may be either species-specific or secondary to the isolation procedures. Obtaining high adiposity samples from mice for lipid profiling is thus possible and could be enhanced via induction of BMA through dietary modification, pharmacological administration, or secondary to chemotherapy. However, as discussed in Chapter 2, the sample size remains very small for subsequent analysis and cell-culture-based studies. Moreover, the BMAd isolated upon BMA induction may be inherently different to the constitutively present BMAd. For these reasons we set to develop alternative *in vitro* methods to test the relationship between BMAd lipid content and hematopoietic function.

To circumvent the challenges of handling and culturing primary BMAd (that are prone to bursting and rapidly de-differentiate in culture), we chose to work with the OP9 cell line (Gao et al. 2010) that readily differentiate to adipocytes in culture (Wolins et al. 2006) under minimal conditions (in the presence of serum) and may be induced by a classical adipocytic differentiation cocktail (containing insulin, dexamethasone, and IBMX). Upon 17 days in culture, both conditions contained a majority of differentiated adipocytes (Figure 4.2) with a significantly greater prevalence of Oil Red O staining of lipids in the induced condition ( $p < 0.01$ ) compared to baseline undifferentiated OP9 cells (Figure 4.2g). The spontaneous condition stained less with Oil Red O and the spontaneous OP9-adipocytes (sOP9 adipocytes) seemed to contain smaller lipid droplets than the induced OP9-adipocytes (iOP9-adipocytes) at day 17.

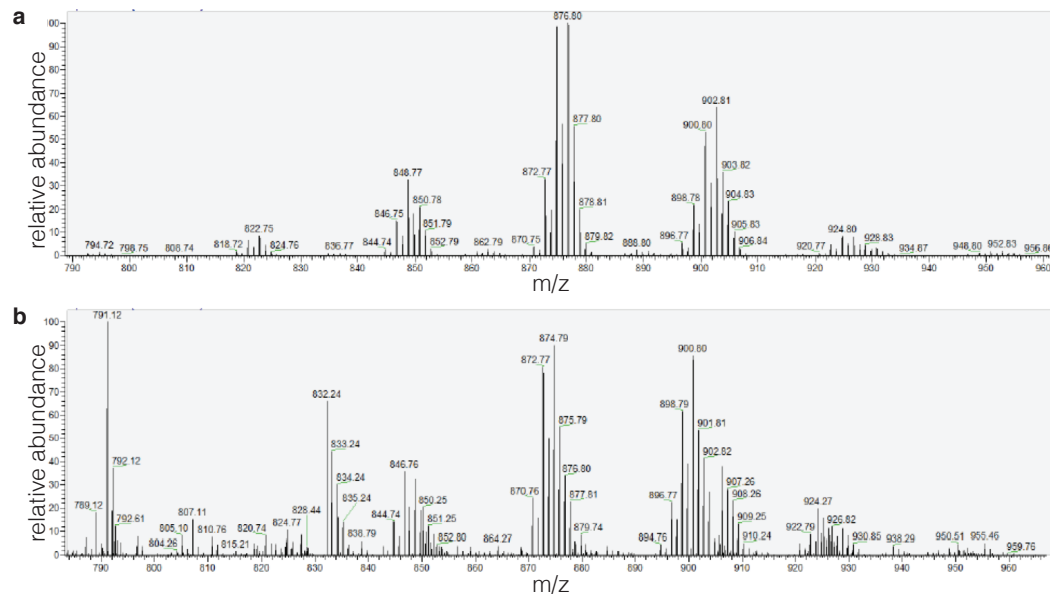


**Figure 4.1** | TAGs are the most abundant lipid species in primary human and murine BMAd. Oil purified from primary BMAd samples obtained from (a) human tibial plate preparation from a 56-year-old female, or (b) flushed murine BM of the distal tibiae pooled from two eight-week-old B6 females, were analyzed by mass spectrometry revealing TAGs as the main lipid species. BMAd: bone marrow adipocytes; TAGs: triacylglycerols.

## Global differences in lipid content measured with high performance liquid chromatography

Following the 17-day *in vitro* culture, we analyzed the global fatty acid composition of the cultured BM-derived OP9 cells on the two differentiated conditions by high performance liquid chromatography (HPLC). Total FA contents and profiles were similar in undifferentiated and spontaneous OP9s (uOP9 cells and sOP9 cells, respectively). When comparing the induced versus spontaneous conditions, classical adipogenic induction of OP9 cells (iOP9) led to a six-fold higher total FA accumulation than the spontaneous OP9 differentiation, sOP9 (Figure 4.3c, note the logarithmic scale). Relative fatty acid composition (Figure 3.3a-b) revealed similar enrichment for saturated FAs (SFAs), and preferential overall enrichment of monounsaturated FAs (MUFAs) in iOP9 (Figure 4.3a). Interestingly, polyunsaturated FAs (PUFAs) were relatively enriched in sOP9 as compared to the iOP9 condition (Figure 4.3a), while the absolute content in PUFAs was similar for both conditions (Figure 4.3c). Fatty acid profiles (Figure 4.3c-d) revealed a preferential enrichment in MUFAs in iOP9 cells (47% against only 36% MUFAS in sOP9 cells), mostly to the detriment of PUFAs (only 2% in iOP9 cells versus 10% PUFAs in sOP9 cells) (Figure 4.3c). The most abundant PUFA species was arachidonic acid (20:4 n-6), whose abundance was significantly higher in the iOP9 condition. In relative terms, though, PUFAs linoleic (18:2 n-6) and arachidonic acid (20:4 n-6) were enriched in the sOP9-adipocytes at 5% of total FA while making up only 1% of FA in iOP9-adipocytes (Figure 4.3b, d). Analysis of individual FA composition for SFAs and MUFAs revealed most notably a significant enrichment for palmitoleic acid (16:1) MUFA in the iOP9 condition (29%) versus the sOP9 (9%) condition, with a trend to consistent

reciprocal enrichment of 18 carbon FAs in the sOP9 condition: stearic acid (18:0, sOP9 11% vs. iOP9 4%), oleic acid (18:1, sOP9 26% vs. iOP9 16%) and linoleic acid (18:2 n-6, sOP9 4% vs. iOP9 1%).

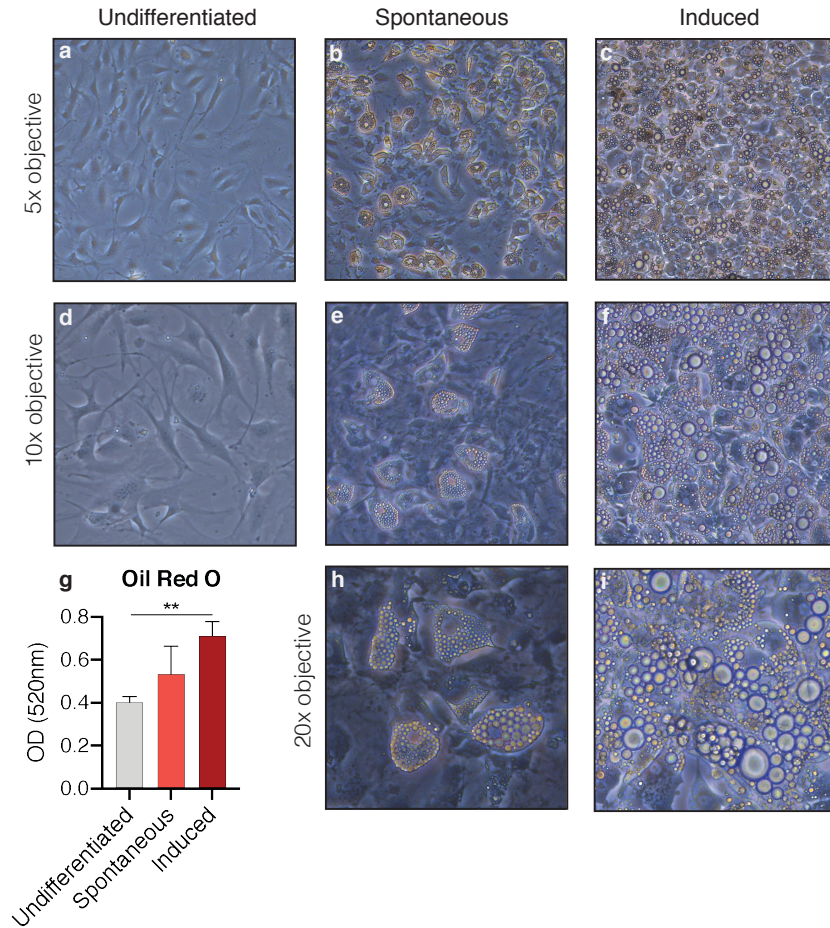


**Figure 4.2** | Population-level differences in minimal and classical induction of adipogenesis. **a-h** OP9 cells were (**a, d**) passaged subconfluently and remained undifferentiated on day 17 in culture, (**b, e, h**) differentiated spontaneously upon confluency in the presence of serum for 17 days, or (**e, f, i**) induced with a classical adipogenic differentiation cocktail in the same serum-containing conditions, also after confluent plating and 17 days in culture. **g** Oil red O measurements show the highest adipogenic differentiation in the induced condition at day 17 in culture. \*\* $P < 0.01$  by Bonferroni's multiple comparisons test. Error bars represent mean  $\pm$  s.d.

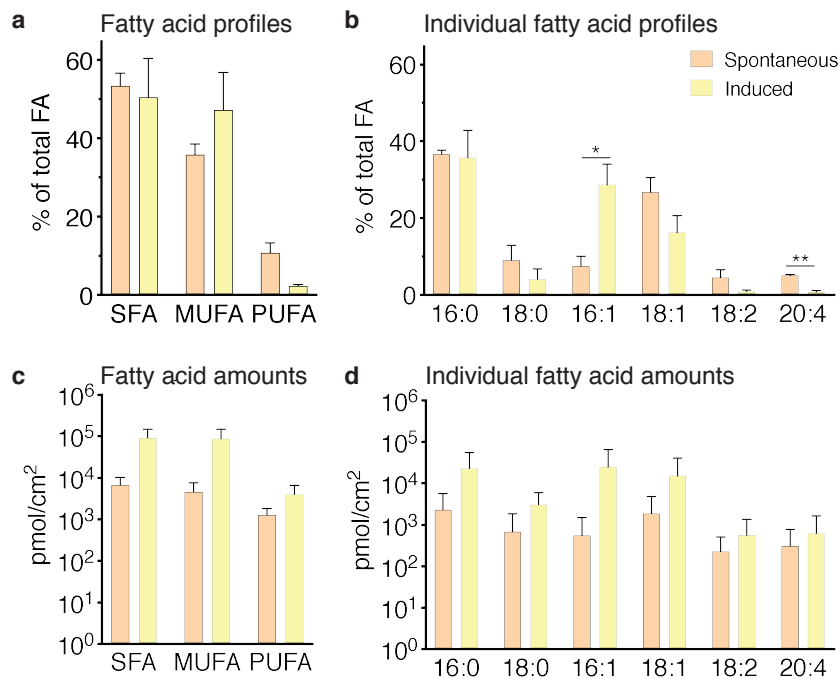


**Figure 4.3** | Classical induction of murine-derived OP9 cells leads to preferential accumulation of unsaturated lipids at the population level. **a-d** HPLC analysis of spontaneously-differentiated or induced OP9-adipocytes revealed **(a)** a higher unsaturation content in induced (67%) versus spontaneous (50%), and **(b, d)** nuances of the most abundant saturated, mono-, and polyunsaturated lipid species. \*\*P<0.01, \*P<0.05 by two-tailed Students t-test. Error bars represent mean  $\pm$  s.e.m.

Overall, the most abundant saturated and unsaturated lipid species revealed by the HPLC profiles were stearic acid (18:0), most prevalent in the sOP9-adipocytes, and palmitoleic acid (16:1), most abundant in the iOP9-adipocytes (Figure 4.3b). The prevalence of palmitoleic acid (16:1) in iOP9-adipocytes corresponds to the most abundant FA species historically described within the highly adipocytic areas of the rabbit skeleton, then-denominated yellow or stable marrow and which encompasses the now-denominated constitutive BMAd. Similarly, the HPLC profiles obtained for the spontaneous condition (sOP9) correspond closely to those described for proximal areas of the skeleton containing adipocytes intermingled within highly hematopoietic marrow (Tavassoli et al. 1977). These results indicate that, at the population level, sOP9 adipocytic cultures may share similarities with the labile/regulated BMAd of the red marrow and that the iOP9 adipocytic cultures may have characteristics of the stable/constitutive BMAd of the yellow marrow.

## Raman microspectroscopy captures unsaturation content at the single droplet level

While HPLC analysis can measure differences in chemical composition at the population level, it does not capture the heterogeneity within the individual adipocytes. Raman microspectroscopy represents a powerful yet non-invasive and label-free method to assess the lipid composition of adipocytes *in vitro*. Molecular imaging allows for the acquisition of individual spectra and the evaluation of morphological features at the level of single lipid droplets (Figure 4.4).

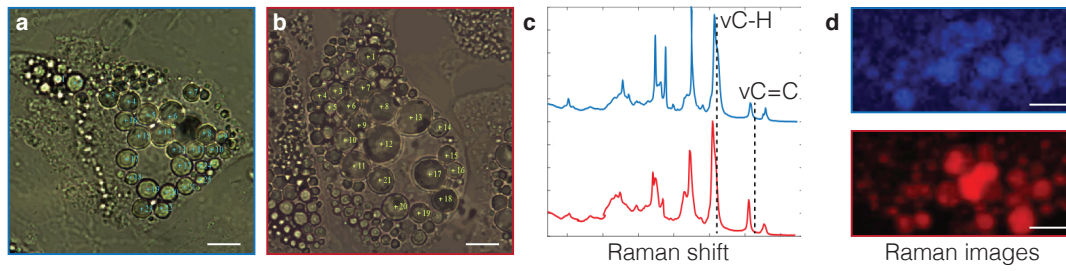


**Figure 4.4** | Single-cell level heterogeneity in differentiating OP9 cells. **a-b** Differentiating OP9 cells in culture show heterogeneity of lipid droplets within cells for which Raman spectra are acquired at a given position in **(a)** spontaneous OP9-adipocytes, and **(b)** induced OP9-adipocytes. Numbers within the lipid droplets indicate the position of the individual Raman spectra acquired per lipid droplet. **c** Individual Raman spectra of saturated (blue) and unsaturated (red) lipids are produced for each lipid droplet measured. **d** Representative Raman images of saturated (top) and unsaturated (bottom) lipids from the same cell. Scale bars are 10 $\mu$ m.

Raman spectra, representative of the molecular composition of LDs, were acquired in adipocytes of the spontaneous and induced conditions only, as the undifferentiated condition presented with very few if any lipid droplets. As a first approach, we assessed the unsaturation ratio at the population level. The unsaturation ratio is recognized as a measure for the content of unsaturated FA and is obtained by the proportion of saturated to unsaturated bands (Equation 4.1).

$$\text{Unsaturation ratio} = \frac{A(vC=C)}{A(vC-H)} \quad (4.1)$$

**Equation 4.1** | Lipid unsaturation ratio measured by Raman microspectroscopy.

Following global analysis, the lipid composition was assessed at the adipocyte level by the analysis of averaged spectra per adipocyte by PCA. It revealed two main Raman spectra characteristic of saturated and unsaturated lipids. On the PCA score plot, each point represents an averaged spectrum per adipocyte. Most of the spectra from iOP9-adipocytes (81%) form a cluster in the negative score along PC1, while the spectra of sOP9-adipocytes are scattered along PC1 (Figure 4.5a). This indicates that the molecular composition of LDs in sOP9-adipocytes is heterogeneous compared to iOP9-adipocytes, and that the conditions are not characterized by LDs that are uniformly composed of either saturated or unsaturated lipids, but rather a mixture thereof.

PC1 captures 78.20% of the variability and separates the Raman spectra based on the saturated and unsaturated profiles (Figure 4.5b). Based on both score plots and PC1, the cluster LDs of iOP9-adipocytes is assigned to unsaturated lipids. The LDs of sOP9-adipocytes are composed of a mixture of unsaturated and saturated lipids. The mixture exists between adipocytes and also within the adipocytes themselves as illustrated by the Raman image showing LDs composed of saturated and unsaturated lipids (Figure 4.4d).

These results are in congruence with the results of Scheller and colleagues who found the unsaturation index to be a discriminant factor between lipid profiles from primary rat lumbar vertebrae, femurs, and proximal tibia (hematopoietic red marrow rich in labile/regulated BMADs) compared to distal tibia and caudal vertebrae (adipocytic yellow marrow rich in stable/constitutive BMADs) (Scheller et al., 2015). Thus, our data on lipid unsaturation of *in vitro* sOP9- versus iOP9-adipocytes agrees well with the extent

of variability explained by the lipid unsaturation ratio measured *in vivo* on proximal BMAdS from hematopoietic marrow versus distal BMAdS from adipocytic marrow.

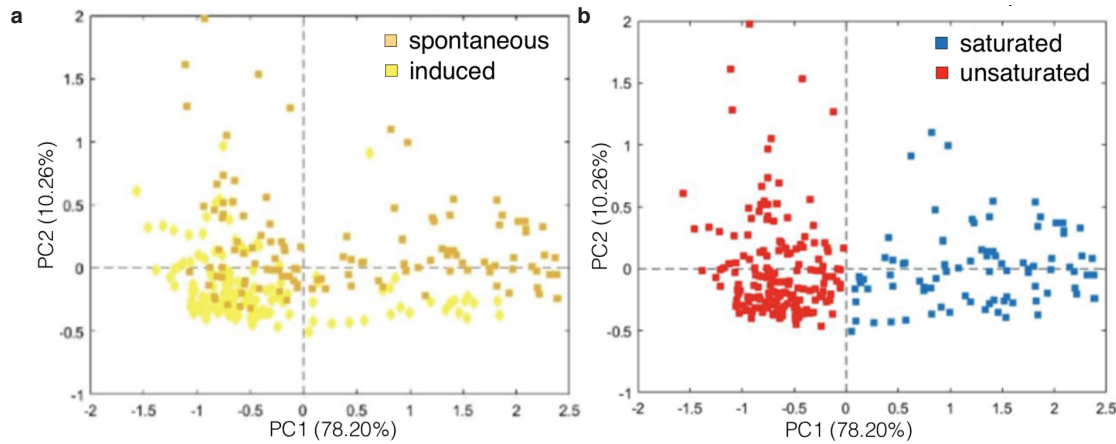


**Figure 4.5** | Raman microspectroscopy measures lipid content at the single droplet level revealing two dominant spectra of saturated and unsaturated spectra. **a** PCA score plot of Raman spectra labelled according to spontaneous (orange) and induced (yellow) conditions. **b** The same PCA score plot as (a) labelled according to the assignment of Raman spectra as saturated (blue) and unsaturated (red) lipids.

We first hypothesized that the smaller size of lipid droplets in sOP9 adipocytes may solely explain their lower unsaturation ratio. While LD diameter was significantly greater ( $p < 0.0001$ ) in the iOP9-adipocytes ( $7.44 \pm 3.47 \mu\text{m}$ ) versus the sOP9-adipocytes ( $4.80 \pm 1.81 \mu\text{m}$ ) (Figure 4.6a), this could not directly predict the difference in unsaturation ratio of  $0.16 \pm 0.05$  versus  $0.12 \pm 0.02$  respectively as obtained by Raman microspectroscopy (data not shown). The overall differences in unsaturation ratio was more pronounced with HPLC analysis ( $p = 0.0004$ ) at  $1.02 \pm 0.27$  versus  $0.19 \pm 0.11$  for iOP9-adipocytes and sOP9-adipocytes respectively, aligning with previous reports for primary stable/constitutive and labile/regulated BMAdS (Scheller et al. 2015). Notably, analysis of the LD diameter to unsaturation ratio, shows that the size of saturated LDs is similar in both conditions (Figure 4.6a). However, unsaturated LDs are overall bigger in size than saturated LDs, with a possible predominance in iOP9 (Figure 4.6b).

Whereas at the population level there is a predominance of saturated or unsaturated lipids in spontaneous or induced OP9-adipocytes, their individual LDs consist not purely of one species but rather a mixture where the largest LDs are predominantly unsaturated. Taken together, this points to possible sequential stages of LD (and adipocyte) maturation in the sOP9 versus the iOP9 conditions, and thus suggests a continuum with smaller LD being mostly saturated, an intermediate stage of LD maturation that are of largely mixed composition, and the most mature LDs that are large and unsaturated.



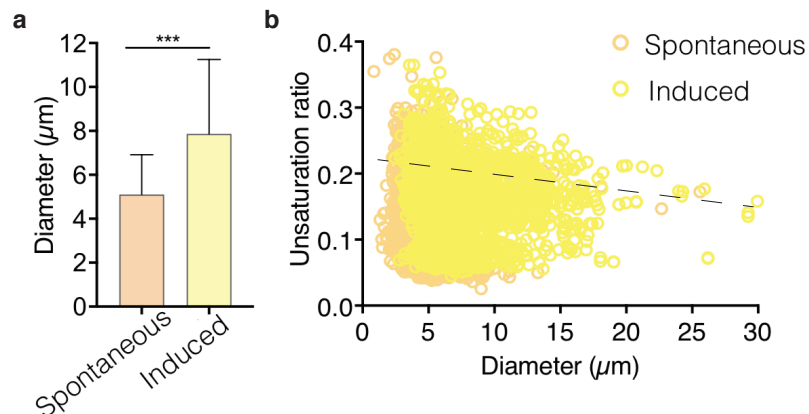


**Figure 4.6** | Raman measures lipid unsaturation ratio at the single droplet level. **a** Lipid droplet diameter is greater in induced OP9-adipocytes (yellow) versus spontaneously differentiated OP9-adipocytes (orange). **b** Lipid droplet diameter does not correspond with difference in mean unsaturation ratio ( $r^2=0.005$ ). A trend toward larger unsaturated lipid droplets in the induced condition is observed. Error bars represent s.e.m. \*\*\* $P<0.0001$  by Student's t-test.

### Saturation differences may be due to incomplete adipogenic maturation

To better understand the kinetics of adipocyte and LD maturation, we analyzed the gene expression profiles by RT-qPCR on the spontaneous and induced OP9-adipocytes after seven or 17 days in culture compared to undifferentiated OP9 cells. While all differentiated OP9 cells expressed the fatty acid binding protein (*Fabp4*), a marker of adipogenesis, at significantly higher levels than undifferentiated OP9 cells, the expression of early transcription factors and mature adipocyte markers in iOP9-adipocytes was slightly shifted compared to that of the sOP9-adipocytes (Figure 4.8a). On day 17, the early stage BMAd marker adiponectin (*AdipoQ*) was slightly more elevated in sOP9-adipocytes however *C/ebpa* was most highly expressed in iOP9-adipocytes on day 17. C/EBPα acts in concert with PPARγ which was more evenly expressed in the differentiated cells. Interestingly, lipoprotein lipase (*Lpl*) which catalyzes the hydrolysis of extracellular TAGs to FAs and glycerol for uptake, was highest in sOP9-adipocytes on day 7 and significantly lower in iOP9-adipocytes on day 17 of culture. The opposite was true for adipose triglyceride lipase (*Atgl*) that catalyzes the initial step of intracellular TAG hydrolysis, which increased with time and differentiation in culture.

From these results it would seem that sOP9-adipocytes tend to express earlier markers of adipogenesis than iOP9-adipocytes and favor FA uptake, whereas the iOP9-adipocytes express maximal levels of classic markers of adipogenic maturation while favoring intracellular lipolysis. This may indicate earlier and later stages of adipocytic maturation, as would be measured by morphological features such as LD accumulation and dissipation over time, leading us to investigate how this could partially be reflected in enzymatic markers of FA biosynthesis (Figure 4.8b). FAs are synthesized by de novo lipogenesis (DNL) via fatty acid synthase (FAS encoded by the fatty acid synthases gene *FASN*) from malonyl-CoA or obtained from the diet (or culture medium) as essential fatty acids (Figure 4.9). SFAs are desaturated to MUFAs by Δ9-desaturases stearyl Co-A desaturase-1 (*Scd1*) and -2 (*Scd2*). These are elongated by elongation of very long chain fatty acids proteins (Elovl5). ω6 essential FAs can be further desaturated by Δ6- and Δ5-fatty acid desaturases (Fads) to long chain PUFAs and eventually converted to eicosanoids. *Scd1* is highly expressed in all differentiating OP9 cells but most significantly upregulated in iOP9-

adipocytes on day 7 (Figure 4.8b). *Scd2* is also significantly increased compared to undifferentiated OP9 cells. *Fads1* and *Fads2* however, are slightly higher in sOP9-adipocytes than in the induced condition. Elov11 similarly decreases with long-term induced differentiation. These gene expression patterns are in agreement with the Raman and HPLC results that showed SFAs and PUFAs to be most frequent in the sOP9-adipocytes while the MUFA palmitoleic acid (16:1n-7) was most abundant in the induced condition (Figure 4.3).

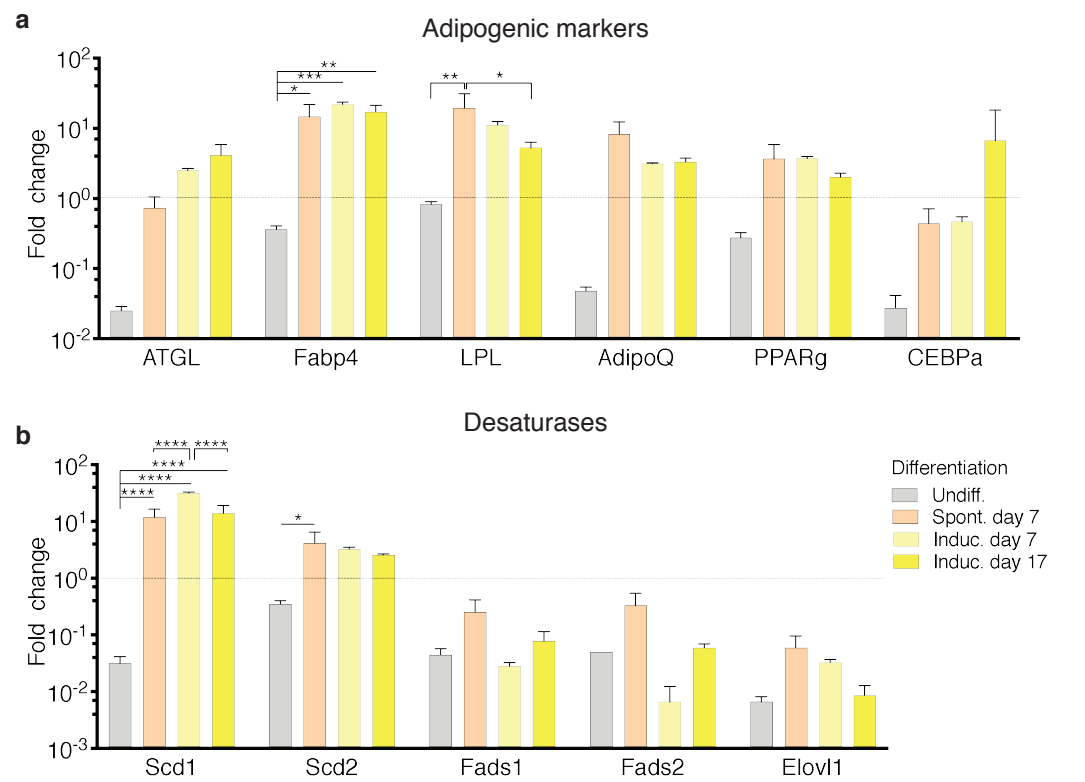


**Figure 4.8** | Kinetics of gene expression in short- and long-term differentiating OP9-adipocytes compared to undifferentiated OP9 cells. **a** Markers of adipogenesis are increased in induced OP9-adipocytes. **b** Desaturase expression is highest in day 17 induced OP9-adipocytes while an elongation marker of fatty acids is decreased. \*\*\*\* $P < 0.0001$ , \*\*\* $P < 0.001$ , \*\* $P < 0.01$ , \* $P < 0.05$  by Bonferroni's multiple comparisons test. Error bars represent mean  $\pm$  s.d. Undiff.: undifferentiated; Spont.: spontaneous; Induc.: Induced. RT-qPCR of the day 17 spontaneous condition did not yield results, likely due to poor RNA quality.

The majorly saturated FA content of sOP9-adipocytes versus unsaturated FAs of iOP9-adipocytes, supported by differences in adipogenic and desaturase gene expression, may reflect an incomplete adipogenic maturation of the OP9 cells *in vitro* that replicates the *in vivo* reported differences of labile and stable BMAd. This is also reproduced in RNA-sequencing (RNA-seq) data (Figure 4.10) where adipogenic genes are most highly expressed in 17-day differentiation of iOP9-adipocytes as is *Scd1*, whereas *Fads* are more upregulated in sOP9-adipocytes, congruent with our results by RT-qPCR.



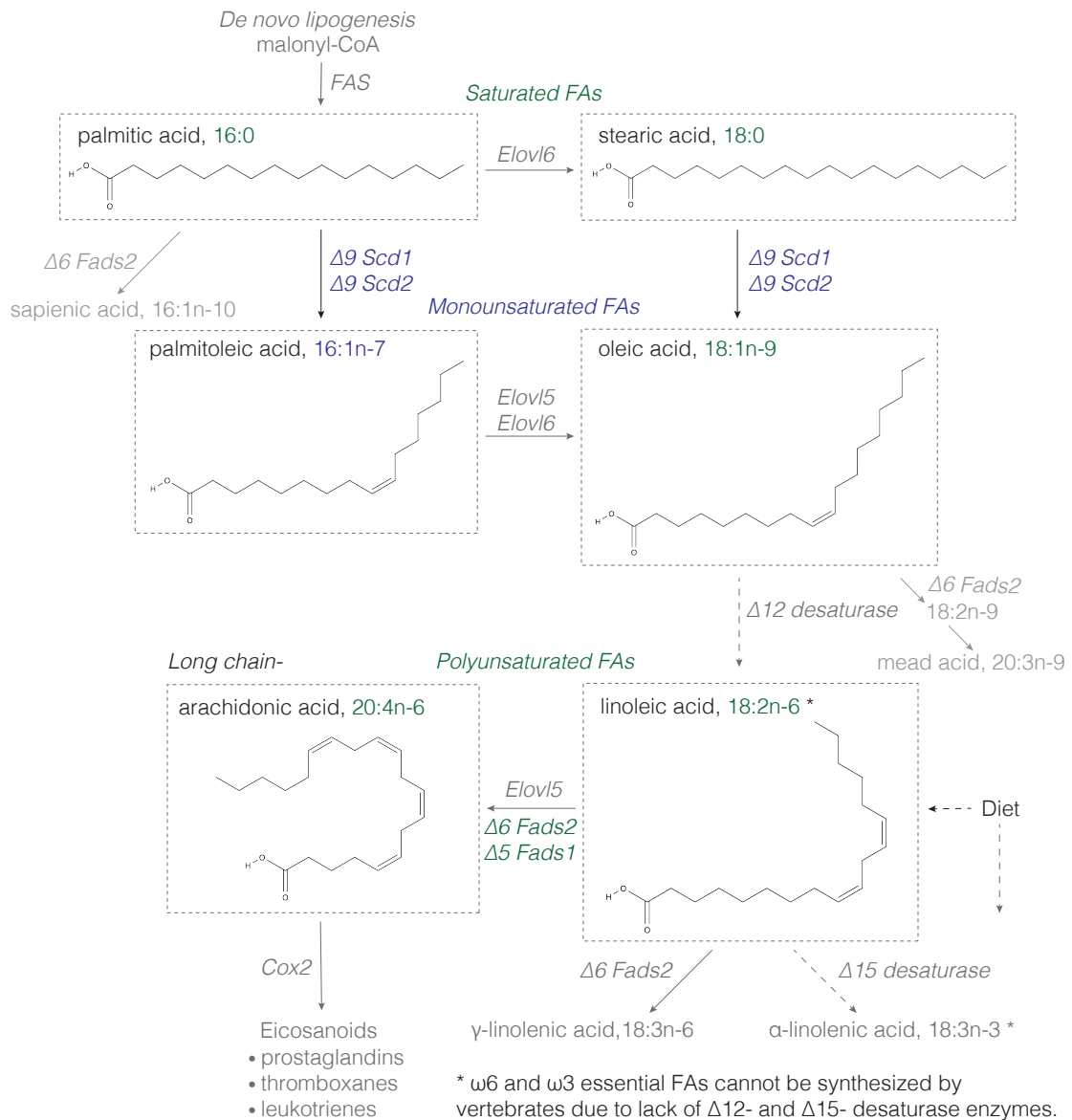


**Figure 4.9** | Schematic of fatty acid synthesis of major lipid species. Green: most frequent in spontaneous OP9-adipocytes by HPLC or RT-qPCR analysis; blue: most frequent in induced OP9-adipocytes by HPLC or RT-qPCR analysis; grey: not measured by HPLC or RT-qPCR; dotted grey arrow: not a process in vertebrates. Chemical structures were generated with MolView v2.4.

Labile BMAdS reside in hematopoietic areas of the marrow whereas stable BMAdS comprise the less hematopoietic, more predominantly adipocytic marrow. Although mature BMAdS inhibit hematopoietic proliferation through the induction of hematopoietic stem cell quiescence (Naveiras et al., 2009), immature BMAdS may be supportive to hematopoiesis (Zhou et al., 2018). Indeed, RNA-seq data revealed that as compared to day 7 iOP9-adipocytes, day 7 sOP9-adipocytes more highly and significantly express the hematopoietic supportive factors C-X-C Motif Chemokine Ligand 12 (*Cxcl12*) and c-Kit Ligand (*KitL*).

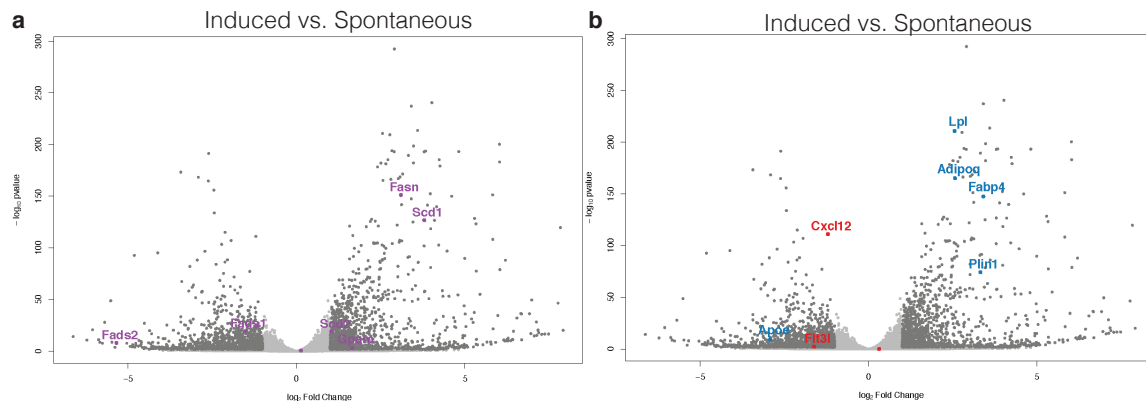


**Figure 4.10** | Expression of significant markers by RNA-seq in short-term differentiation of spontaneous and induced OP9-adipocytes. **a** Expression of desaturases (violet). **b** Adipogenic markers (blue) are upregulated in induced while hematopoietic supportive factors (red) are upregulated in spontaneous OP9-adipocytes.

### Hematopoietic support capacity

The RNA-seq data from the short-term OP9 differentiation, indicate that sOP9-adipocytes express lower levels of adipocyte-specific genes compared to iOP9-adipocytes while expressing hematopoietic supportive factors more highly. To quantify the effect of hematopoietic support in a functional manner, we co-cultured hematopoietic stem and progenitor cells (HSPCs) identified as cKit<sup>+</sup>Lin<sup>-</sup>Sca1<sup>+</sup> (KLS) for seven days with the differentiated OP9 cells at a ratio of 1 HSPC to 10 OP9 cells. A high number of KLS cells was added in proportion to OP9 cells in order to confound the effects of the heterogeneity of the HSPC population. This avoids downstream stochastic, clone effects on analysis secondary to differences in the HSC content across wells, which although small, would be exponentially exaggerated after co-culture. At the end of the seven-day co-culture period, flow cytometric analysis revealed that total hematopoietic expansion of 2,000 seeded HSPCs was 4.5-fold greater ( $p < 0.0001$ ) with the sOP9-adipocytes as feeder (Figure 4.11a). The total hematopoietic cells in suspension were significantly lower in the induced versus spontaneous condition ( $p < 0.05$ ) whereas the more immature progenitor cells that are typically in close contact and adherent to the OP9 cells were significantly lower in the undifferentiated condition ( $p < 0.01$ ). This suggests iOP9-adipocytes may favor support of immature hematopoietic progenitors, although not with the same efficiency as the sOP9-adipocytes. These phenotypic analyses are supported by assessing the functional capacity in cobblestone-forming assays (Figure 4.11b). The total number of hematopoietic colonies per initial number of HSPCs seeded, after the seven-day co-culture was significantly higher with sOP9-adipocytes as feeder cells at 0.13 colonies per KLS versus 0.01 colonies. All three colony categories, from the shiny consisting of more mature hematopoietic cells to the mixed and cobblestone colonies which contain the most immature hematopoietic progenitors were all significantly increased ( $P < 0.05$ ) in the spontaneous condition. Thus, HSPCs co-cultured with sOP9-adipocytes could form cobblestone colonies characteristic of hematopoietic stem and primitive progenitor cells in culture, but not with iOP9-adipocytes reflecting the *in vitro* short-term hematopoietic expansion characteristics. To understand to which extent secreted factors from the OP9-adipocytes contributed to hematopoietic expansion, HSPCs were cultured for two days in different concentrations of conditioned media of OP9 cells. The conditioned media were prepared by allowing OP9 cells to differentiate spontaneously for five days, or by short and long induction of OP9 adipogenesis for five days and seventeen days respectively. Following the differentiation period, the media of the OP9-

adipocytes was then changed to fresh basal medium, and harvested after two days for culture with HSPCs. The conditioned medium from undifferentiated OP9 cells was harvested from confluent OP9 cells that were cultured for two days in basal medium. HSPCs were then sorted and cultured in the absence of stroma in increasing ratios of conditioned medium to basal medium. After two days, hematopoietic expansion was greatest for HSPCs cultured in the highest concentration of undifferentiated-conditioned medium (Figure 4.11c). HSPCs cultured in conditioned medium from iOP9-adipocytes didn't show a significant expansion after two days in culture, independently of an iOP9 induction protocol of seven or seventeen days. However, the conditioned medium from sOP9-adipocytes was substantially more supportive to HSPC maintenance, although less than those cultured in conditioned media from undifferentiated OP9 cells. This effect increased with higher ratios of conditioned-to-basal medium. Thus, secreted factors from OP9 cells are sufficient to maintain HSPCs for at least two days *in-vitro*, while this capacity markedly decreases upon adipocytic differentiation of the OP9 cells.

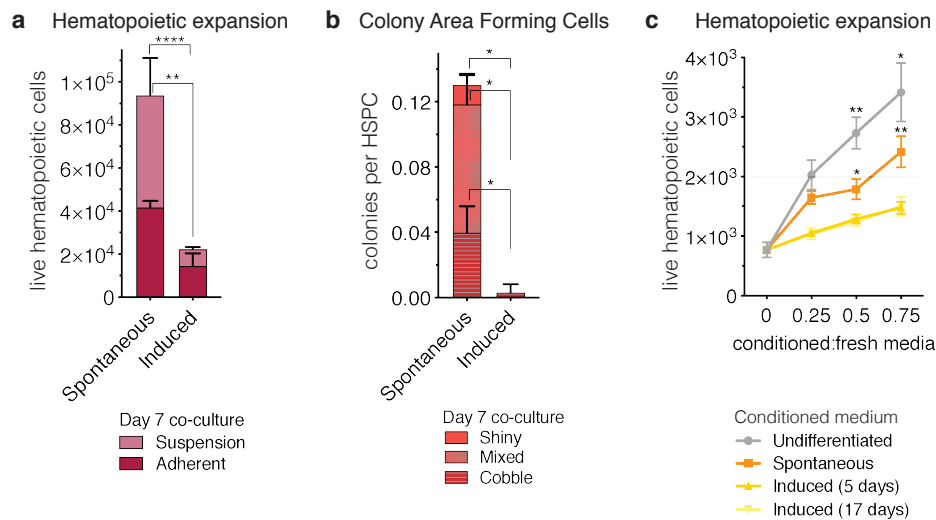


**Figure 4.11** | Short-term co-culture of OP9-adipocytes with hematopoietic stem and progenitor cells favors hematopoietic expansion in the spontaneous condition. **a** Total hematopoietic cell expansion of 2000 initial HSPCs after seven days in co-culture (including cells in adherent and cells in suspension) is significantly higher ( $p < 0.0001$ ) when hematopoietic stem and progenitor cells, HSPCs, (cKit<sup>+</sup>Lin<sup>-</sup>Sca1<sup>+</sup>, KLS) are co-seeded with spontaneous- compared to induced OP9-adipocytes. **b** The colony forming capacity of HSPCs seeded with spontaneous OP9-adipocytes is significantly higher ( $P < 0.05$ ) than when cultured with induced OP9-adipocytes. **c** Total hematopoietic expansion (in the absence of stroma) after two-day co-culture of 2000 HSPCs in conditioned medium from OP9-adipocytes comprising increasing ratios of conditioned-to-fresh media. \*\*\*\* $P < 0.0001$ , \*\* $P < 0.01$ , \* $P < 0.05$  by Bonferroni's multiple comparisons test. Error bars represent mean  $\pm$  s.d.

Indeed, in a competitive transplantation setting, progeny from KLS that had been co-cultured with iOP9-adipocytes had significantly lower short-term reconstitution capacity one month post-transplant compared to those cultured with sOP9-adipocytes (Naveiras, 2008). Interestingly, this was ameliorated in the long-term reconstitution six months post-transplant and was attributed to the hematopoietic cells in suspension, suggesting that iOP9-adipocytes maintain HSCs in quiescence in semi-/suspension. Taken together, the hematopoietic support capacity *in vitro* of sOP9-adipocytes is superior to that of iOP9-adipocytes, aligning with the *in vivo* counterparts of the labile/regulated and stable/constitutive BMADs.

## Conclusions

This chapter presents a novel application of Raman microspectroscopy to measure lipid un/saturation heterogeneity at the individual LD resolution in a label-free, non-destructive manner, which we have applied in the context of *in vitro* adipogenic differentiation. Raman microspectroscopy has allowed us to propose the spontaneous/induced OP9-adipocyte differentiation system as an *in vitro* model to study the metabolic and functional characteristics of the two described subtypes of BMAd: labile or regulated and stable or constitutive.

We show that sOP9-adipocytes resemble primary labile BMAd and are more permissive to hematopoiesis than iOP9-adipocytes, resembling the stable BMAd of the marrow. This is reflected in their gene expression profiles upon adipocytic differentiation, the lipid composition, and hematopoietic supportive properties. OP9 cells that spontaneously differentiate towards adipocytes in the presence of serum more highly express early adipogenic markers and have a high unsaturation content of palmitic and stearic acid. Meanwhile OP9 cells that were actively induced toward adipocytic differentiation have higher levels of unsaturated lipids, in particular palmitoleic acid while also having increased expression of the  $\Delta 9$ -desaturase *Scd1* and showing upregulation of later markers of adipogenesis. These results are in good agreement with reports on primary rat, rabbit, and human BMAT of the red a yellow BM (Tavassoli et al. 1976, Scheller et al. 2015). The sOP9-adipocytes had significantly higher expression of *Lpl* that mediates fatty acid uptake for storage while iOP9-adipocytes had increased expression of *Atgl*, the key enzyme that initiates hydrolysis of TAGs. This could support the notion that these two adipocyte types may present two different maturation stages of the adipogenic differentiation program. Indeed, the sOP9-adipocytes are more supportive to hematopoiesis (either through contact or secreted factors) than the iOP9-adipocytes, as seen by their capacity to form hematopoietic colonies and to stimulate hematopoietic expansion (Figure 4.11). This agrees with reports of adiponectin expressing BM pre/adipocytes being necessary for hematopoietic expansion (Zhou et al. 2017) while mature BMAd rather inducing HSCs in quiescence (Naveiras et al., 2009).

## Outlook

Diseases of lipodystrophy may provide insights into the formation of BMAd that we are still struggling to understand (Scheller and Rosen 2014, Scheller et al. 2015). Patient-derived serpin-deficient lymphoblastoid cell-lines, were shown to have an increased proportion of SFAs with a decrease in MUFAs which are the principle products of *Scd1*, indicating decreased *Scd1* activity. Moreover, LD number and size were increased compared to control (Boutet et al. 2009). Impaired  $\Delta 9$ -desaturase activity in nematodes also led to decreased TAG accumulation and LD size that could not be rescued completely by supplemented dietary oleate (Shi et al. 2013). Therefore, it appears that LD size is driven by the ability of *Scd1* to synthesize unsaturated FAs. Although our results did not show a strong correlation of LD size with lipid unsaturation, which may be marked by the heterogeneity of the combined cultures, we did observe that the largest LDs were always predominantly unsaturated. The increase in *Scd1* that we observe with induced adipocytic differentiation is a promising lead supporting the hypothesis that iOP9-

adipocytes resemble cBMAds which may represent a more stable counterpart to the sOP9-adipocytes. Further studies will reveal if this holds true with knock-down of *Scd1* in OP9 cells that should not be able to then unsaturate FAs during differentiation. Likewise, *Scd1* reporters may facilitate the study of the differential properties of labile/regulated versus stable/constitutive BMAds. All together, these results open avenues for future work on the OP9-adipocyte system to understand the mechanisms underlying BMAd heterogeneity, to then translate findings to primary human BMAds *in vitro*.

## Methods

### Human samples

Human oil sample of tibial plate surgical debris from a 56-year-old female was obtained from upon tissue sample preparation for bone grafting from an anonymous organ and bone tissue donor from the Transplants, Cell Therapy and Regenerative Medicine Unit at the Central University Hospital, Oviedo, Spain after local IRB approval for the collaboration.

### Lipidomics by LC-HRMS

Standards and solvents are listed in the Supplementary Table B.1, Appendix B.

#### *Lipid extraction*

Human oil sample (50 $\mu$ l, 0.041g) and separately mouse oil sample (9 $\mu$ l) were diluted 15 times with chloroform/methanol 1:1. One aliquot of 5 $\mu$ l of each sample was extracted using a modified version of the Bligh and Dyer protocol (Bligh et al. 1959). Briefly, 50 $\mu$ l of methanol and 120 $\mu$ l of chloroform were added to the sample and shaken for 2 minutes. After addition of 45 $\mu$ l of deionized water and vortexing for 1min, the mixture was centrifuged at 4°C for 3min at 2000g and the lower phase was collected. The organic phase was vacuum dried for 20min (ScanVac, Labogene) and solubilized in 50 $\mu$ l mobile phase A prior analysis.

#### *Liquid chromatography and mass spectrometry*

Lipid extracts were separated on a HILIC Kinetex column (2.6 $\mu$ m, 2.1x50mm) on a Shimadzu Prominence UFPLC xr system. Mobile phase A was acetonitrile/methanol 10:1 (v/v) containing 10 mM ammonium formate and 0.5% formic acid. Mobile phase B was deionized water containing 10 mM ammonium formate and 0.5% formic acid. Gradient flow elution at 200 $\mu$ l/min began at 5% B with a linear increase to 50% B over 7 min; the 50% B were held for 1.5 min and lastly the column was re-equilibrated for 2.5 minutes. Sample solvent was chloroform/methanol 1:2(v/v), of which 2 $\mu$ l were injected.

Data were acquired in full scan mode at high resolution on a hybrid Orbitrap Elite (Thermo Fisher Scientific, Bremen, Germany). The system was operated at 240'000 resolution ( $m/z$  400) with an AGC set at 1.0E6 and one microscan set at 10 ms maximum injection time. The heated electro spray source

## Chapter 4 | *In vitro* model of bone marrow adipocyte subtypes

HESI II was operated in positive mode at a temperature of 90°C and a source voltage at 4.0KV. Sheath gas and auxiliary gas were set at 20 and 5 arbitrary units respectively while the transfer capillary temperature was set to 275°C.

### *Data analysis*

Mass spectrometry data were acquired with LTQ Tuneplus2.7SP2 and treated with Xcalibur 4.0QF2 (Thermo Fisher Scientific). Lipid identification was carried out with Lipid Data Analyzer II (LDA v.2.5.2, IGB-TUG Graz University) (Hartler et al. 2011). The LDA algorithm identifies peaks by their respective retention time, m/z and intensity. Care was taken to calibrate the instrument regularly to ensure a mass accuracy consistently lower than 3 ppm thereby leaving only few theoretical possibilities for elemental assignment. Data visualization was improved with LCMSEXplorer in a homemade web tool hosted at EPFL (<https://gecftools.epfl.ch/lcmsexplorer/login>).

### OP9 cell culture

OP9 cells (generously provided by T. Nakano, Kyoto University, Japan, via the Daley Lab, Children's Hospital, Harvard Medical School) were plated in 24-well plates (Falcon) with CaF<sub>2</sub> substrates (Crystran) for Raman microspectroscopy and RT-qPCR, in 6-well plates (Falcon) for HPLC analysis, and in flat-bottom tissue culture-treated 96-well plates (Falcon) for co-culture assays. OP9 cells were plated subconfluent at a density of 5,000 cells per cm<sup>2</sup> (undifferentiated OP9 cells) or at confluency of 20,000 cells per cm<sup>2</sup> (differentiated OP9 cells) in complete medium consisting of Minimum Essential Media alpha (MEM $\alpha$ ) with GlutaMax<sup>TM</sup> (Gibco, catalog no. 32561) and 1% Penicilin/Streptomycin (P/S, Gibco, catalog no. 15140) supplemented 10% fetal bovine serum (FBS, Gibco, catalog no. 10270-106) at 37°C and 5% CO<sub>2</sub> with media changed every 2-3 days.

### *OP9 in vitro adipocytic differentiation and quantification*

Confluent OP9 cells were allowed to spontaneously differentiate over time in culture or induced toward adipocytic differentiation. The adipogenic induction cocktail consisted of complete medium supplemented 10 $\mu$ M dexamethasone (Sigma, catalog no. D4902), 5 $\mu$ g/ml insulin (Sigma, catalog no. I0516), and 0.5mM isobutyl-methylxanthine (IBMX, Sigma, catalog no. I5879). After four days, the adipogenic induction medium was changed to a maintenance medium consisting of complete medium with insulin and dexamethasone only. Media was changed every 3-4 days with aliquots prepared fresh from stock solutions (IBMX in DMSO, insulin in phosphate buffered saline, dexamethasone in ethanol) kept at -20°C in the dark. Short-term experiments were performed at day seven of adipocytic differentiation and long-term experiments were carried out on day 17. Neutral lipids were stained at day 17 of culture with Oil Red O for quantification of adipogenesis in 96-well plates. First, cells were gently washed with phosphate buffered saline (PBS, Gibco, catalog no. 10010015) then fixed for 10 minutes at room temperature with 4% paraformaldehyde (PFA) diluted in PBS from 32% stock solution, and gently washed three times with PBS. 100 $\mu$ l filtered Oil Red O solution prepared from stock solution (Sigma, catalog no. 01391-250ML) diluted 3:2 with distilled water was added to the wells. Cells were incubated with Oil Red O at room temperature for 45 minutes on a shaker, then washed gently with PBS three times. 100 $\mu$ l isopropanol was added to the wells and incubated at room temperature. After 10 minutes, 70 $\mu$ l of the solution was transferred to a new 96 well plate and OD measurements read at 520nm with isopropanol as background.

## Raman microspectroscopy

Raman acquisitions were done on a LabRAM HR800 equipped with an immersion objective (Nikon, numerical aperture = 1, Japan) and a diode laser  $\lambda=785$  nm. The lateral resolution was 1-2  $\mu\text{m}$ . Spectral acquisition was made in the 400–1800  $\text{cm}^{-1}$  range and spectral resolution was 4  $\text{cm}^{-1}$ . The acquisition time was set at 60s per spectrum. Raman spectra were processed using Labspec software (HORIBA, Jobin-Yvon, France). The water immersion objective focused the laser on the center of individual lipid droplets where one spectrum corresponds to one adipocyte lipid droplet. In total 2944 spectra were measured over 120 sOP9-adipocytes (on average 24 spectra per adipocyte) and 2971 spectra over 138 iOP9-adipocytes (with an average of 21 spectra per adipocyte). From the Raman spectra. The number of spectra per well was between 60 to 110. The unsaturation ratio was calculated as ratio of area under the curve of bands 1654 $\text{cm}^{-1}$  / 1441 $\text{cm}^{-1}$ .

## High-performance liquid chromatography

Cells were fixed with PFA as described for the adipocytic quantification above. After washing, 500  $\mu\text{l}$  of PBS was left in the wells, plates were sealed with parafilm and stored at 4°C until processing for HPLC analysis. Cells were detached from the plate with 1 mL (2 x 0.5ml) of PBS and lipids extracted with chloroform/ methanol (2:1; v/v) under agitation for 30 min at room temperature. The resulting lipid extract was then subjected to a saponification, followed by a fatty acid derivatization into naphthacyl esters as described previously (During A. 2017). Fatty acid derivatives were applied into the HPLC Alliance system (2695 Separations Module, Waters, Saint-Quentin-en-Yvelines, France) equipped of an autosampler (200ml-loop sample), a photodiode array detector (model 2998), and the Empower software for data analyses. Fatty acid derivatives were eluted on a reverse phase YMC PRO C18 column (3mm, 4.6x150mm, 120Å) by using two solvent systems: a) methanol/ acetonitrile/ water (64:24:12; v/v/v) and, b) methanol/ dichloromethane/ water (65:28:7; v/v/v) under identical conditions reported previously (During A. 2017). Fatty acid derivatives were detected at 246 nm and quantified by an external standard curve realized with the naphthacyl 19:0 derivative. Note that 19:0 was also used as internal standard to evaluate FA recoveries.

## Real-time quantitative PCR

At day seven or 17 of adipocytic differentiation, RNA was extracted with Trizol and cDNA was synthesized using Taq DNA polymerase (catalog no. 10342020, Life Technologies) according to manufacturer's instructions. Quantitative PCR was performed in technical triplicates using the Fast SYBR Green qPCR Mastermix with 250  $\mu\text{M}$  of primer concentration (Applied Biosystems) on QuantStudio 6 (Life Technologies).  $\Delta\Delta C_t$  method was used with primers pre-validated for high efficiency (Taylor et al., 2019). The geometric mean of housekeeping genes (*RPL13* and *YWHAZ*) was used as reference to calculate the fold expression of each gene relative to the samples of undifferentiated OP9 cells. Primer sequences obtained from Microsynth are listed in Table B.2, Appendix B.

## RNA-sequencing

As described previously (Campos, 2019), following a short-term *in vitro* OP9 adipocytic differentiation as described above, 96-well plates were washed once with PBS and the total RNA was extracted using the ZR-96 Quick-RNA extraction kit (R1050, Zymo Research) following the manufacturer's instructions,

including a DNA-digestion step and was finally reconstituted in 25µl ddH<sub>2</sub>O. 20ng RNA was used to prepare the library following BRB-seq protocol (Alpern et al. 2019). Only genes expressed in at least three samples with a cpm (counts per million) greater than 1 were kept for the rest of the analysis. The data was normalized using DESeq2 (Love et al. 2014). The differential expression analyses were performed using DESeq pipeline with a cut-off of 2-fold increase and FDR>0.05.

### *In vitro* HSPC co-culture

After a short-term *in vitro* adipocyte differentiation of OP9 cells, cells were gently washed with PBS and added pre-warmed Iscove's Modified Dulbecco's Medium (IMDM, catalog no. 12440053, Gibco) supplemented 10 % FBS and 1% Pen/Strep. The washing was done using the Caliper Sciclone ALH 3000 (Caliper Life Sciences, USA) and consisted of four cycles of removing 140µl media and adding 140µl fresh IMDM media, to dilute the previous media. The wells were left with 100µl IMDM 10% FBS and 1% P/S. HSPCs extracted from B6 ACTb-EGFP mice were plated at a ratio of 1:10 initial OP9 cells (in volume of 100µl IMDM, totaling 200µl volume per well).

### *Bone marrow extraction and HSPC sorting*

Total bone marrow was extracted from eight-week-old B6 ACTb-EGFP females housed in 12 hour day-night light cycles and provided ad-libitum sterile food and water as described previously, in accordance to Swiss law and with the approval of cantonal authorities (Service Veterinaire de l'Etat de Vaud). Total bone marrow cells were extracted from femur, tibia and pelvis by crushing using a mortar and pestle in ice-cold PBS supplemented 1mM ethylenediaminetetraacetic acid (EDTA, catalog no. 15575020, Thermo Fisher Scientific). The samples were dissociated and filtered through a 70µm cell strainer (catalog no. 352350, Falcon), lysed for 30 seconds at room temperature in red blood cell lysis buffer (Biolegend, catalog no. 420301), washed with ice-cold PBS-EDTA and centrifuged at 1300rpm for 10 minutes at 4°C. For HSPC sorting prior to co-culture with OP9 stroma, the cell pellet was stained with 50µl biotinylated 'lineage' antibodies (BD, catalog no. 558451) in 1ml PBS-EDTA per six bones for 15 minutes on ice. The sample was washed with PBS-EDTA and stained with 50µl magnetic beads of the same kit in PBS-EDTA for 10 minutes on ice. The samples were then washed and filtered through a 70µm cell strainer (catalog no. 352350, Falcon) prior to lineage depletion using the AutoMACS Pro (Miltenyi Biotec, USA). After depletion the negative fraction was resuspended in an antibody mix containing antibodies against Streptavidin-TxRed (1:200), cKit-PECy7 (1:200), Sca1-APC (1:100) and PI (1:1000). Cell sorting was performed on a FACSAria Fusion (Becton Dickinson, USA) cell sorter.

### *In vitro* HSPC co-culture

As previously described (Campos, 2019), after seven days of co-culture, the 96-well plates were removed from the incubator and placed on ice. To count non-adherent cells, the cells were stained with CD45-PacBlue at final concentration of 1:200, PI at 1:1000 and 5µl CountBright beads (catalog no. C36950, Invitrogen) directly added to the media. Without any further manipulation, the plates were analyzed using the High Throughput Sampler (HTS) module of a LSRII (Becton Dickinson, USA) flow cytometer. For accuracy, the settings were programmed to mix the wells thoroughly before sample uptake. To count adherent cells, separate plates were taken from the incubator, the media manually removed, and wells washed once with 200µl PBS. 40µl of Trypsin EDTA (0.5 %, catalog no. 25300-054, Gibco) was added to each well and incubated for five minutes at 37°C. 160µl of ice-cold PBS containing FBS (to neutralize the trypsin), CD45-APCCy7 (1:200), PI (1:1000) and CountBright beads were added to the plates. The



plates were stained on ice and directly analyzed via flow cytometry with an LSRII cytometer (Becton Dickinson, USA) with the same settings as for the non-adherent cells.

### *In vitro conditioned media preparation and culture*

Conditioned media of four conditions were prepared. Medium from undifferentiated OP9 cells seeded in six-well plates at confluency (20,000 OP9 cells/cm<sup>2</sup>) in IMDM (catalog no. 12440053, Gibco) supplemented 10% FBS and 1% P/S (basal IMDM) was harvest after two days in culture and stored at -20°C. Confluent OP9 cells were grown in MEM $\alpha$  for five days, after which wells were changed to IMDM following three washes, and medium of the spontaneous OP9 cells harvest after two days and stored at -20°C. Conditioned medium from short-term and long-term induced OP9 cells followed the same protocol but with confluent OP9 cells submitted to five-day or 17-day adipogenic induction protocols respectively before change to IMDM for harvest.

2000 live-sorted HSPCs were then plated per well in 96-well round-bottom plates in the absence of stroma. Different ratios of conditioned-to-basal IMDM media were added. After two-day culture the cells were stained with Annexin V, Propidium Iodine (PI) and CD45 to select for live CD45<sup>+</sup> hematopoietic cells via flow cytometric analysis with an LSRII cytometer (Becton Dickinson, USA). CountBright beads were added to count absolute cell numbers.

### *Cobblestone formation assay*

OP9 cells were plated at 20,000 cells/cm<sup>2</sup> in gelatin-pre-coated 6-well plates and cultured with  $\alpha$ -MEM media supplemented with 10%FBS and 1%P/S. The cells were induced to differentiate using the standard differentiation cocktail DMI, which was changed two times per week. After seven days of differentiation, the media was washed three times with PBS and changed to IMDM supplemented with 10%FBS and 1%P/S. On the same day, 200 sorted KLS cells were added into each well. After 7 days of co-culture the hematopoietic colonies are manually counted and scored the following way: (i) shiny colonies (defined as round and bright cells, because they float above the OP9 stromal layer) should not contain more than 10 cobblestone cells; (ii) cobblestone colonies (defined as darker 'cobblestone'-like cells, because they are below the OP9 stromal layer) should not contain more than 20% of shiny cells; and (iii) mixed colonies that contain both shiny and cobblestone cells.

## Statistical Analysis

Values are shown as mean plus or minus the standard deviation or standard error of the mean as indicated. Student's t-test was performed for all experiments when comparing two conditions only, or a Two-Way ANOVA when comparing multiple conditions, with P-values indicated for statistical significance.

Raman spectra were processed by Principal Component Analysis (PCA). Prior to PCA, all the spectra were normalized and mean centered. The PCA analysis allowed to highlight the difference in spectral features between the spontaneous and induced conditions. The PCA was carried out using the PLS Toolbox (v8.7 eigenvector Research, Inc., USA) and Matlab (Mathworks Inc., USA.)

All data are reported as mean  $\pm$  standard deviation. All statistical analyses were performed using GraphPad Prism (version 8.0.0, GraphPad Software). Mean values were compared by one-way or two-

## Chapter 4 | *In vitro* model of bone marrow adipocyte subtypes

way analysis of variance (ANOVA) followed by Bonferroni's post hoc test. Statistical significance was accepted for  $P < 0.05$ , and reported.

### Author contributions

J.T. planned experiments, analyzed and interpreted the results, and wrote the manuscript. J.T. and N.D.T. performed *in vitro* culture. G.F. performed Raman acquisitions. A.D. performed HPLC analyses. V.C. performed co-cultures. J.P.M. performed mass spectrometric analysis. G.F. and L.D. performed statistical analyses for Raman data. J.T., G.F., A.D., and O.N. interpreted the Raman and HPLC data. O.N. initiated the project.

### Competing Interests Statement

The authors declare no conflict of interest at this time.

## **CHAPTER 5**

### **Biomimetic transplantable bone marrow co-culture system**



*This work is part of a pending patent, application EP19020673.0 filed December 4<sup>th</sup> 2019, and entails a modified post-print version of a manuscript published in Biomaterials February 11<sup>th</sup> 2020, entitled*

## **Injectable, Scalable 3D Tissue-Engineered Model of Marrow Hematopoiesis**

Daniel Naveed Tavakol<sup>1\*</sup>, Josefine Tratwal<sup>1\*</sup>, Fabien Bonini<sup>2\*</sup>, Martina Genta<sup>3</sup>, Vasco Campos<sup>1</sup>, Patrick Burch<sup>4</sup>, Sylke Hoehnel<sup>5</sup>, Amélie Bédurier<sup>2,4</sup>, Marco Alessandrini<sup>2</sup>, Olaia Naveiras<sup>1,6‡</sup>, and Thomas Braschler<sup>2‡</sup>

<sup>1</sup>Laboratory of Regenerative Hematopoiesis, Swiss Institute for Experimental Cancer Research & Institute of Bioengineering, Ecole Polytechnique Fédérale de Lausanne (EPFL), Lausanne, Switzerland

<sup>2</sup>Department of Pathology and Immunology, Faculty of Medicine, Université de Genève, Genève, Switzerland

<sup>3</sup>Laboratory of Microsystems Engineering 4, Ecole Polytechnique Fédérale de Lausanne (EPFL), Lausanne, Switzerland

<sup>4</sup>Volumina-Medical SA, Route de la Corniche 5, Epalinges, Switzerland

<sup>5</sup>Sun Bioscience, EPFL Innovation Park, Lausanne, Switzerland

<sup>6</sup>Hematology Service, Departments of Oncology and Laboratory Medicine, Centre Hospitalier Universitaire Vaudois (CHUV), Lausanne, Switzerland

\* Equal author contribution.

‡ Co-Corresponding Authors: Olaia Naveiras and Thomas Braschler

## Preface

The following project sprung from a group of cross-disciplinary and dedicated scientists merging bioengineering and biomedicine. I admire **Thomas Braschler** for his infectious enthusiasm, who seems to have an ease of doing science with creative solutions, and it has been a real pleasure to work with **Fabien Bonini** to make these come to life.

Thomas and Fabien provided the magical scaffold in this context, relentlessly testing it for the optimal conditions for cell-seeding and survival. **Naveed Tavakol** and I performed the cellular assays that quickly amounted to many samples. Together with **Martina Genta**, we carried out the rewarding *in vivo* assays.

As a team, our efforts were rewarded, yet at the same time we were lucky to bring together our own experiences for just the right conditions. This took the form of a manuscript that was accepted without revisions, and within 24 hours we had completed the proofs of the manuscript and filed a patent application. Talk about efficiency!

The approach presented here and the **aim of this chapter** is to provide a minimalistic, scalable, biomimetic *in vitro* model of hematopoiesis in a microcarrier format that preserves the HSPC progenitor function, while being injectable *in-vivo* without disrupting the cell-cell interactions established *in vitro*.

## Introduction

Hematopoietic stem cells give rise to the entirety of cellular blood components. Clinically, hematopoietic stem and progenitor cell (HSPC) transplantation is routinely used to treat a number of hematological diseases, namely blood cancers such as leukemias and lymphomas, as well as genetic diseases of the blood including severe immune deficiencies and hemoglobinopathies. Successful engraftment of the HSPC transplant in the bone marrow (BM), as well as elimination of residual disease, depends on a multitude of factors, including the BM microenvironment or niche (Derakhshani et al., 2019; Wei and Frenette, 2018). Emergent applications for *in vitro* expansion of HSPCs and models of hematopoiesis for drug testing also critically depend on our understanding of the BM microenvironment. Intense research efforts have been made to recapitulate and analyze the BM niche both *in vitro* and *in vivo* (reviewed in Abarrategi et al., 2018; Bello et al., 2018; Raic et al., 2014; Shih et al., 2017). To date, no standardized model, which is applicable both *in vivo* and *in vitro*, exists. To address this limitation, our study aims to provide a bioengineered system to allow for simple and defined culture of hematopoietic populations, while remaining injectable in a minimally invasive fashion for direct transfer of an *in vitro* niche to an *in vivo* environment.

*In vitro* models have the advantage of being relatively inexpensive, and therefore provide the opportunity for potentially large screens of therapeutics and disease conditions. Not only have *in vitro* models been used in developing improved hematopoietic expansion protocols (Tajer et al., 2019), but they have also demonstrated great potential for patient-specific drug screening in “organ-on-a-chip” systems (Ronaldson-Bouchard and Vunjak-Novakovic, 2018). Beyond the classical Dexter 2D cultures, more controlled *in vitro* models include bone marrow-on-a-chip PDMS constructs (Sieber et al., 2018; Torisawa et al., 2014), co-cultures of endothelial cells or bone marrow stromal cells (BMSCs) with HSPCs (Butler et al., 2012; Isern et al., 2013; Jing et al., 2010; Li et al., 2007) in polyethylene glycol (PEG) hydrogels (Blache et al., 2016; Raic et al., 2014), collagen membranes or mineralized scaffolds (Lecarpentier et al., 2018; Bourguine et al., 2018). Yet these models are typically not conceived for intact niche transfer *in vivo*, as they require cells to be recovered from cell culture plates or bulky scaffolds.

3D *in vivo* systems are designed to be physiologically more relevant than 2D models. To create and control ectopic BM niches, *in vivo* approaches have typically focused on the induction of mineralized ossicles. Heterotopic bone structures can be generated under the kidney capsule or subcutaneously by direct transplantation of stromal cells or pre-differentiated cartilage pellets (Tavassoli and Crosby, 1968; Friedenstein et al., 1982; Scotti et al., 2013; Serafini et al., 2014), implantation of biomaterials together with growth factors (Shah et al., 2019), or a combination of both cells and biomaterials (Chen et al., 2012; Vaiselbuh et al., 2010). Such *in vivo* models have paved the way for the development of powerful tools for preclinical research or personalized-medicine. Patient-derived xenografts (PDX) models indeed allow for *in vivo* studies of normal or malignant marrow (reviewed in Abarrategi et al., 2018), and provide a platform for physiological drug screening assays. Major challenges persist in the establishment of PDX marrow models, as ossicles need to be established through rather complex protocols (Reinisch et al., 2017), and expanded via hormonal treatment with daily parathyroid hormone injections for a month or

via *in situ* growth factor delivery (Bolander et al., 2016; Shah et al., 2019). To enable minimally invasive delivery of ossicle precursor material, Matrigel has been used as a carrier (Reinisch et al., 2016) with rising concerns over the heterogeneous and batch-dependent composition of this native extracellular matrix-derived material (Hughes et al., 2010).

Here, we develop a harmonized single system for *in vivo* and *in vitro* experiments in the form of a living, injectable hematopoietic niche. To achieve this goal, we have created a co-culture system that allows for a simple, scalable and chemically well-defined microcarrier culture of HSPCs. Concentrated into minimal volumes, this system is also subcutaneously injectable in mice. To mimic the cellular interactions of the hematopoietic niche, the system enables the *in vitro* co-culture of stromal supportive cells and HSPCs in a scalable culture system, as well as a cytokine-free environment, to facilitate *in vitro* screening and possible mass production. During the injection, the system protects the integrity of the cellular payload while maintaining cellular interactions. Finally, *in vivo*, the biomaterial system reconstitutes a porous, mechanically stable structure that over time allows the ingrowth of a vascular and stromal component of host origin to complete the transplanted niche.

Our choice of scaffold is driven by the partial structural and mechanical resemblance of porous hydrogels to trabecular bone, which have been previously shown conducive to *in vitro* (Raic et al., 2014) and *in vivo* (Shah et al., 2019) support for hematopoiesis. Among the various porous scaffolds, compressible scaffolds are of particular interest due to their high mechanical resilience enabling injectability (Bencherif et al., 2012, 2015). Indeed, bulk “BM cryogels” have recently been used as minimally invasive vehicles to generate ossicles *in situ* for enhancement of T cell generation via presentation of the notch ligand DLL-4 (Shah et al., 2019). Here, we develop a cryogel-based, compressible, Collagen-coated Carboxymethyl Microscaffold (CCM). In dilute suspension, these sub-millimetric scaffolds act as microcarriers, enabling scalable cell culture. Yet, thanks to their specific elastic properties, they can be concentrated into a paste-like living biomaterial, prior to minimally invasive implantation by subcutaneous injection. *In vivo*, the microscaffolds interlock to provide a stable, porous implant (Beduer, Bonini, Verheyen et al., manuscript under revision) with a structure reminiscent of trabecular bone.

Our choice of stroma is driven by biological mimicry of the post-natal hematopoietic bone marrow niche. To favor maintenance and expansion of HSPCs in the bone marrow, the importance of various endogenous cell populations has been highlighted, including osteoblasts, endothelial/perivascular cells, and a subset of BMSCs named CXCL12-expressing adventitial reticular (CAR) cells (Bianco, 2014; Calvi et al., 2003; Ding et al., 2012; Sugiyama et al., 2006; Zhang et al., 2003). CAR-like primary BMSCs cells have been shown capable of expanding human HSPC *in vitro* (Isern et al., 2013), albeit scalability of 3D systems has been limited by HSPC penetrability into the tight spheroids formed by BMSCs cultured in the absence of scaffolds (Schmal et al., 2016). Here we chose to seed our CCM porous scaffolds with the murine, non-clonal BMSC line OP9 (Nakano et al., 1994) to generate a living, injectable stroma supportive for hematopoiesis. The OP9 cell line secretes hematopoietic supportive cytokines *Cxcl12*, *Scf*, and *Angpt1* when co-cultured with HSPCs (Supper et al., 2015) and possesses, in non-clonal assays, the tri-lineage differentiation potential characteristic of BMSCs (Gao et al., 2010), with a particular facility for adipocytic differentiation reminiscent of the recently reported adipoCARs (Baccin et al., 2019). Most importantly, OP9 cells have been shown to provide efficient support of hematopoiesis as compared to other stromal cell lines, probably in large part through paracrine mediated-signaling (Ji et al., 2008; McKinney-Freeman et al., 2008). Indeed, OP9 cells are by themselves sufficient to support hematopoiesis without the need of exogenous cytokines (Naveiras et al., 2009). This minimal co-culture system reduces



interference with *in vitro* screening applications and avoids the difficulty of *in vivo* growth factor delivery (Shah et al., 2019).

Altogether, our approach provides a minimalistic, scalable, biomimetic *in vitro* model of hematopoiesis in a microcarrier format that preserves the HSPC progenitor function in the absence of exogenous cytokines for *in vitro* study, while being injectable for functional *in vivo* readouts, without disrupting the cell-cell interactions established *in vitro*.

## Results

The study aimed to provide a microcarrier co-culture system for convenient and minimally invasive injection of a tissue-like living biomaterial, without disrupting cellular viability and multi-cellular interactions during the injection procedure. We simultaneously seeded stromal OP9 cells and HSPCs on porous CCM microscaffolds (Figure 5.1a). The system self-organized such that the OP9 stroma lined the scaffolds coated with collagen I to support the HSPC subpopulations (Figure 5.1b), and allowed for *in vitro* studies in diluted microcarrier suspension cultures. For subsequent validation *in vivo*, the intact co-cultured CCMs, together with their cellular payload, were dehydrated by a custom dehydration device and delivered *in vivo* by subcutaneous syringe-injection (Figure 5.1d).

Experimentally, our starting biomaterials are highly elastic and porous microscaffolds consisting of crosslinked carboxymethylcellulose (Beduer, Bonini, Verheyen et al., manuscript under revision). A 3D view based on confocal reconstruction after staining with rhodamine 6G is provided in Figure 5.1e. The microscaffolds are designed to be reversibly compressible. This allows for facile exchange of the pore fluid by arbitrary sequences of dehydration and rehydration. To obtain the collagen-coated microscaffolds CCM, we made use of such cycles to efficiently and covalently functionalize the microscaffolds with collagen type I to provide native stromal cell adhesion motives.

For the purpose of scaffold seeding, we generated green fluorescent protein (GFP<sup>+</sup>) OP9 cells and obtained red fluorescent primary murine HSPCs (cKit<sup>+</sup>Lineage<sup>-</sup>Sca1<sup>+</sup>, referred to as KLS) from the marrow of DsRed C57BL/6JRj mice. We then co-seeded a mixture of OP9 stromal cells and KLS<sup>+</sup> cells into our CCM scaffolds by making use of the spontaneous aspiration capacity of dehydrated scaffolds to distribute the cells throughout the microscaffolds. *In vitro* culture of this system demonstrated self-organization into a stromal compartment, adopting the scaffold architecture and hosting the HSPCs and their progeny (Figure 5.1f, Figure 5.1g).

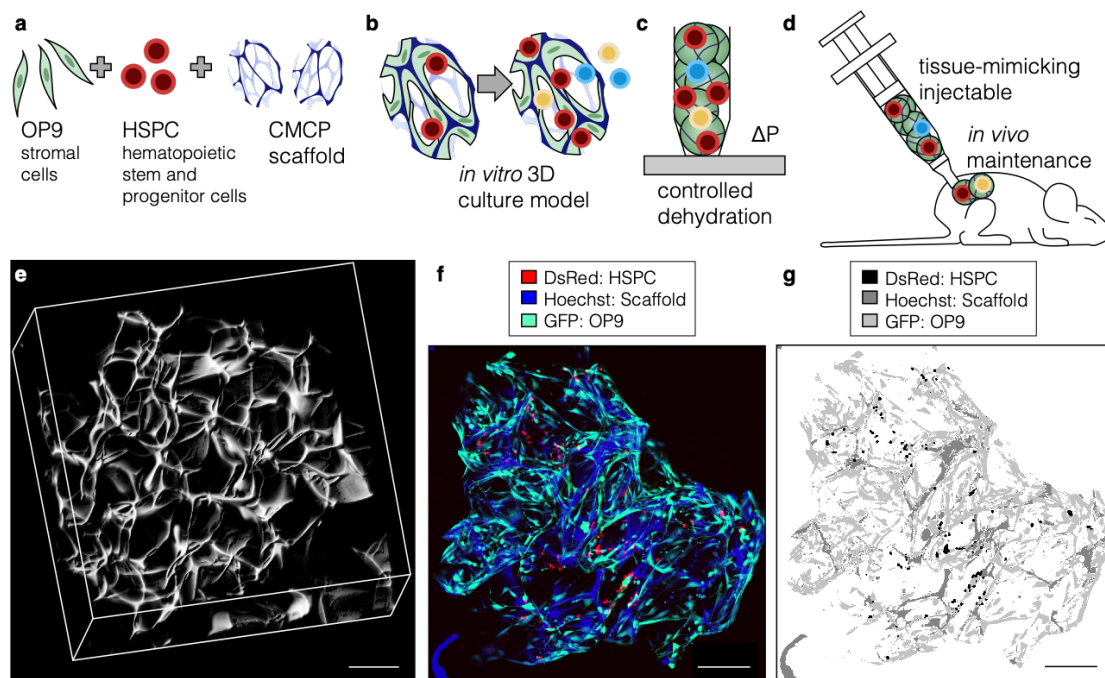


**Figure 5.1** | Transplantable bone marrow niche. **a** For *in vitro* culture, stromal cells (OP9) are combined with hematopoietic stem and progenitor cells (HSPC, selected from bone marrow as lineage<sup>-</sup>, cKit<sup>+</sup>, Sca-1<sup>+</sup> cells); the resulting cell mix is loaded onto collagen-coated carboxymethylcellulose microparticles (CCMs). **b** During *in vitro* culture, the stromal cells adhere to the scaffold and at the same time provide support to the proliferating and differentiating HSPC. **c** For *in vivo* implantation, the cell-loaded CCMs are slowly dehydrated to form a paste-like implantable living biomaterial. Both dehydration speed and final dehydration level are carefully controlled. **d** The resulting tissue-mimicking biomaterial is injected subcutaneously for *in vivo* follow-up. **e** Structure of a CCM. **f** CCM (stained by cell impermeant Hoechst dye) along with green fluorescent stroma and red fluorescent hematopoietic compartment. **g** Assignment of the different areas as scaffold, HSPCs and lineage-committed progenitors, and stromal cells (OP9). Confocal images are linearly contrast adjusted.

## Collagen-coated, mesenchymal stromal cell-seeded scaffolds promote hematopoietic cell proliferation over time

We first assessed the capacity of the artificial stroma, consisting of CCMs lined with OP9 marrow stromal cells, to support hematopoiesis *in vitro*. We made use of the constitutively expressed fluorescent proteins to allow for the visualization and semi-quantitative analysis of co-cultures by confocal microscopy (Figure 5.2).

Indeed, confocal imaging showed effective spreading of OP9 stromal cells on the CCM scaffolds and attachment of the co-seeded HSPCs to the OP9 cells, with continuous proliferation of hematopoietic cells within the scaffold over 11 days in culture (Figure 5.2a). The stromal cells are essential, since at 24 hours HSPCs failed to adhere to the CCMs in the absence of the OP9 cells (Figure 5.2b, Figure 5.2c). In the presence of OP9, we found distinct signs of HSPC supportive characteristics within our *in vitro* hematopoietic niche analog. This included HSPC nestling within OP9 stromal cells (Figure 5.2d) and colony formation within the matrix after 3-4 days of culture (Figure 5.2e). Together with the absolute

requirement for stromal cells in the absence of exogenous cytokines, this indicated intimate and favorable 3D interactions between the two cell types when loaded into the CCMs.

We then quantified the relative proliferation of the HSPCs in our system. To do so, we seeded the CCMs at two relative HSPC densities: high (1:10) and low (1:100) seeding density (HSPCs to OP9 cells). We followed the relative proliferation of the HSPCs and their progeny by evaluating the area occupied by red fluorescence (DsRed) as compared to green fluorescence (green) in confocal sections of the live co-seeded CCMs over time. By also measuring the average area occupied per HSPC and OP9 ( $180\mu\text{m}^2 \pm 90\mu\text{m}^2$  for the HSPC vs.  $1270\mu\text{m}^2 \pm 460\mu\text{m}^2$  for the OP9,  $n=8$  cells in each case), we converted the area measurements to number ratios of HSPC:OP9. Figure 5.2f shows that the ratio of HSPCs (and their descendant progenitors) to OP9 cells within the CCMs increased from  $0.07 \pm 0.02$  to  $1.3 \pm 0.4$  for the high seeding density (intended initial 0.1=1:10 ratio) during 11 days of culture. Likewise, the number ratio HSPCs (and their descendant progenitors) to OP9 increased from  $0.018 \pm 0.01$  to  $0.12 \pm 0.03$  for the low seeding density (1:100).

This indicated that the seeding density after the initial adhesion step, followed by dilution of the CCMs into a large volume of medium, reflected the original 1:10 and 1:100 ratios. In addition, at both seeding densities, a significant increase in relative numbers of HSPCs and their progeny took place within the CCMs, consistent with effective multiplication and expansion of the HSPCs and their differentiated progeny supported by the OP9 cells in an exogenous cytokine-free environment. However, this microscopic assay underestimated the HSPC multiplication, as numerous cells were observed outside of the CCMs in suspension. Moreover, it does not account for the proliferation of OP9 BMSCs. Due to the constitutive expression of DsRed, it is uninformative regarding the fate of the HSPCs in regards to differentiation or maintenance of stem cell properties, which was thus evaluated through surface protein phenotyping and functional colony assays.

### Functional quantification of hematopoietic proliferation on stromal cell-seeded scaffolds as compared to 2D cultures

We next aimed to better characterize the fate of the HSPCs during *in vitro* culture. For this purpose, we used flow cytometry to analyze the co-cultures in 3D on CCMs, and compared them to corresponding standard 2D controls with the same 1:10 and 1:100 initial HSPC:OP9 seeding densities. The constitutive expression of GFP and DsRed by the OP9 cells and HSPCs/progeny, respectively, allowed for the visualization and separation of the OP9 stromal versus the HSPC-derived hematopoietic populations. For example, the dot plot in Figure 5.3a shows the composition in terms of GFP and DsRed expressing cells for a 3D, 1:10 experiment after 12 days of culture. We found that the HSPCs and their progeny, as identified by the DsRed<sup>+</sup>GFP<sup>+</sup> population, consisted nearly exclusively of CD45<sup>+</sup> cells, as expected for all cells of the hematopoietic lineage derived from bone marrow HSPCs (Figure 5.3b) (Weissman and Shizuru, 2008). These cells, which expressed no lineage markers in the cell surface at seeding (Lineage- is part of the KLS definition), consisted at day 12 on a mixture of lineage negative and lineage positive cells (Figure 5.3b). Acquisition of major lineage markers thus revealed hematopoietic differentiation within the CCM coculture. Preservation of c-Kit<sup>+</sup> expression in a subset of the lineage negative DsRed<sup>+</sup>GFP<sup>+</sup> CD45<sup>+</sup> cells (Figure 5.3c) suggested the preservation of progenitor function, as later tested in Colony-forming unit (CFU) assays.

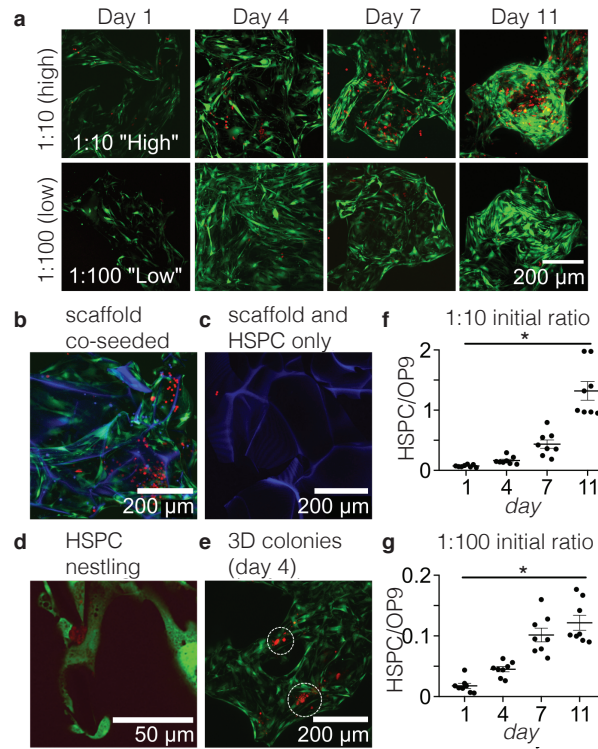


**Figure 5.2** | *In vitro* co-culture of OP9 cells and HSPCs on CCMs. **a** Serial confocal imaging qualitatively demonstrates an increase in hematopoietic populations over the span of nearly two weeks in co-culture, for both 1:10 and 1:100 seeding densities (HSPC:MSC); green: GFP<sup>+</sup>; OP9 MSCs; red: DsRed<sup>+</sup> HSPCs. Qualitative observations from imaging demonstrate large-scale structural outline of the seeded CCMs. **b** DsRed<sup>+</sup> HSPCs requiring MSCs to attach and proliferate very few DsRed<sup>+</sup> cells are found at 24h with OP9 support. **c-e** Confocal imaging of co-seeded scaffolds at higher magnification showing HSPCs nestling within the MSC feeder layers (**d**) and 3D colonies (**e**), appearing throughout the scaffolds over as short as four days in culture. Note that in the absence of OP9 stroma **c** HSPCs are not retrieved within the scaffold at day 4 **f-g** Quantification of proliferation ratios for HSPC to OP9 in co-seeded scaffolds from confocal image z-stacks (**f** for 1:10 seeding ratio, **g** for 1:100 seeding ratio, 25 total images per “n”; n=8 per condition, total of 200 slices). Confocal images are linearly contrast adjusted. Scale bars are 200μm for all images except in **e** where it is 50μm.

Quantitative comparison showed that the total CD45<sup>+</sup> cell expansion was significantly higher in 2D 1:10 “high” ( $254.0 \pm 164.4$ ) compared to 3D 1:10 “high” ( $32.0 \pm 13.0$ ,  $p=0.0094$ ) cultures, as well as in 2D 1:100 “low” ( $530.0 \pm 126.3$ ) versus 3D 1:100 “low” ( $19.0 \pm 11.3$ ,  $p<0.0001$ ) cultures (Figure 5.3d). Very interestingly, although fold expansion of total CD45<sup>+</sup> cells was consistently higher in 2D versus 3D conditions, fold expansion of the hematopoietic progenitor compartment as reflected by quantification of phenotypic progenitors (CD45<sup>+</sup>Lin<sup>-</sup>cKit<sup>+</sup> population) was similar for 2D ( $4.1 \pm 3.0$ ) and 3D ( $2.6 \pm 1.2$ ) cultures of the 1:10 “high” seeding density (Figure 5.3e). Progenitor expansion was higher in 2D versus 3D in the 1:100 condition ( $4.1 \pm 2.7$  versus  $0.4 \pm 0.3$ ,  $p=0.0092$ ). However, total cell recovery from the 3D microscaffolds was challenging to achieve, and thus quantification of hematopoietic expansion may have been underestimated for the 3D conditions, especially for the scarce CD45<sup>+</sup>Lin<sup>-</sup>cKit<sup>+</sup> progenitors in the 1:100 condition, which tightly associate to the stroma to form cobblestone-like colonies.

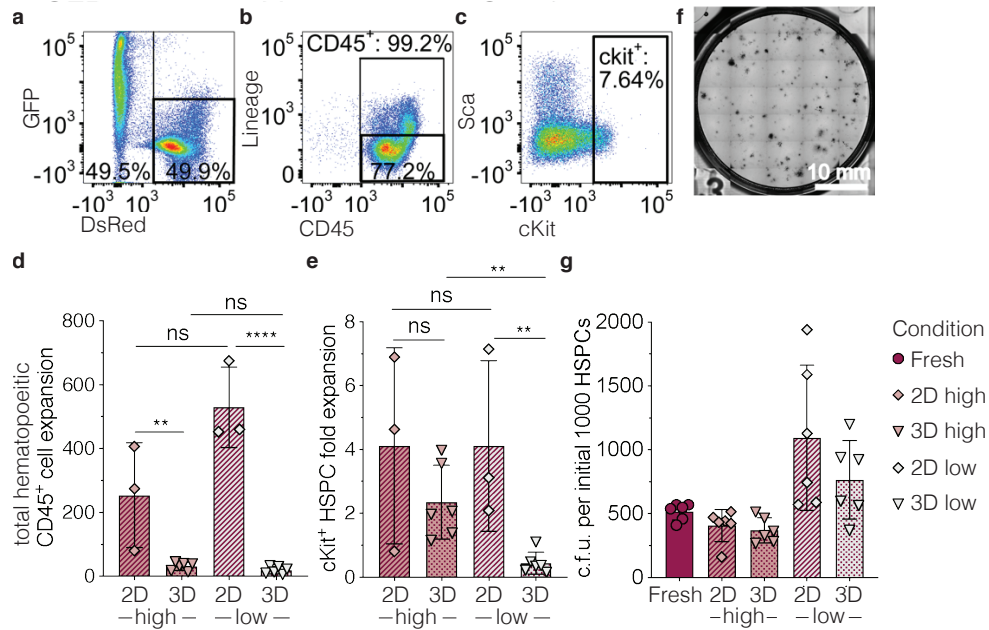


**Figure 5.3** | 3D culture outcome compared to 2D controls via flow cytometry and colony forming unit assays. **a-c** Example flow cytometry analysis gating (Coculture in CCM scaffolds, initial seeding density 1:10 KLS:OP9, analysis at 12 days. After initial gating to live cells (low DAPI labeling due to intact membrane, isolation from counting beads, not shown), we performed a first gating using the intrinsic DsRed (HSPC and progeny) and GFP (OP9) expression (**a**). The DsRed<sup>+</sup>GFP<sup>+</sup> was further analyzed for Lineage and CD45 markers, allowing to isolate the Lin-CD45<sup>+</sup> population (**b**). The stem and progenitor fraction was obtained as cKit<sup>+</sup> cells within the Lin-CD45<sup>+</sup> population (**c**). **d** Total CD45<sup>+</sup> expansion through flow cytometry, identifying 2D and 3D cell proliferation for both the 1:10 and 1:100 seeding densities. **e** Total CD45<sup>+</sup>, cKit<sup>+</sup> cell expansion for the same conditions, demonstrating closer similarities between the four conditions. **f** Total colony count after 7 days in methylcellulose medium, after harvesting total cells from the CCMs (after 12 days of in vitro culture). Scale bar is 10mm. Error bars represent mean  $\pm$  s.d.

In order to complete the analysis with functional hematopoietic potency in the co-cultures, we performed CFU assays, which quantify the number of oligopotent progenitors able to form functional hematopoietic clonal colonies after a 7-10 day culture in semi-solid, cytokine-rich media. Like for the FACS analysis, 2D and 3D HSPC/OP9 co-cultures seeded at “low” (1:100) and “high” (1:10) relative HSPC:OP9 ratios were enzymatically digested to obtain a single cell suspension after a 12 day co-culture and plated for CFU assay. Figure 5.3f shows an example of a CFU assay at 7 days. For the purpose of comparison and to obtain the total number of CFUs produced by each culture condition, CFU counts were normalized per 1000 HSPCs seeded with OP9 cells at Day 0 (starting HSPC concentration: 1000 KLS, n=6 for each condition). The number of CFUs was not significantly different ( $p=0.166$  via Two-Way ANOVA) between the 2D and 3D conditions at each seeding density (1:10 or 1:100, Figure 5.3g), which is congruent with the CD45<sup>+</sup>cKit<sup>+</sup> hematopoietic progenitor quantification by flow cytometry for the 1:10 “high” density (Figure 5.3b). The number of relative colonies is significantly higher in the “low” (1:100) seeding condition (2D:  $1093.86 \pm 567.88$ , 3D:  $764.69 \pm 306.84$ ) as compared to the “high” (1:10) condition (2D:  $408.34 \pm 126.32$ , 3D:  $369.42 \pm 99.46$ ), suggestive of either nutrient competition or a negative paracrine regulation by differentiating hematopoietic cells at higher CFU seeding densities. Compared to controls obtained by direct plating of fresh KLS cells without culture prior to the methylcellulose assay, we

observed a maintenance, or minor expansion, of the functional HSPC compartment. This is expected and reflects a biomimetic, homeostatic condition, as there is no exogenous addition of any of the cytokines commonly used for *in vitro* HSPC expansion (e.g. thrombopoietin, stem cell factor, or Fms-related tyrosine kinase 3 ligand, (Costa et al., 2018)). The aim here was indeed to provide a minimalistic system enabling further screening without interference from exogenous cytokines. Overall, we conclude from the *in vitro* functional characterization of our HSPC/OP9 co-cultures that 3D co-culture in CCMs promotes similar expansion of functional hematopoietic progenitors to conventional 2D conditions, with a reduced output of differentiated CD45<sup>+</sup>cKit<sup>+</sup> hematopoietic cells.

### Injection of co-seeded CCMs demonstrates both OP9 and donor hematopoiesis in the engineered niche over 12 weeks *in vivo* in NSG immunodeficient mice

Compressible porous scaffolds have previously demonstrated promise in providing an injectable solution to traditional cell-based tissue engineering techniques (Bédurier et al., 2015; Bencherif et al., 2012). In addition to the preservation of hematopoietic progenitor function in the 3D HSPC/OP9 co-culture conditions, we were interested in testing the biocompatibility and hematopoietic support capacity of the HSPC/OP9-loaded CCMs *in vivo*.

Figure 5.4a-d shows the workflow for transitioning from a microcarrier-like suspension culture to a transplantable co-culture biomaterial. After a predefined time of *in vitro* culture as a dilute suspension (Figure 5.4a), the CCMs are collected and dehydrated to a controlled level by a device specifically designed for that purpose. The device applies a pre-set hydrostatic pressure to the CCMs by means of a capillary conductor. As the hydrostatic pressure sustained by the biomaterial constituted by the CCM is strongly linked to its concentration, this ensures constant material consistency compatible with regards to injection and hematopoietic niche reconstitution *in vivo*. Here, we set a hydrostatic pressure difference of 0.2kPa, equivalent to a fluid level difference of about 2cm, to concentrate the co-culture biomaterial to  $26 \pm 3 \text{ mg/ml}$ . At this concentration, the material remains easily injectable and matches the kPa range for the vascular part of the bone marrow niche (Bello et al., 2018). After concentration of the co-culture biomaterial, the transfer tip is fitted onto a syringe, and assembled with a catheter (Figure 5.4c) for subcutaneous injection (Figure 5.4d). By performing the injection into a cell-culture dish containing medium, we assessed whether the procedure of partial dehydration and passage through the catheter during the injection would be harmful to the cells (Figure 5.4e). We found that we are able to retain high viability of cells immediately after injection and 24 hours-post injection, as compared to the pre-injection controls in both the GFP<sup>+</sup> OP9 cells and DsRed<sup>+</sup> HSPCs (Figure 4e;  $p=0.822$  via Two-Way ANOVA).

For assessment of the *in vivo* performance of the co-culture biomaterial, we injected the living co-culture biomaterial prepared via the dehydration device into the subcutaneous dorsal region of NSG (NOD SCID- $\gamma$ ) mice. The implants were easily visible externally up to the end of the 12-week follow-up period (Figure 5.4f). At sacrifice, skin flaps from the back of the animal revealed macroscopic vascularization of the injected scaffolds within the dermal tissue of animals.



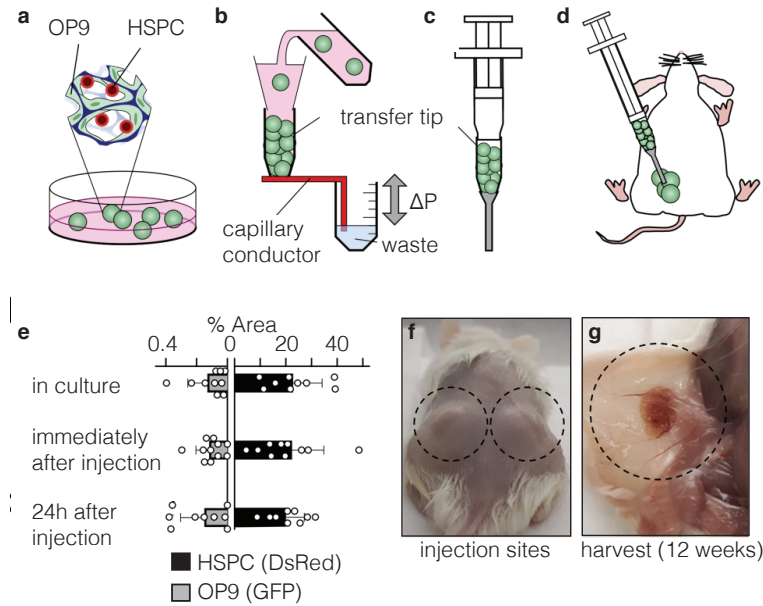


**Figure 5.4** | Implantation of CCM-based co-cultures. **a** After seeding, the co-cultures can be cultured *in-vitro* as classical microcarrier suspension cultures. **b** To prepare an implant, the material is partially dehydrated to by equilibrating to a predefined hydrostatic pressure level ( $\Delta P$ ), typically on the order of 0.2kPa (ca. 2cm water column). This is done in a specifically designed transfer tip. **c** Once equilibrated and filled with implantable co-culture biomaterial, the transfer tip is attached to a syringe and an implantation catheter (to avoid accidental intravascular injection). **d** The co-culture biomaterial is injected subcutaneously. **e** *In vitro* assessment of injection viability as quantified through GFP<sup>+</sup> OP9 BMSC and HSPC cell confluence before, immediately after, and 24 hours after injection (n.s.). Biomaterial seeded 1:100 HSPC:OP9, injected after one day *in vitro*. **f** Macroscopic external view of the implant in the subcutaneous dermal tissue 12-weeks post-implantation. **g** Visibly vascularized scaffold after sacrifice, seen from the inside of the skin flap.

We carried out two independent sets of experiments to assess the *in vivo* evolution of the co-culture biomaterial. In both sets, the samples consisted of CCMs seeded with HSPCs and OP9 cells, at the 1:10 initial seeding ratio and cultured for 14 days prior to partial dehydration and implantation. In the first set, we included a control group of scaffolds seeded with OP9 only, whereas in the second set, the control group consisted of completely cell-free CCMs. The aim was to dissect the effect that the scaffold alone, the OP9-seeded scaffolds, or the OP9/HSPC co-seeded scaffolds would have on the *in vivo* outcome. In both sets, after 12 weeks *in vivo*, hematoxylin and eosin (H&E) standard histological staining revealed intact scaffold particles (Figure 5.5a, 5.5d and 5.5g). In all conditions, the scaffold was host to diverse cell types. Immunohistochemistry (IHC) against GFP revealed strong persistence of confluent OP9 stroma across the scaffolds shown by the large areas stained in brown (Figure 5.5e and 5.5h). Such staining was absent from the initially cell-free CCM implants (Figure 5.5b), providing evidence for the specificity of the anti-GFP staining. Similarly, anti-DsRed IHC revealed a positive signal only for scaffolds loaded with both GFP<sup>+</sup> OP9 cells and DsRed<sup>+</sup> HSPCs (Figure 5.5i), indicating persistence of hematopoietic cells from the donor DsRed<sup>+</sup> HSPCs 12 weeks after implantation. Lack of DsRed<sup>+</sup> signal on scaffolds loaded with only OP9 cells (Figure 5.5f) and initially cell-free implants (Figure 5.5c) attests to the specificity of the anti-DsRed IHC.

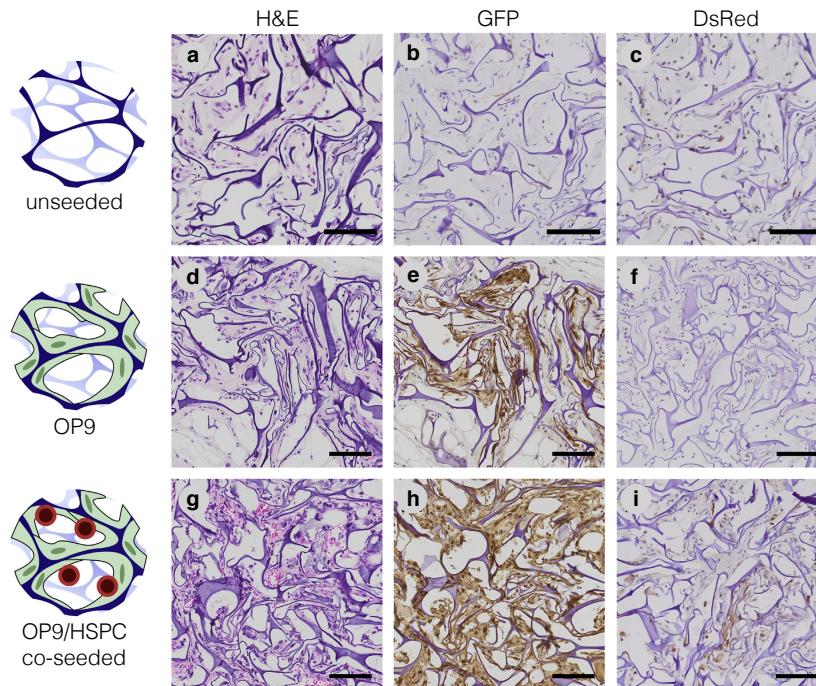


**Figure 5.5** | Histology and cellular composition of implanted scaffolds. Unseeded CCMs (**a-c**), as well as CCMs cultured with OP9 (**d-f**) or with 1:10 “high” co-cultures of OP9 and KLS cells (**g-i**) were implanted into the dorsal skin of NSG mice, and retrieved after sacrifice at 12 weeks. Samples were processed for hematoxylin/eosin (H&E) staining (**a, d, g**), as well as immunohistochemistry with primary antibodies directed against GFP (**b, e, h**, marker for OP9 cells) and DsRed (**c, f, i**, marker of HSPC and progeny). Scale bars are 100 $\mu$ m.

The HSPC/OP9-loaded scaffolds macroscopically appeared to vascularize better and conserved a higher proportion of donor-derived stroma (Figure 5.6f and 5.6i) than cell-free scaffolds (Figure 5.6c). Indeed, HSPC/OP9-seeded scaffolds showed a 6.6 times higher vascularization ( $p=0.003$ , t-test with Welch approximation after log transform) than cell-free scaffolds, as quantified by relative number of CD31<sup>+</sup> vessel segments (Figure 5.6j).

In the study groups, we observed multinucleated DsRed<sup>+</sup> cells, suggesting the presence of specialized donor-derived hematopoietic progeny within the implants, morphologically reminiscent of megakaryocytes, the specialized sessile hematopoietic cells responsible for platelet production. In order to assess megakaryocytic differentiation within the implant, we therefore performed von Willebrand factor (vWF) IHC stains (Figure 5.6a, 5.6d and 5.6g). Only HSPC/OP9-seeded scaffolds contained highly positive vWF<sup>+</sup> cells (Figure 5.6d and 5.6g), indicative of megakaryocyte lineage commitment within the scaffold, and thus of active *in situ* hematopoiesis. Finally, in order to assess adipocytic differentiation within the implanted scaffolds, we performed IHC stains with perilipin (Figure 5.6b, 5.6e and 5.6h). HSPC/OP9-seeded scaffolds (Figure 5.6e and 5.6h) but not the unseeded controls (Figure 5.6b), presented frequent areas of adipocyte ghosts with a cytoplasmic perilipin positive signal characteristic of mature adipocytes. In summary, we can conclude from *in vivo* experiments that murine HSPC/OP9-seeded CCM scaffolds can be implanted in NSG mice to produce highly vascularized structures which retain donor stroma and contain locally active hematopoiesis as well as interspersed adipocytes, features reminiscent of adult marrow (Weiss, 1981).



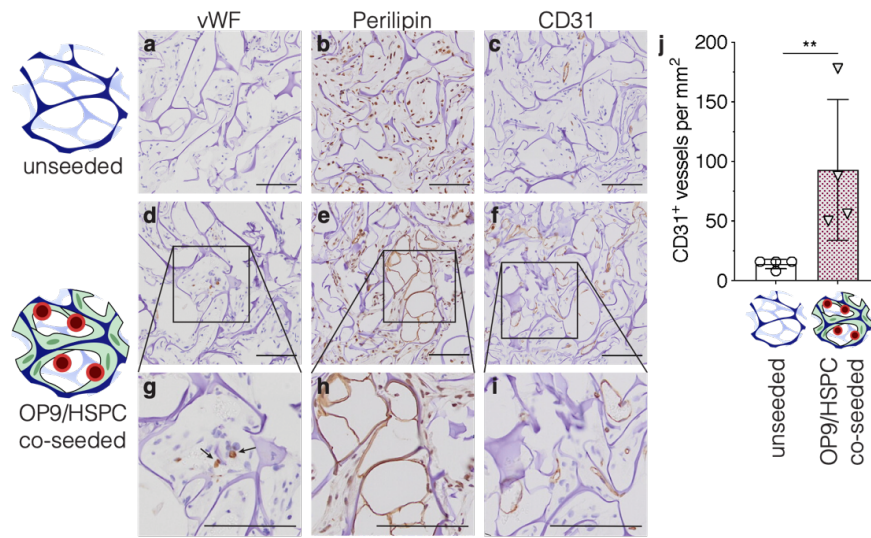


**Figure 5.6** | Immunohistochemistry of scaffolds transplanted *in vivo*. Unseeded scaffolds (a-c) and HSPC/OP9-seeded scaffolds (d-i) were recovered 12 weeks after subcutaneous transplant. Paraffin sections of scaffolds were stained with anti-vWF (a, d, g, arrows indicate megakaryocytes), anti-Perilipin (b, e, h), and anti-CD31 (c, f, i), and antibodies. Scale bars are 100 μm. CD31<sup>+</sup> vessels were quantified (j), error bars indicate mean ± s.d. \*\*P<0.003 by Welch's t-test.

## Conclusions

In this study, we developed an easy-to-use system enabling smooth transition from *in vitro* co-culture to an injectable that self-assembles *in situ* to recapitulate structural and mechanical features of the hematopoietic marrow. Its aim was to bridge the gap between various defined co-culture systems *in vitro* and more realistic but complex *in vivo* niches such as long-described heterotopic ossicle formation (Tavassoli and Crosby, 1968; Maniatis et al., 1971; Friedenstein et al., 1982). In orthopedics, porous scaffolds have long been used in conjunction with BM aspirates to enhance bone formation (Yoshii et al., 2009). More recently, they have also been identified as a solution enabling localization of BM niches to a biomaterial, enabling thorough *in vitro* testing of scaffolds prior to implantation, and also targeted implantation (Shah et al., 2019; Shih et al., 2017). Yet, due to the bulk format of these scaffolds, it is difficult to perform live imaging or high-throughput screening on them. We therefore sought to combine the advantages of a microcarrier culture system with the mechanical robustness of a bulk scaffold for hematopoietic niche engineering.

To achieve this goal, we based our system on compressible sub-millimetric carboxymethylcellulose scaffolds. *In vitro*, they can be used as classical microcarrier cultures. Additionally, *in vivo*, these specifically engineered CCM scaffolds self-assemble by microscaffold interlocking (Beduer, Bonini, Verheyen et al., manuscript under revision). The process creates a mechanically stable implant, inducing

colonization with a fibrovascular stromal tissue. This dual behavior enables smooth injection of arbitrary scaffold volumes, followed by *in situ* regeneration of a porous niche structurally resembling trabecular bone, with mechanical moduli in the vicinity of 1kPa (measured *ex-vivo*, as reported for the vascular niche of the BM (Bello et al., 2018)). From a practical point of view, CCMs are easily fabricated with standard equipment (freezer, autoclave for sterilization, laminar flow hood for coating under sterile condition), such that production is easily scalable at affordable cost and compatible with Good Manufacturing Practice (GMP) production.

To enable the adhesion of the stromal OP9 cells, the CCMs feature covalently bound collagen I (Bédurier et al., 2018; Serex et al., 2018). Indeed, among a series of extracellular matrix molecules, collagen type I has been shown to provide the highest proliferation levels with KLS cells (Choi and Harley, 2017). Further, contrary to Matrigel used for generation of hematopoietic ossicles (Bello et al., 2018; Hughes et al., 2010; Reinisch et al., 2017), collagen type I is a single protein of defined composition that is amenable to clinical use (Lecarpentier et al., 2018; Salvadè et al., 2007). OP9 cells have been shown to direct pluripotent stem cells towards the hematopoietic fate, and also have an ability to maintain engraftable hematopoietic stem cells in *in vitro* 2D co-culture systems for up to 2 weeks in the absence of additional cytokines (Naveiras et al., 2009). In this study, the combination of OP9 cells and CCMs was found not only to enable the baseline culture of HSPCs over 12 days in culture, but also to provide for easy and effective implantation of the hematopoietic scaffolds *in vivo* for a follow-up of 12 weeks in NSG mice.

By stable transfection of OP9 cells with GFP and the usage of KLS from DsRed mice, the CCMs were readily imaged in 3D culture, and serial imaging gave qualitative insight into early-stage HSPC nestling and cobblestone-like colony formation within the 3D scaffolds. We believe this is indicative of a similar hematopoietic supportive behavior from the stromal cells as compared to 2D controls. We further analyzed the cellular populations phenotypically by flow cytometry, and functionally by CFU assays. We found the output of the 3D cultures, measured as total fold hematopoietic expansion (CD45<sup>+</sup>), to be lower in 3D than in 2D (Figure 5.3d). However, the HSPC compartment, as measured by the CFU counts in the 2D versus 3D cultures (Figure 5.3g), is essentially unaffected by this lower output of total hematopoiesis. As the 3D cultures are effectively concentrated in a much smaller volume with higher local cytokine levels (Rödling et al., 2017), our results point towards differential regulation of hematopoiesis in our configuration leading to HSPC enrichment, which may be ascribed to the difference in balance of the hypothesized “vascular” versus “endosteal” niches (Leisten et al., 2012; Sánchez-Aguilera and Méndez-Ferrer, 2017).

Our CCM-based co-culture system was not only amenable to live, high-resolution imaging on sub-samples obtained by simple pipetting, but also allowed for standardized aggregation prior to injection by the use of a specifically designed dehydration device. This avoided loss of cell viability during preparation and injection. At the end of the experiment, the scaffold aggregates were both visible beneath the surface of the animal’s skin and were also easily identifiable with integrated host vasculature after opening of the dermal tissue (Figure 5.4). Histological staining showed the presence of the GFP<sup>+</sup> OP9 cells with colonies of DsRed<sup>+</sup> HSPCs interspersed throughout the recovered tissue sections. Moreover, these implanted CCMs demonstrated no morphologically visible innate inflammatory foreign body response or fibrous capsule surrounding the injected materials. This unique finding supports the hypothesis that homeostatic extramedullary hematopoiesis may be engineered *in vivo* in the form of subcutaneous implants, in the absence of ossification surrounding a marrow cavity, analogous to the soft-tissue masses of benign extramedullary hematopoiesis, often intermixed with adipose tissue, that occur in humans upon extreme

hematopoietic demand (Roberts et al., 2016). Previous systems have employed calcified bone surrounding an engineered niche to model hematopoiesis *in vitro* or to encourage hematopoiesis once implanted *in vivo* (Torisawa et al., 2014; Holzapfel et al., 2015; Shafiee et al., 2017; Ventura Ferreira et al., 2016; Blache et al., 2016; Shih et al., 2017; Reinisch et al., 2017; Bourguine et al., 2018). To our knowledge, the system presented here is the first of its kind to show hematopoiesis after long-term *in vivo* subcutaneous transplantation of BMSCs without any calcified bone component.

### Outlook

In this study, we were also cognizant of the multi-cellular complexities associated with BM function, along with recent models incorporating BM adipose tissue *in vitro* (Henriksson et al., 2017; Fairfield et al., 2019). We found mature adipocytes within the scaffolds transplanted with both OP9 cells and HSPCs, indicating that our model may be of use to study the complex relationships between hematopoiesis and adipocytes *in vitro* and *in vivo* (Mattiucci et al., 2018), a field that has been hampered by the difficulty of immobilizing mature adipocytes in co-culture.

Future work follows the premise of further recapitulating the BM microenvironment by manipulating culture conditions, including addition of hematopoietic cytokines, and the modification of the stromal compartment by replacing the OP9 cells in the CCMs with a human CAR cell line equivalent for a minimalistic niche, or possibly a mix of cell lines to better reflect the niche heterogeneity. Moreover, by using primary human samples, we may be able to further address the limitations of patient-derived xenograft PDX models (de la Puente et al., 2015; Sánchez-Aguilera and Méndez-Ferrer, 2017; Shah and Singh, 2017; Song et al., 2019). In this respect, our system offers new perspectives for personalized-medicine techniques with the possibility for high-throughput screening *in vitro* followed by validation of selected treatments in a direct implantation *in vivo*.

In summary, we present in this report a novel 3D co-culture system of HSPCs and BMSCs for studying BM hematopoiesis on chemically defined, collagen-coated cryogel-based scaffold microcarriers. The method for co-seeding two cell populations of the BM is simple and scalable, requiring no exogenous cytokine supplementation for hematopoietic progenitor cell maintenance and proliferation. We further designed a dehydration device enabling on-the-fly preparation of a paste-like injectable implant from dilute suspension cultures. Through minimally invasive subcutaneous transplantation of this living implant, both the stromal and hematopoietic cell populations were able to survive *in vivo* for 12 weeks, showing incorporation into the native tissue via de novo vascularization and positive staining for donor GFP<sup>+</sup> (OP9 BMSCs) and donor DsRed<sup>+</sup> cells (HSPC progeny), including megakaryocytes. Moreover, our tissue engineered BM has provided a first indicator of supporting subcutaneous, extramedullary hematopoiesis in healthy adult murine tissue without simultaneous ossification. We observe some induction of adipogenesis, pointing towards bidirectional communication between the niche and the hematopoietic compartment. A tool allowing to study such bidirectional signaling could be invaluable in both research on PDX models and radiation-induced BM adiposity. In conclusion, this 3D engineering BM niche demonstrates promise to better model the BM microenvironment through a defined *in vitro* to *in vivo* transition, enabling future work in fundamental and patient-specific applications in hematology and bone marrow biology at large.

## Methods

### Scaffold fabrication

Compressible carboxymethylcellulose scaffolds are produced by cryogel bulk scaffold synthesis, using established protocols with minor modifications. Briefly, a reaction mix consisting of 13.56mg/ml carboxymethylcellulose (AQUALON CMC 7LF PH, 90.5 KDa, DS: 0.84) and 0.486mg/ml adipic acid dihydrazide, buffered with 6.3mg/ml PIPES neutralized to pH 6.7 by 1.2mg/ml NaOH was prepared and filtered through a 0.22 $\mu$ m filter (Stericup). After activation by 2.7mg/ml 1-Ethyl-3-(3-dimethylaminopropyl)-carbodiimide (EDC), the mix was frozen at -20°C in 30ml syringes. After 48 hours of cryo-incubation, the syringes were thawed. The scaffolds thus obtained were then fragmented through a 22G catheter to obtain a suspension of microscaffolds (Beduer, Bonini, Verheyen et al., manuscript under revision). These microscaffolds were then extensively washed, and autoclaved for sterilization.

We express polymer mass, and respectively its concentration, of microscaffold suspensions as dry weight and dry weight per volume. For dry weight determination, microscaffolds contained in a solution or suspension of interest are collected on a 40 $\mu$ m cell strainer, followed by thorough washing with deionized (DI) water three times, and oven- or microwave-drying of the remaining polymerized material to constant weight (within 1mg).

### Collagen CCM surface coating

To allow stromal cell (OP9) adhesion, we modified the surface of the sterile microscaffolds with collagen type I (from bovine skin, catalog no. C4243, Sigma), producing collagen-coated carboxymethylcellulose microscaffolds (CCM). For this, we used a previously published protocol with adaption to the particulate nature of the CCMs (Serex et al., 2018). Briefly, we dehydrated the microscaffolds using a cell strainer in a SteriCup filtration system (catalog no. C3240). They were washed sequentially with DI water and acetic acid buffer (pH=4, 100mM). Then, the microscaffolds were immersed in a coating solution containing 10% collagen type I (mass of protein/dry mass of microscaffolds) diluted in acetic acid buffer (pH=4, 10mM). After coating, the collagen-coated carboxymethylcellulose microscaffolds (CCM) were rinsed twice with DI water in order to remove the excess of non-adsorbed proteins. Thereafter, covalent crosslinking of the collagen was performed by immersing the CCMs in a solution containing EDC (1mg/ml) and MES buffer (pH 4.5, 100mM) in deionized water for ten minutes. Finally, the CCMs were abundantly rinsed with DI water and a solution of Na<sub>2</sub>CO<sub>3</sub> (pH 11, 100 mM) and kept in PBS at 4°C.

### Animals

All experimental procedures were approved by the Animal Care and Use Committee of the Canton of Vaud (ACUC, Vaud, Switzerland). All animals were hosted in the EPFL facilities and were kept under a controlled 12 hours light/dark cycle and at constant room temperature 22 $\pm$ 2°C. DsRed C57BL/6JRj

(DsRed) adult male mice were sacrificed and tibiae and femurs were collected for DsRed<sup>+</sup> HSPC isolation. 8-16 weeks old NOD SCID- $\gamma$  (catalog no. NSG 5557, Jackson laboratories) immunodeficient female mice (n=3 control; n=6 experimental) were used as recipients in the transplantation model.

### Culture of OP9 stromal cells

Using an established murine mesenchymal stromal cell line (OP9 cells) (Nakano et al., 1994), cells were expanded at 70-80% confluency for one to two weeks in alpha-minimum essential media (MEM $\alpha$ ) plus Glutamax (catalog no. 32561, ThermoFisher), 10% fetal bovine serum (FBS, catalog no. 10270-106, GIBCO), and 1% Penicillin/Streptavidin (P/S, catalog no. 15140122, Thermo Fisher Scientific). OP9 cells were donated from the Daley laboratory (McKinney-Freeman et al., 2009), who received them directly from the Nakano laboratory (Nakano et al., 1994). They were transfected at passage 7-10 with a constitutively expressed GFP lentiviral construct, as specified below, and expanded. Cells were kept at 37°C and 5% CO<sub>2</sub>, and were passaged every 2-4 days at 3:1 or 4:1 ratio, until they reached 70-80% confluency. OP9 cells were not kept in culture for more than three weeks before use in experiments. Cells were washed with PBS (10010056, Life Technologies) and trypsinized with 0.05% Trypsin-EDTA (catalog no. 25300054, Life technologies), counted, and kept in suspension on ice prior to use.

### OP9 stromal cell transfection

Lentiviral particles for GFP introduction were produced by transfecting HEK293T cells using XtremeGene HP transfection reagent with lentiviral packaging plasmid pCMVR8.74 (catalog no. 22036, Addgene), VSV-G envelope expressing plasmid pMD2.G (catalog no. 12259, Addgene) and third-generation transfer vector pRRLSIN.cPPT.PGK-GFP.WPRE (catalog no. 12252, Addgene); all three plasmids were a gift from Didier Trono. Supernatants were collected at 36 and 60 hours post transfection, filtered through 0.22 $\mu$ m filters and concentrated 1000x using ultracentrifugation. OP9 cells were stably transfected using the concentrated virus titers. Transfected cells were sorted based on GFP expression using FACS after three weeks of culture.

### Isolation of HSPCs

DsRed adult mice were euthanized with CO<sub>2</sub> according to approved protocols and both tibiae, femurs, and pelvis extracted. After cleaning the bones of all soft tissue, they were kept in PBS on ice until all bones were isolated. Bones from age and gender-matched C57BL/6J wild type controls were isolated in parallel for fluorescence-activated cell sorting (FACS) single-color controls. Bones were subsequently crushed using a mortar and pestle in buffer solution (PBS, 1mM EDTA (catalog no. 15575020, Thermo Fisher Scientific), 2% FBS), until no large chunks of cells were visible. All cell isolation steps were carried out on ice. Cells in suspension and the crushed bones were washed through a 70 $\mu$ m cell strainer and spun down (10 minutes, 300g, 4°C). The cell pellets were resuspended in red blood cell lysis buffer (catalog no. 420301, BioLegend) for 30 seconds, before being diluted with buffer solution, and spun down again (5 min, 300g, 4°C). The cell suspension was stained with a lineage antibody cocktail, washed, and incubated with magnetic beads according to manufacturer's instructions for hematopoietic Lineage depletion (Lin depletion kit, catalog no. 558451, BD Pharmingen). The total bone marrow cell pellet was resuspended in 3mL volume and loaded into a magnetic separation cell Sorter (AutoMACS, Miltenyi) to remove all lineage positive (Lin<sup>+</sup>) cells in suspension. The resulting cells were then blocked for 15 minutes on ice (5 $\mu$ g/ml hIgG; I4506-10MG, Sigma Aldrich), and finally stained for one hour on ice with lineage

## Chapter 5 | Biomimetic transplantable bone marrow co-culture system

Streptavidin-PO (1/200), as a conjugate to label any remaining Lin<sup>+</sup> cells, as well as c-Kit PE-Cy7 (1/200), Sca-1 APC (1/100). After washing the stained cells with buffer solution and straining through a 85µm filter, the cell suspension was run through a FACS system (Aria Fusion) and the resulting Lin<sup>-</sup>c-Kit<sup>+</sup>Sca-1 (KLS) cells were sorted into Iscove's Modified Dulbecco's Medium (IMDM) + Glutamax, 25mM HEPES (31980022, Life Technologies) supplemented with 10% FBS and 1% P/S. In total, 2-3 adult male DsRed<sup>+</sup> mice (aged 8-12 weeks) were euthanized to collect approximately 200,000 KLS<sup>+</sup> cells in suspension for each experiment. After FACS, cells were kept on ice for approximately 1-2 hours until co-seeding with OP9 cells on the scaffold.

### Co-culture of HSPCs and stromal cells

All cells for co-seeding experiments were cultured in 50% fresh basal media (IMDM + Glutamax 25mM HEPES, 10% FBS, 1% P/S) and 50% conditioned IMDM media (CM). Conditioned media was obtained by culturing confluent GFP<sup>+</sup> OP9 cells with IMDM media for two days (48 hours), filtering the CM, and freezing the media for no longer than two months at -20°C. After HSPCs and OP9 cells were collected in suspension and counted, cells were kept on ice for maximum 1 hour.

**3D co-seeding:** Collagen-coated microscaffolds (CCMs, 13.5mg/ml in PBS) were dried using a cell strainer in a SteriCup filtration system (catalog no. C3240), using an autoclave cloth to transmit the capillary pressure. Once dried, the globule of CCMs was transferred to a 6-well ultra-low adhesion plate (catalog no. CLS347, Corning) using the tip of a 2ml stereological pipette. For each condition, the two cell types (HSPCs, OP9 cells) were combined, spun down, and re-suspended in a minimal amount of media (approximately 100µl in total). For 2mg of scaffold per well (dry weight), the following cell ratios were used for the 1:10 “high” seeding (150,000 OP9 cells; 15,000 HSPCs) and 1:100 “low” seeding (150,000 OP9 cells; 1,500 HSPCs). After adding the cell suspension (~100µl) to the dried scaffold on the ultra-low adhesion plates, the CCMs with cells were incubated for one hour at 37°C and 5% CO<sub>2</sub>. After 1 hour, 3ml of IMDM media (50% conditioned, 50% fresh) was added per well. Co-seeded CCMs were then left in culture for 12 days, with a supplementary dose of 3ml IMDM media (50% conditioned to 50% fresh basal media) at day seven, without removing any of the previous media.

**2D co-seeding:** OP9 stromal cells were plated on tissue culture-treated plates at a density of 120,000 cells per well in a 6-well plate one hour prior to HSPC seeding (~13,000 cells/cm<sup>2</sup>), using IMDM media (50% conditioned: 50% fresh). HSPCs were seeded at the previously established co-seeding ratios, 1:10 “high” (12,000 HSPCs per well) and 1:100 “low” (1,200 HSPCs per well). If limited by HSPC cell number, the 2D condition was performed with only the low seeding density. Cells were fed at D7, complementary to the 3D culture timeline, with 3ml added and no media removed, then cultured at 37°C and 5% CO<sub>2</sub> for 12 days in total. Co-seeding experiments were repeated in at least two separate experiments, with technical triplicates within each experiment.

### Compression testing of cells on scaffolds

After three months of culture with weekly half-media changes, the medium was complemented with Hoechst 33342 (0.1µg/ml), which stains DNA but also to some extent scaffold filaments due to its cationic nature. The scaffold suspension was then transferred to a compression chamber, for a first viability assessment (see below). This operation resulted in an estimated CCM concentration of 8±2 mg/ml. On this suspension, we performed a first linear compression by 75% (10µm/s compression rate

at initial sample heights around 2.5mm). In addition, we performed a second compression by nominally 100% for positive control of cell killing by excessive mechanical forces. We assessed viability by confocal imaging. After every defined set point of compression, 0%, 75%, and 100% respectively, at least five images for every tested sample were taken with a confocal microscope (Zeiss LSM 700 Inverted Confocal Microscope). This procedure was repeated for two independent replicates. The images were analyzed by manually counting OP9 cells (green), HSPCs (red) and dead cells (strongly blue nuclei with loss of both red and green fluorescence). From this, both viability and the ratio of OP9 cells to HSPCs within the viable population were determined.

### Isolation of cells at day 12

Cells were collected for each condition (high/low; 2D/3D) in three fractions: cells in suspension, cells adherent to the CCMs, and any cells adherent to the ultra-low adhesion plates. For cells in suspension, media was collected in a 50ml falcon tube, and cells were washed and collected twice with serum-free media. For the CCMs adherent fraction, cells were detached via enzymatic digestion as follows. CCMs were transferred to 24 well plates with a 1000  $\mu$ m pipette tip and 1ml of collagenase I (catalog no. 17100-017, ThermoFisher Scientific) 0.04% was added per well of CCMs for 25 minutes at 37°C and 5% CO<sub>2</sub>. The collagenase digestion was stopped with media complemented with serum, and a stereological pipette was used to dissociate any cells from the CCMs. Finally, cells in solution were run through a 100 $\mu$ m cell strainer and collected for further manipulation. Trypsin digestion was used for the very limited number of cells adherent to the ultra-low adhesion plates. Cells were spun down and re-suspended in a buffer solution. At this point, each of the conditions (four total: 2D/3D, high/low seeding density) and each replicate (n=3 per experiment; two independent experiments) were processed for flow cytometry and for methylcellulose colony forming unit (CFU) assays. Each fraction (non-adherent suspension, collagenase-digested CCM-associated, and bottom-adherent trypsin-digested) was processed separately and the results are presented for all fractions compounded after analysis, based on the total number of cells recovered per well for each of the fractions.

### Flow Cytometry

Cell suspensions for each condition and fraction were re-suspended with blocking solution (5 $\mu$ g/ml hIgG) for 10 minutes at room temperature and then Lineage cocktail was added (1:20 dilution) for 20 minutes on ice. After washing with buffer solution and filtered with a 85 $\mu$ m cell strainer, cells were pelleted and re-suspended with antibody mix for 45 minutes on ice. The antibody mix contained: c-Kit (PE-Cy7; 1:200), Sca-1 (BV711; 1:50), CD45 (AF700; 1:100), CD3 (BV421; 1:50), B220 (PE-Cy5; 1:50), CD11b (APC-eFl. 780; 1:1000), and Gr1 (APC; 1:500), diluted in BD Brilliant Stain Buffer (catalog no. 563794, BD Pharmingen). The antibody mix also contained a 1:4 dilution of BrightCount beads (catalog no. C36950, Invitrogen). Cells were then diluted with DAPI solution (PBS-EDTA and DAPI-UV at 1:5000) and run through a BD LSR II SORP flow cytometer, while resting on ice during the stain preparation.

### Methylcellulose Colony-Forming Unit Assays

Single cell suspensions, as isolated in 3D (non-adherent, scaffold-adherent, and bottom-adherent) and 2D (non-adherent and bottom-adherent), were separately kept on ice. Each fraction was plated in 1.1ml methylcellulose (M3434, STEMCELL Technologies) in duplicate for each condition and each replicate

## Chapter 5 | Biomimetic transplantable bone marrow co-culture system

for hematopoietic colony forming unit (CFU) assay (McNiece et al., 1990). CD45<sup>+</sup> cells were counted with FACS using BrightCount beads (catalog no. C36950, Invitrogen), to be able to back-calculate the exact number of cells plated. At days seven and ten, each CFU plate was read using a StemVision instrument (Stem Cell Technologies), and total colonies were assessed automatically (StemVision proprietary software) and verified manually on the acquired high-resolution whole-plate images according to colony number, size, and cell distribution (McNiece et al., 1990).

### Subcutaneous Transplantation

After 14 days of *in vitro* culture, seeded-CCMs in suspension were collected from the well plate and poured into the column of the drying device allowing for the CCMs to settle down into the reservoir and reach the desired polymer concentration ( $26 \pm 3$  mg/ml). This condenses the CCMs into a paste-like material with a Young modulus of  $1.2 \pm 0.6$  kPa, which we find sufficient to sustain a 3D architecture *in vivo*. Sterile syringes were used to aspirate 0.1ml of coated scaffold without cells, followed by 0.1ml of air to ensure separation between them. The reservoir with the sedimented cultured scaffold (50 $\mu$ l) was connected to a 1mL syringe and a 20G flexible catheter (BD Biosciences 381703) was plugged in the other end.

NSG mice were chosen for the experiments as OP9 stromal cells are derived from a mixed genetic background and therefore purely syngeneic transplantation was not possible. Prior to injections, anesthesia was induced in NSG mice with 4% isoflurane USP-PPC (Animalcare Ltd). An ophthalmic liquid gel (Viscotears, Alcon) was used to protect the eyes and local isoflurane was reduced to 2%. Mice were placed on a heating pad to keep the temperature constant during intervention, and the back of each mouse was shaved at the area of the injections. Betadine (Mundipharma Medical Company) was spread onto the shaved regions to disinfect the skin.

To perform the subcutaneous injection, a small orifice was created in the disinfected skin using a 18G needle and the 20G catheter (Tro-Vensite i.v. canula, Troge, Hamburg), connected to the loaded syringe, which was gently inserted subcutaneously about 2 cm from the pierced skin. For each mouse, two separate injections of 50 $\mu$ l each were performed subcutaneously on either side of the spine. No sutures were required. At the end of the procedure, the mice were placed back in the cage grouped per condition. The entire preparation of the scaffolds and all the injections were performed under the hood to ensure sterility throughout the whole procedure. Each injection, from start to finish, lasted less than 20 minutes per mouse.

Animals were treated with antibiotics in drinking water consisting of 30mg of Enrofloxacin (300 $\mu$ l of Baytril 10% ad us. vet, 100 mg/ml, Bayer) and 5mg of Amoxicillin (100  $\mu$ l of Amoxi-Mepha 200mg/4ml, Mepha Pharma AG) as well as 500mg of Paracetamol (Dafalgan®) in a total of 250ml sterile water for the entire duration of the study and replaced every seven days. Animals were monitored daily by the researchers, and after two weeks, they were monitored daily by animal care services.

### Sacrifice and samples harvesting

NSG immunodeficient mice were euthanized 12 weeks post-injections through inhalation of CO<sub>2</sub> (six minutes). The back was shaved gently to better localize the two implants. The samples were harvested in each mouse being careful to keep some subcutaneous tissue around to study the integration of the scaffolds within the normal tissue. Samples were then fixed for 24 hours in 4% paraformaldehyde at 4°C (10ml PFA in 15ml Falcon tube), washed three times with PBS, and embedded in paraffin.



## Histology

Tissues were fixed in paraformaldehyde (PFA), submitted for stepwise dehydration and embedded in paraffin blocks for sectioning at 3-4  $\mu\text{m}$  thickness with a rotary microtome (RM, Leica microsystems). After floating on a water bath to flatten, sections were mounted on glass slides (Superfrost+ slides, Menzel gläser). Paraffin sections were stained with Hematoxylin and eosine (H&E) using the Tissue-Tek Prisma automate (Sakura) and permanently mounted using the Tissue-Tek glas G2-coverslipper (Sakura) to assess morphology. Detection of rabbit anti-GFP (Abcam, ab6673, diluted 1:400), rabbit anti-Dsred (MBL, PM005, diluted 1:500), rat anti-CD31 (clone SZ31, Dianova, DIA-310-M, diluted 1:50), rabbit anti-vWF (Abcam, ab9378, diluted 1:100) or rabbit anti-Perilipin (Abcam, ab3526, diluted 1:200) was performed manually. After quenching with 3%  $\text{H}_2\text{O}_2$  in PBS 1x for 10 minutes, a heat pretreatment using 0.1M Tri-Na citrate pH6 was applied at 60°C in a water bath overnight. Primary antibodies were incubated overnight at 4°C. After incubation of a goat, a rat or a rabbit Immpress HRP (Ready to use, Vector Laboratories), revelation was performed with DAB (3,3'-Diaminobenzidine, Sigma-Aldrich). Sections were counterstained with Harris hematoxylin and permanently mounted. Number of CD31<sup>+</sup> stained vessels were counted in 2-7 images (500 $\mu\text{m}$  x 500 $\mu\text{m}$ ) covering the entire area of the sectioned scaffold (amounting to 2-7 images per scaffold depending on the size of the scaffold) for four scaffolds each in both the unseeded and seeded conditions.

## Microscopy and image quantification

Co-seeded CCMs were kept in 3D culture for 12 days *in vitro*. At days 1, 4, 7, and 11, a small volume of suspended CCMs were removed and transferred to a deep cavity glass microscope slide (produced in lab for imaging). Within an hour after transferring CCMs to the imaging chamber, they were imaged at varying magnifications (20x for imaging quantification; 63x for cell morphology) using a Zeiss LSM 700 Inverted Confocal Microscope. As the cells were endogenously labeled for GFP (OP9 cells) and DsRed (HSPCs), serial imaging was conducted at each time point without significant cellular manipulation. Each image acquired was kept to the same microscope settings as the D0 condition, though as more cells proliferated on the CCMs, laser power was changed to allow for clear image acquisition. In image processing, the ratio of DsRed<sup>+</sup> to GFP<sup>+</sup> cells was accounted for in order to compare cell proliferation over time. At end point, the seeded CCMs were stained with Hoescht 328 (0.1 $\mu\text{g}/\text{ml}$ ) to visualize the scaffold filaments themselves.

Images used for quantification were composed of a 25-z-stacked, volume-rendered image. To analyze the data, each fluorescent channel was separated and the compiled volume-rendered image was used. Each image/channel was analyzed using Fiji/ImageJ's threshold tool, with the resulting quantified fluorescent areas converted to cell numbers by using the mean area per cell, as established by manual identification of a subset of the cells. For each 3D experiment, a total of eight independent CCMs were analyzed from two experiments to plot the relative cell proliferation over time.

## Statistical Analysis

Values are shown as mean plus or minus the standard deviation (mean  $\pm$  s.d.). Student's t-test was performed for all experiments when comparing two conditions only, or a Two-Way ANOVA for multiple conditions over time. The p-value for statistical significance was  $P < 0.05$ .

## Chapter 5 | Biomimetic transplantable bone marrow co-culture system

### Author contributions

O.N. initiated the collaboration. D.N.T., F.B., J.T., M.A., O.N. and T.B. designed the study. P. B., F.B. and T.B. performed biomaterial fabrication. D.N.T., J.T., V.C. and F.B. optimized in vitro co-culture conditions. D.N.T. and J.T. performed in vitro culture and end-point experiments. M.G., D.N.T., F.B., J.T. and A.B. developed the in-vivo injection method. D.N.T. and M.G. performed in vivo experiments and J.T. performed end-point analysis. D.N.T., F.B. and J.T. analyzed data and compiled figures. S.H., M.A. and A.B. provided critical insights in biomaterial design and in the overall development of the co-culture system. D.N.T., J.T., F.B., T.B., and O.N. wrote the manuscript. All authors approved of the final form of the manuscript.

### Competing interests statement

A. Bédier and T. Braschler declare financial interest in Volumina-Medical SA, Switzerland. P. Burch and A. Bédier are now employees of Volumina-Medical SA. Some of the data in this manuscript has been submitted for a patent application. The other authors declare no conflict of interest.

### Acknowledgements

We would like to thank Aurelien Oggier, Dr. Shanti Rojas-Sutterlin and Dr. Philippe Renaud, (EPFL) their input on the experimental design throughout the project. OP9-GFP cells were generated by S.H., V.C. and O.N. while they were members of Prof. Matthias Lutolf's laboratory (EPFL), who kindly donated the cells for the study. The histology data was performed at or with the help of the EPFL Histology Core Facility, notably Dr. Jessica Sordet-Dessimoz. Flow cytometry analysis / cell sorting was performed in the EPFL Flow Cytometry Core Facility. We would also like to thank Thierry Laroche at the EPFL BioImaging & Optics Core Facility (EPFL-BIOP), as well as the Bioimaging Core Facility of the Faculty of Medicine of the University of Geneva for their assistance in training and imaging set up. Further, we thank the caretakers of the EPFL SV animal facilities for their maintenance and support of the long-term animal experiments. Finally, we would like to acknowledge funding sources from the Whitaker International Program (D.N.T.), the Anna Fuller Fund (J.T.), the Gebert-Rüf foundation (GRS-043/15 to A.B.), Swiss National Science Foundation (PP00P3\_183725 and PP00P3\_176990 to O.N.; PP00P2\_163684 and PZ00P2\_161347 to T.B.).

## **CHAPTER 6**

### **Perspectives and Future Directions**

## Synthesis

In this thesis, we aim to present quantitative imaging tools that allow for monitoring changes in bone marrow adipogenesis across the skeleton, and the identification of lipid composition at the single droplet level. Additionally, we have developed a biomimetic transplantable co-culture system to model the hematopoietic niche *in vitro* and *in vivo*. These novel methodological approaches have helped to reveal site-specific differences in hematopoietic recovery of the long bones and in hematopoietic support capacity of BM pre/adipocytes. Further investigations will reveal the distinct profiles of these cells and place them in the context of the BM niche.

**Chapter 1** explores the history of the BM microenvironment leading to the identification of the hematopoietic and skeletal stem cells through rigorous functional assays. These are beautiful examples of how the BMA field may aspire to approach the search for and eventual identification of the true BMAd precursor. Methodological developments will also aid in further characterize BMAd subpopulations and their differentiation axis, placing them in their niche proper within the marrow. Further, bioengineering approaches will be invaluable for applying BMA research in translating findings from bench to bedside.

With the advent of the BMA Society we have been fortunate to be involved in tackling fundamental and complicated issues in this nascent field. The methodological review presented in **Chapter 2**, discusses advancements in BMA research and minimal reporting guidelines established by the Working Group on BMA Methodologies this past year. We describe existing methodologies and discuss the challenges and future directions for 1) histomorphometry of BMAds, 2) *ex vivo* BMA imaging, 3) *in vivo* BMA imaging, 4) cell isolation, culture, differentiation and *in vitro* modulation of primary BMAds and BM stromal cell precursors, 5) lineage tracing and *in vivo* BMA modulation, and 6) BMA biobanking. We identify as accepted standards in BMA research: manual histomorphometry and OsO<sub>4</sub> 3D CE-μCT for *ex vivo* quantification, specific MRI sequences (WFI and H-MRS) for *in vivo* studies, and gene-expression or lipid-based assays for *in vitro* quantification of BMA. Emerging techniques are described which may soon come to complement or substitute these gold standards. Known confounding factors are presented, and use of the minimal reporting guidelines (Table 2.1) is encouraged to facilitate comparison across studies. These are important steps for facilitating advancement of the field of BMA.

Our first approach to facilitate reliable, reproducible, quantitative comparisons of BMA changes in the skeleton is in the form of a semi-automated bioimaging tool, *MarrowQuant*, developed for quantification of BM components in histological sections described in **Chapter 3**. Histological sample preparation has the advantage of being a standard of laboratories world-wide and sometimes used to aid in diagnosis of disease. A quantifiable approach to detect differences in BMA and other BM compartments would benefit researchers for standardized analysis in an unbiased manner. We have found quantification of BM hematopoietic cellularity with *MarrowQuant* to lie within the range of scoring by four independent clinical pathologists. Quantification of the total adipocyte area in whole bone sections compares with

volumetric measurements of lipid-rich areas by CE- $\mu$ CT upon OsO<sub>4</sub> staining of lipids. As a product of these measurements, we present here a standardized map of BM hematopoietic cellularity and adiposity in mid sections of bones in the standard homeostatic C57BL/6 mouse model. We observe the highly predictable red-to-yellow transitions in the proximal section of the caudal tail and in the proximal versus distal tibia. Additionally, we present a comparative skeletal map of adiposity and hematopoietic cellularity induced by lethal irradiation, with quantification of the red-to-yellow-to-red transition over two months in C57BL/6 femurs and tibiae. We find that, following HSC transplantation, *MarrowQuant* measurements of BM adipogenesis inversely correlates with kinetics of hematopoietic recovery, with comparable kinetics to quantification of the recovery *in vivo* through MRI. *MarrowQuant* was also tested on human trephine biopsies and successfully recognizes the BM adipocytic, hematopoietic and bone compartments, opening avenues for its application in experimental or clinical contexts that require standardized human BM measurements.

In **Chapter 4**, we provide an *in vitro* model of BM adipogenesis in the form of the OP9 adipogenic differentiation system described. By the current standard of lipid content supported by gene expression analyses, we show that spontaneously-differentiated OP9-adipocytes resemble primary labile rBMAdS while induced OP9-adipocytes possess the characteristics of stable cBMAdS. Indeed, sOP9-adipocytes have a higher content of SFAs with decreased *Scd1* but higher *Lpl* expression, while the reverse is true for iOP9-adipocytes with higher unsaturation content and *Atgl* expression, favoring a maturation of adipogenesis. This is supported by their differential hematopoietic support capacities directly on HSPCs in co-culture or indirectly via secreted factors, mimic the increased support by earlier adipogenic progenitors *in vivo*. We present a robust model system for studying the dynamics of BMA, particularly where isolation of primary BMAdS is a limiting step. Furthermore, we show that Raman micro-spectroscopy presents a high-resolution method for studying adipogenesis *in vitro* in a label-free manner, not just as the single cell level, but to the resolution of individual LDs. This has highlighted that there exists a stark heterogeneity of LD composition within the differentiated cells, with a mixture of lipid species also within the droplets themselves.

Modeling the interaction between the supportive stroma and the hematopoietic stem and progenitor cells (HSPCs) is of high interest in the regeneration of the BM niche in blood disorders. The translation of our *in vitro* co-culture system into a three-dimensional system for modeling these interactions was a natural progression. In a collaborative effort, we established a 3D hematopoietic niche by the co-culture of supportive OP9 mesenchymal cells and HSPCs in porous, chemically defined collagen-coated carboxymethylcellulose micro-scaffolds as described in **Chapter 5**. Flow cytometry and hematopoietic colony forming assays demonstrates the stromal supportive capacity for *in vitro* hematopoiesis in the absence of exogenous cytokines. Following culture, we recovered the paste-like biomimetic niche by partial dehydration. Cell viability and the association between stroma and HSPCs were maintained in this process. We were able to subcutaneous inject this living artificial niche *in vivo*, observed maintenance of stromal and hematopoietic populations over 12 weeks in immunodeficient mice with enhanced vascularization in the presence of HSPCs. The application of such a platform of BM organoids, or marroids, is far-reaching. From studying BMA to pharmacological screenings and direct application in the clinic, it has promising potential. Some of these possibilities are discussed below.

## Discussion

### On BMAT distinctions: the cBMAT/rBMAT conundrum

There remains significant debate in the field about a clear division between rBMAT and cBMAT. Is the rBMAT/cBMAT distinction a simplistic approach? While general BMAT expansion is similar between species, specific differences exist in its development within the marrow. There is a temporal onset of BMAT in the distal versus proximal tibia of rodents, yet in humans BMAT radiates from the central location of the midshaft and from the metaphyses in the long bones. Is it then justified to distinguish BMAT as functionally different defined by skeletal site? We know that some BMAds are labile and others are stable. Yet the possibility remains that what we currently distinguish as rBMAds and cBMAds within the long bones are cells that are nearly identical, defined by their microenvironment but not necessarily by location. How so?

### Nuances of bone marrow adipocytes

The cBMAds in the metatarsals, phalanges, and distal tail vertebrae of mice have higher trabecular bone mass and are contained within small bone compartments at the extremities, while long bones contain a mixture of rBMAds and cBMAds in close contact. This makes the division of the so-called rBMAT and cBMAT a challenge without a physical delineation between the two. At present when performing *ex vivo* experiments (e.g. image analysis, cell processing), the fibula-tibia junction is used as a marker for this distinction. However, this is based on a rough visual estimation and not the appropriate location at which to separate the bone for least contamination between the two regions, presenting challenges to data interpretation. An example is illustrated below.

We observe variations in size and number of BMAds as quantified on histological sections (Chapter 3) in the proximal tibia of 8 week-old C57BL/6 female mice at the peak of bone marrow aplasia in the irradiation and transplant setting versus homeostatic conditions. This is reflected in changes to the hematopoietic compartment. Figure 6.1a shows a significant decrease in hematopoietic cellularity by quantification of total CD45<sup>+</sup> cells with flow cytometry analysis in the proximal tibia at days 17 and 21 post lethal irradiation and total BM transplant compared to homeostatic controls. We also observe a drop in cellularity in the distal tibia on day 17 with a small increase on day 21 post BM transplant. Overall there is a larger number of total CD45<sup>+</sup> hematopoietic cells in the BM of the proximal compared to the distal tibia. These differences in hematopoietic cellularity of the proximal and distal tibia in homeostasis and at peak of bone marrow aplasia is partially reflected in their functional hematopoietic colony forming unit capacity. The frequencies of CFUs per 10,000 CD45<sup>+</sup> cells in the proximal and distal tibia are significantly higher in the homeostatic C57BL/6 female as compared to day 17 which is slightly lower than on day 21 post BM transplant (Figure 6.1b). Surprisingly, the CFU capacity of the marrow from the proximal versus distal tibia are not significantly different within each condition although with a tendency toward more

CFUs in the proximal tibia. This tendency is not observed on day 17, however. Taking into account that the total hematopoietic cellularity is reduced in the distal tibia on day 17 post BM transplant compared to the proximal tibia (Figure 6.1a), but that the CFU frequencies from these locations are similar, raising the question whether HSCs present in the distal tibia are more potent. Transplants of sorted HSCs from the distal versus proximal tibia would determine their reconstitution and long-term engraftment capacity.

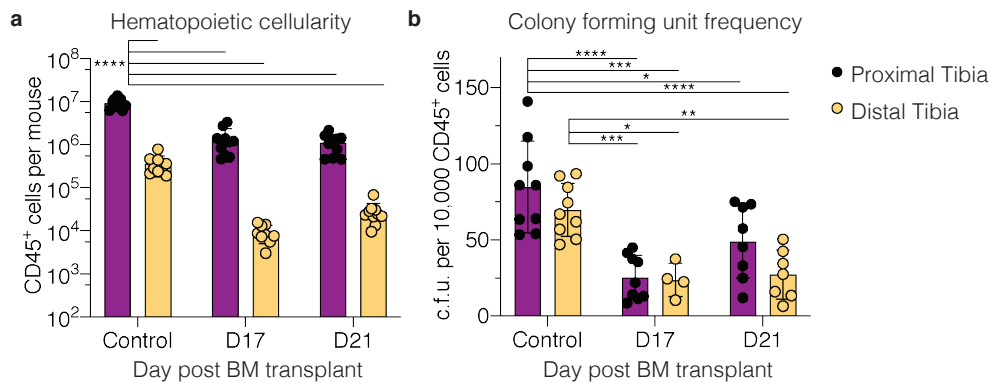


**Figure 6.1** | Hematopoietic cellularity and colony forming unit capacity of the proximal and distal tibia in homeostatic control versus at peak of bone marrow aplasia on day 17 and 21 post lethal irradiation and total bone marrow transplant. **a** Total number of CD45<sup>+</sup> bone marrow cells per mouse from two tibiae, measured by flow cytometry and CountBright beads. **b** Number of colonies per 10,000 CD45<sup>+</sup> bone marrow cells seven days after plating in methylcellulose. Some samples were pooled for sufficient cell numbers for plating. Error bars represent mean  $\pm$  s.d., n=10 mice per condition. \*\*\*\*P<0.0001, \*\*\*P<0.001, \*\*P<0.01, \*P<0.05 by Bonferroni's multiple comparisons test. BM: bone marrow; c.f.u.: colony forming unit; D: day.

Differences in hematopoietic phenotype and function of marrow in distal skeletal locations rich in cBMAT compared to marrow from proximal sites containing rBMAT have been described for the thorax versus tail vertebrae (Naveiras et al., 2009) but not within long bones such as in the proximal versus distal tibia.

## On the formation of the microenvironment

Largely similar to the general exo- and endo- skeletal classifications of vertebrate species, human skeletal tissue has multiple embryonic origins. Most of the skeleton derives from the mesoderm. That is, the axial skeleton (i.e. vertebrae, ribs, sternum) derive from the paraxial mesoderm and the appendicular skeleton (i.e. limb bones) from the lateral plate mesoderm. The flat bones of the skull, clavicle, and most of the cranial bones, however, originate from the neural crest of the ectoderm (Bianco and Robey, 2015). In the adult bone/marrow organ, a common SSC exists that joins skeletal, adipogenic, and hematopoietic physiology by regulating osteoclasts and the microvascular network (Bianco and Robey, 2015). Prx1-expressing cells overlap with a major proportion of SSCs in BM limb bones but not the axial skeleton, a notable difference in the adult marrow of these skeletal sites (Yue et al., 2016). What other disparities exist in the organization of the bone/marrow organ? To answer this, we can turn to the sequential formation of the marrow and its effect on the hematopoietic niche.

*Vascularization*

Mesodermal cells that differentiate into hemangioblasts migrate to the primary ossification center, forming the first primitive vessels through vasculogenesis with subsequent angiogenesis expanding the vascularization (Riseau and Flamme, 1995; reviewed in Sivaray and Adams, 2016). Blood vessels extend within the growing bone towards the epiphyses and morphologically distinct capillary beds can be distinguished. Blood vessels then invade the epiphysis contributing to formation of the secondary ossification center (Sivaray and Adams, 2016). Arterial blood thus enters long bones through the afferent artery ( $CD31^{hi}Endomucin^{lo}\alpha SMA^{+}$ ) at the inner surface of compact bone and at its distal ends (Ramasamy et al., 2016). In the metaphysis, the blood flows through type H capillaries ( $CD31^{hi}Endomucin^{hi}$ ) that are densely packed and organized as vessel columns interconnected at the distal end of the long bones near the growth plate (Kusumbe et al., 2014; Ramasamy et al., 2016; Sivaray and Adams, 2016). At the interface between the metaphysis and diaphysis, the blood flows from type H capillaries ( $CD31^{hi}Endomucin^{hi}$ ) into the branched sinusoidal network that constitutes the type L capillaries ( $CD31^{lo}Endomucin^{lo}$ ) (Kusumbe et al., 2014; Aird, 2007; Kopp et al., 2005). The blood is then drained by the central vein ( $CD31^{lo}Endomucin^{hi}\alpha SMA^{+}$ ) running through the center of the diaphysis. Type H vessels are surrounded by  $PDGFR\beta^{+}$  cells also expressing neural/glial antigen 2. They secrete osteogenic factors maintaining  $Osx^{+}$  progenitors that associate with these vessels (Kusumbe et al., 2016; Ramasamy et al., 2016). Meanwhile, type L vessels, are covered by two types of perivascular cells, namely  $LepR^{+}PDGFR\alpha^{+}$  cells and CAR cells (Sivaray and Adams, 2016). Interestingly, in aging animals and in ovariectomized mice, type H vessels and thereby blood flow declines, whereas type L vessels do not decline with age (Kusumbe et al., 2014). Recently a new type of capillary has been identified, the trans-cortical vessels, that are either arterial or venous in nature connecting the periosteum with the BM, with the greatest contribution of blood flow in and out of the bone (Grüneboom et al., 2019). Whereas the more recent study identified trans-cortical vessels in the entire length of the tibia, other studies mainly show results for the femur or proximal metaphysis and diaphysis of the tibia (Kusumbe et al., 2014; Ramasamy et al., 2016). Although it may seem evident, it would indeed be interesting to ascertain whether there are similarities or differences in the capillary network of the distal tibia, as variations in the vasculature and associated niche cells have an effect on the regulation of hematopoiesis.

BMA within the marrow is essential for HSCs however the reciprocity between vascularization and BMA indicates that reduced vascularization in cBMAT negatively affects HSC frequency (Zhou et al., 2017). Thus, a balance must exist for optimal HSC maintenance in the form of stimulatory and inhibitory interactions and cytokines through their microenvironment (Gainsfor et al., 1996; Camacho et al., 2017). Irradiation and chemotherapy disrupt the sinusoidal blood vessels within the marrow, depleting stromal cells and HSCs (Zhou et al., 2015). BMAds of the tail vertebrae inhibit vascularization whereas those of the long bones promote hematopoietic recovery after irradiation consistent with decline in BMA (Zhou et al., 2017). The majority of HSCs reside near sinusoidal vessels although arteriolar niches have also been identified (Acar et al., 2015; Kunisaki et al., 2013). The more primitive quiescent HSCs with lower metabolic state and low ROS are localized to hypoxic arteriolar niches proximal to endosteal zones, whereas active HSPCs higher in metabolic state and high ROS are localized near sinusoids of the central marrow (Itkin et al., 2016; Kunisaki et al., 2013; Suda et al., 2011; Ito et al., 2014; Yu et al., 2013; Suda et al., 2013).



## On lipids and hematopoiesis

cBMAd-dense regions of the distal skeleton maintain HSCs, and the rBMAd-containing red marrow contributes to expansion of their progenitors, which differ in their metabolic profiles. Most HSCs with low mitochondrial potential rely mainly on anaerobic glycolysis while HSPCs require a high energy production through mitochondrial oxidative phosphorylation (Takubo et al., 2013; Yu et al., 2013; Simsek et al., 2010). Studies have also revealed that HSCs and leukemic cells can rely on PPAR-mediated FA oxidation (Ito et al., 2012). Indeed, we have shown that BM stromal cells with lower overall lipid content (e.g. sOP9 cells versus iOP9 cells, Chapter 4) associate to increased hematopoietic expansion capacity compared with more mature BMAds that are high in lipid content (or iOP9 cells). Studies suggest that there is an optimum of maturation along this axis with regard to hematopoietic support in particular through the expression of *Angpt1*, *SCF*, and *Cxcl12* that are attenuated in terminally differentiated adipocytes (Oh et al., 2007). Specific differences in FA of BMAds may contribute to the nuances of differential hematopoietic support. For example, palmitic acid was shown to have a lipotoxic effect on hematopoietic-supportive osteoblasts, and high levels are present in aged and osteoporotic bone associated with decreased hematopoiesis (Saedi et al., 2019; Sing et al., 2018). This may in part explain the overt myeloproliferation that is seen on the aged skeleton. Future studies will focus on lipase- and desaturase-deficient animal models (such as the *Atgl*-KO or *Scd1*-KO) to better understand the role of FA mobilization on hematopoiesis.

### *In age*

Changes in BMAd number and size occur in the proximal and distal tibia upon ageing of the C57BL/6 female mouse (Chapter 3). At 18 months old, BMAds in both parts of the tibia appear more frequent and larger in size compared to young controls at eight weeks of age. However, upon BMA stimulation by irradiation and total BM transplant, such a drastic effect in the changes of adipocyte morphology at peak of aplasia is not seen. The rBMAds of the distal tibia increase in number and slightly in size while the cBMAds remain largely unchanged. Moreover, the effect of BM aplasia upon irradiation is reversed with the engraftment and expansion of the BM transplant, whereas the reversibility of aging BMAT is non-obvious. This could suggest different mechanisms of BMAd expansion in ageing versus conditions of induced BMA, either with distinctive progenitors giving rise to the BMAds formed or comprising different kinetics of BMAd maturation (especially considering the gradient of red-to-yellow marrow in the proximal-to-distal tibia). Interesting to understand would be whether the stable cBMAT compartment also expands with aging, and if the existing cBMAds proliferate or differentiate from pre-existing progenitors.

Of note, all experiments in this thesis were carried out with female juvenile mice 8-12 weeks of age, unless another age was a requirement for the experiment, with endpoint analyses up to several months after initiation. This has several implications for the results obtained that should be considered. Markedly, mice of 8-12 weeks old are adolescent and not yet fully mature. Adult mice range in age from two to three months old and whereas mice ranging 18 - 24 months of age are considered old (Hagan C., 2017). Furthermore, skeletal and metabolic differences are known to vary with gender. While, for example, leptin correlates positively with BMD in females, the opposite holds true for males (Scheller and Rosen, 2014).

Remarkably, CR is one of the interventions that has been most reliably associated with a reduced rate of aging, extension in lifespan, and decreased risk of age-related diseases including diabetes and cancer (Yuan et al., 2011). CR induces BMA while aging and diabetes are also accompanied by increased marrow

## Chapter 6 | Perspectives and Future Directions

adiposity. How do we reconcile the notion that something beneficial to the organism may also be associated with a detrimental state? Is BMA “good” or “bad”, or both? Are distinct subtypes induced or determined by different patho/physiological states? Could BMAd lipids be a source of regulatory molecules in the bone/marrow organ in homeostasis or disease?

### Methodological challenges

#### *OP9 cells and other cell lines*

We propose a first BMAd model to study BMAd subtypes (Chapter 4). The OP9 cells used for the *in vitro* studies are calvarial in origin derived from a (C57BL/6xC3H)F<sub>2</sub>-op/op mouse. C3H/HeJ mice have been reported to have significant marrow adiposity and a large pool of adipocytic progenitors (Fuijwara et al., 2019). While this indeed seems favorable for our studies, these cells also have the potential to differentiate into osteoblasts which could also have an effect on their hematopoietic supportive potential. Other cell lines supportive to hematopoiesis include the BM-derived MS5 cell line that have low adipogenic potential, or the fetal liver-derived AFT024 cell line with moderate osteogenic and mild adipogenic differentiation potential (Naveiras, 2008). Other cell lines also primed for adipocytic differentiation include the 3T3-L1 and C3H10T1/2 lines established from mouse embryonic fibroblasts. With a change in cell lines and/or culture conditions, LD formation, DNL, FA species, and unsaturation levels could be affected and thus influence the results. It would be interesting to observe, however, whether the unsaturation ratio in the presented differentiation conditions would change.

The Raman spectra obtained with Raman microspectroscopy allows for the assessment of the molecular content at a precise location. In our analyses, this provided insight into the lipid composition of individual lipid droplets with the differentiating OP9 cells. We observed not only LDs and OP9 adipocytes that are either mostly saturated and mostly unsaturated in lipid content, but also the important distinction that there exist LDs with a mixture of saturated and unsaturated lipids. Thus, the deconstruction of Raman images would provide a closer analysis of the complete content of the lipid droplets to better highlight their heterogeneity.

#### *Primary human cells*

The OP9 differentiation model closely mimics characteristics of primary BMAT *in vivo*. It would be a natural continuation to translate this model into a setting with primary human cells that resembles the native niche. However, isolation of primary BMSCs is prone to variations in protocols which in turn influence results (Figure 6.2). Whether in mouse or human models, even the initial steps such as the mode of isolation (e.g. centrifugation, flushing, cutting) or digestion could have an impact. For example, many researchers in the field isolate prospective BMAds with collagen-I or -II digestion that is not only present in the BM but has been shown to provide the highest proliferation levels with KLS cells (Craft and Scheller, 2017; Choi and Harley, 2017). However, another highly relevant candidate for enzymatic treatment is collagen-IV that is a component of peripheral adipose tissue and also associated with BMAds (e.g. Ding and Morrison, Nature 2014; Dai et al., Cell 2007). Other downstream processes, such as isolation by surface marker expression, lend themselves to further variations in protocols.

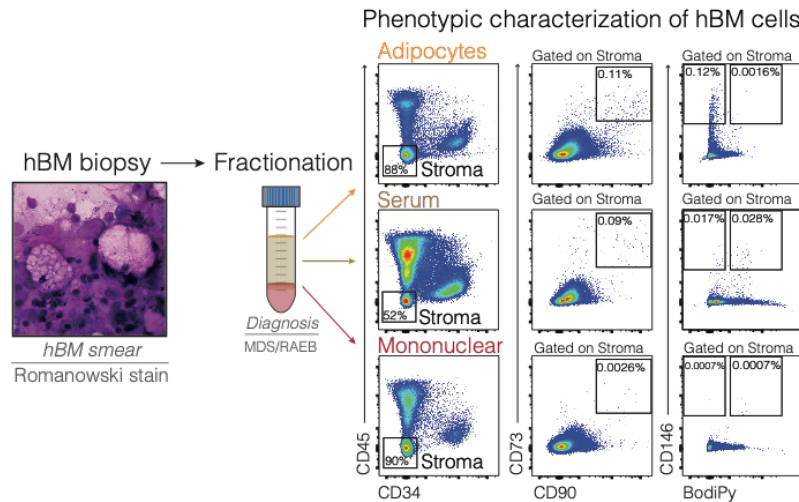


**Figure 6.2** | Phenotypic characterization of human bone marrow biopsies. Three fractions of cells (floating adipocytes (yellow), serum (beige), mononuclear cells (red)) were prepared for flow cytometric analysis with markers negative for hematopoietic cells (stroma, CD45-CD34-) that was further analyzed for mesenchymal markers (CD73+CD90+) or putative pre-adipocytes (CD146+Bodipy<sup>10</sup>) with highest presence in the adipocyte and serum fractions. hBM: human bone marrow; MDS: myelodysplastic syndrome; RAEB: refractory anemia and excess blasts. Romanowski stain kindly provided by Prof. Olaia Naveiras.

### Supportive matrices

Once the relevant cell population has been identified and isolated, a 3D matrix would lend itself well as support for adipogenic differentiation of the seeded stroma and hematopoietic co-culture to recapitulate the BM niche. BMA within the marrow is essential for HSCs however the reciprocity between vascularization and BMA indicates that reduced vascularization in cBMAT negatively affects HSC frequency (Zhou et al., 2017). Thus, a balance must exist for optimal HSC maintenance in the form of stimulatory and inhibitory interactions and cytokines through their microenvironment (Gainsfor et al., 1996; Camacho et al., 2017). With the advancements in material and cell biology, multifactorial combinations of scaffold properties (including architecture, composition, stiffness), culture conditions (such as cytokines, oxygen concentration, pH, shear stress), and supporting cells (for structural organization, cell-cell interactions, and cytokine secretion) can be tested. As an example, scaffolds can be composed of a variety of synthetic (e.g. polyurethanes, poly-olefins, PEG, CMC) or natural polymers (e.g. polysaccharides such as cellulose, agarose, alginate, starch, chitosan, or polypeptides such as silk, collagen, gelatin), or decellularized matrix of a biodegradable or permanent nature. The scaffold material can furthermore be functionalized with a plethora of bioactive molecules (e.g. antibodies, hormones, cytokines, adhesion molecules).

Microcarriers particles (e.g. Cytodex, Cytopore, and Cultispheres) are used for culturing adherent cells in suspension. Porous microcarriers vary in size between 1µm and 10mm, reflecting the diversity. It derives then that porosity and cell-adhesivity are critical for the success of cell seeding, maintenance, and differentiation. They are well-established in the large-scale production of cells or antibodies and are also increasingly used for cell delivery in cell therapy as they provide adhesion during the transplantation process (Newland et al., 2015). The challenge of transplanting a microcarrier culture is addressed in Chapter 5.

## Chapter 6 | Perspectives and Future Directions

Our biomimetic BM model presented in Chapter 5 is based on minimal requirements for hematopoietic maintenance (i.e. cytokine-free) and complies with GMP standards. Indeed, there is beauty in its simplicity. Through future elaboration of this model there is potential for many applications, including: HSC engraftment or expansion, ectopic BM generation, understand mechanisms of disease and lipid utilization, and drug screening.

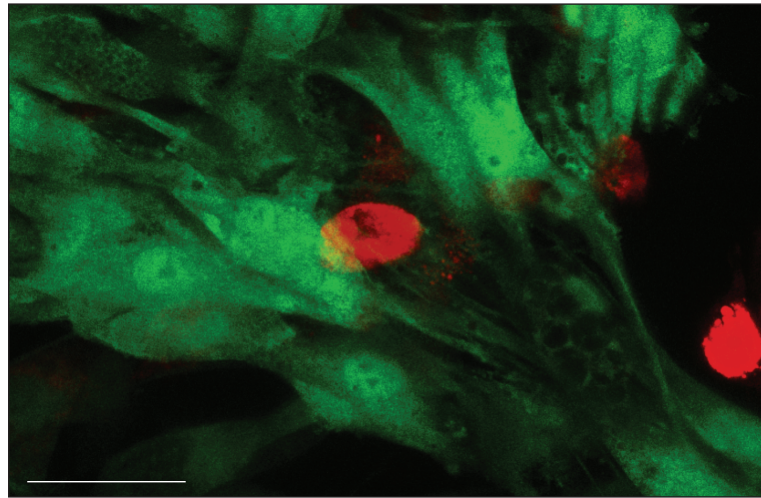


**Figure 6.3** | OP9-HSPC co-culture on 3D scaffolds. Red HSPCs associate to green stromal cells. Morphological features resembling small (upper left) and large (lower right) lipid droplets can be seen in the OP9 cells. Image by confocal microscopy at 63x with a Zeiss LSM 700 Inverted Confocal Microscope produced with Naveed D. Tavakol. Scale bar is 20 $\mu$ m. Green: OP9 cells; Red: DsRed cells.

## Concluding remarks

Many advancements have been made in the last decade. BMA has developed from an emerging to a vibrant field and the hematopoietic niche is being explored in greater detail than ever before. This is possible due to the transformation in technological advancements for *in vitro* and *in vivo* studies, tackling the hurdles of BM research. Transgenic models of specific stromal markers (i.e. Prx1, Nestin, Lepr, Osx, and Tie2, Col.2.3) have identified clonogenic multipotent progenitors of the hematopoietic niche. Isolation methods for these cells are becoming mainstay in labs around the world and those for BMAd isolation are also being perfected. We have, however, yet to identify a marker that ablates or delineates all BMAds. Though we are on our way in recognizing defining properties of the putative rBMAd (e.g. via the *Ptrf*<sup>-/-</sup> model of CGL-4), we have yet to do the same for the so-called cBMAd and potential other populations. Distinguishing the effects of systemic changes in metabolic states that occur with the loss (e.g. genetic models) or induction of BMA (e.g. irradiation-induced aplasia, CR, HFD, glitazone treatment) could be important in deciphering the specific effects of BMAds on hematopoiesis from inflammation or extramedullary adipogenesis (van der Heijden et al., 2015; Pez-Otin et al., 2016). While such *in vivo* models

may powerful, deciphering single cell from whole population effects of BMAdS is challenging and *in vitro* models provide essential alternatives. Notably, inducible progenitors should be seen as distinct from determined progenitors which natively express master regulatory genes, and at the present time this can only be determined by *in vivo* transplantation assays. Thus, it is imperative that we generate and apply such assays for the identification of true BMAd progenitors.

With inspiration from the HSC and SSC fields, my hope is that the work presented here is a small step in contributing to rigorous methods for identifying well-defined BMAd populations in the near future, in order to help us to continue identifying important properties of these fascinating cells. With this, and through the study of their interaction with other members of the bone marrow microenvironment (e.g. through cell contact or lipid transfer), may we have better opportunities in combating skeletal and hematopoietic malignancies.

Since the dawn of the hematopoietic lineage tree of Arthur Pappenheim in 1905, a century of research has seen the hematopoietic hierarchy evolve significantly, and in these footsteps are we today beginning to decipher the intricate stromal niche.

*How far have we come and where are we going?*

The sentiments of Paolo Bianco 30 years ago may resonate with us today as we appreciate the plasticity of bone marrow adipocytes on our endeavor to uncover their truth:

“Reticular cells and marrow adipocytes should be regarded as two different phenotypes of the same individual stromal cell rather than as two separate cell types.” (Bianco et al., 1988).

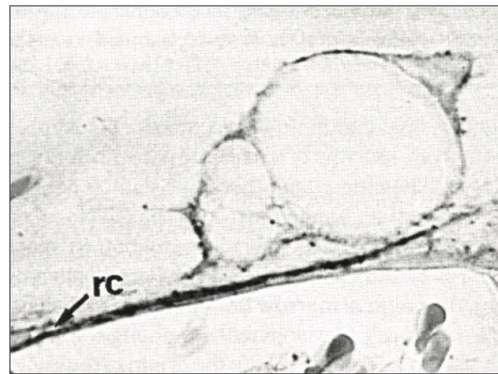


**Figure 6.4** | Morphology of human pre/adipocytes. Cytoplasmic protrusions of a multi-locular maturing bone marrow adipocyte is in close contact with an alkaline-positive reticular cell (rc). (Bianco et al., 1988)



## **APPENDIX**





## Appendix A

## Supplementary Information to Chapter 3

## Supplementary Figures

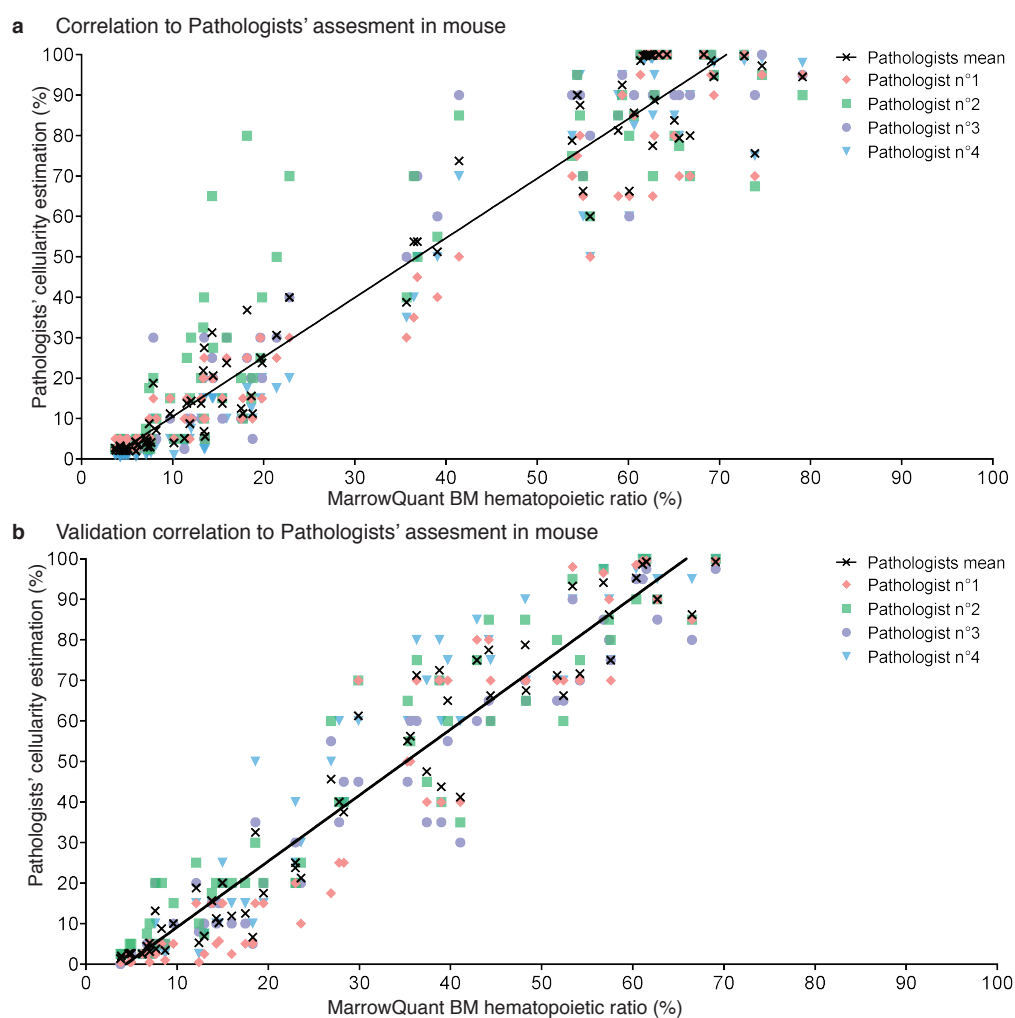


**Figure A1.1** | MarrowQuant versus pathologists' correlations on the validation set. **a** MarrowQuant nucleated cell ratio versus pathologists' estimation (image samples as in Figure 3.3c). **b** Final validation of MarrowQuant with pathologists' estimation (pathologists  $n=4$ , images  $n=59$ ,  $R^2=0.93$ ).

Appendix

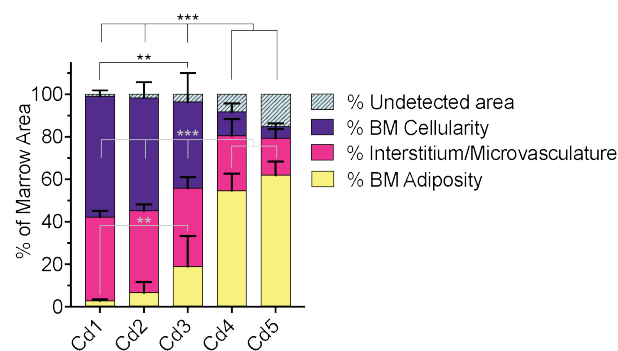


**Figure A1.2**| Quantification of bone marrow compartments in the proximal-to-distal caudal vertebrae. Cd: caudal.

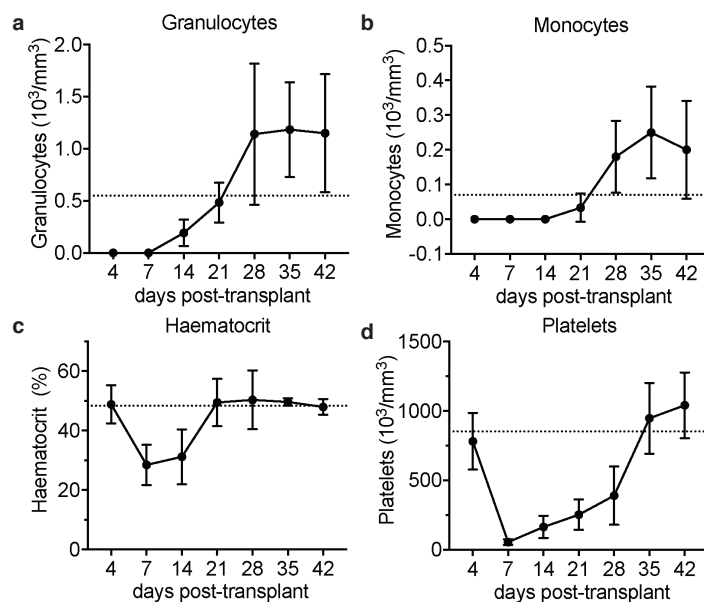


**Figure A1.3**| Peripheral blood recovery curves of 8-week-old C57BL/6 female mice having undergone lethal whole-body irradiation and total bone marrow transplantation. Recovery of **a** granulocytes, **b** monocytes, **c** hematocrit, **d** platelets. Error bars represent s.e.m.

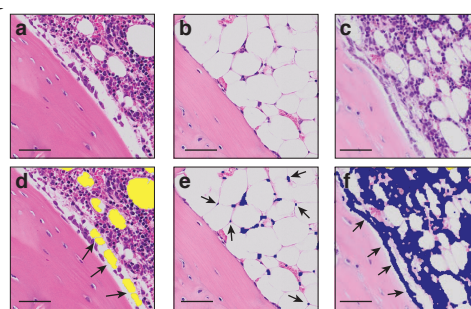


**Figure A1.4** | Detection errors attributed to false positives and negatives. **a,d** Fragmented artifact region (arrows) as adipocyte ghosts (yellow). **b,e** Nuclei (arrows) detected as nucleated cell area (purple). **c,f** Osteoblasts (arrows) detected as nucleated cell area.

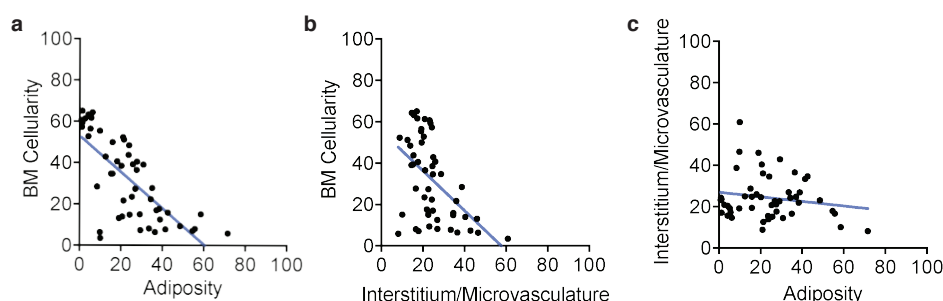


**Figure A1.5** | Reciprocity of the bone marrow compartments. **a** Hematopoietic bone marrow cellularity versus BM adiposity, **b** Hematopoietic bone marrow cellularity versus bone marrow interstitium and microvasculature, **c** Bone marrow interstitium and microvasculature versus bone marrow adiposity.

## Supplementary 2: Tutorial

The following supplementary information supports code for the usage of the designed plug-in. The source code will be made available with the published manuscript.

### *AdipoQuant instructions*

The AdipoQuant function was devised for the purpose of adipocyte segmentation in extramedullary adipose tissue samples. The script works with QuPath where projects can be created with raw image files (for example .vsi or .tiff formats).

Steps from launch to results

- Creation of a project in QuPath.
- Define “Tissue Boundaries” and “Artifacts” annotations.
- Open the script: Atumate/Shared scripts/ExtraMed\_MarrowQuant
- Press Run/Run to launch the processing.

## Appendix

- At the beginning of the script, the user may modify the minimum and/or maximum size of adipocytes to be detected. Recommended values are set by default ( $1000\mu\text{m}^2 - 15,000\mu\text{m}^2$ ).
- To export results, open and run the ExtraMed\_ExportData script.

The resulting outputs can be found in the "Results" folder found in the project folder. The results are exported as a .txt format. Upon opening the file, the results can be copied from the file and pasted in an excel sheet to be able to view and sort the data as preferred.

### *MarrowQuant installation*

MarrowQuant is a script initially developed as a plugin for the image processing software Fiji/ImageJ and adapted for QuPath using Fiji as an extension. We will first outline QuPath installation steps, and then we will describe how to use MarrowQuant within QuPath.

#### QuPath installation

Download and extract the zip file provided with the manuscript for windows 10 or Mac accordingly. The BIOP (EPFL Bioimaging and optics platform) has been working closely with the developer of QuPath. We therefore recommend the user to use the version 0.1.4 provided in the zip file for which the BIOP provides support.

In the extracted zip archive, you will find within the folder the QuPath executable, as well as other folders that contain the required scripts to run MarrowQuant. If you are a Mac user, move your QuPath executable to the Mac Applications folder.

#### Setting up QuPath

Upon opening QuPath, in Help>Show setup options, make sure to uncheck the verification of updates at launch, as it is not recommended to use more recent versions of QuPath as they may be unsupported by the BIOP. Also set the correct maximum amount of RAM you need. The typical value recommended is around three quarter of the maximum RAM that the computer possesses, depending on your usage of other programs simultaneously with QuPath.

There are three important folders to consider in the extracted zip file, namely the "Extensions", "ij-plugin" and "common-scripts" folders. In QuPath you need to indicate the directories of those three folders. To do that, go to Edit>Preferences, and copy the path of your Extensions folder in "Extensions directory", the path of your "ij-plugins" folder in "ImageJ plugin directory" and the path of your "common-scripts" folder in "Script directory".

#### Creation of a project

Users must create a QuPath project in order to work on the images of interest. It is important that you execute the next steps in the same order that is indicated.

The image formats compatible with the program are the .vsi and .tif ones. Note that if you want to build a project with .tif images, those do not need to be downsampled beforehand.

First create an empty folder where you intend to put your project that can be named "Qproject", for example.

In QuPath, in the "Project" tab, click "Create project" and select the empty folder you just created.

Now gather all the images you want to work on in a folder, including other needed folders containing .ets files for example. You can call this folder "Images". Put this folder in the empty folder where you created your project.

Back on QuPath, in the "Project" tab, click "Add images", then click "Choose files". Select the images in the "Images" folder you want to import in the project. Finally, click "Import".

Now that your project is created, each image should be displayed in a list in the "Project" tab and should have corresponding "Overview" and "Label" files following it, as seen in Figure A2.1a. As you do not need these files, the easiest way to remove all of them at once is to use a script we provide for that purpose. In Automate>Shared scripts, click on the "Remove OverviewAndLabel" script. This will open the script editor and display the script you selected. Click Run>Run. A few arbitrary error messages may pop up after running the script but can be disregarded. Now your project should only contain the corresponding images without their Overview and Label equivalents.

Another script that you must run before commencing, is a script that will create all the annotations needed for the processing. Go to Automate>Shared scripts, and click on the "CreateClasses" script. Click Run>Run.

Now that your project is all set, in the next section you will find the steps perform before applying MarrowQuant's segmentation analysis.

#### Pre-processing of an image

Before running the main script of MarrowQuant in QuPath, the user must first design the regions of interest needed for the program to work.

We recommend having a look at Dr. Pete Bankhead's QuPath series of tutorial videos that can be found on this link: [[https://www.youtube.com/playlist?list=PL4ta8RxZklWkPB\\_pwW-ZDVAGPGktAIE5Y](https://www.youtube.com/playlist?list=PL4ta8RxZklWkPB_pwW-ZDVAGPGktAIE5Y)]. It will prove very useful to become familiar with the QuPath interface and understand how the different tools available in QuPath to design regions of interest work. Several basics tips and guidelines for drawing regions can be found in the [User technical tips] file.

In the "Annotations" tab, you can find the different classes that are possible to assign to an object you drew. Those classes are called annotations. The three annotations that are needed in order for MarrowQuant to work are the [Tissue Boundaries], [BG] (which stands for Background), and [Artifact].

It could be useful to enable and conversely disable some QuPath features. First, users can disable the View>"Show slide overview" function. A useful function to enable is View>"Fill annotations", which will make it easier to visualize the shape of your different annotations. As we think the Wand drawing tool is very useful, we also recommend changing values at the bottom of Edit>Preferences, to 1.0 and 2.0 for Wand smoothing and Wand sensitivity respectively, which will make it easier to use.

The [Tissue Boundaries] class affects the region that needs to be processed. As the aim of MarrowQuant is to segment and quantify bone marrow compartments including the cortical bone region if desired, users should try to exclude other regions than those of the Tissue Boundaries.

## Appendix

The [BG] class is an annotation that is needed for background correction. We recommend to simply draw a small rectangle in a region of the same color of the background. That annotation must be contained in the [Tissue Boundaries] annotation. When drawing the [BG] annotation, users must make sure that the region within the annotation is as homogenous as possible. Even a few pixels of tissue residue of different color can influence the background correction algorithm. An example can be found in Figure A2.1b, the background being the region highlighted in yellow.

The [Artifact] annotation is an optional compartment which functions to exclude the affected regions from the processing. Like the [BG] annotation, all of the [Artifact] annotations must be strictly contained within the Tissue Boundaries, otherwise they may be not considered in the segmentation process. Typical regions affected as [Artifact] are large fixation artifacts. The reason is that those regions may be assigned as adipocytic compartment by MarrowQuant since adipocyte ghosts are the same color as the background. If not originally excluded from the [Tissue Boundaries], other regions such as muscle or cartilage should be affected as [Artifact] as well. An example can be found in Figure A2.1c, the artifacts being the regions highlighted in black.

### Processing

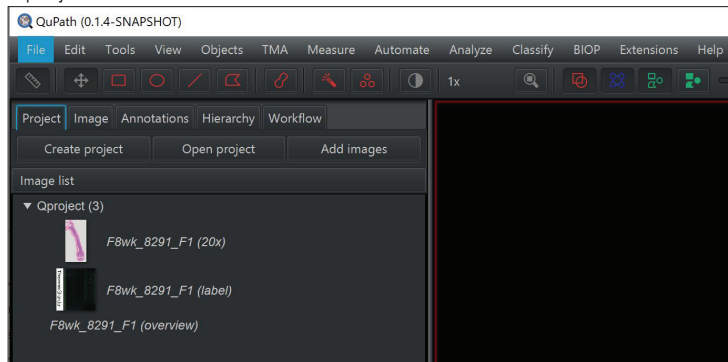
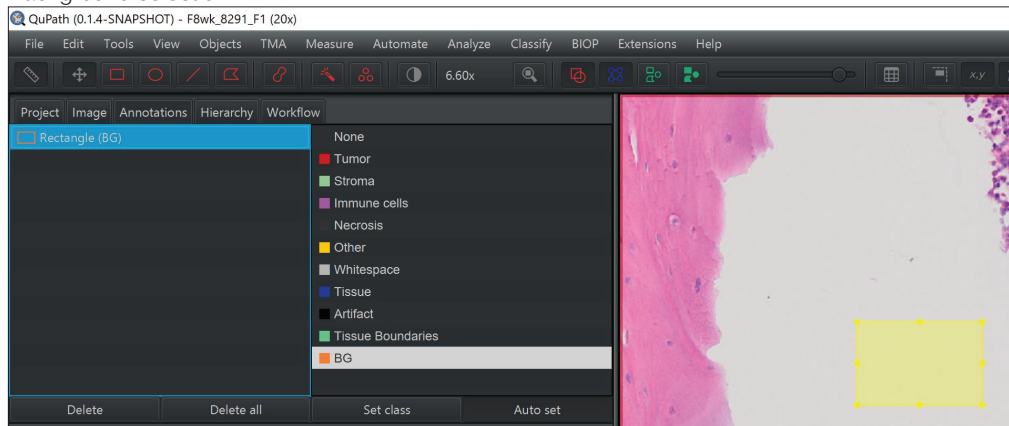
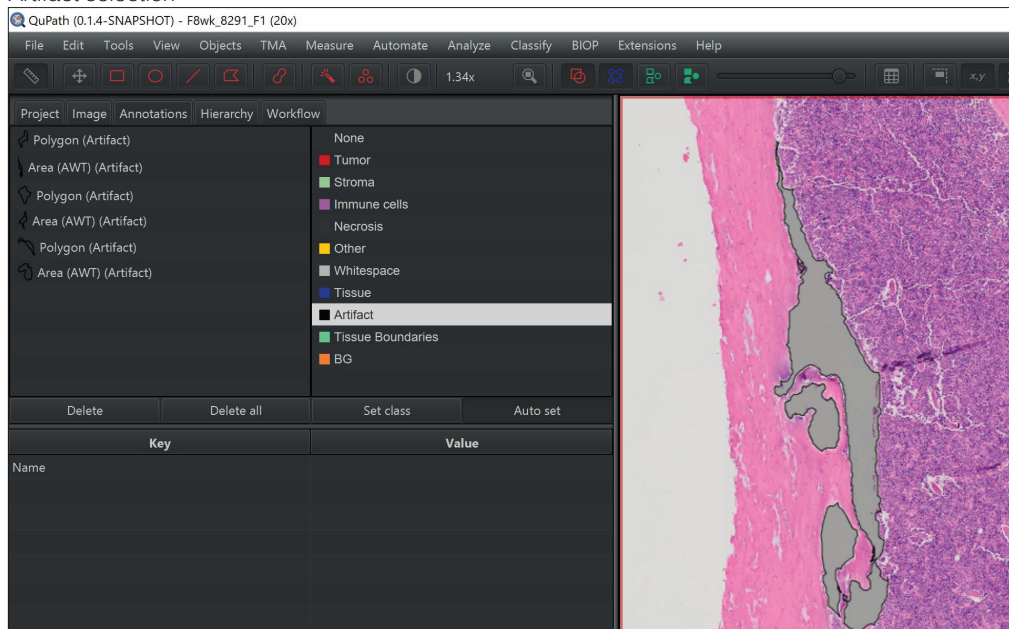
Once all the annotations (Tissue boundaries, BG and artifacts) are done, the user can launch the plugin (Automate > shared scripts [MarrowQuant]). Then click "run">"run" or "run">"run for project" if you want to process multiple images of the same project at the same time. At the top of the script, the user may modify the minimum and/or the maximum size of the adipocytes (s)he wants to be able to detect. Our recommended sizes are the ones that are in the script by default, that is 120 $\mu\text{m}^2$  as a minimum and 5000 $\mu\text{m}^2$  as a maximum size.

### Post-processing

Once all the images needed in a certain project have been processed, you need to export the outputs from QuPath. A specific script was made in order to do that for the current project opened in QuPath. Simply open the script [MarrowQuant\_ExportData] and click "run">"run for project", and select the images from which you want to export the results.

The resulting outputs can be found in the "results" folder, found in the project folder.

The results are exported as a .txt format, but upon opening the file, the user can simply copy everything from the file and paste it in an excel sheet for further analysis.

**a** Qproject in QuPath**b** Background selection**c** Artifact selection

**Figure A2.1** | QuPath selections. **a** Project creation, **b** clear background selection, **c** artefact selection.

## Appendix

### *MarrowQuant user guidelines*

Below is a list of items the user should be paying attention to when designing the [Tissue Boundaries] and [Artifacts] regions:

The main reason it is recommended to the user to manually design what we call "artifact" regions, is to reduce the detection of false positive adipocytes by the program. Adipocyte ghosts are the same color as the background, therefore as much fixation artifacts as possible must be selected as Artifacts.

The segmentation of the bone compartment includes an automatic thresholding step. This will work well when working with images where the bone staining appears as expected in standard histology samples. On the other hand, given the type of automatic threshold we use, it means that a significant difference in bone color, for example if the bone appears as very bright, might result either in a mis-segmented bone compartment, or in detection of bone in regions where there is none. Conversely, very darkly stained bone can be mis-detected as nucleated cells. The best workaround is to exclude as much of the mis-colorings from the [Tissue Boundaries] region as possible so that the thresholding will not be affected and works properly.

Muscle will generally be assigned as "interstitium" by the program. Hence our suggestion to the user to either not include muscle in the Tissue Boundary, or to assign it as artifact.

In rare cases, cartilage may be assigned as hematopoietic compartment. When it happens, the incidence on the results is negligible, and it is also very easy for the user to assign some cartilage areas as artifacts if wanted.

### QuPath technical tips

#### *Lock / unlock regions*

Once you have drawn the Tissue Boundaries region, in order to be able to design artifacts within it, you must lock the Tissue Boundaries region so it cannot be modified. This is done by:

Select the region, by using the Move tool and double clicking the region, or selecting it via the Annotations tab.

Right click > Annotations > lock/unlock

#### *Undo / redo*

You can "Undo" actions such as deleting or creating a new region with ctrl+z on the keyboard. To "redo" them back, press ctrl+shift+z.

Note however that you cannot undo a specific modification of an annotation. Performing "Undo" while having a region selected will simply have the effect of removing it

The way the Wand tool works is mostly dependent on the sensitivity you set (edit>preferences>Wand smoothing/sensitivity) and the zoom you are at. If you want to be very precise, you may want to zoom closer. If conversely you want to quickly draw big regions, it will be easier when zooming out.



When using either the Brush or the Wand tool, maintaining Alt on the keyboard while clicking will have the effect of erasing instead of drawing. This proves very useful when trying to remove everything that is external to the bone edge with the Wand tool, for example.

### Supplementary 3: Magnetic Resonance Imaging setup

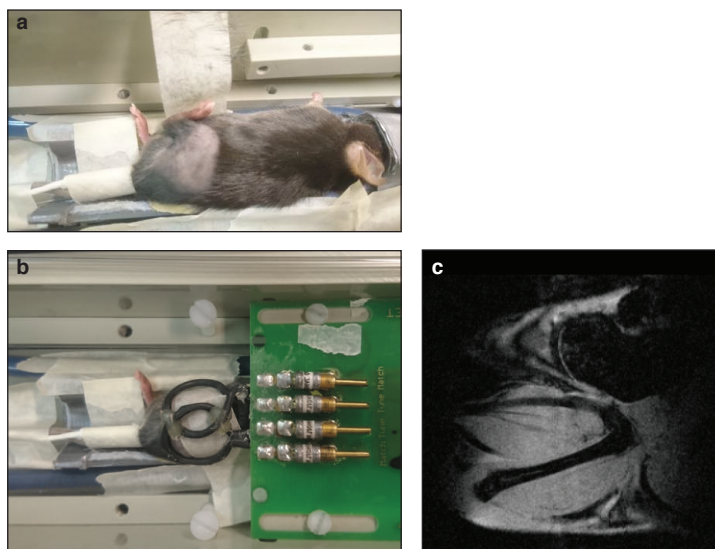


**Figure A3.1** | *In vivo* magnetic resonance imaging (MRI). **a** The mouse hindlimb is maintained in a fixed position for imaging. **b** A home-made magnetic coil is placed over the place of the left femur before MRI acquisition. **c** Sample image obtained, here with the marrow cavity of the femur in view.

## Appendix B

### List of reagents

Pertaining to Chapter 4

**Table B1.1** | Lipidomics LC-HRMS standards and solvents

| Standard/Solvent   | Supplier                                 |
|--|--|
| Chloroform stabilized by 0.5-1% ethanol  | Merck (Darmstadt, Germany)               |
| Methanol (UPLC grade)  | Merck (Darmstadt, Germany)               |
| Formic acid (98-100%, for analysis)  | Merck (Darmstadt, Germany)               |
| Acetonitrile (UPLC grade)  | Biosolve (Valkenswaard, Netherlands)     |
| Deionized water  | B. Braun (Melsungen, Germany)            |
| Ammonium formate   | Avanti Polar Lipids (Alabaster, AL, USA) |
| 1,2-didodecanoyl-sn-glycero-3-phosphocholine   | Avanti Polar Lipids (Alabaster, AL, USA) |
| 1-heptadecanoyl-2-myristoleoyl-sn-glycero-3-phosphocholine                                     | Avanti Polar Lipids (Alabaster, AL, USA) |
| 1-heptadecanoyl-2-myristoleoyl-sn-glycero-3-phospho-(1'-myo-inositol)                          | Avanti Polar Lipids (Alabaster, AL, USA) |
| 1-heptadecanoyl-2-myristoleoyl-sn-glycero-3-phospho-L-serine                                   | Avanti Polar Lipids (Alabaster, AL, USA) |
| N-(dodecanoyl)-sphing-4-enine-1-phosphocholine   | Avanti Polar Lipids (Alabaster, AL, USA) |
| N-(heptadecanoyl)-sphing-4-enine   | Avanti Polar Lipids (Alabaster, AL, USA) |
| D-glucosyl- $\beta$ -1,1'-N-octanoyl-D-erythro-sphingosine                                     | Avanti Polar Lipids (Alabaster, AL, USA) |
| sn-(3-tetradecanoyl-2-hydroxy)-glycerol-1-phospho-sn-3'-(1'-tetradecanoyl-2'-hydroxy)-glycerol | Avanti Polar Lipids (Alabaster, AL, USA) |
| Bis-[2-(9Z-octadecenoyl)-3-lyso-sn-glycero]-1-phosphate  | Avanti Polar Lipids (Alabaster, AL, USA) |
| 1,2-ditetradecanoyl-sn-glycero-3-phospho-(1'-sn-glycerol)                                      | Avanti Polar Lipids (Alabaster, AL, USA) |
| 1,2-di-(9E-octadecenoyl)-sn-glycero-3-phospho-(1'-sn-glycerol)                                 | Sigma (St. Louis, MO, USA)               |
| 1,2,3-Trioctanoyl-sn-glycerol  | Sigma (St. Louis, MO, USA)               |
| 1,2,3-Tridecanoyl-sn-glycerol  | Sigma (St. Louis, MO, USA)               |
| 1,2,3-Tridodecanoyl-sn-glycerol  | Sigma (St. Louis, MO, USA)               |
| 1,2,3-Tritetradecanoyl-sn-glycerol   | Sigma (St. Louis, MO, USA)               |
| 1,2,3-Trihexadecanoyl-sn-glycerol  | Sigma (St. Louis, MO, USA)               |
| 1,3-Dioctadecanoyl-sn-glycerol   | Sigma (St. Louis, MO, USA)               |
| (18:1(9Z)/18:1(9Z)/0:0)1,2-di-(9Z-octadecenoyl)-sn-glycerol                                    | Sigma (St. Louis, MO, USA)               |
| 1,2-Dihexadecanoyl-sn-glycerol   | Sigma (St. Louis, MO, USA)               |

**Table B.2** | RT-qPCR primer sequences

| <b>Gene</b> | <b>Forward primer (5' – 3')</b>   | <b>Reverse primer (5' – 3')</b> |
|-------------|-----------------------------------|---------------------------------|
| AdipoQ      | TGT TCC TCT TAA TCC TGC CCA       | CCA ACC TGC ACA AGT TCC CTT     |
| Atgl        | TGA CCA TCT GCC TTC CAG A         | TGT AGG TGG CGC AAG ACA         |
| C/ebpa      | GGT GGA CAA GAA CAG CAA CGA       | GCG GTC ATT GTC ACT GGT CA      |
| Elovl1      | CAT GCT TTC CAA GGT CAT TGA GCT G | TCT CAG TTG GCC TGACC TTGGTGG   |
| Fads1       | CCA GAT TGA ACA CCA CCT CTT       | GAC TCA TAC TTG ATG CCG TAC TT  |
| Fads2       | CAC AAG GAC CCG GAC ATA AA        | TGG TTG TAG GGC AGG TAT TTC     |
| Fabp4       | ATGTGCGACCAAGTTTGTG               | TTT GCC ATC CCA CTT CTG         |
| Lpl         | GGC CGC CCT GTA CAA GAG A         | AAC TCC TCC TCC ATC CAG TTG A   |
| Pparg       | CCT GCA TCT CCA CCT TAT TAT TCT   | AAA CCC TTG CAT CCT TCA CA      |
| Rpl13       | CTC ATC CTG TTC CCC AGG AA        | GGG TGG CCA GCT TAA GTT CTT     |
| Scd1        | TTC CCT CCT GCA AGC TCT AC        | CAG AGC GCT GGT CAT GTA GT      |
| Scd2        | GGC CCA CAT ACT GCA AGA G         | TTC AAA CTT CTC GCC TCC AT      |
| Ywhaz       | CAA AGA CAG CAC GCT AAT AAT GC    | GTG GGA CAG CAT GGA TGA CA      |

## BIBLIOGRAPHY

- Abarrategi, A., Mian, S.A., Passaro, D., Rouault-Pierre, K., Grey, W., and Bonnet, D. (2018). Modeling the human bone marrow niche in mice: From host bone marrow engraftment to bioengineering approaches. *J. Exp. Med.* 215, 729–743.
- Abdallah, B.M., Alzahrani, A.M., and Kassem, M. (2018). Secreted Clusterin protein inhibits osteoblast differentiation of bone marrow mesenchymal stem cells by suppressing ERK1/2 signaling pathway. *Bone* 110, 221–229.
- Ackert-Bicknell, C.L., Shockley, K.R., Horton, L.G., Lecka-Czernik, B., Churchill, G.A., and Rosen, C.J. (2009). Strain-specific effects of rosiglitazone on bone mass, body composition, and serum insulin-like growth factor-I. *Endocrinology* 150, 1330–1340.
- Adams, G. B., Chabner, K. T., Alley, I. R., Olson, D. P., Szczepiorkowski, Z. M., Poznansky, M. C., et al. (2006). Stem cell engraftment at the endosteal niche is specified by the calcium-sensing receptor. *Nature*, 439(7076), 599.
- Agarwal, A. K., Simha, V., Oral, E. A., Moran, S. A., Gorden, P., O’Rahilly, S., et. al. (2003). Phenotypic and genetic heterogeneity in congenital generalized lipodystrophy. *The Journal of Clinical Endocrinology & Metabolism*, 88(10), 4840–4847.
- Alpern, D., Gardeux, V., Russeil, J., Mangeat, B., Meireles-Filho, A. C., Breysse, R., et. al. (2019). BRB-seq: ultra-affordable high-throughput transcriptomics enabled by bulk RNA barcoding and sequencing. *Genome biology*, 20(1), 71.
- Ambrosi, T.H., Scialdone, A., Graja, A., Gohlke, S., Jank, A.M., Bocian, C., et al. (2017). Adipocyte Accumulation in the Bone Marrow during Obesity and Aging Impairs Stem Cell-Based Hematopoietic and Bone Regeneration. *Cell Stem Cell* 20, 771–784 e776.
- Aoki, T., Yamaguchi, S., Kinoshita, S., Hayashida, Y., & Korogi, Y. (2016). Quantification of bone marrow fat content using iterative decomposition of water and fat with echo asymmetry and least-squares estimation (IDEAL): reproducibility, site variation and correlation with age and menopause. *The British journal of radiology*, 89(1065), 20150538.
- Ara, T., Tokoyoda, K., Sugiyama, T., Egawa, T., Kawabata, K., & Nagasawa, T. (2003). Long-term hematopoietic stem cells require stromal cell-derived factor-1 for colonizing bone marrow during ontogeny. *Immunity*, 19(2), 257–267.
- Arcidiacono, J.A., Bauer, S.R., Kaplan, D.S., Allocca, C.M., Sarkar, S., and Lin-Gibson, S. (2018). FDA and NIST collaboration on standards development activities supporting innovation and translation of regenerative medicine products. *Cytotherapy* 20, 779–784.
- Arentsen, T., Raith, H., Qian, Y., Forssberg, H., and Diaz Heijtz, R. (2015). Host microbiota modulates development of social preference in mice. *Microb Ecol Health Dis* 26, 29719.
- Arentsen, L., Hansen, K.E., Yagi, M., Takahashi, Y., Shanley, R., McArthur, A., et al. (2017). Use of dual-energy computed tomography to measure skeletal-wide marrow composition and cancellous bone mineral density. *J Bone Miner Metab* 35, 428–436.
- Arranz, L., Sánchez-Aguilera, A., Martín-Pérez, D., Isern, J., Langa, X., Tzankov, A., et. al. (2014). Neuropathy of haematopoietic stem cell niche is essential for myeloproliferative neoplasms. *Nature*, 512(7512), 78.
- Attané, C., Estève, D., Chaoui, K., Iacovoni, J., Corre, J., Moutahir, M., . et. al. (2019). Yellow adipocytes comprise a new adipocyte sub-type present in human bone marrow. *bioRxiv*, 641886.
- Baccin, C., Al-Sabah, J., Velten, L., Helbling, P.M., Grünschlager, F., Hernández-Malmierca, P., Nombela-Arrieta, C., Steinmetz, L.M., Trumpp, A., and Haas, S. (2019). Combined single-cell and spatial transcriptomics reveals the molecular, cellular and spatial bone marrow niche organization. *BioRxiv* 718395.

- Balani, D.H., Ono, N., and Kronenberg, H.M. (2017). Parathyroid hormone regulates fates of murine osteoblast precursors in vivo. *Journal of Clinical Investigation* 127, 3327-3338.
- Bani Hassan, E., Demontiero, O., Vogrin, S., Ng, A., and Duque, G. (2018). Marrow Adipose Tissue in Older Men: Association with Visceral and Subcutaneous Fat, Bone Volume, Metabolism, and Inflammation. *Calcif Tissue Int* 103, 164-174.
- Barbin, F. F., & Oliveira, C. C. (2017). Gelatinous transformation of bone marrow. *Autopsy & case reports*, 7(2), 5.
- Barker, J. E. (1994). Sl/Sld hematopoietic progenitors are deficient in situ. *Experimental hematology*, 22(2), 174-177.
- Baum, T., Yap, S.P., Dieckmeyer, M., Ruschke, S., Eggers, H., Kooijman, H., et al. (2015). Assessment of whole spine vertebral bone marrow fat using chemical shift-encoding based water-fat MRI. *J Magn Reson Imaging* 42, 1018-1023.
- Baum, T., Rohrmeier, A., Syvari, J., Diefenbach, M.N., Franz, D., Dieckmeyer, M., et al. (2018). Anatomical Variation of Age-Related Changes in Vertebral Bone Marrow Composition Using Chemical Shift Encoding-Based Water-Fat Magnetic Resonance Imaging. *Front Endocrinol (Lausanne)* 9, 141.
- Beck-Cormier, S., Lelliott, C.J., Logan, J.G., Lafont, D.T., Meramtdjian, L., Leitch, V.D., et al. (2019). Slc20a2, Encoding the Phosphate Transporter Pit2, Is an Important Genetic Determinant of Bone Quality and Strength. *J Bone Miner Res* 34, 1101-1114.
- Becker, A. J., McCulloch, E. A., & Till, J. E. (1963). Cytological demonstration of the clonal nature of spleen colonies derived from transplanted mouse marrow cells.
- Bédier, A., Braschler, T., Peric, O., Fantner, G.E., Mosser, S., Fraering, P.C., Benchérif, S., Mooney, D.J., and Renaud, P. (2015). A compressible scaffold for minimally invasive delivery of large intact neuronal networks. *Adv. Healthc. Mater.* 4, 301–312.
- Bédier, A., Piacentini, N., Aeberli, L., Da Silva, A., Verheyen, C.A., Bonini, F., Rochat, A., Filippova, A., Serex, L., Renaud, P., et al. (2018). Additive manufacturing of hierarchical injectable scaffolds for tissue engineering. *Acta Biomater.* 76, 71–79.
- Bédier, A., Verheyen, C. A., Bonini, F., Burch, P. & Braschler, T. *submitted* (2019).
- Beekman, K.M., Veldhuis-Vlug, A.G., Van Der Veen, A., Den Heijer, M., Maas, M., Kerckhofs, G., et al. (2018). The effect of PPAR $\gamma$  inhibition on bone marrow adipose tissue and bone in C3H/HeJ mice. *American Journal of Physiology-Endocrinology and Metabolism* 316, E96-E105.
- Beekman, K.M., Veldhuis-Vlug, A.G., Den Heijer, M., Maas, M., Oleksik, A.M., Tanck, M.W., et al. (2019a). The effect of raloxifene on bone marrow adipose tissue and bone turnover in postmenopausal women with osteoporosis. *Bone* 118, 62-68.
- Beekman, K.M., Veldhuis-Vlug, A.G., Van Der Veen, A., Den Heijer, M., Maas, M., Kerckhofs, G., et al. (2019b). The effect of PPAR $\gamma$  inhibition on bone marrow adipose tissue and bone in C3H/HeJ mice. *Am J Physiol Endocrinol Metab* 316, E96-E105.
- Belavy, D.L., Quittner, M.J., Ridgers, N.D., Shiekh, A., Rantalainen, T., and Trudel, G. (2018). Specific Modulation of Vertebral Marrow Adipose Tissue by Physical Activity. *J Bone Miner Res* 33, 651-657.
- Belazi, D., Solé-Domènech, S., Johansson, B., Schalling, M., & Sjövall, P. (2009). Chemical analysis of osmium tetroxide staining in adipose tissue using imaging ToF-SIMS. *Histochemistry and cell biology*, 132(1), 105-115.
- Bello, A.B., Park, H., and Lee, S.-H. (2018). Current approaches in biomaterial-based hematopoietic stem cell niches. *Acta Biomater.* 72, 1–15.

## Bibliography

- Bencherif, S.A., Sands, R.W., Bhatta, D., Arany, P., Verbeke, C.S., Edwards, D.A., and Mooney, D.J. (2012). Injectable preformed scaffolds with shape-memory properties. *Proc. Natl. Acad. Sci. U. S. A.* *109*, 19590–19595.
- Bencherif, S.A., Warren Sands, R., Ali, O.A., Li, W.A., Lewin, S.A., Braschler, T.M., Shih, T.-Y., Verbeke, C.S., Bhatta, D., Dranoff, G., et al. (2015). Injectable cryogel-based whole-cell cancer vaccines. *Nat. Commun.* *6*, 7556.
- Bernal, A., & Arranz, L. (2018). Nestin-expressing progenitor cells: function, identity and therapeutic implications. *Cellular and Molecular Life Sciences*, *75*(12), 2177-2195.
- Berry, R., & Rodeheffer, M. S. (2013). Characterization of the adipocyte cellular lineage in vivo. *Nature cell biology*, *15*(3), 302.
- Bianco, P., Costantini, M., Dearden, L. C., & Bonucci, E. (1988). Alkaline phosphatase positive precursors of adipocytes in the human bone marrow. *British journal of haematology*, *68*(4), 401-403.
- Bianco, P., and Gehron Robey, P. (2000). Marrow stromal stem cells. *J Clin Invest* *105*, 1663-1668.
- Bianco, P., Robey, P. G., & Simmons, P. J. (2008). Mesenchymal stem cells: revisiting history, concepts, and assays. *Cell stem cell*, *2*(4), 313-319.
- Bianco, P. (2011). Bone and the Hematopoietic Niche: A Tale of Two Stem Cells. *Blood* *117* (20): 5281–88.
- Bianco, P. (2014). “Mesenchymal” stem cells. *Annu. Rev. Cell Dev. Biol.* *30*, 677–704.
- Bianco, P., & Robey, P. G. (2015). Skeletal stem cells. *Development*, *142*(6), 1023-1027.
- Bigelow, C. L., & Tavassoli, M. (1984). Fatty involution of bone marrow in rabbits. *Cells Tissues Organs*, *118*(1), 60-64.
- Bixel, M.G., Kusumbe, A.P., Ramasamy, S.K., Sivaraj, K.K., Butz, S., Vestweber, D., et al. (2017). Flow Dynamics and HSPC Homing in Bone Marrow Microvessels. *Cell Reports* *18*, 1804-1816.
- Bizzozzero, G. (1868). Sulla funzione ematopoetica del midollo delle ossa. *Zentralbl Med Wissensch*, *6*, 885.
- Bizzozzero, G. (1869). *Sulla funzione ematopoetica del midollo delle ossa: seconda comunicazione preventiva.*
- Blache, U., Metzger, S., Vallmajo-Martin, Q., Martin, I., Djonov, V., and Ehrbar, M. (2016). Dual Role of Mesenchymal Stem Cells Allows for Microvascularized Bone Tissue-Like Environments in PEG Hydrogels. *Adv. Healthc. Mater.* *5*, 489–498.
- Blebea, J. S., Houseni, M., Torigian, D. A., Fan, C., Mavi, A., Zhuge, Y., et. al. (2007, May). Structural and functional imaging of normal bone marrow and evaluation of its age-related changes. In *Seminars in nuclear medicine* (Vol. 37, No. 3, pp. 185-194). WB Saunders.
- Böhm, J. (2000). Gelatinous transformation of the bone marrow: the spectrum of underlying diseases. *The American journal of surgical pathology*, *24*(1), 56.
- Bolan, P.J., Arentsen, L., Sueblinvong, T., Zhang, Y., Moeller, S., Carter, J.S., et al. (2013). Water-fat MRI for assessing changes in bone marrow composition due to radiation and chemotherapy in gynecologic cancer patients. *J Magn Reson Imaging* *38*, 1578-1584.
- Bolander, J., Ji, W., Geris, L., Bloemen, V., Chai, Y.C., Schrooten, J., and Luyten, F.P. (2016). The combined mechanism of bone morphogenetic protein- and calcium phosphate-induced skeletal tissue formation by human periosteum derived cells. *Eur. Cell. Mater.* *31*, 11–25.
- Bornstein, S., Moschetta, M., Kawano, Y., Sacco, A., Huynh, D., Brooks, D., et al. (2017). Metformin Affects Cortical Bone Mass and Marrow Adiposity in Diet-Induced Obesity in Male Mice. *Endocrinology* *158*, 3369-3385.

- Botolin, S., and McCabe, L.R. (2006). Inhibition of PPARgamma prevents type I diabetic bone marrow adiposity but not bone loss. *J Cell Physiol* 209, 967-976.
- Boulais, P.E., Mizoguchi, T., Zimmerman, S., Nakahara, F., Vivie, J., Mar, J.C., et al. (2018). The Majority of CD45(-) Ter119(-) CD31(-) Bone Marrow Cell Fraction Is of Hematopoietic Origin and Contains Erythroid and Lymphoid Progenitors. *Immunity* 49, 627-639 e626.
- Bourgine, P.E., Klein, T., Paczulla, A.M., Shimizu, T., Kunz, L., Kokkaliaris, K.D., et al. (2018). In vitro biomimetic engineering of a human hematopoietic niche with functional properties. *Proc Natl Acad Sci USA* 115, E5688-E5695.
- Boyd, A.L., Reid, J.C., Salci, K.R., Aslostovar, L., Benoit, Y.D., Shapovalova, Z., et al. (2017). Acute myeloid leukaemia disrupts endogenous myelo-erythropoiesis by compromising the adipocyte bone marrow niche. *Nat Cell Biol* 19, 1336-1347.
- Bradley, T. R., & Metcalf, D. (1966). The growth of mouse bone marrow cells in vitro. *Australian Journal of Experimental Biology and Medical Science*, 44(3), 287-300.
- Bredella, M.A., Fazeli, P.K., Miller, K.K., Misra, M., Torriani, M., Thomas, B.J., et al. (2009). Increased bone marrow fat in anorexia nervosa. *J Clin Endocrinol Metab* 94, 2129-2136.
- Bredella, M. A., Torriani, M., Ghomi, R. H., Thomas, B. J., Brick, D. J., Gerweck, A. V., et. al. (2011). Vertebral bone marrow fat is positively associated with visceral fat and inversely associated with IGF-1 in obese women. *Obesity*, 19(1), 49-53.
- Bredella, M. A., Gerweck, A. V., Barber, L. A., Breggia, A., Rosen, C. J., Torriani, M., & Miller, K. K. (2014). Effects of growth hormone administration for 6 months on bone turnover and bone marrow fat in obese premenopausal women. *Bone*, 62, 29-35.
- Bredella, M.A., Daley, S.M., Kalra, M.K., Brown, J.K., Miller, K.K., and Torriani, M. (2015). Marrow Adipose Tissue Quantification of the Lumbar Spine by Using Dual-Energy CT and Single-Voxel (1)H MR Spectroscopy: A Feasibility Study. *Radiology* 277, 230-235.
- Brennan, T.A., Egan, K.P., Lindborg, C.M., Chen, Q., Sweetwyne, M.T., Hankenson, K.D., et al. (2014). Mouse models of telomere dysfunction phenocopy skeletal changes found in human age-related osteoporosis. *Dis Model Mech* 7, 583-592.
- Brochu-Gaudreau, K., Rehfeldt, C., Blouin, R., Bordignon, V., Murphy, B. D., & Palin, M. F. (2010). Adiponectin action from head to toe. *Endocrine*, 37(1), 11-32.
- Budzik, J.F., Lefebvre, G., Forzy, G., El Rafei, M., Chechin, D., and Cotten, A. (2014). Study of proximal femoral bone perfusion with 3D T1 dynamic contrast-enhanced MRI: a feasibility study. *Eur Radiol* 24, 3217-3223.
- Butler, J.M., Gars, E.J., James, D.J., Nolan, D.J., Scandura, J.M., and Rafii, S. (2012). Development of a vascular niche platform for expansion of repopulating human cord blood stem and progenitor cells. *Blood* 120, 1344-1347.
- Caers, J., Deleu, S., Belaid, Z., De Raeve, H., Van Valckenborgh, E., De Bruyne, E., et. al. (2007). Neighboring adipocytes participate in the bone marrow microenvironment of multiple myeloma cells. *Leukemia*, 21(7), 1580.
- Cahu, X., Carre, M., Recher, C., Pigneux, A., Hunault-Berger, M., Vey, N., et al. (2017). Impact of body-surface area on patients' outcome in younger adults with acute myeloid leukemia. *Eur J Haematol* 98, 443-449.
- Calvi, L.M., Adams, G.B., Weinreb, K.W., Weber, J.M., Olson, D.P., Knight, M.C., Martin, R.P., Schipani, E., Divieti, P., Bringham, F.R., et al. (2003). Osteoblastic cells regulate the haematopoietic stem cell niche. *Nature* 425, 841-846.

## Bibliography

- Calvo, W., Fliedner, T.M., Herbst, E., Hugl, E., and Bruch, C. (1976). Regeneration of blood-forming organs after autologous leukocyte transfusion in lethally irradiated dogs. II. Distribution and cellularity of the marrow in irradiated and transfused animals. *Blood* 47, 593-601.
- Camacho V, McClearn V, Patel S, Welner RS. Regulation of normal and leukemic stem cells through cytokine signaling and the micro- environment. *Int J Hematol*. 2017;105(5):566–77.
- Campos, V., Rappaz, B., Kuttler, F., Turcatti, G., and Naveiras, O. (2018). High-throughput, nonperturbing quantification of lipid droplets with digital holographic microscopy. *J Lipid Res* 59, 1301-1310.
- Campos, V. (2019). *Metabolic and microenvironmental strategies to accelerate hematopoietic recovery post-aplasia* (Thesis No. 9395). EPFL.
- Cannon, B., & Nedergaard, J. (2011). Nonshivering thermogenesis and its adequate measurement in metabolic studies. *Journal of Experimental Biology*, 214(2), 242-253.
- Caroti, C.M., Ahn, H., Salazar, H.F., Joseph, G., Sankar, S.B., Willett, N.J., et al. (2017). A Novel Technique for Accelerated Culture of Murine Mesenchymal Stem Cells that Allows for Sustained Multipotency. *Sci Rep* 7, 13334.
- Carrelha, J., Meng, Y., Kettyle, L. M., Luis, T. C., Norfo, R., Alcolea, V., et. al. (2018). Hierarchically related lineage-restricted fates of multipotent haematopoietic stem cells. *Nature*, 554(7690), 106.
- Carta, G., Murru, E., Banni, S., & Manca, C. (2017). Palmitic acid: Physiological role, metabolism and nutritional implications. *Frontiers in physiology*, 8, 902.
- Cartwright, B. R., & Goodman, J. M. (2012). Seipin: from human disease to molecular mechanism. *Journal of lipid research*, 53(6), 1042-1055.
- Cawthorn, W.P., Scheller, E.L., Learman, B.S., Parlee, S.D., Simon, B.R., Mori, H., et al. (2014). Bone marrow adipose tissue is an endocrine organ that contributes to increased circulating adiponectin during caloric restriction. *Cell Metab* 20, 368-375.
- Cawthorn, W.P., Scheller, E.L., Parlee, S.D., Pham, H.A., Learman, B.S., Redshaw, C.M., et al. (2016). Expansion of Bone Marrow Adipose Tissue During Caloric Restriction Is Associated With Increased Circulating Glucocorticoids and Not With Hypoleptinemia. *Endocrinology* 157, 508-521.
- Cawthorn, W.P., and Scheller, E.L. (2017). Editorial: Bone Marrow Adipose Tissue: Formation, Function, and Impact on Health and Disease. *Front Endocrinol (Lausanne)* 8, 112.
- Chan, C.K.F., Gulati, G.S., Sinha, R., Tompkins, J.V., Lopez, M., Carter, A.C., et al. (2018). Identification of the Human Skeletal Stem Cell. *Cell* 175, 43-56 e21.
- Chandra, A., Lin, T., Tribble, M.B., Zhu, J., Altman, A.R., Tseng, W.J., et al. (2014). PTH1-34 alleviates radiotherapy-induced local bone loss by improving osteoblast and osteocyte survival. *Bone* 67, 33-40.
- Chen, J.R., Lazarenko, O.P., Wu, X., Tong, Y., Blackburn, M.L., Shankar, K., et al. (2010). Obesity reduces bone density associated with activation of PPARgamma and suppression of Wnt/beta-catenin in rapidly growing male rats. *PLoS One* 5, e13704.
- Chen, Y., Jacamo, R., Shi, Y., Wang, R., Battula, V.L., Konoplev, S., Strunk, D., Hofmann, N.A., Reinisch, A., Konopleva, M., et al. (2012). Human extramedullary bone marrow in mice: a novel in vivo model of genetically controlled hematopoietic microenvironment. *Blood* 119, 4971–4980.
- Choi, J.S., and Harley, B.A.C. (2017). Marrow-inspired matrix cues rapidly affect early fate decisions of hematopoietic stem and progenitor cells. *Sci. Adv.* 3.



## Bibliography

- Cock, T.A., Back, J., Eleftheriou, F., Karsenty, G., Kastner, P., Chan, S., et al. (2004). Enhanced bone formation in lipodystrophic PPARgamma(hyp/hyp) mice relocates haematopoiesis to the spleen. *EMBO Rep* 5, 1007-1012.
- Colvin, G.A., Lambert, J.F., Abedi, M., Hsieh, C.C., Carlson, J.E., Stewart, F.M., et al. (2004). Murine marrow cellularity and the concept of stem cell competition: geographic and quantitative determinants in stem cell biology. *Leukemia* 18, 575-583.
- Conklin, E. G. (1939). Predecessors of Schleiden and Schwann. *The American Naturalist*, 73(749), 538-546.
- Corselli, M., Chin, C. J., Parekh, C., Sahaghian, A., Wang, W., Ge, S., et al. (2013). Perivascular support of human hematopoietic stem/progenitor cells. *Blood*, 121(15), 2891-2901.
- Costa, M.H.G., Soure, A.M. de, Cabral, J.M.S., Ferreira, F.C., and Silva, C.L. da (2018). Hematopoietic Niche – Exploring Biomimetic Cues to Improve the Functionality of Hematopoietic Stem/Progenitor Cells. *Biotechnol. J.* 13, 1700088.
- Costa, S., Fairfield, H., and Reagan, M.R. (2019). Inverse correlation between trabecular bone volume and bone marrow adipose tissue in rats treated with osteoanabolic agents. *Bone* 123, 211-223.
- Coutel, X., Olejnik, C., Marchandise, P., Delattre, J., Behal, H., Kerckhofs, G., et al. (2018). A Novel microCT Method for Bone and Marrow Adipose Tissue Alignment Identifies Key Differences Between Mandible and Tibia in Rats. *Calcified Tissue International* 103, 189-197.
- Coutu, D.L., Kokkalis, K.D., Kunz, L., and Schroeder, T. (2017). Three-dimensional map of nonhematopoietic bone and bone-marrow cells and molecules. *Nature Biotechnology* 35, 1202-1210.
- Craft, C. S., & Scheller, E. L. (2017). Evolution of the marrow adipose tissue microenvironment. *Calcified tissue international*, 100(5), 461-475.
- Craft, C. S., Li, Z., MacDougald, O. A., & Scheller, E. L. (2018). Molecular differences between subtypes of bone marrow adipocytes. *Current molecular biology reports*, 4(1), 16-23.
- Cui, X., Wang, Y., Tang, Y., Liu, Y., Zhao, L., Deng, J., et al. (2011). Seipin ablation in mice results in severe generalized lipodystrophy. *Human molecular genetics*, 20(15), 3022-3030.
- Cuminetti, V., and Arranz, L. (2019). Bone Marrow Adipocytes: The Enigmatic Components of the Hematopoietic Stem Cell Niche. *J Clin Med* 8.
- Dalamaga, M., Karmaniolas, K., Panagiotou, A., Hsi, A., Chamberland, J., Dimas, C., et al. (2009). Low circulating adiponectin and resistin, but not leptin, levels are associated with multiple myeloma risk: a case–control study. *Cancer Causes & Control*, 20(2), 193-199.
- De Bournonville, S., Vangrunderbeeck, S., and Kerckhofs, G. (2019). Contrast-enhanced microCT for virtual 3D anatomical pathology of biological tissues: A literature review. *Contrast Media and Molecular Imaging* 2019.
- de la Puente, P., Muz, B., Gilson, R.C., Azab, F., Luderer, M., King, J., Achilefu, S., Vij, R., and Azab, A.K. (2015). 3D tissue-engineered bone marrow as a novel model to study pathophysiology and drug resistance in multiple myeloma. *Biomaterials* 73, 70–84.
- Dempster, D.W., Compston, J.E., Drezner, M.K., Glorieux, F.H., Kanis, J.A., Malluche, H., et al. (2013). Standardized nomenclature, symbols, and units for bone histomorphometry: a 2012 update of the report of the ASBMR Histomorphometry Nomenclature Committee. *J Bone Miner Res* 28, 2-17.
- Derakhshani, M., Abbaszadeh, H., Movassaghpour, A.A., Mehdizadeh, A., Ebrahimi-Warkiani, M., and Yousefi, M. (2019). Strategies for elevating hematopoietic stem cells expansion and engraftment capacity. *Life Sci.* 232, 116598.

## Bibliography

- Desdoits-Lethimonier, C., Lesne, L., Gaudriault, P., Zalko, D., Antignac, J.P., Deceuninck, Y., et al. (2017). Parallel assessment of the effects of bisphenol A and several of its analogs on the adult human testis. *Hum Reprod* 32, 1465-1473.
- Devlin, M. J., Cloutier, A. M., Thomas, N. A., Panus, D. A., Lotinun, S., Pinz, I., et. al. (2010). Caloric restriction leads to high marrow adiposity and low bone mass in growing mice. *Journal of Bone and Mineral Research*, 25(9), 2078-2088.
- Devlin, M. J. (2011). Why does starvation make bones fat?. *American Journal of Human Biology*, 23(5), 577-585.
- Devlin, M.J., Brooks, D.J., Conlon, C., Vliet, M., Louis, L., Rosen, C.J., et al. (2016). Daily leptin blunts marrow fat but does not impact bone mass in caloric-restricted mice. *J Endocrinol* 229, 295-306.
- Devlin, M.J., Robbins, A., Cosman, M.N., Moursi, C.A., Cloutier, A.M., Louis, L., et al. (2018). Differential effects of high fat diet and diet-induced obesity on skeletal acquisition in female C57BL/6J vs. FVB/NJ Mice. *Bone Rep* 8, 204-214.
- Dexter, T. M., & Lajtha, L. G. (1974). Proliferation of haemopoietic stem cells in vitro. *British journal of haematology*, 28(4), 525-530.
- Dexter, T. M., & Testa, N. G. (1976). Differentiation and proliferation of hemopoietic cells in culture. In *Methods in cell biology* (Vol. 14, pp. 387-405). Academic Press.
- Dexter, T. M., Allen, T. D., & Lajtha, L. G. (1977). Conditions controlling the proliferation of haemopoietic stem cells in vitro. *Journal of cellular physiology*, 91(3), 335-344.
- Dieckmeyer, M., Ruschke, S., Cordes, C., Yap, S.P., Kooijman, H., Hauner, H., et al. (2015). The need for T(2) correction on MRS-based vertebral bone marrow fat quantification: implications for bone marrow fat fraction age dependence. *NMR Biomed* 28, 432-439.
- Ding, L., Saunders, T.L., Enikolopov, G., and Morrison, S.J. (2012). Endothelial and perivascular cells maintain haematopoietic stem cells. *Nature* 481, 457-462.
- Ding, L., & Morrison, S. J. (2013). Haematopoietic stem cells and early lymphoid progenitors occupy distinct bone marrow niches. *Nature*, 495(7440), 231.
- Ding, S. Y., Lee, M. J., Summer, R., Liu, L., Fried, S. K., & Pilch, P. F. (2014). Pleiotropic effects of cavin-1 deficiency on lipid metabolism. *Journal of Biological Chemistry*, 289(12), 8473-8483.
- Döhner, H., Estey, E. H., Amadori, S., Appelbaum, F. R., Büchner, T., Burnett, A. K., et. al. (2010). Diagnosis and management of acute myeloid leukemia in adults: recommendations from an international expert panel, on behalf of the European LeukemiaNet. *Blood, The Journal of the American Society of Hematology*, 115(3), 453-474.
- Dollet, L., Magre, J., Cariou, B., & Prieur, X. (2014). Function of seipin: new insights from Bsc12/seipin knockout mouse models. *Biochimie*, 96, 166-172.
- Dominici, M., Le Blanc, K., Mueller, I., Slaper-Cortenbach, I., Marini, F., Krause, D., et al. (2006). Minimal criteria for defining multipotent mesenchymal stromal cells. The International Society for Cellular Therapy position statement. *Cytotherapy* 8, 315-317.
- Dominietto, A., Lamparelli, T., Raiola, A. M., Van Lint, M. T., Gualandi, F., Berisso, G., et. al. (2002). Transplant-related mortality and long-term graft function are significantly influenced by cell dose in patients undergoing allogeneic marrow transplantation. *Blood*, 100(12), 3930-3934.
- Doucette, C. R., Horowitz, M. C., Berry, R., MacDougald, O. A., Anunciado-Koza, R., Koza, R. A., & Rosen, C. J. (2015). A high fat diet increases bone marrow adipose tissue (MAT) but does not alter trabecular or cortical bone mass in C57BL/6J mice. *Journal of cellular physiology*, 230(9), 2032-2037.

## Bibliography

- Du Verney, J.G (1700). De la structure et du setiment de la moelle. In Histoire de l'Academie Royale de Sciences. Amsterdam: Chez Pierre Mortier, 202-205.
- Du, W.J., Chi, Y., Yang, Z.X., Li, Z.J., Cui, J.J., Song, B.Q., et al. (2016). Heterogeneity of proangiogenic features in mesenchymal stem cells derived from bone marrow, adipose tissue, umbilical cord, and placenta. *Stem Cell Res Ther* 7, 163.
- Dunlop, H. (1907). Note on horse fat and “animal” oil. *Analyst*, 32(378), 317-320.
- Duque, G., Li, W., Vidal, C., Bermeo, S., Rivas, D., and Henderson, J. (2013). Pharmacological inhibition of PPARgamma increases osteoblastogenesis and bone mass in male C57BL/6 mice. *J Bone Miner Res* 28, 639-648.
- Ehrlich, P. (1879). Über die spezifischen Granulationen des Blutes. *Arch Anat Physiol.*, 571.
- Emery, J. L., & Follett, G. F. (1964). Regression of bone-marrow haemopoiesis from the terminal digits in the foetus and infant. *British journal of haematology*, 10(4), 485-489.
- Erben, R.G. (1997). Embedding of Bone Samples in Methylmethacrylate: An Improved Method Suitable for Bone Histomorphometry, Histochemistry, and Immunohistochemistry. *Journal of Histochemistry & Cytochemistry* 45, 307-313.
- Erben, R.G., and Glosmann, M. (2012). Histomorphometry in rodents. *Methods Mol Biol* 816, 279-303.
- Evans, A. G., & Calvi, L. M. (2015). Notch signaling in the malignant bone marrow microenvironment: implications for a niche-based model of oncogenesis. *Annals of the New York Academy of Sciences*, 1335(1), 63.
- Fairfield, H., Falank, C., Farrell, M., Vary, C., Boucher, J.M., Driscoll, H., et al. (2019). Development of a 3D bone marrow adipose tissue model. *Bone* 118, 77-88.
- Falank, C., Fairfield, H., & Reagan, M. R. (2016). Signaling interplay between bone marrow adipose tissue and multiple myeloma cells. *Frontiers in endocrinology*, 7, 67.
- Fan, Y., Hanai, J.I., Le, P.T., Bi, R., Maridas, D., Demambro, V., et al. (2017). Parathyroid Hormone Directs Bone Marrow Mesenchymal Cell Fate. *Cell Metab* 25, 661-672.
- Fowler, J. A., Lwin, S. T., Drake, M. T., Edwards, J. R., Kyle, R. A., Mundy, G. R., & Edwards, C. M. (2011). Host-derived adiponectin is tumor-suppressive and a novel therapeutic target for multiple myeloma and the associated bone disease. *Blood*, 118(22), 5872-5882.
- Friedenstein, A. J., Piatetzky-Shapiro, I. I., & Petrakova, K. V. (1966). Osteogenesis in transplants of bone marrow cells. *Development*, 16(3), 381-390.
- Friedenstein, A.J., Petrakova, K.V., Kurolesova, A.I., and Frolova, G.P. (1968). Heterotopic of bone marrow. Analysis of precursor cells for osteogenic and hematopoietic tissues. *Transplantation* 6, 230-247.
- Friedenstein, A. J., Chailakhjan, R. K., & Lalykina, K. (1970). The development of fibroblast colonies in monolayer cultures of guinea-pig bone marrow and spleen cells. *Cell Proliferation*, 3(4), 393-403.
- Friedenstein, A.J., Latzinik, N.W., Grosheva, A.G., and Gorskaya, U.F. (1982). Marrow microenvironment transfer by heterotopic transplantation of freshly isolated and cultured cells in porous sponges. *Exp. Hematol.* 10, 217–227.
- Gainsford, T., Willson, T. A., Metcalf, D., Handman, E., McFarlane, C., Ng, A., et. al. (1996). Leptin can induce proliferation, differentiation, and functional activation of hemopoietic cells. *Proceedings of the National Academy of Sciences*, 93(25), 14564-14568.
- Gao, J., Yan, X.-L., Li, R., Liu, Y., He, W., Sun, S., Zhang, Y., Liu, B., Xiong, J., and Mao, N. (2010). Characterization of OP9 as authentic mesenchymal stem cell line. *J. Genet. Genomics Yi Chuan Xue Bao* 37, 475–482.

## Bibliography

- Gee, C. S., Nguyen, J. T., Marquez, C. J., Heunis, J., Lai, A., Wyatt, C., et. al. (2015). Validation of bone marrow fat quantification in the presence of trabecular bone using MRI. *Journal of Magnetic Resonance Imaging*, 42(2), 539-544.
- Geissler, E. N., & Russell, E. S. (1983). Analysis of the hematopoietic effects of new dominant spotting (W) mutations of the mouse. I. Influence upon hematopoietic stem cells. *Experimental hematology*, 11(6), 452-460.
- Ghali, O., Broux, O., Falgayrac, G., Haren, N., van Leeuwen, J. P., Penel, G., et. al. (2015). Dexamethasone in osteogenic medium strongly induces adipocyte differentiation of mouse bone marrow stromal cells and increases osteoblast differentiation. *BMC cell biology*, 16(1), 9.
- Ghiglia, D. C., & Pritt, M. D. (1998). *Two-dimensional phase unwrapping: theory, algorithms, and software* (Vol. 4). New York: Wiley.
- Glover, G. H. (1991). Multipoint Dixon technique for water and fat proton and susceptibility imaging. *Journal of Magnetic Resonance Imaging*, 1(5), 521-530.
- Gobaa, S., Hoehnel, S., and Lutolf, M.P. (2015). Substrate elasticity modulates the responsiveness of mesenchymal stem cells to commitment cues. *Integr Biol (Camb)* 7, 1135-1142.
- Gomariz, A., Helbling, P.M., Isringhausen, S., Suessbier, U., Becker, A., Boss, A., et al. (2018). Quantitative spatial analysis of haematopoiesis-regulating stromal cells in the bone marrow microenvironment by 3D microscopy. *Nature Communications* 9.
- Gong, J. K. (1978). Endosteal marrow: a rich source of hematopoietic stem cells. *Science*, 199(4336), 1443-1445.
- González-Chávez, S.A., Pacheco-Tena, C., Macías-Vázquez, C.E., and Luévano-Flores, E. (2013). Assessment of different decalcifying protocols on Osteopontin and Osteocalcin immunostaining in whole bone specimens of arthritis rat model by confocal immunofluorescence. *International Journal of Clinical and Experimental Pathology* 6, 1972-1983.
- Goodsitt, M.M., and Rosenthal, D.I. (1987). Quantitative computed tomography scanning for measurement of bone and bone marrow fat content. A comparison of single- and dual-energy techniques using a solid synthetic phantom. *Invest Radiol* 22, 799-810.
- Gosselin and Regnauld (1849). On the Medullary Substance of Bones. *Arch. Gen. Med.* 10, 257
- Goujon, E. (1869). Recherches expérimentales sur les propriétés physiologiques de la moelle des os. *J de l'Anatomie et de la Physiologie Normales et Pathologiques de l'Homme et des Animaux*, 6, 399.
- Greenbaum, A., Chan, K.Y., Dobrev, T., Brown, D., Balani, D.H., Boyce, R., et al. (2017). Bone CLARITY: Clearing, imaging, and computational analysis of osteoprogenitors within intact bone marrow. *Sci Transl Med* 9.
- Grüneboom, A., Hawwari, I., Weidner, D., Culemann, S., Müller, S., Henneberg, S., et. al. (2019). A network of trans-cortical capillaries as mainstay for blood circulation in long bones. *Nature Metabolism*, 1(2), 236.
- Gubelmann, C., Schwalie, P.C., Raghav, S.K., Roder, E., Delessa, T., Kiehlmann, E., et al. (2014). Identification of the transcription factor ZEB1 as a central component of the adipogenic gene regulatory network. *Elife* 3, e03346.
- Guo, Y., Cordes, K. R., Farese, R. V., & Walther, T. C. (2009). Lipid droplets at a glance. *J Cell Sci*, 122(6), 749-752.
- Gupta, R. K., Arany, Z., Seale, P., Mepani, R. J., Ye, L., Conroe, H. M., . et. al. (2010). Transcriptional control of preadipocyte determination by Zfp423. *Nature*, 464(7288), 619.
- Gupta, R. K., Mepani, R. J., Kleiner, S., Lo, J. C., Khandekar, M. J., Cohen, P., et. al. (2012). Zfp423 expression identifies committed preadipocytes and localizes to adipose endothelial and perivascular cells. *Cell metabolism*, 15(2), 230-239.
- Haeckel, E. (1868). *Natürliche Schöpfungsgeschichte*. Berlin: Georg Reimer.

## Bibliography

- Hagberg, C.E., Li, Q., Kutschke, M., Bhowmick, D., Kiss, E., Shabalina, I.G., et al. (2018). Flow Cytometry of Mouse and Human Adipocytes for the Analysis of Browning and Cellular Heterogeneity. *Cell Rep* 24, 2746-2756 e2745.
- Halade, G.V., Rahman, M.M., Williams, P.J., and Fernandes, G. (2011). Combination of conjugated linoleic acid with fish oil prevents age-associated bone marrow adiposity in C57Bl/6J mice. *J Nutr Biochem* 22, 459-469.
- Hamrick, M.W., Della Fera, M.A., Choi, Y.H., Hartzell, D., Pennington, C., and Baile, C.A. (2007). Injections of leptin into rat ventromedial hypothalamus increase adipocyte apoptosis in peripheral fat and in bone marrow. *Cell Tissue Res* 327, 133-141.
- Hamrick, M.W., Pennington, C., Newton, D., Xie, D., and Isales, C. (2004). Leptin deficiency produces contrasting phenotypes in bones of the limb and spine. *Bone* 34, 376-383.
- Hamrick, M.W., Della-Fera, M.A., Choi, Y.H., Pennington, C., Hartzell, D., and Baile, C.A. (2005). Leptin treatment induces loss of bone marrow adipocytes and increases bone formation in leptin-deficient ob/ob mice. *J Bone Miner Res* 20, 994-1001.
- Hanoun, M., & Frenette, P. S. (2013). This niche is a maze; an amazing niche. *Cell stem cell*, 12(4), 391-392.
- Hardouin, P., Rharass, T., and Lucas, S. (2016). Bone Marrow Adipose Tissue: To Be or Not To Be a Typical Adipose Tissue? *Front Endocrinol (Lausanne)* 7, 85.
- Hayashi, Y. K., Matsuda, C., Ogawa, M., Goto, K., Tominaga, K., Mitsuhashi, S., et. al. (2009). Human PTRF mutations cause secondary deficiency of caveolins resulting in muscular dystrophy with generalized lipodystrophy. *The Journal of clinical investigation*, 119(9), 2623-2633.
- Haylock, D. N., Williams, B., Johnston, H. M., Liu, M. C., Rutherford, K. E., Whitty, G. A., et. al. (2007). Hemopoietic stem cells with higher hemopoietic potential reside at the bone marrow endosteum. *Stem cells*, 25(4), 1062-1069.
- Henriksson, I., Gatenholm, P., and Hägg, D.A. (2017). Increased lipid accumulation and adipogenic gene expression of adipocytes in 3D bioprinted nanocellulose scaffolds. *Biofabrication* 9, 015022.
- Hill, M. M., Bastiani, M., Luetterforst, R., Kirkham, M., Kirkham, A., Nixon, S. J., et. al. (2008). PTRF-Cavin, a conserved cytoplasmic protein required for caveola formation and function. *Cell*, 132(1), 113-124.
- Holzapfel, B.M., Hutmacher, D.W., Nowlan, B., Barbier, V., Thibadeau, L., Theodoropoulos, C., Hooper, J.D., Loessner, D., Clements, J.A., Russell, P.J., et al. (2015). Tissue engineered humanized bone supports human hematopoiesis in vivo. *Biomaterials* 61, 103-114.
- Hooke, R. (1665). *Micrographia*.
- Horowitz, M. C., Berry, R., Holtrup, B., Sebo, Z., Nelson, T., Fretz, J. A., et. al. (2017). Bone marrow adipocytes. *Adipocyte*, 6(3), 193-204.
- Houlihan, D.D., Mabuchi, Y., Morikawa, S., Nübe, K., Araki, D., Suzuki, S., et al. (2012). Isolation of mouse mesenchymal stem cells on the basis of expression of Sca-1 and PDGFR-alpha. *Nat Protoc* 7, 2103-2111.
- Hozumi, A., Osaki, M., Sakamoto, K., Goto, H., Fukushima, T., Baba, H., & Shindo, H. (2010). Dexamethasone-induced plasminogen activator inhibitor-1 expression in human primary bone marrow adipocytes. *Biomedical research*, 31(5), 281-286.
- Hu, H.H., Bornert, P., Hernando, D., Kellman, P., Ma, J., Reeder, S., et al. (2012). ISMRM workshop on fat-water separation: insights, applications and progress in MRI. *Magn Reson Med* 68, 378-388.
- Hu, H.H., and Kan, H.E. (2013). Quantitative proton MR techniques for measuring fat. *NMR Biomed* 26, 1609-1629.

## Bibliography

- Huang, S., Xu, L., Sun, Y., Wu, T., Wang, K., and Li, G. (2015). An improved protocol for isolation and culture of mesenchymal stem cells from mouse bone marrow. *J Orthop Translat* 3, 26-33.
- Huggins, C., and Blocksom, B.H. (1936). Changes in Outlying Bone Marrow Accompanying a Local Increase of Temperature within Physiological Limits. *J Exp Med* 64, 253-274.
- Hughes, C.S., Postovit, L.M., and Lajoie, G.A. (2010). Matrigel: a complex protein mixture required for optimal growth of cell culture. *Proteomics* 10, 1886–1890.
- Hui, S.K., Arentsen, L., Sueblinvong, T., Brown, K., Bolan, P., Ghebre, R.G., et al. (2015). A phase I feasibility study of multi-modality imaging assessing rapid expansion of marrow fat and decreased bone mineral density in cancer patients. *Bone* 73, 90-97.
- Isern, J., Martín-Antonio, B., Ghazanfari, R., Martín, A.M., López, J.A., del Toro, R., Sánchez-Aguilera, A., Arranz, L., Martín-Pérez, D., Suárez-Lledó, M., et al. (2013). Self-renewing human bone marrow mesospheres promote hematopoietic stem cell expansion. *Cell Rep.* 3, 1714–1724.
- Iwaniec, U. T., & Turner, R. T. (2013). Failure to generate bone marrow adipocytes does not protect mice from ovariectomy-induced osteopenia. *Bone*, 53(1), 145-153.
- Iwaniec, U. T., Philbrick, K. A., Wong, C. P., Gordon, J. L., Kahler-Quesada, A. M., Olson, D. A., ... & Turner, R. T. (2016). Room temperature housing results in premature cancellous bone loss in growing female mice: implications for the mouse as a preclinical model for age-related bone loss. *Osteoporosis International*, 27(10), 3091-3101.
- Jain, S. K., & Subrahmanyam, D. (1978). On the mechanism of phenylhydrazine-induced hemolytic anemia. *Biochemical and biophysical research communications*, 82(4), 1320-1324.
- Janssens, R., Struyf, S., & Proost, P. (2018). The unique structural and functional features of CXCL12. *Cellular & molecular immunology*, 15(4), 299-311.
- Jeffery, E., Berry, R., Church, C.D., Yu, S., Shook, B.A., Horsley, V., et al. (2014). Characterization of Cre recombinase models for the study of adipose tissue. *Adipocyte* 3, 206-211.
- Ji, J., Vijayaragavan, K., Bosse, M., Menendez, P., Weisel, K., and Bhatia, M. (2008). OP9 stroma augments survival of hematopoietic precursors and progenitors during hematopoietic differentiation from human embryonic stem cells. *Stem Cells Dayt. Ohio* 26, 2485–2495.
- Jiang, Y., Bonig, H., Ulyanova, T., Chang, K., & Papayannopoulou, T. (2009). On the adaptation of endosteal stem cell niche function in response to stress. *Blood*, 114(18), 3773-3782.
- Jing, D., Fonseca, A.-V., Alakel, N., Fierro, F.A., Muller, K., Bornhauser, M., Ehninger, G., Corbeil, D., and Ordemann, R. (2010). Hematopoietic stem cells in co-culture with mesenchymal stromal cells--modeling the niche compartments in vitro. *Haematologica* 95, 542–550.
- Jing, D., Zhang, S., Luo, W., Gao, X., Men, Y., Ma, C., et al. (2018). Tissue clearing of both hard and soft tissue organs with the pegasos method. *Cell Research* 28, 803-818.
- Johnson, J.T., Hansen, M.S., Wu, I., Healy, L.J., Johnson, C.R., Jones, G.M., et al. (2006). Virtual histology of transgenic mouse embryos for high-throughput phenotyping. *PLoS Genetics* 2, 471-477.
- Justesen, J., Stenderup, K., Ebbesen, E.N., Mosekilde, L., Steiniche, T., and Kassem, M. (2001). Adipocyte tissue volume in bone marrow is increased with aging and in patients with osteoporosis. *Biogerontology* 2, 165-171.
- Kalajzic, Z., Li, H., Wang, L.-P., Jiang, X., Lamothe, K., Adams, D.J., et al. (2008). Use of an alpha-smooth muscle actin GFP reporter to identify an osteoprogenitor population. *Bone* 43, 501-510.

## Bibliography

- Karampinos, D.C., Melkus, G., Baum, T., Bauer, J.S., Rummeny, E.J., and Krug, R. (2014). Bone marrow fat quantification in the presence of trabecular bone: initial comparison between water-fat imaging and single-voxel MRS. *Magn Reson Med* 71, 1158-1165.
- Karampinos, D. C., Ruschke, S., Gordijenko, O., Grande Garcia, E., Kooijman, H., Burgkart, R., ... & Baum, T. (2015). Association of MRS-based vertebral bone marrow fat fraction with bone strength in a human in vitro model. *Journal of osteoporosis*.
- Karampinos, D. C., Ruschke, S., Dieckmeyer, M., Diefenbach, M., Franz, D., Gersing, A. S., ... & Baum, T. (2018). Quantitative MRI and spectroscopy of bone marrow. *Journal of Magnetic Resonance Imaging*, 47(2), 332-353.
- Kassem, M., and Bianco, P. (2015). Skeletal stem cells in space and time. *Cell* 160, 17-19.
- Kerckhofs, G., Durand, M., Vangoitsenhoven, R., Marin, C., Van Der Schueren, B., Carmeliet, G., et al. (2016). Changes in bone macro- and microstructure in diabetic obese mice revealed by high resolution microfocus X-ray computed tomography. *Scientific Reports* 6, 1-13.
- Kerckhofs, G., Stegen, S., Van Gastel, N., Sap, A., Falgayrac, G., Penel, G., et al. (2018). Simultaneous three-dimensional visualization of mineralized and soft skeletal tissues by a novel microCT contrast agent with polyoxometalate structure. *Biomaterials* 159, 1-12.
- Keune, J. A., Wong, C. P., Branscum, A. J., Iwaniec, U. T., & Turner, R. T. (2017). Bone marrow adipose tissue deficiency increases disuse-induced bone loss in male mice. *Scientific reports*, 7, 46325.
- Khoury, B.M., Bigelow, E.M.R., Smith, L.M., Schlecht, S.H., Scheller, E.L., Andarawis-Puri, N., et al. (2015). The use of nano-computed tomography to enhance musculoskeletal research. *Connective Tissue Research* 56, 106-119.
- Kiel, M. J., Yilmaz, Ö. H., Iwashita, T., Yilmaz, O. H., Terhorst, C., & Morrison, S. J. (2005). SLAM family receptors distinguish hematopoietic stem and progenitor cells and reveal endothelial niches for stem cells. *Cell*, 121(7), 1109-1121.
- Kiel, M. J., & Morrison, S. J. (2006). Maintaining hematopoietic stem cells in the vascular niche. *Immunity*, 25(6), 862-864.
- Kim, H.J., Bae, Y.C., Park, R.W., Choi, S.W., Cho, S.H., Choi, Y.S., et al. (2002). Bone-protecting effect of safflower seeds in ovariectomized rats. *Calcif Tissue Int* 71, 88-94.
- Kimmel, A. R., & Sztalryd, C. (2016). The perilipins: Major cytosolic lipid droplet-associated proteins and their roles in cellular lipid storage, mobilization, and systemic homeostasis. *Annual review of nutrition*, 36, 471-509.
- Ko, F.C., Martins, J.S., Reddy, P., Bragdon, B., Hussein, A.I., Gerstenfeld, L.C., et al. (2016). Acute Phosphate Restriction Impairs Bone Formation and Increases Marrow Adipose Tissue in Growing Mice. *J Bone Miner Res* 31, 2204-2214.
- Kretzschmar, K., and Watt, F.M. (2012). Lineage tracing. *Cell* 148, 33-45.
- Kricun, M. E. (1985). Red-yellow marrow conversion: its effect on the location of some solitary bone lesions. *Skeletal radiology*, 14(1), 10-19.
- Krings, A., Rahman, S., Huang, S., Lu, Y., Czernik, P.J., and Lecka-Czernik, B. (2012). Bone marrow fat has brown adipose tissue characteristics, which are attenuated with aging and diabetes. *Bone* 50, 546-552.
- Kunisaki, Y., Bruns, I., Scheiermann, C., Ahmed, J., Pinho, S., Zhang, D., ... & Mar, J. C. (2013). Arteriolar niches maintain haematopoietic stem cell quiescence. *Nature*, 502(7473), 637.
- Kusumbe, A.P., Ramasamy, S.K., Starsichova, A., and Adams, R.H. (2015). Sample preparation for high-resolution 3D confocal imaging of mouse skeletal tissue. *Nature Protocols* 10, 1904-1914.

## Bibliography

- Kusumbe, A.P., Ramasamy, S.K., Itkin, T., Mae, M.A., Langen, U.H., Betsholtz, C., et al. (2016). Age-dependent modulation of vascular niches for haematopoietic stem cells. *Nature* 532, 380-384.
- Laval-Jeantet, A.M., Roger, B., Bouysee, S., Bergot, C., and Mazess, R.B. (1986). Influence of vertebral fat content on quantitative CT density. *Radiology* 159, 463-466.
- Lazarenko, O.P., Rzonca, S.O., Suva, L.J., and Lecka-Czernik, B. (2006). Netoglitazone is a PPAR-gamma ligand with selective effects on bone and fat. *Bone* 38, 74-84.
- Lazarenko, O.P., Rzonca, S.O., Hogue, W.R., Swain, F.L., Suva, L.J., and Lecka-Czernik, B. (2007). Rosiglitazone induces decreases in bone mass and strength that are reminiscent of aged bone. *Endocrinology* 148, 2669-2680.
- Le Ster, C., Gambarota, G., Lasbleiz, J., Guillin, R., Decaux, O., and Saint-Jalmes, H. (2016). Breath-hold MR measurements of fat fraction, T1, and T2\* of water and fat in vertebral bone marrow. *J Magn Reson Imaging* 44, 549-555.
- Le, P.T., Bishop, K.A., Maridas, D.E., Motyl, K.J., Brooks, D.J., Nagano, K., et al. (2017). Spontaneous mutation of Dock7 results in lower trabecular bone mass and impaired periosteal expansion in aged female Misty mice. *Bone* 105, 103-114.
- Lecarpentier, Y., Schussler, O., Sakic, A., Rincon-Garriz, J.M., Soulie, P., Bochaton-Piallat, M.-L., and Kindler, V. (2018). Human Bone Marrow Contains Mesenchymal Stromal Stem Cells That Differentiate In Vitro into Contractile Myofibroblasts Controlling T Lymphocyte Proliferation. *Stem Cells Int.* 2018, 6134787.
- Lecka-Czernik, B., Stechschulte, L.A., Czernik, P.J., Sherman, S.B., Huang, S., and Krings, A. (2017). Marrow Adipose Tissue: Skeletal Location, Sexual Dimorphism, and Response to Sex Steroid Deficiency. *Front Endocrinol (Lausanne)* 8, 188.
- Lee, H. J., Li, N., Evans, S. M., Diaz, M. F., & Wenzel, P. L. (2013). Biomechanical force in blood development: extrinsic physical cues drive pro-hematopoietic signaling. *Differentiation*, 86(3), 92-103.
- Leisten, I., Kramann, R., Ventura Ferreira, M.S., Bovi, M., Neuss, S., Ziegler, P., Wagner, W., Knüchel, R., and Schneider, R.K. (2012). 3D co-culture of hematopoietic stem and progenitor cells and mesenchymal stem cells in collagen scaffolds as a model of the hematopoietic niche. *Biomaterials* 33, 1736-1747.
- Lewis, J. P., & Trobaugh, F. E. (1964). Haematopoietic stem cells. *Nature*, 204(4958), 589-590.
- Li, N., Feugier, P., Serrurier, B., Latger-Cannard, V., Lesesve, J.-F., Stoltz, J.-F., and Eljaafari, A. (2007). Human mesenchymal stem cells improve ex vivo expansion of adult human CD34+ peripheral blood progenitor cells and decrease their allostimulatory capacity. *Exp. Hematol.* 35, 507-515.
- Li, X., Kuo, D., Schafer, A. L., Porzig, A., Link, T. M., Black, D., & Schwartz, A. V. (2011). Quantification of vertebral bone marrow fat content using 3 Tesla MR spectroscopy: reproducibility, vertebral variation, and applications in osteoporosis. *Journal of Magnetic Resonance Imaging*, 33(4), 974-979.
- Li, G.W., Chang, S.X., Fan, J.Z., Tian, Y.N., Xu, Z., and He, Y.M. (2013a). Marrow adiposity recovery after early zoledronic acid treatment of glucocorticoid-induced bone loss in rabbits assessed by magnetic resonance spectroscopy. *Bone* 52, 668-675.
- Li, H., Li, H., Guo, H., and Liu, F. (2013b). Cholesterol suppresses adipocytic differentiation of mouse adipose-derived stromal cells via PPARgamma2 signaling. *Steroids* 78, 454-461.
- Li, G.W., Xu, Z., Chang, S.X., Zhou, L., Wang, X.Y., Nian, H., et al. (2014a). Influence of early zoledronic acid administration on bone marrow fat in ovariectomized rats. *Endocrinology* 155, 4731-4738.



## Bibliography

- Li, H., Ghazanfari, R., Zacharaki, D., Ditzel, N., Isern, J., Ekblom, M., et al. (2014b). Low/negative expression of PDGFR- $\alpha$  identifies the candidate primary mesenchymal stromal cells in adult human bone marrow. *Stem Cell Reports* 3, 965-974.
- Li, G., Xu, Z., Hou, L., Li, X., Li, X., Yuan, W., et al. (2016). Differential effects of bisphenol A diglycidyl ether on bone quality and marrow adiposity in ovary-intact and ovariectomized rats. *Am J Physiol Endocrinol Metab* 311, E922-E927.
- Li, G., Xu, Z., Gu, H., Li, X., Yuan, W., Chang, S., ... & Hu, J. (2017a). Comparison of chemical shift-encoded water-fat MRI and MR spectroscopy in quantification of marrow fat in postmenopausal females. *Journal of Magnetic Resonance Imaging*, 45(1), 66-73.
- Li, X., Shet, K., Xu, K., Rodríguez, J. P., Pino, A. M., Kurhanewicz, J., ... & Rosen, C. J. (2017b). Unsaturation level decreased in bone marrow fat of postmenopausal women with low bone density using high resolution magic angle spinning (HRMAS)  $^1\text{H}$  NMR spectroscopy. *Bone*, 105, 87-92.
- Li, Q., Wu, Y., and Kang, N. (2018). Marrow Adipose Tissue: Its Origin, Function, and Regulation in Bone Remodeling and Regeneration. *Stem Cells International* 2018, 1-11.
- Lightbourne, M., & Brown, R. J. (2017). Genetics of lipodystrophy. *Endocrinology and Metabolism Clinics*, 46(2), 539-554.
- Limonard, E.J., Veldhuis-Vlug, A.G., Van Dussen, L., Runge, J.H., Tanck, M.W., Endert, E., et al. (2015). Short-Term Effect of Estrogen on Human Bone Marrow Fat. *J Bone Miner Res* 30, 2058-2066.
- Lindenmaier, L.B., Philbrick, K.A., Branscum, A.J., Kalra, S.P., Turner, R.T., and Iwaniec, U.T. (2016). Hypothalamic Leptin Gene Therapy Reduces Bone Marrow Adiposity in ob/ob Mice Fed Regular and High-Fat Diets. *Front Endocrinol (Lausanne)* 7, 110.
- Litzlbauer, H.D., Neuhaeuser, C., Moell, A., Greschus, S., Breithecker, A., Franke, F.E., et al. (2006). Three-dimensional imaging and morphometric analysis of alveolar tissue from microfocal X-ray-computed tomography. *American Journal of Physiology-Lung Cellular and Molecular Physiology* 291, L535-L545.
- Liu, C.Y., Mckenzie, C.A., Yu, H., Brittain, J.H., and Reeder, S.B. (2007). Fat quantification with IDEAL gradient echo imaging: correction of bias from T(1) and noise. *Magn Reson Med* 58, 354-364.
- Liu, L., Brown, D., McKee, M., LeBrasseur, N. K., Yang, D., Albrecht, K. H., ... & Pilch, P. F. (2008). Deletion of Cavin/PTRF causes global loss of caveolae, dyslipidemia, and glucose intolerance. *Cell metabolism*, 8(4), 310-317.
- Liu, S.H., Chen, C., Yang, R.S., Yen, Y.P., Yang, Y.T., and Tsai, C. (2011). Caffeine enhances osteoclast differentiation from bone marrow hematopoietic cells and reduces bone mineral density in growing rats. *J Orthop Res* 29, 954-960.
- Liu, Z., Xu, J., He, J., Liu, H., Lin, P., Wan, X., et al. (2015). Mature adipocytes in bone marrow protect myeloma cells against chemotherapy through autophagy activation. *Oncotarget*, 6(33), 34329.
- Liu, P., Ji, Y., Yuen, T., Rendina-Ruedy, E., Demambro, V.E., Dhawan, S., et al. (2017). Blocking FSH induces thermogenic adipose tissue and reduces body fat. *Nature* 546, 107-112.
- Love, M. I., Huber, W., & Anders, S. (2014). Moderated estimation of fold change and dispersion for RNA-seq data with DESeq2. *Genome biology*, 15(12), 550.
- Lu, W., Wang, W., Wang, S., Feng, Y., and Liu, K. (2016). Rosiglitazone Promotes Bone Marrow Adipogenesis to Impair Myelopoiesis under Stress. *PLoS ONE* 11, e0149543.
- Lu, W., Weng, W., Zhu, Q., Zhai, Y., Wan, Y., Liu, H., ... & Shi, J. (2018). Small bone marrow adipocytes predict poor prognosis in acute myeloid leukemia. *haematologica*, 103(1), e21-e24.

## Bibliography

- Luo, Y., Chen, G.L., Hannemann, N., Ipseiz, N., Kronke, G., Bauerle, T., et al. (2015). Microbiota from Obese Mice Regulate Hematopoietic Stem Cell Differentiation by Altering the Bone Niche. *Cell Metab* 22, 886-894.
- MacEwan, I. J., Glembotski, N. E., D'Lima, D., Bae, W., Masuda, K., Rashidi, H. H., ... & Bydder, M. (2014). Proton density water fraction as a biomarker of bone marrow cellularity: validation in ex vivo spine specimens. *Magnetic resonance imaging*, 32(9), 1097-1101.
- Maciel, J.G., De Araujo, I.M., Carvalho, A.L., Simao, M.N., Bastos, C.M., Troncon, L.E., et al. (2017). Marrow Fat Quality Differences by Sex in Healthy Adults. *J Clin Densitom* 20, 106-113.
- Magome, T., Froelich, J., Takahashi, Y., Arentsen, L., Holtan, S., Verneris, M.R., et al. (2016). Evaluation of Functional Marrow Irradiation Based on Skeletal Marrow Composition Obtained Using Dual-Energy Computed Tomography. *Int J Radiat Oncol Biol Phys* 96, 679-687.
- Majka, S. M., Barak, Y., & Klemm, D. J. (2011). Concise review: adipocyte origins: weighing the possibilities. *Stem Cells*, 29(7), 1034-1040.
- Makarovsky, I., Markel, G., Hoffman, A., Schein, O., Finkelstien, A., Brosh-Nissimov, T., et al. (2007). Osmium tetroxide: A new kind of weapon. *Israel Medical Association Journal* 9, 750-752.
- Malhan, D., Muelke, M., Rosch, S., Schaefer, A.B., Merboth, F., Weisweiler, D., et al. (2018). An Optimized Approach to Perform Bone Histomorphometry. *Frontiers in Endocrinology* 9.
- Maniatis, A., Tavassoli, M., and Crosby, W.H. (1971). Origin of osteogenic precursor cells in extramedullary marrow implants. *Blood* 38, 569-575.
- Maridas, D.E., Rendina-Ruedy, E., Helderman, R.C., Demambro, V.E., Brooks, D., Guntur, A.R., et al. (2019). Progenitor recruitment and adipogenic lipolysis contribute to the anabolic actions of parathyroid hormone on the skeleton. *FASEB J* 33, 2885-2898.
- Martin, R.B., and Zissimos, S.L. (1991). Relationships between marrow fat and bone turnover in ovariectomized and intact rats. *Bone* 12, 123-131.
- Mattiucci, D., Maurizi, G., Izzi, V., Cenci, L., Ciarlantini, M., Mancini, S., et al. (2018a). Bone marrow adipocytes support hematopoietic stem cell survival. *J Cell Physiol* 233, 1500-1511.
- Mattiucci, D., Naveiras, O., and Poloni, A. (2018b). Bone Marrow "Yellow" and "Red" Adipocytes: Good or Bad Cells ? , 117-122.
- Maurice, F., Dutour, A., Vincentelli, C., Abdesselam, I., Bernard, M., Dufour, H., et al. (2018). Active cushing syndrome patients have increased ectopic fat deposition and bone marrow fat content compared to cured patients and healthy subjects: a pilot 1H-MRS study. *Eur J Endocrinol* 179, 307-317.
- Mayo-Smith, W., Rosenthal, D.I., Goodsitt, M.M., and Klibanski, A. (1989). Intravertebral fat measurement with quantitative CT in patients with Cushing disease and anorexia nervosa. *Radiology* 170, 835-838.
- McKinney-Freeman, S.L., Naveiras, O., and Daley, G.Q. (2008). Isolation of hematopoietic stem cells from mouse embryonic stem cells. *Curr. Protoc. Stem Cell Biol. Chapter 1*, Unit 1F.3.
- McKinney-Freeman, S.L., Naveiras, O., Yates, F., Loewer, S., Philitas, M., Curran, M., Park, P.J., and Daley, G.Q. (2009). Surface antigen phenotypes of hematopoietic stem cells from embryos and murine embryonic stem cells. *Blood* 114, 268-278.
- Mcnicie, I.K., Bertoncello, I., Kriegler, A.B., and Quesenberry, P.J. (1990). Colony-forming cells with high proliferative potential (HPP-CFC). *Int. J. Cell Cloning* 8, 146-160.

## Bibliography

- Medina, E. A., Oberheu, K., Polusani, S. R., Ortega, V., Velagaleti, G. V. N., & Oyajobi, B. O. (2014). PKA/AMPK signaling in relation to adiponectin's antiproliferative effect on multiple myeloma cells. *Leukemia*, 28(10), 2080.
- Menagh, P. J., Turner, R. T., Jump, D. B., Wong, C. P., Lowry, M. B., Yakar, S., ... & Iwaniec, U. T. (2010). Growth hormone regulates the balance between bone formation and bone marrow adiposity. *Journal of Bone and Mineral Research*, 25(4), 757-768.
- Mendelson, A., & Frenette, P. S. (2014). Hematopoietic stem cell niche maintenance during homeostasis and regeneration. *Nature medicine*, 20(8), 833.
- Méndez-Ferrer, S., Michurina, T. V., Ferraro, F., Mazloom, A. R., MacArthur, B. D., Lira, S. A., ... & Frenette, P. S. (2010). Mesenchymal and haematopoietic stem cells form a unique bone marrow niche. *Nature*, 466(7308), 829.
- Metscher, B.D. (2009). MicroCT for developmental biology: A versatile tool for high-contrast 3D imaging at histological resolutions. *Developmental Dynamics* 238, 632-640.
- Miranda, M., Pino, A. M., Fuenzalida, K., Rosen, C. J., Seitz, G., & Rodríguez, J. P. (2016). Characterization of fatty acid composition in bone marrow fluid from postmenopausal women: modification after hip fracture. *Journal of cellular biochemistry*, 117(10), 2370-2376.
- Mizoguchi, T., Pinho, S., Ahmed, J., Kunisaki, Y., Hanoun, M., Mendelson, A., et al. (2014). Osterix marks distinct waves of primitive and definitive stromal progenitors during bone marrow development. *Dev Cell* 29, 340-349.
- Moore, S.G., and Dawson, K.L. (1990). Red and yellow marrow in the femur: age-related changes in appearance at MR imaging. *Radiology* 175, 219-223.
- Moosbrugger, C. (2002). Atlas of stress-strain curves. *ASM International, Materials Park*, 375.
- Motyl, K.J., and McCabe, L.R. (2009). Leptin treatment prevents type I diabetic marrow adiposity but not bone loss in mice. *J Cell Physiol* 218, 376-384.
- Motyl, K.J., Dick-De-Paula, I., Maloney, A.E., Lotinun, S., Bornstein, S., De Paula, F.J., et al. (2012). Trabecular bone loss after administration of the second-generation antipsychotic risperidone is independent of weight gain. *Bone* 50, 490-498.
- Mukohira, H., Hara, T., Abe, S., Tani-Ichi, S., Sehara-Fujisawa, A., Nagasawa, T., et al. (2019a). Mesenchymal Stromal Cells in Bone Marrow Express Adiponectin and Are Efficiently Targeted by an Adiponectin Promoter-Driven Cre Transgene. *Int Immunol*.
- Mukohira, H., Hara, T., Abe, S., Tani-Ichi, S., Sehara-Fujisawa, A., Nagasawa, T., et al. (2019b). Mesenchymal stromal cells in bone marrow express adiponectin and are efficiently targeted by an adiponectin promoter-driven Cre transgene.
- Muzumdar, M.D., Tasic, B., Miyamichi, K., Li, L., and Luo, L. (2007). ARTICLE A Global Double-Fluorescent Cre Reporter Mouse. 605, 593-605.
- Nagasawa, T., Omatsu, Y., and Sugiyama, T. (2011). Control of hematopoietic stem cells by the bone marrow stromal niche: the role of reticular cells. *Trends Immunol* 32, 315-320.
- Nakakoshi, M., Nishioka, H., and Katayama, E. (2011). New versatile staining reagents for biological transmission electron microscopy that substitute for uranyl acetate. *Journal of Electron Microscopy* 60, 401-407.
- Nakamura, Y., Arai, F., Iwasaki, H., Hosokawa, K., Kobayashi, I., Gomei, Y., ... & Suda, T. (2010). Isolation and characterization of endosteal niche cell populations that regulate hematopoietic stem cells. *Blood*, 116(9), 1422-1432.
- Nakano, T., Kodama, H., and Honjo, T. (1994). Generation of lymphohematopoietic cells from embryonic stem cells in culture. *Science* 265, 1098-1101.

## Bibliography

- Nallamshetty, S., Wang, H., Rhee, E.J., Kiefer, F.W., Brown, J.D., Lotinun, S., et al. (2013). Deficiency of retinaldehyde dehydrogenase 1 induces BMP2 and increases bone mass in vivo. *PLoS One* 8, e71307.
- Naveiras, O., Nardi, V., Wenzel, P.L., Hauschka, P.V., Fahey, F., and Daley, G.Q. (2009a). Bone-marrow adipocytes as negative regulators of the haematopoietic microenvironment. *Nature* 460, 259-263.
- Naveiras, O. (2009b). Novel determinants of the hematopoietic microenvironment in development and homeostasis - ProQuest. Harvard University.
- Nerking, J. (1908). The partition of lecitin in the animal organism. *Journal of the Chemical Society*, 608.
- Neues, F., and Epple, M. (2008). X-ray microcomputer tomography for the study of biomineralized endo- and exoskeletons of animals. *Chemical Reviews* 108, 4734-4741.
- Neumann, E. (1868). Über die Bedeutung des Knochenmarkes für die Blutbildung. *Zentralbl Med Wissensch*, 6, 689.
- Neumann, E. (1869). Du rôle de la moelle des os dans la formations du sang. *CR Acad Sci (Paris)*, 68, 1112-1113.
- Neumann, E. (1870). *Ein Fall von Leukemie mit Erkrankung des Knochenmarkes*.
- Neumann, E. (1882). The law of distribution of yellow and red marrow in the bones of the extremities. *Cent J Med Sci*, 20, 321-323.
- Neumann, E. (1912). Hematology studies III: leukocytes and leukemia. *Anatomy and History of the Development*, 207, 480-520.
- Omatsu, Y., Sugiyama, T., Kohara, H., Kondoh, G., Fujii, N., Kohno, K., & Nagasawa, T. (2010). The essential functions of adipo-osteogenic progenitors as the hematopoietic stem and progenitor cell niche. *Immunity*, 33(3), 387-399.
- Omatsu, Y., Seike, M., Sugiyama, T., Kume, T., & Nagasawa, T. (2014). Foxc1 is a critical regulator of haematopoietic stem/progenitor cell niche formation. *Nature*, 508(7497), 536.
- Osawa, M., Hanada, K. I., Hamada, H., & Nakauchi, H. (1996). Long-term lymphohematopoietic reconstitution by a single CD34-low/negative hematopoietic stem cell. *Science*, 273(5272), 242-245.
- Ouchi, N., Parker, J. L., Lugus, J. J., & Walsh, K. (2011). Adipokines in inflammation and metabolic disease. *Nature reviews immunology*, 11(2), 85.
- Özçivici, E. (2013). Effects of spaceflight on cells of bone marrow origin. *Turkish Journal of Hematology*, 30(1), 1.
- Paccou, J., Hardouin, P., Cotten, A., Penel, G., and Cortet, B. (2015). The Role of Bone Marrow Fat in Skeletal Health: Usefulness and Perspectives for Clinicians. *J Clin Endocrinol Metab* 100, 3613-3621.
- Palade, B.Y.G.E. (1951). A Study of Fixation for Electron Microscopy. *Journal of Experimental Medicine* 95, 285-307.
- Palumbo, A., & Anderson, K. (2011). Multiple myeloma. *New England journal of medicine*, 364(24), 2364-2364.
- Pappenheim, A. (1896). Ueber entwicklung und ausbildung der erythroblasten. *Archiv für pathologische Anatomie und Physiologie und für klinische Medizin*, 145(3), 587-643.
- Parfitt, A.M. (1976). "Terminology and symbols in bone morphometry. .," in *Proceedings of the First International Workshop on Bone Morphometry*, ed. J. Zfg. (Ottawa: Ottawa University Press), 331-335.
- Parfitt, A.M., Drezner, M.K., Glorieux, F.H., Kanis, J.A., Malluche, H., Meunier, P.J., et al. (1987). Bone Histomorphometry: Standardization of Nomenclature, Symbols, and Units.pdf. *Journal of Bone and Mineral Metabolism* 2, 595-610.

## Bibliography

- Patsch, J.M., Li, X., Baum, T., Yap, S.P., Karampinos, D.C., Schwartz, A.V., et al. (2013). Bone marrow fat composition as a novel imaging biomarker in postmenopausal women with prevalent fragility fractures. *J Bone Miner Res* 28, 1721-1728.
- Peister, A., Mellad, J.A., Larson, B.L., Hall, B.M., Gibson, L.F., and Prockop, D.J. (2004). Adult stem cells from bone marrow (MSCs) isolated from different strains of inbred mice vary in surface epitopes, rates of proliferation, and differentiation potential. *Blood* 103, 1662-1668.
- Peled, A., Petit, I., Kollet, O., Magid, M., Ponomaryov, T., Byk, T., ... & Lider, O. (1999). Dependence of human stem cell engraftment and repopulation of NOD/SCID mice on CXCR4. *Science*, 283(5403), 845-848.
- Pelleymounter MA, Cullen MJ, Baker MB, et al. Effects of the obese gene product on body weight regulation in ob/ob mice. *Science*. 1995; 269:540–543
- Philbrick, K.A., Turner, R.T., Branscum, A.J., Wong, C.P., and Iwaniec, U.T. (2015). Paradoxical effects of partial leptin deficiency on bone in growing female mice. *Anat Rec (Hoboken)* 298, 2018-2029.
- Pinho, S., Lacombe, J., Hanoun, M., Mizoguchi, T., Bruns, I., Kunisaki, Y., & Frenette, P. S. (2013). PDGFR $\alpha$  and CD51 mark human nestin<sup>+</sup> sphere-forming mesenchymal stem cells capable of hematopoietic progenitor cell expansion. *Journal of Experimental Medicine*, 210(7), 1351-1367.
- Pino, A. M., & Rodríguez, J. P. (2019). Is fatty acid composition of human bone marrow significant to bone health?. *Bone*, 118, 53-61.
- Plummer, J., Park, M., Perodin, F., Horowitz, M.C., and Hens, J.R. (2017). Methionine-Restricted Diet Increases miRNAs That Can Target RUNX2 Expression and Alters Bone Structure in Young Mice. *J Cell Biochem* 118, 31-42.
- Pluznik, D. H., & Sachs, L. (1966). The induction of clones of normal mast cells by a substance from conditioned medium. *Experimental cell research*, 43(3), 553-563.
- Poloni, A., Maurizi, G., Serrani, F., Mancini, S., Zingaretti, M.C., Frontini, A., et al. (2013). Molecular and functional characterization of human bone marrow adipocytes. *Exp Hematol* 41, 558-566 e552.
- Potter, J. E., & Wright, E. G. (1980). Bone marrow lipids in normal and anemic mice. *American journal of hematology*, 8(4), 361-367.
- Prasad, P., and Donoghue, M. (2013). A comparative study of various decalcification techniques. *Indian J Dent Res* 24, 302-308.
- Prieur, X., Dollet, L., Takahashi, M., Nemani, M., Pillot, B., Le May, C., ... & Fève, B. (2013). Thiazolidinediones partially reverse the metabolic disturbances observed in Bcl2/seipin-deficient mice. *Diabetologia*, 56(8), 1813-1825.
- Raajendiran, A., Tsiloulis, T., and Watt, M.J. (2016). Adipose tissue development and the molecular regulation of lipid metabolism. *Essays In Biochemistry* 60, 437-450.
- Raic, A., Rödling, L., Kalbacher, H., and Lee-Thedieck, C. (2014). Biomimetic macroporous PEG hydrogels as 3D scaffolds for the multiplication of human hematopoietic stem and progenitor cells. *Biomaterials* 35, 929–940.
- Ramalho-Santos, M., & Willenbring, H. (2007). On the origin of the term “stem cell”. *Cell stem cell*, 1(1), 35-38.
- Razidlo, D.F., Whitney, T.J., Casper, M.E., Mcgee-Lawrence, M.E., Stensgard, B.A., Li, X., et al. (2010). Histone deacetylase 3 depletion in osteo/chondroprogenitor cells decreases bone density and increases marrow fat. *PLoS One* 5, e11492.
- Reeder, S.B., Cruite, I., Hamilton, G., and Sirlin, C.B. (2011). Quantitative Assessment of Liver Fat with Magnetic Resonance Imaging and Spectroscopy. *J Magn Reson Imaging* 34, 729-749.

## Bibliography

- Reeder, S.B., Hu, H.H., and Sirlin, C.B. (2012). Proton density fat-fraction: a standardized MR-based biomarker of tissue fat concentration. *J Magn Reson Imaging* 36, 1011-1014.
- Reinisch, A., Thomas, D., Corces, M.R., Zhang, X., Gratzinger, D., Hong, W.-J., Schallmoser, K., Strunk, D., and Majeti, R. (2016). A humanized bone marrow ossicle xenotransplantation model enables improved engraftment of healthy and leukemic human hematopoietic cells. *Nat. Med.* 22, 812–821.
- Reinisch, A., Hernandez, D.C., Schallmoser, K., and Majeti, R. (2017). Generation and use of a humanized bone-marrow-ossicle niche for hematopoietic xenotransplantation into mice. *Nat. Protoc.* 12, 2169–2188.
- Ren, J., Dimitrov, I., Sherry, A. D., & Malloy, C. R. (2008). Composition of adipose tissue and marrow fat in humans by 1H NMR at 7 Tesla. *Journal of lipid research*, 49(9), 2055-2062.
- Ribi, W., Senden, T.J., Sakellariou, A., Limaye, A., and Zhang, S. (2008). Imaging honey bee brain anatomy with micro-X-ray-computed tomography. *Journal of Neuroscience Methods* 171, 93-97.
- Ritman, E. L. (2011). Current status of developments and applications of micro-CT. *Annual review of biomedical engineering*, 13, 531-552.
- Roberts, A.S., Shetty, A.S., Mellnick, V.M., Pickhardt, P.J., Bhalla, S., and Menias, C.O. (2016). Extramedullary haematopoiesis: radiological imaging features. *Clin. Radiol.* 71, 807–814.
- Robey, P.G., Kuznetsov, S.A., Riminucci, M., and Bianco, P. (2014). Bone marrow stromal cell assays: in vitro and in vivo. *Methods Mol Biol* 1130, 279-293.
- Robey, P.G., Kuznetsov, S.A., Ren, J., Klein, H.G., Sabatino, M., and Stroncek, D.F. (2015). Generation of clinical grade human bone marrow stromal cells for use in bone regeneration. *Bone* 70, 87-92.
- Robin, C. (1875). Moelle des os. In DeChambre A., *Dictionnaire encyclopédique des sciences médicales*. Paris;:1-33.
- Robles, H., Park, S., Joens, M. S., Fitzpatrick, J. A., Craft, C. S., & Scheller, E. L. (2019). Characterization of the bone marrow adipocyte niche with three-dimensional electron microscopy. *Bone*, 118, 89-98.
- Rödling, L., Schwedhelm, I., Kraus, S., Bieback, K., Hansmann, J., and Lee-Thedieck, C. (2017). 3D models of the hematopoietic stem cell niche under steady-state and active conditions. *Sci. Rep.* 7, 4625.
- Rodrigues, A.C., Leal, T.F., Costa, A., Silva, F.J., Soares, L.L., Brum, P.C., et al. (2019). Effects of aerobic exercise on the inflammatory cytokine profile and expression of lipolytic and thermogenic genes in beta1-AR(-/-) mice adipose tissue. *Life Sci* 221, 224-232.
- Rodriguez-Fraticelli, A. E., Wolock, S. L., Weinreb, C. S., Panero, R., Patel, S. H., Jankovic, M., ... & Camargo, F. D. (2018). Clonal analysis of lineage fate in native haematopoiesis. *Nature*, 553(7687), 212.
- Ronaldson-Bouchard, K., and Vunjak-Novakovic, G. (2018). Organs-on-a-Chip: A Fast Track for Engineered Human Tissues in Drug Development. *Cell Stem Cell* 22, 310–324.
- Rosen, E. D., & Spiegelman, B. M. (2014). What we talk about when we talk about fat. *Cell*, 156(1-2), 20-44.
- Rosenthal, D.I., Hayes, C.W., Rosen, B., Mayo-Smith, W., and Goodsitt, M.M. (1989). Fatty replacement of spinal bone marrow due to radiation: demonstration by dual energy quantitative CT and MR imaging. *J Comput Assist Tomogr* 13, 463-465.
- Ruschke, S., Pokorney, A., Baum, T., Eggers, H., Miller, J. H., Hu, H. H., & Karampinos, D. C. (2017). Measurement of vertebral bone marrow proton density fat fraction in children using quantitative water–fat MRI. *Magnetic Resonance Materials in Physics, Biology and Medicine*, 30(5), 449-460.

## Bibliography

- Sacchetti, B., Funari, A., Michienzi, S., Di Cesare, S., Piersanti, S., Saggio, I., ... & Bianco, P. (2007). Self-renewing osteoprogenitors in bone marrow sinusoids can organize a hematopoietic microenvironment. *Cell*, 131(2), 324-336.
- Salmon, L.P.S., Y. Alexander (2007). "Application of Nano-CT and High-Resolution Micro-CT to Study Bone Quality and Ultrastructure, Scaffold Biomaterials and Vascular Networks," in *Advanced Bioimaging Technologies in Assessment of the Quality of Bone and Scaffold Materials*. Springer, Berlin, Heidelberg), 323-331.
- Salvadè, A., Belotti, D., Donzelli, E., D'Amico, G., Gaipa, G., Renoldi, G., Carini, F., Baldoni, M., Pogliani, E.M., Tredici, G., et al. (2007). GMP-grade preparation of biomimetic scaffolds with osteo-differentiated autologous mesenchymal stromal cells for the treatment of alveolar bone resorption in periodontal disease. *Cytotherapy* 9, 427–438.
- Sánchez-Aguilera, A., & Méndez-Ferrer, S. (2017). The hematopoietic stem-cell niche in health and leukemia. *Cellular and Molecular Life Sciences*, 74(4), 579-590.
- Sanchez-Gurmaches, J., Hsiao, W.Y., and Guertin, D.A. (2015). Highly selective in vivo labeling of subcutaneous white adipocyte precursors with Prx1-Cre. *Stem Cell Reports* 4, 541-550.
- Sanchez-Gurmaches, J., Hung, C.M., and Guertin, D.A. (2016). Emerging Complexities in Adipocyte Origins and Identity. *Trends Cell Biol* 26, 313-326.
- Sato, M., Westmore, M., Ma, Y.L., Schmidt, A., Zeng, Q.Q., Glass, E.V., et al. (2004). Teriparatide [PTH(1-34)] strengthens the proximal femur of ovariectomized nonhuman primates despite increasing porosity. *J Bone Miner Res* 19, 623-629.
- Sato, K., Feng, X., Chen, J., Li, J., Muranski, P., Desierto, M.J., et al. (2016). PPARgamma antagonist attenuates mouse immune-mediated bone marrow failure by inhibition of T cell function. *Haematologica* 101, 57-67.
- Savi, F.M., Brierly, G.I., Baldwin, J., Theodoropoulos, C., and Woodruff, M.A. (2017). Comparison of Different Decalcification Methods Using Rat Mandibles as a Model. *The Journal of Histochemistry and Cytochemistry: Official Journal of the Histochemistry Society* 65, 705-722.
- Schaffer, J. E., & Lodish, H. F. (1994). Expression cloning and characterization of a novel adipocyte long chain fatty acid transport protein. *Cell*, 79(3), 427-436.
- Scheller, E.L., & Rosen, C. J. (2014a). What's the matter with MAT? Marrow adipose tissue, metabolism, and skeletal health. *Annals of the New York Academy of Sciences*, 1311(1), 14.
- Scheller, E.L., Troiano, N., Vanhoutan, J.N., Bouxsein, M.A., Fretz, J.A., Xi, Y., et al. (2014b). Use of osmium tetroxide staining with microcomputerized tomography to visualize and quantify bone marrow adipose tissue in vivo. *Methods Enzymol* 537, 123-139.
- Scheller, E.L., Doucette, C.R., Learman, B.S., Cawthorn, W.P., Khandaker, S., Schell, B., et al. (2015). Region-specific variation in the properties of skeletal adipocytes reveals regulated and constitutive marrow adipose tissues. *Nat Commun* 6, 7808.
- Scheller, E. L., Khoury, B., Moller, K. L., Wee, N. K., Khandaker, S., Kozloff, K. M., ... & Singer, K. (2016). Changes in skeletal integrity and marrow adiposity during high-fat diet and after weight loss. *Frontiers in endocrinology*, 7, 102.
- Scheller, E.L., Khandaker, S., Learman, B.S., Cawthorn, W.P., Anderson, L.M., Pham, H.A., et al. (2019). Bone marrow adipocytes resist lipolysis and remodeling in response to beta-adrenergic stimulation. *Bone* 118, 32-41.
- Schleiden, MY (1838). *Contributions to phytogenesis*.

## Bibliography

- Schmal, O., Seifert, J., Schäffer, T.E., Walter, C.B., Aicher, W.K., and Klein, G. (2016). Hematopoietic Stem and Progenitor Cell Expansion in Contact with Mesenchymal Stromal Cells in a Hanging Drop Model Uncovers Disadvantages of 3D Culture.
- Schmitz, N., Beksac, M., Hasenclever, D., Bacigalupo, A., Ruutu, T., Nagler, A., ... & Szer, J. (2002). Transplantation of mobilized peripheral blood cells to HLA-identical siblings with standard-risk leukemia. *Blood*, 100(3), 761-767.
- Schofield, R. (1978). The relationship between the spleen colony-forming cell and the haemopoietic stem cell. *Blood cells*, 4(1-2), 7-25.
- Schwalie, P.C., Dong, H., Zachara, M., Russeil, J., Alpern, D., Akchiche, N., et al. (2018). A stromal cell population that inhibits adipogenesis in mammalian fat depots. *Nature* 559, 103-108.
- Schwann, T. H. (1847). *Microscopical Researches into the Accordance in the Structure and Growth of Animals and Plants*. РИПОЛ Класик.
- Scott, M.A., Nguyen, V.T., Levi, B., and James, A.W. (2011). Current methods of adipogenic differentiation of mesenchymal stem cells. *Stem Cells Dev* 20, 1793-1804.
- Scotti, C., Piccinini, E., Takizawa, H., Todorov, A., Bourguine, P., Papadimitropoulos, A., Barbero, A., Manz, M.G., and Martin, I. (2013). Engineering of a functional bone organ through endochondral ossification. *Proc. Natl. Acad. Sci. U. S. A.* 110, 3997–4002.
- Seale, P., Kajimura, S., Yang, W., Chin, S., Rohas, L. M., Uldry, M., ... & Spiegelman, B. M. (2007). Transcriptional control of brown fat determination by PRDM16. *Cell metabolism*, 6(1), 38-54.
- Seale, P., Bjork, B., Yang, W., Kajimura, S., Chin, S., Kuang, S., ... & Tempst, P. (2008). PRDM16 controls a brown fat/skeletal muscle switch. *Nature*, 454(7207), 961.
- Seimandi, M., Lemaire, G., Pillon, A., Perrin, A., Carlván, I., Voegel, J.J., et al. (2005). Differential responses of PPARalpha, PPARdelta, and PPARgamma reporter cell lines to selective PPAR synthetic ligands. *Analytical Biochemistry* 344, 8-15.
- Serafini, M., Sacchetti, B., Pievani, A., Redaelli, D., Remoli, C., Biondi, A., et al. (2014). Establishment of bone marrow and hematopoietic niches in vivo by reversion of chondrocyte differentiation of human bone marrow stromal cells. *Stem Cell Res* 12, 659-672.
- Serex, L., Bräschler, T., Filippova, A., Rochat, A., Bédier, A., Bertsch, A., and Renaud, P. (2018). Pore Size Manipulation in 3D Printed Cryogels Enables Selective Cell Seeding. *Adv. Mater. Technol.* 3, 1700340.
- Shafat, M. S., Oellerich, T., Mohr, S., Robinson, S. D., Edwards, D. R., Marlein, C. R., et. al. (2017). Leukemic blasts program bone marrow adipocytes to generate a protumoral microenvironment. *Blood*, 129(10), 1320-1332.
- Shafiee, A., Baldwin, J.G., Patel, J., Holzapfel, B.M., Fisk, N.M., Khosrotehrani, K., and Huttmacher, D.W. (2017). Fetal Bone Marrow-Derived Mesenchymal Stem/Stromal Cells Enhance Humanization and Bone Formation of BMP7 Loaded Scaffolds. *Biotechnol. J.* 12.
- Shah, S.B., and Singh, A. (2017). Creating artificial lymphoid tissues to study immunity and hematological malignancies. *Curr. Opin. Hematol.* 24, 377–383.
- Shah, N.J., Mao, A.S., Shih, T.-Y., Kerr, M.D., Sharda, A., Raimondo, T.M., Weaver, J.C., Vrbanc, V.D., Deruaz, M., Tager, A.M., et al. (2019). An injectable bone marrow-like scaffold enhances T cell immunity after hematopoietic stem cell transplantation. *Nat. Biotechnol.* 37, 293–302.



## Bibliography

- Shao, M., Vishvanath, L., Busbuso, N. C., Hepler, C., Shan, B., Sharma, A. X., ... & Holland, W. L. (2018). De novo adipocyte differentiation from Pdgfr $\beta$ + preadipocytes protects against pathologic visceral adipose expansion in obesity. *Nature communications*, 9(1), 890.
- Shergill, K. K., Shergill, G. S., & Pillai, H. J. (2017). Gelatinous transformation of bone marrow: rare or underdiagnosed?. *Autopsy & case reports*, 7(4), 8.
- Shih, Y.-R., Kang, H., Rao, V., Chiu, Y.-J., Kwon, S.K., and Varghese, S. (2017). In vivo engineering of bone tissues with hematopoietic functions and mixed chimerism. *Proc. Natl. Acad. Sci. U. S. A.* 114, 5419–5424.
- Sieber, S., Wirth, L., Cavak, N., Koenigsmark, M., Marx, U., Lauster, R., and Rosowski, M. (2018). Bone marrow-on-a-chip: Long-term culture of human haematopoietic stem cells in a three-dimensional microfluidic environment. *J. Tissue Eng. Regen. Med.* 12, 479–489.
- Silbernagel, G., Kovarova, M., Cegan, A., Machann, J., Schick, F., Lehmann, R., ... & Peter, A. (2012). High hepatic SCD1 activity is associated with low liver fat content in healthy subjects under a lipogenic diet. *The Journal of Clinical Endocrinology & Metabolism*, 97(12), E2288-E2292.
- Silva, J., Zanette, I., Noël, P.B., Cardoso, M.B., Kimm, M.A., and Pfeiffer, F. (2015). Three-dimensional non-destructive soft-tissue visualization with X-ray staining micro-tomography. *Scientific Reports* 5, 1-7.
- Smus, J.P., Moura, C.C., Mcmorrow, E., Tare, R.S., Oreffo, R.O.C., and Mahajan, S. (2015). Tracking adipogenic differentiation of skeletal stem cells by label-free chemically selective imaging. *Chem Sci* 6, 7089-7096.
- Soleimani, M., and Nadri, S. (2009). A protocol for isolation and culture of mesenchymal stem cells from mouse bone marrow. *Nat Protoc* 4, 102-106.
- Song, Y., Rongvaux, A., Taylor, A., Jiang, T., Tebaldi, T., Balasubramanian, K., Bagale, A., Terzi, Y.K., Gbyli, R., Wang, X., et al. (2019). A highly efficient and faithful MDS patient-derived xenotransplantation model for pre-clinical studies. *Nat. Commun.* 10, 366.
- Soriano, P. (1999). Generalized lacZ expression with the ROSA26 Cre reporter strain. *Nat Genet* 21, 70-71.
- Sottile, V., Seuwen, K., and Kneissel, M. (2004). Enhanced marrow adipogenesis and bone resorption in estrogen-deprived rats treated with the PPAR $\gamma$  agonist BRL49653 (rosiglitazone). *Calcif Tissue Int* 75, 329-337.
- Spangrude, G. J., Heimfeld, S., & Weissman, I. L. (1988). Purification and characterization of mouse hematopoietic stem cells. *Science*, 241(4861), 58-62.
- Spindler, T. J., Tseng, A. W., Zhou, X., & Adams, G. B. (2013). Adipocytic cells augment the support of primitive hematopoietic cells in vitro but have no effect in the bone marrow niche under homeostatic conditions. *Stem cells and development*, 23(4), 434-441.
- Sreejit, P., Dilip, K.B., and Verma, R.S. (2012). Generation of mesenchymal stem cell lines from murine bone marrow. *Cell Tissue Res* 350, 55-68.
- Stiebing, C., Schmölz, L., Wallert, M., Matthäus, C., Lorkowski, S., & Popp, J. (2017). Raman imaging of macrophages incubated with triglyceride-enriched oxLDL visualizes translocation of lipids between endocytic vesicles and lipid droplets. *Journal of lipid research*, 58(5), 876-883.
- Strable, M. S., & Ntambi, J. M. (2010). Genetic control of de novo lipogenesis: role in diet-induced obesity. *Critical reviews in biochemistry and molecular biology*, 45(3), 199-214.
- Styner, M., Thompson, W.R., Galior, K., Uzer, G., Wu, X., Kadari, S., et al. (2014). Bone marrow fat accumulation accelerated by high fat diet is suppressed by exercise. *Bone* 64, 39-46.

## Bibliography

- Styner, M., Pagnotti, G.M., Mcgrath, C., Wu, X., Sen, B., Uzer, G., et al. (2017). Exercise Decreases Marrow Adipose Tissue Through ss-Oxidation in Obese Running Mice. *J Bone Miner Res* 32, 1692-1702.
- Suchacki, K.J., and Cawthorn, W.P. (2018). Molecular Interaction of Bone Marrow Adipose Tissue with Energy Metabolism. *Curr Mol Biol Rep* 4, 41-49.
- Sugiyama, T., Kohara, H., Noda, M., and Nagasawa, T. (2006). Maintenance of the hematopoietic stem cell pool by CXCL12-CXCR4 chemokine signaling in bone marrow stromal cell niches. *Immunity* 25, 977-988.
- Sugiyama, T., and Takashi N. (2012). Bone Marrow Niches for Hematopoietic Stem Cells and Immune Cells. *Inflammation & Allergy-Drug Targets* 11 (3): 201-6.
- Sui, B., Hu, C., Liao, L., Chen, Y., Zhang, X., Fu, X., et al. (2016). Mesenchymal progenitors in osteopenias of diverse pathologies: differential characteristics in the common shift from osteoblastogenesis to adipogenesis. *Sci Rep* 6, 30186.
- Suire, C., Brouard, N., Hirschi, K., and Simmons, P.J. (2012). Isolation of the stromal-vascular fraction of mouse bone marrow markedly enhances the yield of clonogenic stromal progenitors. *Blood* 119, e86-95.
- Sulston, R.J., Learman, B.S., Zhang, B., Scheller, E.L., Parlee, S.D., Simon, B.R., et al. (2016). Increased Circulating Adiponectin in Response to Thiazolidinediones: Investigating the Role of Bone Marrow Adipose Tissue. *Front Endocrinol (Lausanne)* 7, 128.
- Supper, E., Tahir, S., Imai, T., Inoue, J., and Minato, N. (2015). Modification of Gene Expression, Proliferation, and Function of OP9 Stroma Cells by Bcr-Abl-Expressing Leukemia Cells. *PLOS ONE* 10, e0134026.
- Syed, F.A., Oursler, M.J., Hefferanm, T.E., Peterson, J.M., Riggs, B.L., and Khosla, S. (2008). Effects of estrogen therapy on bone marrow adipocytes in postmenopausal osteoporotic women. *Osteoporos Int* 19, 1323-1330.
- Szymanski, K. M., Binns, D., Bartz, R., Grishin, N. V., Li, W. P., Agarwal, A. K., ... & Goodman, J. M. (2007). The lipodystrophy protein seipin is found at endoplasmic reticulum lipid droplet junctions and is important for droplet morphology. *Proceedings of the National Academy of Sciences*, 104(52), 20890-20895.
- Tajer, P., Pike-Overzet, K., Arias, S., Havenga, M., and Staal, F.J.T. (2019). Ex Vivo Expansion of Hematopoietic Stem Cells for Therapeutic Purposes: Lessons from Development and the Niche. *Cells* 8, 169.
- Takeshita, S., Fumoto, T., Naoe, Y., and Ikeda, K. (2014). Age-related marrow adipogenesis is linked to increased expression of RANKL. *J Biol Chem* 289, 16699-16710.
- Tanavde, V., Vaz, C., Rao, M.S., Vemuri, M.C., and Pochampally, R.R. (2015). Research using Mesenchymal Stem/Stromal Cells: quality metric towards developing a reference material. *Cytotherapy* 17, 1169-1177.
- Tang, H., Brennan, J., Karl, J., Hamada, Y., Raetzman, L., & Capel, B. (2008). Notch signaling maintains Leydig progenitor cells in the mouse testis. *Development*, 135(22), 3745-3753.
- Tavassoli, M., & Crosby, W. H. (1968). Transplantation of marrow to extramedullary sites. *Science*, 161(3836), 54-56.
- Tavassoli, M., & Crosby, W. H. (1970). Bone marrow histogenesis: a comparison of fatty and red marrow. *Science*, 169(3942), 291-293.
- Tavassoli, M. (1974). Differential response of bone marrow and extramedullary adipose cells to starvation. *Cellular and Molecular Life Sciences*, 30(4), 424-425.
- Tavassoli, M. (1976a). Marrow adipose cells. Histochemical identification of labile and stable components. *Arch Pathol Lab Med* 100, 16-18.
- Tavassoli, M. (1976b). Ultrastructural development of bone marrow adipose cell. *Cells Tissues Organs*, 94(1), 65-77.

- Tavassoli, M., & Yoffey, J. M. (1983). *Bone marrow, structure and function*. AR Liss.
- Tavassoli, M. (1989). *Handbook of the hemopoietic microenvironment*. Springer Science & Business Media.
- Tencerova, M., Figeac, F., Ditzel, N., Taipaleenmäki, H., Nielsen, T. K., & Kassem, M. (2018). High-Fat Diet–Induced Obesity Promotes Expansion of Bone Marrow Adipose Tissue and Impairs Skeletal Stem Cell Functions in Mice. *Journal of Bone and Mineral Research*, 33(6), 1154-1165.
- Thiam, A. R., & Beller, M. (2017). The why, when and how of lipid droplet diversity. *Journal of cell science*, 130(2), 315-324.
- Thouzeau, C., Massemin, S., & Handrich, Y. (1997). Bone marrow fat mobilization in relation to lipid and protein catabolism during prolonged fasting in barn owls. *Journal of Comparative Physiology B*, 167(1), 17-24.
- Till, J. E., & McCulloch, E. A. (1961). A direct measurement of the radiation sensitivity of normal mouse bone marrow cells. *Radiation research*, 14(2), 213-222.
- Till, J. E., McCulloch, E. A., & Siminovitch, L. (1964). A stochastic model of stem cell proliferation, based on the growth of spleen colony-forming cells. *Proceedings of the National Academy of Sciences of the United States of America*, 51(1), 29.
- Till, J. E., & McCulloch, E. A. (1980). Hemopoietic stem cell differentiation. *Biochimica et Biophysica Acta (BBA)-Reviews on Cancer*, 605(4), 431-459.
- Torisawa, Y.S., Spina, C.S., Mammoto, T., Mammoto, A., Weaver, J.C., Tat, T., et al. (2014). Bone marrow-on-a-chip replicates hematopoietic niche physiology in vitro. *Nat Methods* 11, 663-669.
- Tormin, A., Li, O., Brune, J.C., Walsh, S., Schutz, B., Ehinger, M., et al. (2011). CD146 expression on primary nonhematopoietic bone marrow stem cells is correlated with in situ localization. *Blood* 117, 5067-5077.
- Tornvig, L., Mosekilde, L.I., Justesen, J., Falk, E., and Kassem, M. (2001). Troglitazone treatment increases bone marrow adipose tissue volume but does not affect trabecular bone volume in mice. *Calcif Tissue Int* 69, 46-50.
- Trentin, J. J. (1970). Regulation of Hematopoiesis, vol. 1 (Gordon, AS, ed.). *Appleton-Century-Crofts, New York*, 161-186.
- Trentin, J. J. (1971). Determination of bone marrow stem cell differentiation by stromal hemopoietic inductive microenvironments (HIM). *The American journal of pathology*, 65(3), 621.
- Trudel, G., Payne, M., Mädler, B., Ramachandran, N., Lecompte, M., Wade, C., ... & Uhthoff, H. K. (2009). Bone marrow fat accumulation after 60 days of bed rest persisted 1 year after activities were resumed along with hemopoietic stimulation: the Women International Space Simulation for Exploration study. *Journal of Applied Physiology*, 107(2), 540-548.
- Trudel, G., Uhthoff, H. K., Solanki, S., & Laneuville, O. (2017). The effects of knee immobilization on marrow adipocyte hyperplasia and hypertrophy at the proximal rat tibia epiphysis. *Acta histochemica*, 119(7), 759-765.
- Tucci, J., Alhushki, W., Chen, T., Sheng, X., Kim, Y.M., and Mittelman, S.D. (2018). Switch to low-fat diet improves outcome of acute lymphoblastic leukemia in obese mice. *Cancer Metab* 6, 15.
- Tuljapurkar, S.R., Mcguire, T.R., Brusnahan, S.K., Jackson, J.D., Garvin, K.L., Kessinger, M.A., et al. (2011). Changes in human bone marrow fat content associated with changes in hematopoietic stem cell numbers and cytokine levels with aging. *J Anat* 219, 574-581.
- Turello, R., Snyder, D., and Hartman, H.A. (1984). A Modification the Osmium Tetroxide Post-Fixation Technique for the Demonstration of Extracellular Lipid in Paraffin-Embedded Tissue Sections. *Journal of Histotechnology* 7, 75-77.

## Bibliography

- Turner, R. T., Wong, C. P., & Iwaniec, U. T. (2011). Effect of Reduced c-Kit Signaling on Bone Marrow Adiposity. *The Anatomical Record: Advances in Integrative Anatomy and Evolutionary Biology*, 294(7), 1126-1134.
- Turner, R.T., Philbrick, K.A., Wong, C.P., Olson, D.A., Branscum, A.J., and Iwaniec, U.T. (2014). Morbid obesity attenuates the skeletal abnormalities associated with leptin deficiency in mice. *J Endocrinol* 223, M1-15.
- Vaiselbuh, S.R., Edelman, M., Lipton, J.M., and Liu, J.M. (2010). Ectopic human mesenchymal stem cell-coated scaffolds in NOD/SCID mice: an in vivo model of the leukemia niche. *Tissue Eng. Part C Methods* 16, 1523–1531.
- Van Leeuwen, S.P., Bovee, T.F., Awchi, M., Klijnstra, M.D., Hamers, A.R., Hoogenboom, R.L., et al. (2019). BPA, BADGE and analogues: A new multi-analyte LC-ESI-MS/MS method for their determination and their in vitro (anti)estrogenic and (anti)androgenic properties. *Chemosphere* 221, 246-253.
- Veldhuis-Vlug, A.G., and Rosen, C.J. (2018). Clinical implications of bone marrow adiposity. *Journal of Internal Medicine* 283, 121-139.
- Velten, L., Haas, S. F., Raffel, S., Blaszkiewicz, S., Islam, S., Hennig, B. P., ... & Boch, T. (2017). Human haematopoietic stem cell lineage commitment is a continuous process. *Nature cell biology*, 19(4), 271.
- Ventura Ferreira, M.S., Bergmann, C., Bodensiek, I., Peukert, K., Abert, J., Kramann, R., Kachel, P., Rath, B., Rütten, S., Knuchel, R., et al. (2016). An engineered multicomponent bone marrow niche for the recapitulation of hematopoiesis at ectopic transplantation sites. *J. Hematol. Oncol.* J Hematol Oncol 9, 4.
- Visnjic, D., Kalajzic, I., Gronowicz, G., Aguila, H. L., Clark, S. H., Lichtler, A. C., & Rowe, D. W. (2001). Conditional ablation of the osteoblast lineage in Col2. 3 $\Delta$ tk transgenic mice. *Journal of bone and mineral research*, 16(12), 2222-2231.
- Visnjic, D., Kalajzic, Z., Rowe, D. W., Katavic, V., Lorenzo, J., & Aguila, H. L. (2004). Hematopoiesis is severely altered in mice with an induced osteoblast deficiency. *Blood*, 103(9), 3258-3264.
- Wang, F.S., Lian, W.S., Weng, W.T., Sun, Y.C., Ke, H.J., Chen, Y.S., et al. (2016). Neuropeptide Y mediates glucocorticoid-induced osteoporosis and marrow adiposity in mice. *Osteoporos Int* 27, 2777-2789.
- Wang, J., Chen, G.L., Cao, S., Zhao, M.C., Liu, Y.Q., Chen, X.X., et al. (2017). Adipogenic niches for melanoma cell colonization and growth in bone marrow. *Lab Invest* 97, 737-745.
- Wang, Q. A., Song, A., Chen, W., Schwalie, P. C., Zhang, F., Vishvanath, L., et. al. (2018). Reversible de-differentiation of mature white adipocytes into preadipocyte-like precursors during lactation. *Cell metabolism*, 28(2), 282-288.
- Wei, Q., and Frenette, P.S. (2018). Niches for Hematopoietic Stem Cells and Their Progeny. *Immunity* 48, 632–648.
- Weiss, L. (1976). The hematopoietic microenvironment of the bone marrow: an ultrastructural study of the stroma in rats. *The Anatomical Record*, 186(2), 161-184.
- Weiss, L. (1981). Haemopoiesis in Mammalian Bone Marrow. In Ciba Foundation Symposium 84 - Microenvironments in Haemopoietic and Lymphoid Differentiation, (Wiley-Blackwell), pp. 5–21.
- Weissman, I.L. (2000). Translating stem and progenitor cell biology to the clinic: barriers and opportunities. *Science*, 287(5457), 1442-1446.
- Weissman, I.L., and Shizuru, J.A. (2008). The origins of the identification and isolation of hematopoietic stem cells, and their capability to induce donor-specific transplantation tolerance and treat autoimmune diseases. *Blood* 112, 3543–3553.
- Wesseling-Perry, K., Makitie, R.E., Valimaki, V.V., Laine, T., Laine, C.M., Valimaki, M.J., et al. (2017). Osteocyte Protein Expression Is Altered in Low-Turnover Osteoporosis Caused by Mutations in WNT1 and PLS3. *J Clin Endocrinol Metab* 102, 2340-2348.

- Whitfield, M.J., Cheng, W., Lee, J., and Vliet, K.J.V. (2013). ScienceDirect Onset of heterogeneity in culture-expanded bone marrow stromal cells. *Stem Cell Research* 11, 1365-1377.
- Wilson, A., Fu, H., Schiffrin, M., Winkler, C., Koufany, M., Jouzeau, J.Y., et al. (2018). Lack of Adipocytes Alters Hematopoiesis in Lipodystrophic Mice. *Front Immunol* 9, 2573.
- Wolf, N. S., & Trentin, J. J. (1968). Hemopoietic colony studies: V. Effect of hemopoietic organ stroma on differentiation of pluripotent stem cells. *Journal of Experimental Medicine*, 127(1), 205-214.
- Wolins, N. E., Quaynor, B. K., Skinner, J. R., Tzekov, A., Park, C., Choi, K., & Bickel, P. E. (2006). OP9 mouse stromal cells rapidly differentiate into adipocytes: characterization of a useful new model of adipogenesis. *Journal of lipid research*, 47(2), 450-460.
- Worthley, D.L., Churchill, M., Compton, J.T., Taylor, Y., Rao, M., Si, Y., et al. (2015). Gremlin 1 identifies a skeletal stem cell with bone, cartilage, and reticular stromal potential. *Cell* 160, 269-284.
- Worton, R. G., McCulloch, E. A., & Till, J. E. (1969). Physical separation of hemopoietic stem cells from cells forming colonies in culture. *Journal of cellular physiology*, 74(2), 171-182.
- Wu, J., Boström, P., Sparks, L. M., Ye, L., Choi, J. H., Giang, A. H., ... & Huang, K. (2012). Beige adipocytes are a distinct type of thermogenic fat cell in mouse and human. *Cell*, 150(2), 366-376.
- Xiao, Z., Cao, L., Liang, Y., Huang, J., Stern, A.R., Dallas, M., et al. (2014). Osteoblast-specific deletion of Pkd2 leads to low-turnover osteopenia and reduced bone marrow adiposity. *PLoS One* 9, e114198.
- Yang, R., Davies, C.M., Archer, C.W., and Richards, R.G. (2003). Immunohistochemistry of matrix markers in Technovit 9100 New-embedded undecalcified bone sections. *European Cells & Materials* 6, 57-71; discussion 71.
- Yang, Y., Luo, X., Xie, X., Yan, F., Chen, G., Zhao, W., et al. (2016). Influences of teriparatide administration on marrow fat content in postmenopausal osteopenic women using MR spectroscopy. *Climacteric* 19, 285-291.
- Yang, Y.J., Zhu, Z., Wang, D.T., Zhang, X.L., Liu, Y.Y., Lai, W.X., et al. (2018). Tanshinol alleviates impaired bone formation by inhibiting adipogenesis via KLF15/PPARGgamma2 signaling in GIO rats. *Acta Pharmacol Sin* 39, 633-641.
- Yeung, D.K., Griffith, J.F., Antonio, G.E., Lee, F.K., Woo, J., and Leung, P.C. (2005). Osteoporosis is associated with increased marrow fat content and decreased marrow fat unsaturation: a proton MR spectroscopy study. *J Magn Reson Imaging* 22, 279-285.
- Yokota, T., Meka, C. R., Kouro, T., Medina, K. L., Igarashi, H., Takahashi, M., et. al. (2003). Adiponectin, a fat cell product, influences the earliest lymphocyte precursors in bone marrow cultures by activation of the cyclooxygenase-prostaglandin pathway in stromal cells. *The Journal of Immunology*, 171(10), 5091-5099.
- Yoshii, T., Sotome, S., Torigoe, I., Tsuchiya, A., Maehara, H., Ichinose, S., and Shinomiya, K. (2009). Fresh bone marrow introduction into porous scaffolds using a simple low-pressure loading method for effective osteogenesis in a rabbit model. *J. Orthop. Res. Off. Publ. Orthop. Res. Soc.* 27, 1–7.
- Yu, H., Shimakawa, A., McKenzie, C.A., Brodsky, E., Brittain, J.H., and Reeder, S.B. (2008). Multiecho water-fat separation and simultaneous R2\* estimation with multifrequency fat spectrum modeling. *Magn Reson Med* 60, 1122-1134.
- Yu, B., Huo, L., Liu, Y., Deng, P., Szymanski, J., Li, J., et al. (2018). PGC-1alpha Controls Skeletal Stem Cell Fate and Bone-Fat Balance in Osteoporosis and Skeletal Aging by Inducing TAZ. *Cell Stem Cell* 23, 193-209 e195.
- Yue, R., Zhou, B.O., Shimada, I.S., Zhao, Z., and Morrison, S.J. (2016). Leptin Receptor Promotes Adipogenesis and Reduces Osteogenesis by Regulating Mesenchymal Stromal Cells in Adult Bone Marrow. *Cell Stem Cell* 18, 782-796.

## Bibliography

- Zechner, R., Zimmermann, R., Eichmann, T. O., Kohlwein, S. D., Haemmerle, G., Lass, A., & Madeo, F. (2012). FAT SIGNALS-lipases and lipolysis in lipid metabolism and signaling. *Cell metabolism*, 15(3), 279-291.
- Zhang, J., Niu, C., Ye, L., Huang, H., He, X., Tong, W. G., ... & Harris, S. (2003). Identification of the haematopoietic stem cell niche and control of the niche size. *Nature*, 425(6960), 836.
- Zhang, Y., Marsboom, G., Toth, P. T., & Rehman, J. (2013). Mitochondrial respiration regulates adipogenic differentiation of human mesenchymal stem cells. *PLoS one*, 8(10), e77077.
- Zhang, T., Duan, Y., Ye, J., Xu, W., Shu, N., Wang, C., et al. (2018a). Brain MRI Characteristics of Patients with Anti-N-Methyl-D-Aspartate Receptor Encephalitis and Their Associations with 2-Year Clinical Outcome. *AJNR Am J Neuroradiol* 39, 824-829.
- Zhang, Y., Zhou, Z., Wang, C., Cheng, X., Wang, L., Duanmu, Y., ... & Guglielmi, G. (2018b). Reliability of measuring the fat content of the lumbar vertebral marrow and paraspinal muscles using MRI mDIXON-Quant sequence. *Diagnostic and Interventional Radiology*, 24(5), 302.
- Zhou, B.O., Yue, R., Murphy, M.M., Peyer, J.G., and Morrison, S.J. (2014). Leptin-receptor-expressing mesenchymal stromal cells represent the main source of bone formed by adult bone marrow. *Cell Stem Cell* 15, 154-168.
- Zhou, H., Lei, X., Benson, T., Mintz, J., Xu, X., Harris, R. B., ... & Chen, W. (2015). Berardinelli-Seip congenital lipodystrophy 2 regulates adipocyte lipolysis, browning, and energy balance in adult animals. *Journal of lipid research*, 56(10), 1912-1925.
- Zhou, B.O., Yu, H., Yue, R., Zhao, Z., Rios, J.J., Naveiras, O., et al. (2017). Bone marrow adipocytes promote the regeneration of stem cells and haematopoiesis by secreting SCF. *Nat Cell Biol* 19, 891-903.
- Zhu, H., Guo, Z.K., Jiang, X.X., Li, H., Wang, X.Y., Yao, H.Y., et al. (2010). A protocol for isolation and culture of mesenchymal stem cells from mouse compact bone. *Nat Protoc* 5, 550-560.
- Zhu, R.J., Wu, M.Q., Li, Z.J., Zhang, Y., and Liu, K.Y. (2013). Hematopoietic recovery following chemotherapy is improved by BADGE-induced inhibition of adipogenesis. *Int J Hematol* 97, 58-72.
- Zhu, H.H., Jiang, H., Jiang, Q., Jia, J.S., Qin, Y.Z., and Huang, X.J. (2016). Homoharringtonine, aclarubicin and cytarabine (HAA) regimen as the first course of induction therapy is highly effective for acute myeloid leukemia with t (8;21). *Leuk Res* 44, 40-44.
- Zhu, Y., Zhao, H., Zhang, X., Wu, Y., Xie, Y., Li, Y., et al. (2017). Decitabine before Low-Dose Cytarabine-Based Chemotherapy Combined with Human Leukocyte Antigen-Mismatched Stem Cell Microtransplantation Improved Outcomes in Elderly Patients with Newly Diagnosed Acute Myeloid Leukemia. *Biol Blood Marrow Transplant* 23, 830-835.
- Zimmermann, R., Strauss, J. G., Haemmerle, G., Schoiswohl, G., Birner-Gruenberger, R., Riederer, M., ... & Zechner, R. (2004). Fat mobilization in adipose tissue is promoted by adipose triglyceride lipase. *Science*, 306(5700), 1383-1386.
- Zou, Q., Hong, W., Zhou, Y., Ding, Q., Wang, J., Jin, W., et al. (2016). Bone marrow stem cell dysfunction in radiation-induced abscopal bone loss. *J Orthop Surg Res* 11, 3.
- Zwick, R. K., Rudolph, M. C., Shook, B. A., Holtrup, B., Roth, E., Lei, V., et al. (2018). Adipocyte hypertrophy and lipid dynamics underlie mammary gland remodeling after lactation. *Nature communications*, 9(1), 3592.

# CURRICULUM VITAE

## Josefine Tratwal

Address IBI/ISREC, SV-2518, Station 19, EPFL, 1015 Lausanne, Switzerland  
 Phone +41 (0) 21 693 72 17 (lab)  
 E-mail josefine.tratwal@epfl.ch  
 Languages English, German, Danish (primary), French, Polish (secondary)

### EDUCATION & EXPERIENCE

|             |  |
|-------------|--|
| 2014 – 2019 | <b>PhD, Biotechnology &amp; Bioengineering</b>   Laboratory of Regenerative Hematopoiesis<br>École polytechnique fédérale de Lausanne, Switzerland // Prof. Naveiras |
| 2012 – 2014 | <b>Research Assistant</b>   Cardiology Stem Cell Center, University Hospital Copenhagen, Denmark   |
| 2009 – 2012 | <b>MSc, Molecular Biomedicine</b>   University of Copenhagen, Denmark // Prof. Kastrup   |
| 2010        | <b>Research Intern</b>   Center of Regenerative Medicine in Barcelona, Spain // Prof. Izpisua Belmonte   |
| 2006 – 2009 | <b>BSc, Molecular Biomedicine</b>   University of Copenhagen, Denmark // Prof. Høiriis-Nielsen   |
| 2004 – 2006 | <b>International Baccalaureate</b>   Rensselaer Medalist. American School of Warsaw, Poland  |

### SELECTED ACTIVITIES

|                       |   |
|-----------------------|---|
| 2018 – <i>present</i> | <b>Coordinator</b>   Methodologies Working Group, International Bone Marrow Adiposity Society   |
| 2019                  | <b>Course</b>   PRINCE2 Foundation Certificate in Project Management<br><b>Invited talk</b>   26 <sup>th</sup> European Congress on Obesity, Glasgow, Scotland  |
| 2018                  | <b>Selected talk</b>   Grant. 18 <sup>th</sup> International Congress of Endocrinology, Cape Town, South Africa   |
| 2016 – 2017           | <b>Conference manager</b>   3 <sup>rd</sup> International Meeting on Bone Marrow Adiposity, Lausanne, Switzerland   |
| 2016                  | <b>Selected talk</b>   5 <sup>th</sup> Faculty and Staff Retreat of the Swiss Cancer Center Lausanne, Switzerland<br><b>Poster</b>   Grant. Keystone Symposium: Obesity and Adipose Tissue Biology, Banff, Canada |
| 2013                  | <b>Course</b>   Intensive Hands-on Flow Cytometry, University of York, England  |
| 2012                  | <b>Poster</b>   Grant. European Summer School on Stem Cells & Regenerative Medicine, Hydra, Greece  |

### SELECTED PUBLICATIONS

- \* equal author contribution*
- Bonini F, **Tratwal J**, Tavakol DN, Genta M, Bédier A, Naveiras O, Braschler T. Device and process for tissue engineering and regenerative medicine. *Application EP19020673.0* (2019). (*inventor order unknown*)
  - Tratwal J**\*, Falgayrac G\*, During A, Bertheaume N, Tavakol DN, Duponchel L, Penel G, Naveiras O. *In vitro* model of bone marrow adipocyte subtypes with distinct lipid signatures at the single droplet level. (*manuscript in preparation*)
  - Tratwal J**, Bekri I\*, Boussema C\*, Kunz N, Koliqi T, Rojas-Sutterlin S, Schyrr F, Tavakol DN, Campos V, Scheller EL, Sarro R, Bárcena C, Bisig B, Nardi V, De Leval L, Burri O, Naveiras O. MarrowQuant: Semi-Automated digital pathology quantification tool for histological bone marrow sections. (*manuscript in preparation*)
  - Rojas-Sutterlin S, Aaron P, S Frédérica, **Tratwal J**, Dorier J, Sizzano F, Guex N, Miguel G, Naveiras O. Flow Cytometry-based Unbiased Clustering Algorithm Discriminates Rare Bone Marrow Stromal Compartments in the Reversible Radiation-Induced Bone Marrow Adipocytic Aplasia. (*manuscript in preparation*)
  - Tratwal J**, Rossella L, Bravenboer N, Kerckhofs G, Douni E, Scheller E, Badr S, Karampinos D, Beck-Cormier S, Palmisano B, Poloni A, Moreno-Aliaga MJ, Fretz J, Rodeheffer M, Boroumand P, Rosen CJ, Horowitz M, van der Eerden B, Veldhuis-Vlug AG, Naveiras O. Bone Marrow Adiposity: a review of methodological standards and challenges towards harmonization. *Front Endocrinol.* 2020 Jan 31; 10:65. (*manuscript accepted*)
  - Tavakol DN\*, **Tratwal J**\*, Bonini F\*, Genta M, Campos V, Burch P, Hoehnel S, Bédier A, Allesandrini M, Naveiras O, Braschler T. Injectable, Scalable 3D Tissue-Engineered Model of Marrow Hematopoiesis. *Biomaterials.* 2020 Feb 11; 232:119665.
  - Vannini N\*, Campos V\*, Girotra M, Trachsel V, Rojas-Sutterlin S, **Tratwal J**, Ragusa S, Stefanidis E, Ryu D, Rainer PY, Nikitin G, Giger S, Tertyty YL, Semilietof A, Yersin Y, Cheng WC, Tauzin L, Pirinen E, Ratajczak J, Canto C, Ehrbar M, Sizzano F, Palini A, Petrova TV, Vanhecke D, Nahimana A, Duchosal MA, Ho PC, Deplancke B, Coukos G, Auwerx J, Lutolf MP, Naveiras O. The NAD-Booster Nicotinamide Riboside Potently Stimulates Hematopoiesis through Increased Mitochondrial Clearance. *Cell Stem Cell.* 2019 Mar 7; 24(3):405-418.
  - Tratwal J**, Mathiasen AB, Juhl M, Brorsen SK, Kastrup J, Ekblond A. Influence of VEGF stimulation and serum deprivation on gene activation patterns of human adipose tissue-derived stromal cells. *Stem Cell Res Ther* 2015 Apr 13; 6:62.
  - Follin B\*, **Tratwal J**\*, Haack-Sorensen M, Elberg JJ, Kastrup J, Ekblond A. Identical effects of VEGF and serum-deprivation on phenotype and function of adipose-derived stromal cells from healthy donors and patients with ischemic heart disease. *J Transl Med.* 2013 Sep 18; 11:219.

